

Measuring water-vapour and carbon-dioxide Fluxes at Field scales with Scintillometry

A.J.H. (Bram) van Kesteren

Thesis committee

Promoters

Prof.dr. A.A.M Holtslag
Professor of Meteorology
Wageningen University

Co-promoter

Dr.ir. O.K. Hartogensis
Assistant professor, Meteorology and Air Quality Group
Wageningen University

Other members

Prof.dr.ir. R. Uijlenhoet, Wageningen University
Dr. F. Beyrich, Deutscher Wetterdienst, Tauche OT Lindenberg, Germany
Dr. B. Kruijt, Alterra, Wageningen
Prof. Dr.ir. B.J.J.M van den Hurk, KNMI, De Bilt/Utrecht University

This research was conducted under the auspices of the SENSE research school

Measuring water-vapour and carbon-dioxide Fluxes at Field scales with Scintillometry

Abraham (Bram) J.H. van Kesteren

Thesis

Submitted in fulfilment of the requirements for the degree of doctor
at Wageningen University

by the authority of the Rector Magnificus

Prof.dr. M.J. Kropff,

in the presence of the

Thesis Committee appointed by the Academic Board

to be defended in public

on Monday 17 December 2012

at 4 p.m. in the Aula.

A.J.H. (Bram) van Kesteren

Measuring water-vapour and carbon-dioxide Fluxes at Field scales with Scintillometry
212 pages.

PhD thesis, Wageningen University, Wageningen, NL (2012)

With references, with summaries in Dutch and English

ISBN 978-94-6173-423-5

Abstract

Scintillometry is a measurement technique that has proven itself to be of great value for measuring spatial-averaged fluxes of sensible heat, momentum, and evapotranspiration. Furthermore, for crop fields (field scales), scintillometry has been shown to accurately determine the sensible-heat and momentum flux over time intervals as short as 6 seconds. As a consequence, interests in scintillometry are growing and scintillometers that determine sensible-heat fluxes and momentum fluxes have become commercially available.

This thesis deals with two aspects of scintillometry. First, after a general introduction of scintillometry, measurement errors that have been observed in the large-aperture scintillometer from Kipp&Zonen and in the SLS field-scale scintillometer from Scintec are evaluated. For both scintillometer types, we discuss the variability in the measurement errors among different instruments and, where possible, we give solutions to remove these errors. Furthermore, we present the results of a prototype scintillometer that was developed as part of the research project. With our proposed design, we aim to overcome the measurement errors in the Scintec scintillometer and extend the applicability of the field-scale scintillometer to paths that are longer than 200 m.

Second, we extend the application of field-scale scintillometry to the flux measurements of latent-heat, carbon-dioxide, and other passive scalars. Until now, scintillometers could not be used for measuring passive-scalar fluxes over crop fields and we show that with our extended methodology these fluxes can be accurately determined over time intervals as short as 1 minute. The methodology is based on a combination of scintillometer measurements and additional high-frequency scalar measurements and works under conditions of homogeneous turbulence, i.e. single crop fields. We introduce four methods, notably the energy-balance method, the Bowen-variance method, the flux-variance method, and the structure-parameter method. Using several validation methods, we show that the energy-balance method is unsuitable for estimating scalar fluxes over 1-min averaging intervals. The Bowen-variance and flux-variance method perform better and the structure-parameter method accurately resolves 1-minute fluxes. Thus, with this methodology fluxes can be resolved with a high temporal resolution, making it possible to study vegetation in a natural environment under non-stationary conditions. This allows us to show that the wheat vegetation affects fluxes upon changes in solar radiation in time periods clearly shorter than 30 minutes and that the canopy resistance can change significantly within several minutes.

Table of Contents

1. Introduction	3
1.1. The lower part of the atmosphere.....	3
1.2. Measuring turbulent fluxes	5
1.3. Thesis overview	8
2. Theory	11
2.1. Atmospheric turbulence.....	11
2.1.1. Description of the atmospheric boundary-layer equations	11
2.1.2. Simplification tools for the description of turbulence.....	14
2.1.3. Structure functions and spectra of the turbulent atmosphere.....	21
2.1.4. Solutions to the atmospheric equations using similarity theory	30
2.2. Scintillometry.....	37
2.2.1. Wave-propagation through the turbulent atmosphere.....	38
2.2.2. Scintillometer measurements.....	46
2.2.3. From C_n^2 and l_0 to C_T^2 and ε	53
3. Analysis of the systematic errors found in the Kipp & Zonen large-aperture scintillometer	59
3.1. Introduction.....	59
3.2. Theory.....	61
3.3. Experiment and instrumentation	62
3.3.1. Description of the field site.....	62
3.3.2. Specification of the scintillometers	63
3.3.3. Design of the experiment.....	64
3.3.4. Logging and filtering of the scintillometer data.....	65
3.4. Results	67
3.4.1. Comparison of H_{EC} with H_{WagLAS} and $H_{K\&ZLAS09}$	67
3.4.2. Comparison C_n^2 between WagLAS and K&ZLASs	68
3.4.3. Discussion and solutions of the K&ZLAS systematic errors	71
3.5. Conclusions.....	77
4. Instrument development: Revisiting a scintillometer design	79
4.1. DBLS inter-comparison experiment	79
4.1.1. Structure parameters from the DBLS data.....	80
4.1.2. SLS-20 / 40 instrumental uncertainty.....	81
4.2. A new field-scale scintillometer for measuring u^* and H	82
4.2.1. Theoretical considerations	83
4.2.2. Design and experiment	85
4.2.3. Results	87
4.3. Conclusions for scintillometer development	91
5. Measuring H₂O and CO₂ fluxes at field scales with scintillometry: Part I – introduction and validation of four methods.....	93
5.1. Introduction.....	93
5.2. Theory.....	95
5.2.1. Eddy-covariance method	95
5.2.2. Scintillometer method	96
5.2.3. Combined methods.....	98
5.3. Material and methods	101
5.3.1. Experimental set-up.....	101
5.3.2. Data processing	102
5.3.3. Sensitivity analysis.....	104

5.4.	Sensitivity analysis of the combined methods	105
5.4.1.	Flux-variance method	107
5.4.2.	Bowen-variance method	107
5.4.3.	Structure-parameter method	108
5.4.4.	Energy-balance method	108
5.5.	Validation of the combined methods with experimental data	109
5.5.1.	Scintillometer u^* and H	109
5.5.2.	Fluxes of the combined methods	110
5.6.	Conclusions.....	116
	Appendix A: Estimating stability and the sign of the flux.....	118
6.	Measuring H₂O and CO₂ fluxes at field scales with scintillometry: Part II – evapotranspiration for 1-30 minute averaging intervals.....	121
6.1.	Introduction.....	121
6.2.	Theory and methods	123
6.2.1.	Eddy covariance and scintillometry	123
6.2.2.	Combined methods.....	124
6.2.3.	Validation methods	124
6.3.	Experimental set-up and data treatment	130
6.4.	Results and discussion	131
6.4.1.	Error analysis	131
6.4.2.	Validation of 1-minute evapotranspiration.....	138
6.5.	Conclusions.....	145
7.	Measuring H₂O and CO₂ fluxes at field scales with scintillometry: Part III – carbon-dioxide fluxes and vegetation processes for 1-30 minute averaging intervals	149
7.1.	Introduction.....	149
7.2.	Theory and methods	151
7.2.1.	Eddy covariance and scintillometry	151
7.2.2.	Combined methods.....	151
7.2.3.	Validation methods	152
7.2.4.	Determining 1-min averaged values of the canopy resistance	154
7.3.	Experimental set-up and data treatment	155
7.4.	Validation of the combined methods.....	157
7.4.1.	Validating the combined methods with an analysis of systematic errors.....	158
7.4.2.	Validating the combined methods with an analysis of random errors	161
7.4.3.	Validating the combined methods with Q_s	162
7.4.4.	Validating the structure-parameter method with Transregio2008 and LITFASS2009 data.....	164
7.5.	Applications of 1-min evapotranspiration and CO ₂ fluxes.....	165
7.5.1.	Exploring mechanisms that drive L_vE and FCO_2	166
7.5.2.	Light-response curves.....	168
7.5.3.	Canopy resistance on 1-min time scales.....	170
7.6.	Conclusions.....	172
8.	General discussion and perspective.....	175
9.	References	179
10.	Summary	188
11.	Samenvatting.....	194
	Dankwoord/Acknowledgements/Danksagung	201
	Sense certificate	204
	Professional CV	206
	Index	209

1. Introduction

1.1. *The lower part of the atmosphere*

Most people spend all their lives in the lowest part of the atmosphere, known as the boundary layer. We live in it, we breathe its air, and we experience and change its characteristics every day. Hence, one can imagine that human life quality is greatly affected by the state of the boundary layer and the dynamics within it.

The boundary layer is defined as the layer of air that experiences the influence of the surface and responds to surface forcings with a timescale of about an hour or less (Stull, 1988). These responses can be observed every day, when the boundary layer goes through its typical diurnal cycle (Figure 1.1):

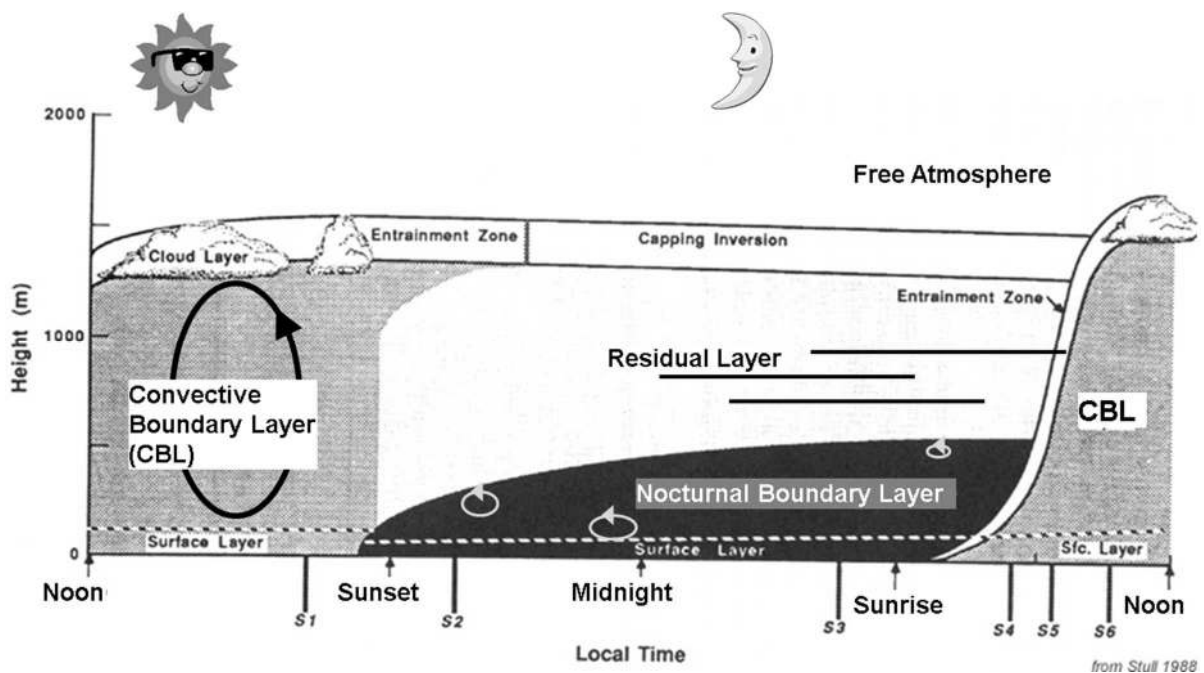


Figure 1.1: Schematic picture of the development of the boundary layer after Stull (1988).

In the morning, when the sun rises, the solar radiation starts heating the earth surface. On its turn, the warm surface heats the air, which gets increasingly unstable and causes thermals of warm air to rise into the atmosphere – a process called convection. Convection does not only transport heat, but also passively transports water vapour, car gasses, pollen etc. When reaching the boundary-layer top the thermals stop rising, but before sinking back slowly, they ‘grab’ some of the clean, dry air from the free atmosphere above the boundary layer – a process called entrainment. The combined effect of convection and entrainment makes the

boundary layer growing in the course of the day. In winter it can reach depths of a couple of hundreds of meters, whereas in summer it can reach depths of several kilometres over dry land.

Within the boundary layer convection causes a vigorous mixing of air. This mixing is a turbulent process, i.e. a very efficient process that is chaotic in its nature. Close to the surface, convection is supported by the wind, which because of shear also generates some turbulent mixing. The mixing removes heat from the surface and keeps the temperature agreeable for us. Furthermore, an unpleasant, large humidity close to the surface is prevented and cloud formation at larger heights is made possible. Moreover, the upward transport prevents high concentrations of pollutants or other gasses, and for example also benefits plant fertilization by bringing pollen into the atmosphere.

In the evening, when the sun sets, the earth's surface starts to cool and loses the energy that was stored during the day. The surface, on its turn, cools the air, which therefore gets increasingly stable. Often, mainly the wind induces turbulent mixing. Depending on the mean wind, the nocturnal boundary layer can be several tens of meters up to a couple of hundred of meters in both winter and summer. The reduced turbulent mixing compared to daytime prevents heating of the near-surface air with the warmer air aloft (the residual air from the convective boundary layer), so that temperatures get clearly lower than during daytime. In summer and even more often in winter it can happen that the cooling is so strong (or the wind so weak) that all turbulent mixing is suppressed. In that case, humidity, CO₂ etc. are not carried upward anymore so that humidity increases, creating the possibility for dew fall or fog. Furthermore, while plants continue their respiration and humans keep adding pollutants to the atmosphere, the CO₂ concentration and pollution (smog) increase. This continues until the wind or wind gusts are strong enough to generate turbulent mixing, which in winter can fail to occur for several days because of the weak solar strength. Usually, however, the new day brings refreshment at latest. Then, the whole process of convection and boundary-layer growth starts again.

From the above it may appear that all the solar energy goes as (sensible) heat into the air. However, this is not the case. Part of the energy goes as heat into the soil and vegetation, and in humid areas another part is used for evaporating water from the surface and vegetation (latent heat). Finally, a small, but nevertheless essential, amount of energy is used for plant photosynthesis. Hence, the solar energy forms the foundation of the upward transport of heat, water vapour, CO₂, etc. through what are called turbulent fluxes.

The turbulent fluxes are important measures for several phenomena. Firstly, the sensible-heat flux is a measure for the heating or cooling within the boundary layer. The latent-heat flux indicates how much moisture is evaporated to the atmosphere. Even though it is the only source of water for the atmosphere, it is very important to limit the water loss in (semi-)arid areas. Finally, the CO₂-flux, during daytime mainly governed by photosynthesis, plays a crucial role in fixing the solar energy and carbon, which is not only essential for plant health and plant growth, but through the plants ultimately also for animals, humans and even the climate.

Thus, understanding the nature of the turbulent fluxes and measuring them can be understood to be of high importance. Measurements of these turbulent fluxes are applied in e.g. water management, in which accurate estimates of the evapotranspiration are essential; in studies to gain understanding about CO₂ fixation and water loss of plants to optimize the harvest and limit water loss; in model validations of hydrological and meteorological models, which benefits e.g. weather forecast and fog predictions; in pollution studies, which ultimately affects e.g. traffic, construction, spatial planning; in security studies, because large sensible-heat fluxes (through optical air scintillations) blur camera images; and in telecommunication studies, because large turbulent fluxes disturb wireless telecommunication. In other words, the measurements of the turbulent fluxes are used for applications that greatly benefit human and environmental wellbeing.

1.2. *Measuring turbulent fluxes*

This thesis deals with scintillometry, a measurement technique for observing the turbulent fluxes of momentum, heat, and mass (water vapour, CO₂ etc.) in the atmospheric surface layer, i.e. the lowest 10% of the boundary layer. At present, eddy covariance is extensively used to do these flux measurements (Baldocchi, 2003; Shuttleworth, 2007). Eddy covariance, ideally, measures these fluxes in a straight forward manner and its set-up is relatively easy in maintenance. However, the use of the eddy-covariance method is limited in four ways. Firstly, flow distortion (by the mast or instrument itself) is not negligible for unfavourable wind directions. Secondly, the eddy-covariance method needs to sample all eddy scales relevant to the turbulent flux (Finnigan et al., 2003). Thirdly, as a point-sampling measurement technique it requires time to adequately sample the largest eddy scales and during the whole flux-averaging interval turbulence needs to be stationary. Fourthly, point-sampling measurements only represent a limited area, which especially in heterogeneous conditions limits their

applicability as a reference in e.g. numerical models or water/carbon-balance estimates (Aubinet, 2008; Foken, 2008; Hartogensis et al., 2002; Mahrt, 2010; Vickers et al., 2009).

Scintillometry is an indirect flux estimation method that neither is perfect, but that overcomes these four limitations. Scintillometers spatially average fluxes over field scales (100 m - 500 m) to kilometre scales (up to 10 km). Therefore, flow distortion of the instrument is negligible (Thiermann and Grassl, 1992) and the obtained fluxes represent larger areas than fluxes obtained with eddy-covariance (Wyngaard and Clifford, 1978). Furthermore, scintillometers sample only one eddy scale. The advantage is that the larger measurement path enhances the amount of independent samples of eddies to which the scintillometers are sensitive. Therefore, statistically stable fluxes can rapidly (< 1 min) be obtained. Consequently, scintillometry does not require turbulence to be stationary for 10-30 minutes.

Research has confirmed these results and shows that optical large-aperture scintillometers yield accurate estimates of the area-averaged sensible-heat flux over moderately heterogeneous terrain. (Meijninger et al., 2006; Meijninger et al., 2002b). Furthermore, area-averaged latent-heat fluxes have been determined accurately on kilometre scales over heterogeneous terrain, by combining an optical large-aperture and microwave scintillometer (Green et al., 2001; Green et al., 2000; Lüdi et al., 2005; Meijninger et al., 2006; Meijninger et al., 2002a). Finally, for field scales it has been shown that accurate estimates of both the sensible-heat flux and momentum flux can be obtained with a displaced-beam laser scintillometer for averaging intervals shorter than one minute (Hartogensis et al., 2002; Wyngaard and Clifford, 1978).

Initially, only prototype large-aperture scintillometers were employed and research focused on theoretical and practical issues regarding the method (De Bruin et al., 1995; Hill, 1981; Hill, 1992; Meijninger and De Bruin, 2000; Nieveen et al., 1998a; Ochs and Wang, 1978; Thiermann, 1992; Thiermann and Grassl, 1992; Wang et al., 1978). Based on this research the large-aperture scintillometer was made commercially available and has been widely used since (Asanuma and Iemoto, 2007; Hartogensis, 2007; Kleissl et al., 2008). Furthermore, also for field-scales a prototype displaced-beam scintillometer was developed into a commercial product, i.e. the surface layer scintillometer (Scintec, Rottenburg, Germany).

The ideal method one could say. However, there remained several issues that limited the success of the method, some of which initiated the project “Innovations in Scintillometry - Measuring surface fluxes of water vapour, sensible heat and momentum on field to kilometre scale” from the Dutch Technology Foundation (STW). This project consists of two parts.

One, measuring sensible-heat and latent-heat fluxes on kilometre scales, using an optical-microwave scintillometer system and two, measuring fluxes of momentum, sensible heat, and mass fluxes of water vapour (latent heat) and other passive scalars on field scales. Oscar Hartogensis focused on the first part of the project that has the aim to make the optical-microwave scintillometer system commercially available, while my focus was on the second part of the project.

As such, this thesis deals with two issues of interest regarding scintillometry. First, there is a practical focus on measurement errors in the two above-mentioned scintillometers that are commercially available. Studies have shown that the large-aperture scintillometers from Kipp&Zonen systematically overestimate the sensible-heat flux (Kleissl et al., 2008; Kleissl et al., 2009). Similarly, the Scintec surface-layer scintillometers suffer from systematic errors in both their estimates of the friction velocity as well as in those of the structure parameter of temperature, which relates to the sensible-heat flux (Beyrich et al., 2012; Hartogensis et al., 2002). The innovation of this part of the project lies therein that we want to understand why these systematic errors occur and based on that knowledge develop a prototype scintillometer that overcomes the measurement errors of the Scintec scintillometer and aims to extend the application of field-scale scintillometers to scintillometer paths of 200 m or longer.

Second, and this is the main focus of the thesis, there is the need for measuring passive-scalar fluxes on field scales (<500 m). Until now, none of the commercially available scintillometers can measure mass fluxes of passive scalar quantities. Prototype scintillometer systems that measure evapotranspiration on large scales (> 1 km) are available (Evans, 2009; Green et al., 2001; Green et al., 2000; Meijninger et al., 2006; Meijninger et al., 2002a) and a commercial system is in preparation, but unfortunately these systems cannot be operated on field scales (< 500m) and cannot measure mass fluxes of CO₂, CH₄, or other passive-scalar quantities. Furthermore, scintillometry is challenged by the fact that scintillometers cannot directly estimate the flux direction.

Thus, we introduce and validate four methods that combine field-scale scintillometer measurements of stability and friction velocity with additional turbulence measurements of humidity and CO₂. With these methods we can estimate the flux, as well as the flux direction. These so-called combined methods are: the flux-variance method, the Bowen-variance method, the structure-parameter method, and the energy-balance method. With these methods, the spatial-averaging advantages of scintillometry can be used to evaluate evapotranspiration,

CO₂ flux and other mass fluxes of passive scalars over averaging intervals as short as 1 minute.

The motivation to explore these relatively short flux intervals is that it provides us a detailed flux description even for non-stationary circumstances, something that is highly relevant for plant studies. Using these methods, crops and other vegetation can be studied under natural, often non-stationary conditions (e.g. (Foken et al., 2001)) and so greatly add to the highly controlled laboratory experiments that are usually performed on plants (e.g. (Cardon et al., 1994)). Moreover, by reducing the averaging time the flux comparison with snap-shot remote-sensing estimates can be improved. This improvement can especially be achieved in non-stationary conditions, when the snapshot of the satellite (Bastiaanssen et al., 1997) does not represent the 15-30 minute flux data. A similar argument holds for the validation and performance of hydrological/meteorological models. Models with fine horizontal or vertical resolution need to be operated on small time steps in order to keep the models stable. At present, these models are confronted with 15-30 minute averaged fluxes, which partly conceals the qualities of/uncertainties in the models.

1.3. Thesis overview

The research described above is presented in this thesis as follows. After a general introduction of the theory on measuring surface fluxes with scintillometers, chapter 3 deals with the measurement errors in the large-aperture scintillometer from Kipp&Zonen. We show the intercomparison of several large-aperture scintillometers from Kipp&Zonen with one large-aperture scintillometer from Wageningen University. Based on that intercomparison, we discuss two systematic errors: the low- C_n^2 error and the high- C_n^2 error. Furthermore, we discuss the variability of these errors among instruments and their impact on the estimation of the sensible-heat flux. Where possible, we also give solutions to remove the error.

Subsequently, chapter 4 discusses the measurement errors in the displaced-beam laser scintillometer from Scintec, i.e. the surface-layer scintillometer (SLS20/40). First, we discuss the variability of these measurement errors among instruments. Subsequently, we discuss the development of a prototype scintillometer that must overcome these measurement errors and aims to extend the application of field-scale scintillometers to scintillometer paths of 200 m or longer. This discussion is supported by the comparison of an SLS20 with a prototype scintillometer that we developed based on small adaptations of existing large-aperture scintillometers.

Then, chapter 5, 6, and 7 consider the extension of field-scale scintillometry to measuring fluxes of passive scalars. Chapter 5 starts with the introduction and validation of the four methods. This chapter aims to thoroughly test the methods by analysing the sensitivity of the methods to the variables that are used by them. In addition, we also validate the methods with 30-minute eddy-covariance data. The whole analysis is performed based on data from a field experiment over a winter-wheat field near Merken, Germany, in May – June 2009 in the framework of the TransRegio32 program.

Chapter 6 continues with the validation of the four methods by evaluating the accuracy of their 1-minute estimates of the evapotranspiration. To validate the combined methods for these short averaging intervals, two methods are applied. We start by determining the averaging-time-dependent systematic error and the averaging-time-dependent random error in the evapotranspiration. Subsequently, we validate the combined methods with a limited set-up of the Penman-Monteith model. In addition to the validation, we also discuss the applicability of Monin-Obukhov similarity theory for 1-minute averaging intervals and give an analysis of plant physiology in order to answer the question whether wheat plants can rapidly open and close their stomata.

Chapter 7 finishes the validation of the four methods by evaluating the accuracy of 1-minute estimates of the CO₂ flux. We start this chapter by validating the 1-min CO₂ flux and determine the averaging-time-dependent systematic error and the averaging-time-dependent random error in the CO₂ flux, followed by an evaluation based on the incoming short-wave radiation. After the validation we show some examples that illustrate the relevance of measuring 1-min fluxes. Thus, we show that the evapotranspiration and CO₂ flux respond differently on abrupt changes in solar radiation. In addition, we show that 1-min fluxes benefit the comparison of light-response curves from two mornings with different atmospheric conditions. Finally, we study the 1-min values of the canopy resistance and show that vegetation can change its canopy resistance within several minutes under conditions of non-stationary turbulence.

2. Theory

Scintillometers can be used to estimate turbulent surface fluxes of momentum, sensible heat, and latent heat. Scintillometry is based on an extensive and complex theoretical framework that combines the theoretical physics of atmospheric turbulence with the theory of electromagnetic-wave propagation. In this chapter, we expound the theoretical framework of scintillometry in the light of these two underlying theories. In section 2.1, we introduce the theoretical physics of atmospheric turbulence, followed by the theory on electromagnetic-wave propagation through the turbulent atmosphere in section 2.2.

2.1. Atmospheric turbulence

The atmospheric boundary layer is the layer that is directly influenced by the presence of the earth's surface, responding to surface forcings within an hour or less (Stull, 1988). The air flow and the transport of quantities through the boundary layer are turbulent, i.e. chaotic but very efficient as compared to molecular diffusion. Irregular swirls of motions, eddies, characterise the turbulent transport, which is mainly driven by frictional drag, surface heating by the sun, and surface cooling during the night (Stull, 1988).

In this section, we introduce the basic flow and budget equations of the atmospheric boundary layer. These equations are highly non-linear and in order to get to solutions for them, we introduce (statistical) tools to simplify them. Subsequently, we describe and quantify the turbulence fields of the atmosphere with these simplification tools. In doing so, we define several statistical variables, which as we show in section 2.2 can be estimated with scintillometers. Finally, we apply Monin-Obukhov similarity theory to derive solutions of the atmospheric flow and budget equations. These solutions form the foundation for measuring surface fluxes with scintillometers, because they link the surface fluxes to the statistical variables that can be estimated with scintillometers.

2.1.1. Description of the atmospheric boundary-layer equations

There are five equations describing the flow and budgets of the atmospheric boundary layer. The first equation concerns the state of gases. Within the boundary layer the state of gases can be adequately described by the ideal gas law (Stull, 1988)

$$p = \rho R_d T_v, \quad (2.1)$$

where p is the pressure, ρ is the density of the air, R_d is the gas constant for dry air ($287 \text{ J K}^{-1} \text{ kg}^{-1}$), and T_v is the virtual temperature.

The second equation concerns the conservation of mass. In combination with the fact that the velocities in the atmosphere are much smaller than the speed of sound, the conservation of mass results in the incompressibility approximation (Monin and Yaglom, 1971; Stull, 1988)

$$\frac{\partial u_i}{\partial x_i} = 0, \quad (2.2)$$

where u_i represents the components of the wind vector and x_i represents the three directions in space, identified by $i = 1, 2, 3$. Here and onward, we use the Einstein summation notation for brevity. For the full description of this notation we refer to Monin and Yaglom (1971) or Stull (1988). We only elaborate on two special signs in this notation. First, the Kronecker delta, δ_{ij} , for which applies $\delta_{ij} \equiv 1$ for $i = j$ and $\delta_{ij} \equiv 0$ for $i \neq j$. Second, the alternating unit tensor, ε_{ijk} , for which applies $\varepsilon_{ijk} \equiv 1$ for $ijk = 123, 231, \text{ or } 312$, $\varepsilon_{ijk} \equiv -1$ for $ijk = 321, 213, \text{ or } 132$, and $\varepsilon_{ijk} \equiv 0$ for any other combination (Monin and Yaglom, 1971; Stull, 1988).

The third equation concerns Newton's second law. Newton's second law states that the acceleration of a body is directly proportional to the net force exerted on it and inversely proportional to its mass. From this follows that momentum is conserved. Together with the assumption of incompressibility, this results in the Navier-Stokes equations (Monin and Yaglom, 1971; Stull, 1988)

$$\frac{\partial u_i}{\partial t} + u_j \frac{\partial u_i}{\partial x_j} = -\delta_{i3} g - 2\varepsilon_{ijk} \Omega_j u_k - \frac{1}{\rho} \frac{\partial p}{\partial x_i} + \nu \frac{\partial^2 u_i}{\partial x_j^2} \quad (2.3)$$

I II III IV V VI

Term I represents the storage of momentum

Term II describes advection

Term III allows gravity to act vertically (g is the gravitational acceleration)

Term IV describes the influence of the earth's rotation (Ω_j is the angular velocity vector)

Term V describes the pressure gradient forces

Term VI represents the influence of viscous stress (ν is the kinematic viscosity)

The fourth equation concerns the first law of thermodynamics. The first law of thermodynamics describes the conservation of enthalpy, i.e. considers the total heat of a system. For the atmosphere the heat budget is not only governed by the sensible heat, associated with temperature, but also the latent heat, which has the potential to release or adsorb heat upon phase changes of water (Monin and Yaglom, 1971; Stull, 1988)

$$\frac{\partial \theta}{\partial t} + u_i \frac{\partial \theta}{\partial x_i} = D \frac{\partial^2 \theta}{\partial x_i^2} - \frac{1}{\rho c_{pm}} \frac{\partial Q_{*i}}{\partial x_i} - \frac{L_p E}{\rho c_{pm}} \quad (2.4)$$

I II VI VII VIII

Term I, II, VI are the storage, advection and molecular diffusion as in the momentum equation (θ is the potential temperature, D is the diffusivity). Term VII is a term associated with radiation divergence (Q_{*i} is the component of the net radiation in the i^{th} direction, c_{pm} is the specific heat for moist air at constant pressure). Term VIII is the term associated with latent heat released during phase changes (E is the mass of water vapour per unit volume per unit time created by a phase change from liquid or solid, L_p is the latent heat that corresponds to the phase change).

The fifth equation concerns the budget of scalar quantities. Within the boundary layer, moisture and other scalar quantities are conserved (Stull, 1988)

$$\frac{\partial C}{\partial t} + u_i \frac{\partial C}{\partial x_i} = D_C \frac{\partial^2 C}{\partial x_i^2} - S_C \quad (2.5)$$

I II VI VII

Term I, II, VI are the storage, advection and molecular diffusion as in the previous equations. Term VII is a source-sink term representing processes not already included in the equation like for example precipitation and phase changes for water, or chemical reactions for chemical quantities.

2.1.2. Simplification tools for the description of turbulence

Analytical solutions for the fundamental fluid-dynamics equations only exist for the most simple laboratory cases. Those cases are rarely observed in our turbulent atmospheric boundary layer and therefore simplification methods are used to describe this turbulence. In this section the most important (statistical) methods are described.

2.1.2.1. Dimensional analysis

Buckingham-Pi theory gives a systematic procedure for performing dimensional analysis. The relevance of this theory lays therein that dimensionless groups can be formed from the variables that are relevant to a problem. A proper choice of variables results in empirical relationships that can be determined experimentally and, ideally, are universal applicable (Stull, 1988).

The whole procedure consists of seven steps from which the general outline is presented in e.g. Stull (1988) and shortly repeated here. The first step consists of selecting the important variables for the problem in question. This step is essential, because none of the relevant variables may be lacking in order to arrive at useful solutions. The second step consists of finding the dimensions of each variable in terms of the fundamental dimensions, i.e. in terms of length, mass, time, temperature, electric current, or irradiance. The third step consists of counting the number of fundamental dimensions present in the problem. The fourth step consists of selecting a subset of key variables from the selected variables. These key variables must meet the requirement that they contain all the fundamental dimensions. Furthermore, no dimensionless group may be possible from any given combination of these key variables. The fifth step consists of forming dimensionless equations from the remaining variables in terms of the key variables. These equations must be dimensionally consistent, which can be achieved by raising the variables to the proper power. The sixth step consists of forming dimensionless (Pi) groups, by dividing each key variable by its corresponding equation. When this procedure has been performed correctly, the number of Pi groups will always equal the number of variables minus the number of dimensions. The seventh and final step consists of empirically determining the values of the dimensionless groups that are formed and the relations between the groups (Stull, 1988).

2.1.2.2. Reynolds decomposition

Reynolds decomposition is one of the most important tools in statistical turbulence. The theory states that a random variable, u , can be decomposed into a mean part, \bar{u} , and a fluctuating part, u' , around its mean,

$$u = \bar{u} + u' \quad (2.6)$$

By definition, the mean of u' is zero,

$$\overline{u'} \equiv 0 \quad (2.7)$$

and the overbar denotes the ensemble average. For the full conditions to which this averaging must satisfy, the reader is referred to Monin and Yaglom (1971) or Stull (1988).

2.1.2.3. Statistical moments

Another important tool that is used in the statistical description of turbulence is the concept of the probability distributions moments (Monin and Yaglom, 1971). If we consider N random variables u_1, u_2, \dots, u_N with a N -dimensional probability density $p(u_1, u_2, \dots, u_N)$, then the central moments, B , are defined by

$$B_{k_1 k_2 \dots k_N} \equiv \overline{(u_1')^{k_1} (u_2')^{k_2} \dots (u_N')^{k_N}} = \overline{(u_1 - \bar{u}_1)^{k_1} (u_2 - \bar{u}_2)^{k_2} \dots (u_N - \bar{u}_N)^{k_N}} = \int \int \dots \int (u_1')^{k_1} (u_2')^{k_2} \dots (u_N')^{k_N} p(u_1', u_2', \dots, u_N') du_1' du_2' \dots du_N' \quad (2.8)$$

where $k_1 \dots k_N$ are integers of which the sum gives the order of the moment. By definition the first order central moment is zero. Furthermore, the second order central moment, B_2 , B_{uu} , or B_u^2 , is the variance and the general second order moment B_{11} or B_{uv} is the covariance. It is impossible to determine all the statistical moments of the turbulent flow. Therefore, only the simple (lower order) moments are used.

The concept of moments can be extended with the time and space variability of the moments, i.e. the type (one-point, two-point etc.) of the moment. For example, the two-point second-order central moment is defined by

$$B_{uu}(M_1, M_2) = \overline{u'(M_1)u'(M_2)}, \quad (2.9)$$

where M denotes a three dimensional position at time t , so $M = (x, y, z, t)$. One can also consider only spatial or temporal moments. In that case, M is replaced with $r_n = (x_n, y_n, z_n)$ or t .

The concept of moments can be used to define three simple turbulent cases: the stationary case, the homogeneous case and the isotropic case. A random field (or process) is stationary when its mean value $\overline{u(t)}$ is constant and B_{uu} depends only on $\tau = t_1 - t_2$ (Monin and Yaglom, 1975; Tatarskii, 1961),

$$B_{uu}(t_1, t_2) = B_{uu}(t_1 - t_2) = B_{uu}(t_2 - t_1). \quad (2.10)$$

A random field is homogeneous when its mean value, $\overline{u(r_n)}$, is constant and B_{uu} depends only on $r_1 - r_2$ (Monin and Yaglom, 1975; Tatarskii, 1961),

$$B_{uu}(r_1, r_2) = B_{uu}(r_1 - r_2) = B_{uu}(r_2 - r_1). \quad (2.11)$$

A random field is isotropic when its mean value, $\overline{u(r_n)}$, is constant and B_{uu} depends only on $|r_1 - r_2|$, i.e. on the distance, r , between two points and not on its direction or position (Monin and Yaglom, 1975; Tatarskii, 1961),

$$B_{uu}(r_1, r_2) = B_{uu}(r_1 - r_2) = B_{uu}(|r_1 - r_2|) = B_{uu}(r), \quad (2.12)$$

Note that a homogeneous random field is not necessarily an isotropic random field, whereas an isotropic random field is always homogeneous.

2.1.2.4. Structure function

The variance and covariance are comprehensible statistical parameters, but unfortunately they depend on the mean value of the process or field in question. In case of a stationary random field or process, these parameters are clearly defined, because the mean value is constant. However, in the atmosphere fields or processes are hardly stationary. Thus, Kolmogorov

(1941) introduced the principle of stationary increments. The main thought behind the idea of stationary increments is that rather than the mean value, $\overline{u(t)}$, the difference $U_\tau(t) = u(t + \tau) - u(t)$ is constant.

The second-point second-order moment of $U_\tau(t)$ has the form

$$B_{U_\tau U_\tau}(t_1, t_2) = \overline{U_\tau(t_1)U_\tau(t_2)} = \overline{(u(t_1 + \tau) - u(t_1))(u(t_2 + \tau) - u(t_2))}. \quad (2.13)$$

As $U_\tau(t)$ is stationary, $B_{U_\tau U_\tau}(t_1, t_2)$ only depends on τ , so that $(u(t_1 + \tau) - u(t_1)) = (u(t_2 + \tau) - u(t_2))$. This leads to the structure function definition for any random process with stationary increments (Monin and Yaglom, 1975; Tatarskii, 1961)

$$D_{uu}(\tau) \equiv \overline{(u(t + \tau) - u(t))^2}. \quad (2.14)$$

In case a field is stationary, D_{uu} and B_{uu} are related (Monin and Yaglom, 1975; Tatarskii, 1961):

$$D_{uu}(\tau) = 2[B_{uu}(0) - B_{uu}(\tau)]. \quad (2.15)$$

Kolmogorov (1941) extended the concept of stationary increments with the principle of local homogeneous and isotropic random fields. Tatarskii (1961) gives the basic assumption behind this theory: "The difference between the values of the field $u(r)$ at two points r_1 and r_2 is chiefly affected only by inhomogeneities of the field $u(r)$ with dimensions which do not exceed the distance $|r_1 - r_2|$. If this distance is not too large, the largest inhomogeneities have no effect on $u(r_1) - u(r_2)$ and therefore on the structure function."

The assumption that fields or processes in the atmosphere are locally stationary, homogeneous, or isotropic is less stringent and more realistic than the assumption that they are non-locally. Hence, and this we want to stress, D_{uu} can be used under a wider range of turbulent conditions than B_{uu} (Tatarskii, 1961).

Similar as for the concept of moments, the structure function can be used to define local homogeneity and local isotropy. A random field is locally homogeneous when D_{uu} depends only on $r_1 - r_2$ (Monin and Yaglom, 1975; Tatarskii, 1961),

$$D_{uu}(r_1, r_2) = D_{uu}(r_1 - r_2) = D_{uu}(\vec{r}) = \overline{(u(r_1) - u(r_2))^2}, \quad (2.16)$$

where \vec{r} is the three-dimensional space vector. A random field is locally isotropic when D_{uu} depends only on r , i.e. $|r_1 - r_2|$ (Monin and Yaglom, 1975; Tatarskii, 1961),

$$D_{uu}(r_1, r_2) = D_{uu}(r_1 - r_2) = D_{uu}(\vec{r}) = D_{uu}(r) = \overline{(u(r + r_1) - u(r_1))^2}. \quad (2.17)$$

2.1.2.5. Fourier analysis

“The significance of the Fourier expansion lies in the possibility that any stationary random process, $u(t)$, can be replaced, to any required approximation, by the sum of uncorrelated harmonic oscillations with random amplitudes and phases.” (Monin and Yaglom, 1975). The advantage of Fourier expansions is that they can be used to study which oscillations are of greatest importance to a random process or signal. Thus, Fourier analysis can be helpful in e.g. analysing the major time/length scales of processes or identifying noise in measurements signals (Stull, 1988), see chapter 3.

Unlike mentioned above, the random process $u(t)$ cannot simply be represented by a Fourier integral, because as Monin and Yaglom (1975) remark: “In the presence of a discrete spectrum, the function $B(\tau)$ would contain undamped periodic terms, and therefore could be represented only by a Fourier-Stieltjes integral”. Thus, $u(t)$ is expanded as

$$u(t) = \int_{-\infty}^{\infty} e^{i\omega t} dZ(\omega), \quad (2.18)$$

where $dZ(\omega)$ is the sum of the random complex amplitudes, Z_k , corresponding to frequencies $\omega_k < \omega$. $Z(\omega)$ is defined such that $\overline{Z(\omega)} \equiv 0$ if $\overline{u(t)} = 0$ and because complex pairs are orthogonal

$$\overline{dZ^*(\omega) dZ(\omega_1)} = 0, \text{ when } \omega \neq \omega_1 \quad (2.19)$$

where Z^* is the complex conjugate of Z (Monin and Yaglom, 1975).

The statistical moment of a stationary random field, as described in the previous section, can be expanded into a Fourier series by substituting Eq. (2.18) into Eq. (2.10),

$$B_{uu}(t_1, t_2) = B_{uu}(t_1 - t_2) = \overline{u(t_1)u^*(t_2)} = \int_{-\infty}^{\infty} \int_{-\infty}^{\infty} e^{i(\omega_1 t_1 - \omega_2 t_2)} \overline{dZ(\omega) dZ^*(\omega_1)}. \quad (2.20)$$

The spectral density, F , and the spectrum, S , are connected to $Z(\omega)$ in the following way:

$$\overline{[dZ(\omega)]^2} = F(\omega) d\omega = 0.5 S(\omega) d\omega. \quad (2.21)$$

In a stationary random field $B_{uu}(t_1, t_2)$ depends only on $t_1 - t_2$, and therefore $\overline{dZ(\omega) dZ^*(\omega_1)}$ must satisfy (Tatarskii, 1961):

$$\overline{dZ(\omega) dZ^*(\omega_1)} = \delta(\omega - \omega_1) F(\omega) d\omega d\omega_1 = 0.5 \delta(\omega - \omega_1) S(\omega) d\omega d\omega_1, \quad (2.22)$$

with $\delta(\omega)$ being the improper Dirac delta-function that has the property

$$\int_{-\infty}^{\infty} \delta(x - y) f(x) dx = f(y). \quad (2.23)$$

Using Euler's formula and substituting Eq. (2.22) into Eq. (2.20), leads to the Fourier transform of $B_{uu}(\tau)$ (Monin and Yaglom, 1975)

$$B_{uu}(\tau) = \int_{-\infty}^{\infty} e^{i\omega\tau} F_{uu}(\omega) d\omega = \int_{-\infty}^{\infty} \cos(\omega\tau) F_{uu}(\omega) d\omega = \int_0^{\infty} \cos(\omega\tau) S_{uu}(\omega) d\omega. \quad (2.24)$$

The physical meaning of $S(\omega)$ and $F(\omega)$ becomes clear when Eq. (2.24) is evaluated for $\tau = 0$. Recall, that $B_{uu}(0)$ is the variance of the process $u(t)$. Then, it appears that “the total energy of the process $u(t)$ is the sum of the energies of the individual spectral components” (Monin and Yaglom, 1975); (Stull, 1988).

Using Eq. (2.24), the Fourier expansion of $D_{uu}(\tau)$ can be obtained for stationary, homogeneous, or isotropic conditions as well. When the field is stationary $D_{uu}(\tau)$ relates to $B_{uu}(\tau)$ by Eq. (2.15) (Monin and Yaglom, 1975; Tatarskii, 1961)

$$D_{uu}(\tau) = 2[B_{uu}(0) - B_{uu}(\tau)] = 2 \left[\int_{-\infty}^{\infty} F(\omega) d\omega - \int_{-\infty}^{\infty} e^{i\omega\tau} F(\omega) d\omega \right] =$$

$$2 \int_{-\infty}^{\infty} (1 - e^{i\omega\tau}) F(\omega) d\omega = 2 \int_{-\infty}^{\infty} (1 - \cos(\omega\tau)) F(\omega) d\omega. \quad (2.25)$$

Eq. (2.15) is also valid for homogenous conditions. Thus for a (locally) homogeneous field the harmonic oscillations $e^{i\omega t}$ are replaced by the plane waves $e^{i\vec{k}\vec{r}}$ and the Fourier transform is defined as

$$D_{uu}(\vec{r}) = 2 \iiint_V (1 - \cos(\vec{k}\vec{r})) \Phi_{uu}(\vec{k}) d\vec{k}, \quad (2.26)$$

in which \vec{k} is the wavenumber vector (eddy wavenumber) and Φ_{uu} denotes the spectral density of the field (both three-dimensional (3D)) (Monin and Yaglom, 1975).

When the field is (locally) isotropic Eq. (2.26) can be simplified, by inserting spherical coordinates and apply the integration over the angular coordinates (Tatarskii, 1961),

$$D_{uu}(\vec{r}) = D_{uu}(r) = 8\pi \int_0^{\infty} \left(1 - \frac{\sin(kr)}{kr}\right) \Phi_{uu}(k) k^2 dk = 2 \int_0^{\infty} \left(1 - \frac{\sin(kr)}{kr}\right) E_{uu}(k) dk, \quad (2.27)$$

where k is the length of \vec{k} and $E_{uu}(k) = 4\pi k^2 \Phi_{uu}(k)$ is the spectral density of the 3D spectrum projected on one dimension (Hartogensis, 2006). The 3D spectrum is related to the 1D spectrum by (Monin and Yaglom, 1975; Tatarskii, 1961)

$$E_{uu}(k) = -\frac{1}{2\pi k} \frac{dS_{uu}}{dk}. \quad (2.28)$$

Thus, Eq. (2.25), (2.26), and (2.27) show for a random field or process the relation of the structure function to its Fourier transform, which is a function of the spectrum.

2.1.3. Structure functions and spectra of the turbulent atmosphere

Structure functions and spectra are relative simple tools to describe random fields of turbulent processes. In this section we apply these tools to the atmosphere in order to describe the structure functions and spectra for the turbulent velocity and temperature fields. It begins with a descriptive picture of the atmospheric turbulence, followed by a quantification of the structure functions and spectra.

2.1.3.1. Descriptive picture of the atmospheric energy cascade

Within the atmospheric boundary layer flows are characterized by small gradients, a chaotic structure, and a transport that is very efficient as compared to laminar flows. The Reynolds number is a dimensionless number, describing the relative role of the inertia forces and the friction forces in the flow dynamics (Monin and Yaglom, 1971). The Reynolds number is given by

$$\text{Re} = \frac{UL_s}{\nu}, \quad (2.29)$$

where U is the characteristic velocity, L_s a characteristic length scale, and ν is the kinematic viscosity. Small Reynolds numbers occur for laminar flows ($\text{Re} < 1000$) and large Reynolds numbers occur for turbulent flows ($\text{Re} > 1 \times 10^5$).

In the boundary layer, shear, and by daytime also buoyancy, create large unstable eddies. These large eddies break down into smaller eddies, which subsequently break down into even smaller eddies. As eddies break down they eventually become so small that viscous forces become important. At those scales, the eddies become stable and dissipate into heat. This process of large eddies breaking down is known as the cascade process (Stull, 1988; Tatarskii, 1961).

The size of the smallest eddies that dissipate into heat was defined by Kolmogorov (1941) using dimensional analysis and is referred to as the Kolmogorov micro scale,

$$\eta = \left(\frac{\nu^3}{\varepsilon} \right)^{\frac{1}{4}}, \quad (2.30)$$

where ε is the dissipation rate of turbulent kinetic energy. Using ν and ε , one can also define a corresponding velocity scale v_η and time scale τ_η (Tatarskii et al., 1992). For typical values of $\nu = 1.5 \cdot 10^{-5} \text{ m}^2 \text{ s}^{-1}$ and $\varepsilon = 5 \cdot 10^{-3} \text{ m}^2 \text{ s}^{-3}$, $\eta \approx 1 \times 10^{-3} \text{ m}$, $v_\eta \approx 2 \times 10^{-2} \text{ m s}^{-1}$, and $\tau_\eta \approx 5.5 \times 10^{-2} \text{ s}$. Per definition, the Reynolds number corresponding to these length and velocity scales, Re_η , equals one.

The process of generating and breaking down of eddies is a turbulent process and chaotic by its nature. However, when considering the velocity spectrum (the kinetic energy spectrum) from these eddies, a surprising order is found.

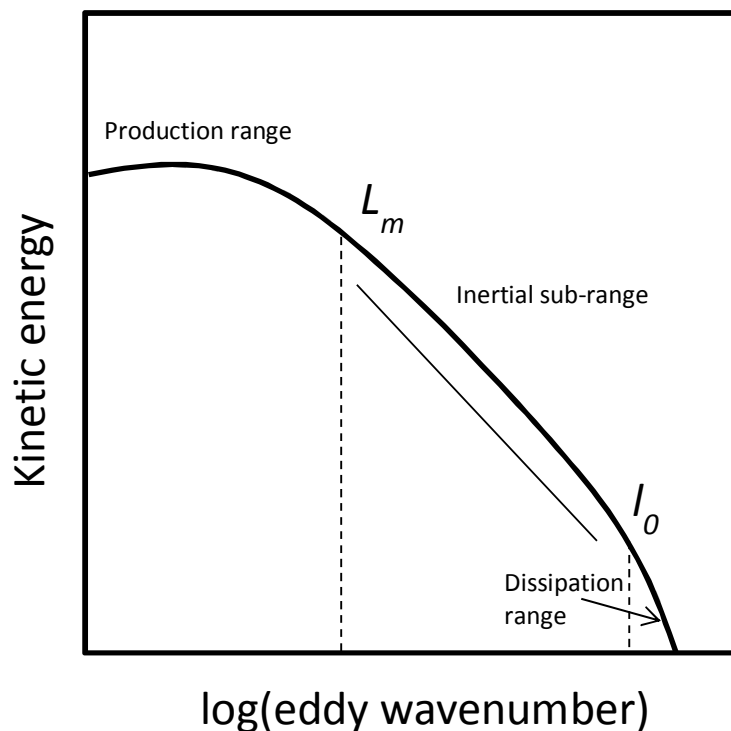


Figure 2.1: Schematic view of the atmospheric velocity spectrum

Figure 2.1 shows an example of the velocity spectrum as is it can be found in the atmosphere. This spectrum can be classified into three parts. In the first part, the production range, the largest eddies are produced by the main flow and the energy comes into the cascade. Eddies in this part of the spectrum are not isotropic and can have a size as large as the boundary layer ($Re \approx 5 \times 10^8$).

In the second part, the inertial sub-range, eddies get their energy from the larger unstable eddies and transfer it to the smaller eddies. Eddies in the inertial range do not

produce, store or release energy, so only the inertial transfer of energy is important. The boundaries of this range are the outer scale, L_m , and the inner scale, l_0 .

In the third part, the dissipation range, viscosity plays an important role and all the energy dissipates into heat. The upper boundary is given by l_0 and the lower boundary is given by η . Eddies smaller than η do not exist, and the spectrum goes to zero (Meijninger, 2003; Stull, 1988). Eddies in the dissipation range vary from sizes of about 1 mm to sizes of about a few centimetres. An important characteristic of the turbulent eddies is that they can be considered isotropic when they are much smaller than L_m , i.e. in the inertial sub-range and the dissipation range (Tatarskii, 1961).

2.1.3.2. Quantification of the atmospheric energy cascade

The cascade process illustrates in a descriptive way how the successive eddies in the atmosphere relate to each other. For the inertial sub-range and dissipation range, Kolmogorov (1941) and Obukhov and Yaglom (1951) quantified the cascade process. They derived the structure function of the 3-D velocity field, u_i , by assuming the flow to be locally isotropic. From this assumption follows that (Tatarskii, 1961)

$$D_{u_i u_j}(r) = [D_{ll}(r) - D_{tt}(r)] n_i n_j + D_{ll} \delta_{ij}, \quad (2.31)$$

where n is the unit vector along \vec{r} , D_{tt} is the transverse structure function, and D_{ll} is the longitudinal structure function. From the assumption of incompressibility it follows that (Tatarskii, 1961)

$$\frac{\partial D_{u_i u_j}(r)}{\partial x_i} = 0. \quad (2.32)$$

Substituting Eq. (2.31) into Eq. (2.32) leads to

$$D_{tt} = \frac{1}{2r} \frac{d}{dr} (r^2 D_{ll}). \quad (2.33)$$

Thus, D_{ii} or D_{ll} solely determine the tensor $D_{u_i u_j}$, which means that under locally isotropic conditions the structure function does not depend on the flow direction.

Then, Buckingham-Pi theory is applied. The important variables (besides r and D_{ll}) are selected to be ε in the inertial sub-range and ε and ν in the dissipation range. Hence, the following relations are obtained (Kolmogorov, 1941; Monin and Yaglom, 1975; Tatarskii, 1961)

$$D_{ll}(r) = C \varepsilon^{\frac{2}{3}} r^{\frac{2}{3}} \quad \text{for } r \text{ in the inertial sub-range,} \quad (2.34)$$

$$D_{ll}(r) = \frac{1}{15} \frac{\varepsilon}{\nu} r^2 \quad \text{for } r \text{ in the dissipation range.} \quad (2.35)$$

and

$$D_{ii}(r) = \frac{4}{3} C \varepsilon^{\frac{2}{3}} r^{\frac{2}{3}} \quad \text{for } r \text{ in the inertial sub-range,} \quad (2.36)$$

$$D_{ii}(r) = \frac{2}{15} \frac{\varepsilon}{\nu} r^2 \quad \text{for } r \text{ in the dissipation range.} \quad (2.37)$$

Eliminating ν from these equations and rewriting them in terms of the longitudinal-velocity inner scale $l_{0,l}$ and the transversal-velocity inner scale, $l_{0,t}$, (the points of intersection between the inertial sub-range and the dissipation range), leads to

$$D_{ll}(r) = C_{\nu^2} r^{\frac{2}{3}} \quad \text{for } r \text{ in the inertial sub-range,} \quad (2.38)$$

$$D_{ll}(r) = C_{\nu^2} l_{0,l}^{\frac{2}{3}} \left(\frac{r}{l_{0,l}} \right)^2 \quad \text{for } r \text{ in the dissipation range.} \quad (2.39)$$

and

$$D_{ii}(r) = \frac{4}{3} C_{\nu^2} r^{\frac{2}{3}} \quad \text{for } r \text{ in the inertial sub-range,} \quad (2.40)$$

$$D_u(r) = \frac{4}{3} C_v^2 l_{0,t}^{\frac{2}{3}} \left(\frac{r}{l_{0,t}} \right)^2 \quad \text{for } r \text{ in the dissipation range.} \quad (2.41)$$

In Eq. (2.38) - (2.41) $C_v^2 = C\varepsilon^{2/3} = (3\Gamma(1/3)/2)\alpha\varepsilon^{2/3} = 2.09\varepsilon^{2/3}$ is the structure parameter of velocity, with α the Kolmogorov constant (0.52) and $\Gamma(1/3)$ the gamma function with argument 1/3 (Högström, 1996; Monin and Yaglom, 1975; Wyngaard and Clifford, 1978). With Eqs. (2.38) - (2.41), i.e. the “two-third” law and the “squared law”, the cascade process is quantified, describing the velocity field of the atmosphere for the inertial sub-range and dissipation range.

By equating Eq. (2.34) with Eq. (2.35) and Eq. (2.36) with Eq. (2.37), one can obtain expressions for $l_{0,l}$ and $l_{0,t}$ that relates them to η . Using $C = (3\Gamma(1/3)/2)\alpha$, this leads to

$$l_{0,l} = \left(\frac{15\alpha 3\Gamma\left(\frac{1}{3}\right)}{2} \right)^{\frac{3}{4}} \left(\frac{v^3}{\varepsilon} \right)^{\frac{1}{4}} = 13.8\eta, \quad (2.42)$$

$$l_{0,t} = \left(\frac{10\alpha 3\Gamma\left(\frac{1}{3}\right)}{2} \right)^{\frac{3}{4}} \left(\frac{v^3}{\varepsilon} \right)^{\frac{1}{4}} = 10.2\eta. \quad (2.43)$$

As Eq. (2.34) and Eq. (2.36) differ by a factor 4/3 and Eq. (2.35) and Eq. (2.37) differ by a factor 2, the ratio $l_{0,l}/l_{0,t}$ equals $(3/2)^{3/4}$, regardless of the exact value of C .

Analogue to the wind field, Obukhov (1949) derived the structure function of the temperature field. He assumed the temperature to act passively in the turbulent flow and selected the important variables (besides r and D_{TT}) to be ε and ε_θ in the inertial sub-range and ε , ε_θ and v in the dissipation range, where ε_θ is the amount of temperature inhomogeneity that disappears per unit time because of molecular diffusion, i.e. the dissipation rate of temperature. Hence, the following relations are obtained (Obukhov, 1949; Tatarskii, 1961)

$$D_{TT}(r) = a\varepsilon_\theta \varepsilon^{\frac{-1}{3}} r^{\frac{2}{3}} \quad \text{for } r \text{ in the inertial sub-range,} \quad (2.44)$$

$$D_{TT}(r) = \frac{1}{3} \frac{\varepsilon_\theta}{D} r^2 \quad \text{for } r \text{ in the dissipation range.} \quad (2.45)$$

Eliminating D from Eq. (2.45), and rewriting Eq. (2.44) and Eq. (2.45) in terms of the temperature inner scale, $l_{0,T}$, (the point of intersection between the inertial sub-range and the dissipation range), leads to (Tatarskii, 1961)

$$D_{TT}(r) = C_{T^2} r^{\frac{2}{3}} \quad \text{for } r \text{ in the inertial sub-range,} \quad (2.46)$$

$$D_{TT}(r) = C_{T^2} l_{0,T}^{\frac{2}{3}} \left(\frac{r}{l_{0,T}} \right)^2 \quad \text{for } r \text{ in the dissipation range.} \quad (2.47)$$

where $C_T^2 = a \varepsilon_\theta \varepsilon^{-1/3} = (3\Gamma(1/3)/2)\beta_\theta \varepsilon_\theta \varepsilon^{-1/3} = 3.46 \varepsilon_\theta \varepsilon^{-1/3}$ is the structure parameter of temperature, with β_θ (0.86) the Obukhov-Corrsin constant. Eq. (2.46) and Eq. (2.47) are analogue to the ‘‘two-third’’ and ‘‘squared’’ law for a vector quantity and valid for any passive scalar. In the scintillometer literature the inner scale of the refractive index is assumed to equal the inner scale of temperature and it is often called the inner scale of turbulence or short the inner scale, l_0 (Hill, 1982; Hill and Ochs, 1978; Thiermann and Grassl, 1992). Henceforward we follow this convention.

As for the velocity field, one can relate l_0 to η , the smallest scale of the velocity field. Equating Eq. (2.44) with Eq. (2.45) and multiplying the derived expression for l_0 with $(v^{3/4}/v^{3/4})$, leads to

$$l_0 = \left(\frac{3\beta_\theta 3\Gamma\left(\frac{1}{3}\right)}{2 \text{Pr}} \right)^{\frac{3}{4}} \left(\frac{v^3}{\varepsilon} \right)^{\frac{1}{4}} = 7.4\eta, \quad (2.48)$$

where Pr is the Prandtl-number (ν/D). Regarding the constants in this equation, Hill (1997) concludes that $\beta_\theta = 0.86$ and $\text{Pr} = 0.72$ are most appropriate.

Three remarks need to be made regarding Eq. (2.48). First, note that Hill (1997) actually gives $\beta_\theta = 0.43$ instead of $\beta_\theta = 0.86$. This difference occurs, because two definitions for ε_θ are used in literature. $\beta_\theta = 0.43$ corresponds to the definition $\varepsilon_\theta = 2D \overline{(\nabla \theta')^2}$, whereas β_θ

$= 0.86$ corresponds to the definition $\varepsilon_\theta = D \overline{(\nabla \theta')^2}$. For sake of analogy with the kinetic energy, we chose the latter definition and use the rate of dissipation of $0.5 \overline{\theta'^2}$ (Kaimal et al., 1972; Monin and Yaglom, 1975; Sreenivasan, 1996; Stull, 1988).

Second, η is not the length scale for which the temperature spectrum goes to zero. This length scale is the Obukhov-Corrsin scale, η_θ (Hartogensis, 2006; Tatarskii et al., 1992)

$$\eta_\theta = \left(\frac{D^3}{\varepsilon} \right)^{\frac{1}{4}} = \text{Pr}^{\frac{-3}{4}} \eta. \quad (2.49)$$

From this follows that the length scale for which the temperature spectrum goes to zero is approximately 1.28η . Hence, the dissipation range of the temperature spectrum lays between 7.4η and 1.28η , which is considerably smaller than the dissipation range of the velocity spectrum.

Third, Eq. (2.48) relates the turbulent velocity field to the turbulent temperature field. Consequently, information from the velocity field can be inferred from the temperature field and the other way around. Thus, despite the fact that scintillometers can only determine information from the temperature field (C_T^2 and l_0) they provide enough information to estimate the surface fluxes related to both turbulent fields, i.e. the fluxes of sensible heat and momentum, see section 2.1.4.

Before proceeding with the fluxes, we first have to quantify the atmospheric temperature spectrum, because without an accurate description of the refractive index (temperature) spectrum, scintillometers cannot provide C_T^2 and l_0 . For the inertial sub-range the spectrum can be quantified by substituting the $r^{2/3}$ -law for temperature, i.e. Eq. (2.46), into Eq.(2.27). This yields an expression for the temperature spectrum that is valid in the inertial sub-range (Tatarskii, 1961)

$$\Phi_{TT}(k, C_T^2) = \frac{\Gamma\left(\frac{8}{3}\right) \cdot \sin\left(\frac{\pi}{3}\right)}{4\pi^2} \cdot C_T^2 k^{\frac{-11}{3}} = 0.033 \cdot C_T^2 k^{\frac{-11}{3}}. \quad (2.50)$$

The form of this spectrum is known as the Kolmogorov spectrum. As temperature is assumed to be a passive scalar, Eq. (2.50) is valid for any passive scalar, e.g. humidity, CO₂, and also the refractive index, which is required for scintillometry (Tatarskii, 1961).

Using Eq. (2.28), the 1D spectral density is obtained (Tatarskii, 1961)

$$F_{TT}(k, C_{T^2}) = \frac{\Gamma\left(\frac{5}{3}\right) \cdot \sin\left(\frac{\pi}{3}\right)}{2\pi} \cdot C_{T^2} k^{-\frac{5}{3}} = 0.1245 \cdot C_{T^2} k^{-\frac{5}{3}} \quad (2.51)$$

With this equation, C_T^2 and for example also C_q^2 can be derived from a point sensor, like thermocouples or fast-response hygrometers.

Eq. (2.50) is invalid in the dissipation range, but a solution for the spectrum in the dissipation range analogue to Eq. (2.50) could not be ascertained exactly (Tatarskii, 1961). Therefore, an extra term has been added to Eq. (2.50)

$$\Phi_{TT}(k, C_{T^2}, l_0) = 0.033 \cdot C_{T^2} k^{-\frac{11}{3}} \cdot f_A(k, l_0), \quad (2.52)$$

where $f_A(k, l_0)$ describes the deviation from the inertial sub-range in the dissipation range.

Figure 2 shows different forms of $f_A(k, l_0)$ for the dissipation range. In earlier works, the Tatarskii cut-off was commonly used (Tatarskii, 1961), meaning that $f_A(k, l_0)$ was assumed to be an exponential function equal to one in the inertial sub-range and rapidly decreasing to zero in the dissipation range. However, many studies have shown that on the transition from the inertial sub-range to the dissipation range f_A displays a bump. The bump was first observed in experiments of atmospheric turbulence (Champagne et al., 1977; Frehlich, 1992; Hill, 1978b; McBean, 1982; Mestayer, 1982; Williams and Paulson, 1977) and later on also in numerical studies ((Donzis and Sreenivasan, 2010; Gotoh and Watanabe, 2005; Verma and Donzis, 2007) and references therein).

Various models have been proposed to describe this bump (Andrews, 1992; Churnside, 1990; Falkovich, 1994; Grayshan et al., 2008; Hill, 1978a; Lohse and Mullergroeling, 1995; Qian, 1984; Tatarskii et al., 1992). Most of which are comprehensive fits to data, but some are more or less sophisticated explanations of these data. For an overview about literature that deals with the bump or “bottleneck phenomenon” as it is called in some disciplines we refer to (Coantic and Lasserre, 1999; Donzis and Sreenivasan, 2010; Verma and Donzis, 2007).

The existence of a bump in turbulence-temperature spectra is in itself not surprising. For fluids with arbitrary Prandtl or Schmidt number, Batchelor in the 1950s put forward a

model that explains the different parts of the scalar spectrum for a fluid with a passive scalar (Hill and Clifford, 1978; Monin and Yaglom, 1975; Tatarskii et al., 1992). He defined multiple wave-number ranges that defined the state of the fluid and the scalar field. These ranges are the inertial-convective range (inertial sub-range), the inertial-diffusive range, the viscous-convective range, and the viscous-diffusive range (dissipation range) (Hill and Clifford, 1978; Monin and Yaglom, 1975; Tatarskii et al., 1992). For $Pr \gg 1$, i.e. $D \ll \nu$, the viscous-convective range describes a range of wavenumbers for which molecular viscosity is already important to the velocity spectrum, whereas convection still is important to the scalar spectrum. It is this difference between viscous and convective decay of inhomogeneities, which gives rise to a bump in the spectrum (Hill and Clifford, 1978; Monin and Yaglom, 1975).

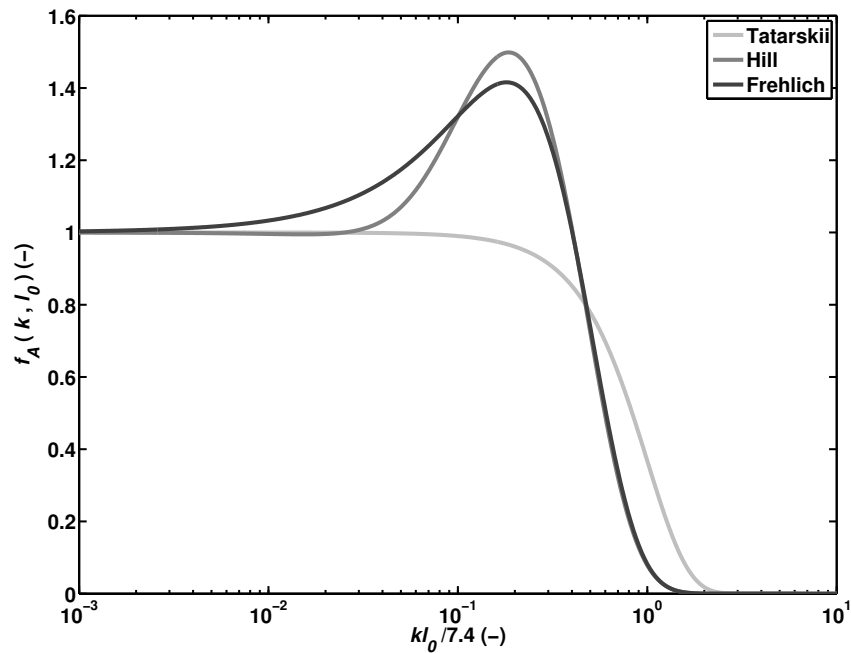


Figure 2.2: Temperature spectra of inertial sub-range and dissipation range normalized with the inertial sub-range values

The above described theory offers an explanation of a spectral bump in fluids with a large Prandtl/Schmidt-number, but this theory does neither explain why a bump in the temperature spectrum exists for the atmosphere, where $Pr \approx 0.72$ ($D > \nu$), nor explains the observed bump in the atmospheric velocity spectrum. Yet, the semi-empirical theory described above shows that in the atmosphere the inner scales of velocity, $l_{0,t} = 13.8\eta$ and $l_{0,v} = 10.2\eta$, are larger than the inner scale of temperature, $l_0 = 7.4\eta$. Consequently, as for fluids with $Pr \gg 1$, there exists

a viscous-convective range in the atmosphere (Dole et al., 2001). Many physical explanations have been suggested (Donzis and Sreenivasan, 2010; Verma and Donzis, 2007; Williams and Paulson, 1977), but up to the present day no consensus has been reached.

The model of Hill (1978a), which basically is a clever fit to the high-frequency temperature data of Champagne et al. (1977) and Williams and Paulson (1977) (Tatarskii et al., 1992), is commonly used in the application of scintillometry (Hartogensis, 2006; Hill and Clifford, 1978; Scintec, 2006). In doing so, it is assumed that the refractive-index spectrum, which is required for scintillometry, equals the temperature spectrum (Hill, 1982). Furthermore, a static form of the spectral bump is assumed.

Small-aperture scintillometer studies that were performed over land show good agreement of scintillometer data with independent data (Hartogensis, 2006; Hill et al., 1992; Thiermann and Grassl, 1992). These scintillometers are dependent on f_A , whereas the measurement systems through which the independent data were obtained are not. Hence, the good agreement suggests that the assumption of a static form of the bump is justified.

Nevertheless, some remarks should be made about the assumption concerning the form and position of the bump. First, the amplitude of the bump seems to vary with the Reynolds number for $Re < 1000$ (Donzis and Sreenivasan, 2010). However, as these Reynolds numbers hardly occur in the atmosphere the relevance for scintillometry is uncertain. Furthermore, in extreme humid conditions over the Salton sea the amplitude of the refractive-index bump is larger due to the influence of humidity (Grayshan et al., 2008; Hill, 1978b). In that case the assumption that the refractive-index spectrum equals the temperature spectrum does not remain valid. Finally, Frehlich (1992), using scintillation measurements over land, determines a spectral bump with a different amplitude and width than described by the model of Hill. So, even though the spectral bump in itself is not disputed, there is no general consensus about its exact form under all circumstances. Fortunately, for most scintillometer types an accurate description of the spectrum at these large wavenumbers is not required. Only for optical-wave scintillometers with small apertures the exact form of the bump is essential (Hartogensis, 2006).

2.1.4. Solutions to the atmospheric equations using similarity theory

With an accurate description of the refractive-index spectrum, scintillometry can provide estimates of C_T^2 and l_0 (which relates to ε). In this section, we discuss the atmospheric flow

and budget equations in order to show how C_T^2 and ε relate to the atmospheric surface fluxes, the quantities that we are interested in. In addition to C_T^2 and ε , the structure parameter of humidity, C_q^2 , is presented here, because C_q^2 can be directly resolved with scintillometry as well. Furthermore, q serves as representing an arbitrary passive scalar, since estimating fluxes with structure parameters is not limited to temperature and humidity only, see chapter 5.

As we study turbulence within the boundary layer we are merely interested in the turbulent part of the flow and budget equations that were presented in section 2.1.1. To obtain these turbulent equations, Reynolds decomposition is applied to Eqs. (2.3), (2.4), and (2.5) and the mean terms are subtracted from them. If we then multiply the obtained turbulent equations with $-2u_i'$, $-2\theta'$, and $-2q'$, we get the variance budget equations for velocity, temperature, and humidity (Stull, 1988)

$$\begin{aligned} \frac{\partial \overline{u_i'^2}}{\partial t} + \overline{u_j} \frac{\partial \overline{u_i'^2}}{\partial x_j} = & 2\delta_{i3} \frac{g(\overline{u_i'\theta_v'})}{\theta_v} - \overline{2u_i'u_j} \frac{\partial \overline{u_i}}{\partial x_j} - \frac{\partial (\overline{u_j'u_i'^2})}{\partial x_j} - \frac{2}{\rho} \frac{\partial (\overline{u_i'p'})}{\partial x_i} - 2\varepsilon \end{aligned} \quad (2.53)$$

I II III IV V VI VII

Term I represents the storage of variance (turbulent kinetic energy)

Term II describes advection of variance by the mean wind

Term III is a production or loss term depending on the buoyancy flux

Term IV is a production term related to the momentum flux

Term V is a turbulent transport term

Term VI describes the redistribution of variance due to pressure forces

Term VII is the dissipation of turbulent kinetic energy

Two major changes are evident when comparing Eq. (2.53) with Eq. (2.3). Firstly, term III contains buoyancy information. This results from the Boussinesq approximation that additionally was applied to Eq. (2.3). In doing so, it is assumed that density variations are negligible in the inertia, but not in the buoyancy term, because gravity enhances the density differences (Stull, 1988). Secondly, the original term IV, the coriolis term, describing the earth's rotation has cancelled out, because its components equal zero. This means that the coriolis force cannot produce or break down turbulent kinetic energy (Stull, 1988).

For heat the variance equation reads (Stull, 1988)

$$\frac{\partial \overline{\theta'^2}}{\partial t} + \overline{u_j} \frac{\partial \overline{\theta'^2}}{\partial x_j} = -2 \overline{\theta' u_j'} \frac{\partial \overline{\theta}}{\partial x_j} - \frac{\partial (\overline{u_j' \theta'^2})}{\partial x_j} - 2 \varepsilon_\theta - \frac{2}{\rho c_{pm}} \overline{\theta' \frac{\partial Q_{*j}'}{\partial x_j}} \quad (2.54)$$

I II IV V VII VIII

The terms I, II, IV, V, and VII are analogue to the terms in the momentum equation and term VIII is the radiation destruction term.

Finally, for humidity the variance equation reads (Stull, 1988)

$$\frac{\partial \overline{q'^2}}{\partial t} + \overline{u_j} \frac{\partial \overline{q'^2}}{\partial x_j} = -2 \overline{q' u_j'} \frac{\partial \overline{q}}{\partial x_j} - \frac{\partial (\overline{u_j' q'^2})}{\partial x_j} - 2 \varepsilon_q \quad (2.55)$$

I II IV V VII

The terms I, II, IV, V, and VII are analogue to the terms in the momentum and heat equations. Furthermore, it is assumed for humidity that the original term VII in Eq. (2.5), the storage/sink term, is a mean term only and not a perturbation term.

If we then assume quasi steady state and horizontal homogeneity, Eq. (2.53) - (2.55) reduce to

$$0 = 2 \frac{g(\overline{w' \theta_v'})}{\theta_v} - 2 \overline{u_i' w'} \frac{\partial \overline{u_i}}{\partial z} - \frac{\partial (\overline{w' u_i'^2})}{\partial z} - \frac{2}{\rho} \frac{\partial (\overline{w' p'})}{\partial z} - 2 \varepsilon \quad (2.56)$$

$$0 = -2 \overline{\theta' w'} \frac{\partial \overline{\theta}}{\partial z} - \frac{\partial (\overline{w' \theta'^2})}{\partial z} - 2 \varepsilon_\theta - \frac{2}{\rho c_{pm}} \overline{\theta' \frac{\partial Q_{*z}'}{\partial z}} \quad (2.57)$$

$$0 = -2 \overline{q' w'} \frac{\partial \overline{q}}{\partial z} - \frac{\partial (\overline{w' q'^2})}{\partial z} - 2 \varepsilon_q \quad (2.58)$$

Assuming that the flux divergence, the radiation divergence, and the pressure flux are negligible these equations can be further simplified to a balance between the production and destruction terms, aligned in the mean flow direction (Wyngaard and Kosovic, 1994)

$$\varepsilon = \frac{g(\overline{w' \theta_v'})}{\theta_v} - \overline{u' w'} \frac{\partial \overline{u}}{\partial z} \quad (2.59)$$

$$\varepsilon_\theta = -\overline{\theta'w'} \frac{\partial \bar{\theta}}{\partial z} \quad (2.60)$$

$$\varepsilon_q = -\overline{q'w'} \frac{\partial \bar{q}}{\partial z} \quad (2.61)$$

Even though these assumptions greatly reduced the amount of variables, the number of unknowns in the atmospheric-flow and budget equations still is larger than the number of equations. Consequently, the system of equations is unclosed. However, as we are interested in surface fluxes, we can close the system of equations by using a zero-order closure technique based on the dimensional considerations that were first introduced by Monin and Obukhov (1954).

Monin and Obukhov (1954) solved the closure problem by applying Buckingham-Pi theory, thereby creating dimensionless groups of the important surface layer variables (Monin and Yaglom, 1971; Stull, 1988). As long as the flux is more or less constant with height, so is the assumption, the surface fluxes can be deduced from these important variables. These variables were selected to be g/θ_v , $\overline{w'\theta_v'}$, u_* , and z , where g is the gravitational acceleration, $\overline{w'\theta_v'}$ is the buoyancy flux, z is the height above the surface, and u_* is the friction velocity, for which applies $u_* = \left(\overline{u'w'^2} + \overline{v'w'^2}\right)^{1/4}$ or when aligned with the mean wind $u_* = \left(\overline{u'w'}\right)^{1/2}$. From these variables two independent length scales can be derived, namely the height, z , and the Obukhov length, L_O . This leads to one dimensionless group ($\zeta \equiv z/L_O$), where L_O is defined as (Monin and Obukhov, 1954; Stull, 1988; Wyngaard and Kosovic, 1994)

$$L_O = \frac{-\overline{\theta_v} u_*^2}{k_{kar} g \theta_{v*}}, \quad (2.62)$$

with $k_{kar} = 0.4$, the von-Kármán constant and θ_{v*} a typical temperature scale for the surface layer. θ_{v*} is defined by

$$\theta_{v*} = -\overline{w'\theta_v'}/u_* . \quad (2.63)$$

where $\overline{w'\theta_v'}$ is the kinematic buoyancy flux at the surface. The Obukhov length is understood as the height above the surface where the shear and convective production of turbulence are

equal. This means that for large values of $|\zeta|$ (small values of L_O or large values of z) the production of turbulent energy by buoyancy is large compared to that of shear (Wyngaard and Clifford, 1978).

In addition to L_O , z is the other important parameter in the Monin-Obukhov similarity theory. At a first glance it seems that z is easy to determine, but depending on the complexity of the terrain or the height of the vegetation the effective value of z differs from the true value above the ground. Therefore, an accurate description of the effective height, z_{eff} , is important in scintillometry. Hartogensis et al. (2003) and Evans and De Bruin (2011) derived methods to estimate z_{eff} for two scintillometers types and showed the importance of an accurate estimate of z_{eff} . Furthermore, there is the concept of the zero-displacement height or displacement distance (Stull, 1988). For example, dense crops cause the logarithmic wind profile to be displaced as compared to the surface with a height that is roughly 2/3 of the crop height (Green et al., 1994). Also this effect needs to be taken into account in determining z_{eff} , especially for scintillometers that measure at a relatively low height ($z < 10\text{m}$) or when the displacement height is large (e.g. over forest or cities) (Stull, 1988).

Similarly as for the buoyancy flux, a typical temperature and humidity scale can be defined

$$T_* = -\overline{w'T'}/u_*, \quad (2.64)$$

$$q_* = -\overline{w'q'}/u_*, \quad (2.65)$$

where $\overline{w'T'}$ and $\overline{w'q'}$ are the kinematic temperature and humidity flux at the surface. In their dynamic form these fluxes read $H = \rho c_p \overline{w'T'}$ and $L_v E = \rho L_v \overline{w'q'}$, with c_p the heat capacity of air at constant pressure ($\text{J kg}^{-1} \text{K}^{-1}$) and L_v the latent heat of vaporization (J kg^{-1}).

Following Monin-Obukhov similarity theory, every dimensionless group that can be formed must be a function of ζ . In this way the gradients can be made dimensionless (Stull, 1988; Wyngaard and Kosovic, 1994)

$$\frac{k_{kar} z}{u_*} \frac{\partial u}{\partial z} = \phi_m(\zeta), \quad (2.66)$$

$$\frac{k_{kar} z}{\theta_*} \frac{\partial \theta}{\partial z} = \phi_T(\zeta), \quad (2.67)$$

$$\frac{k_{kar} z}{q_*} \frac{\partial q}{\partial z} = \phi_q(\zeta), \quad (2.68)$$

where $\phi_x(\zeta)$ are dimensionless functions of ζ . If we then nondimensionalize the flow equations and use the shorthand notation $\phi_x(\zeta) = \phi_x$, we arrive at (Wyngaard and Kosovic, 1994)

$$\varepsilon = \frac{g(\overline{w'\theta_v'})}{\theta_v} - \overline{u'w'} \frac{\partial \bar{u}}{\partial z} = \frac{u_*^3}{k_{kar} z} (-\zeta + \phi_m) \quad (2.69)$$

$$\varepsilon_\theta = -\overline{\theta'w'} \frac{\partial \bar{\theta}}{\partial z} = \frac{1}{k_{kar}} \frac{u_* \theta_*^2}{z} \phi_T \quad (2.70)$$

$$\varepsilon_q = -\overline{q'w'} \frac{\partial q}{\partial z} = \frac{1}{k_{kar}} \frac{u_* q_*^2}{z} \phi_q \quad (2.71)$$

Substituting $C_v^2 = (3\Gamma(1/3)/2)\alpha\varepsilon^{2/3}$, $C_T^2 = (3\Gamma(1/3)/2)\beta_\theta\varepsilon_\theta\varepsilon^{-1/3}$, and $C_q^2 = (3\Gamma(1/3)/2)\beta_q\varepsilon_q\varepsilon^{-1/3}$ into Eqs. (2.69) - (2.71) leads to (Andreas, 1988; Wyngaard and Kosovic, 1994)

$$\frac{C_v^2 z^{2/3}}{u_*^2} = \frac{3\Gamma(1/3)\alpha}{2k_{kar}^{2/3}} (-\zeta + \phi_m)^{2/3} = f_v(\zeta) \quad (2.72)$$

$$\frac{C_T^2 z^{2/3}}{\theta_*^2} = \frac{3\Gamma(1/3)\beta_\theta}{2k_{kar}^{2/3}} \phi_T (\phi_m - \zeta)^{-1/3} = f_T(\zeta) \quad (2.73)$$

$$\frac{C_q^2 z^{2/3}}{q_*^2} = \frac{3\Gamma(1/3)\beta_q}{2k_{kar}^{2/3}} \phi_q (\phi_m - \zeta)^{-1/3} = f_q(\zeta) \quad (2.74)$$

where $f_v(\zeta)$, $f_T(\zeta)$, and $f_q(\zeta)$ are dimensionless functions of ζ . Usually, it is assumed that $\beta_q = \beta_\theta$, and $\phi_q = \phi_T$, so that the similarity equations for heat and humidity are essentially the same (Wyngaard and Kosovic, 1994). Assuming that $\phi_m = \phi_T = 1$ for $\zeta = 0$ and $k_{kar} = 0.4$, yields $f_T(0) = 6.37$ (Thiermann and Grassl, 1992). Furthermore, for scintillometry, also the dimensionless form of Eq. (2.69) is relevant for obtaining u_*

$$\frac{u_*}{(k_{kar} z \varepsilon)^{1/3}} = (-\zeta + \phi_m)^{-1/3} = f_\varepsilon(\zeta), \quad (2.75)$$

Similarity theory states that $f_\varepsilon(\zeta)$ and $f_T(\zeta)$ are functions that can be universally applied. Unfortunately, it seems hard to determine these functions, especially for stable conditions. In addition, the assumptions in the theory can easily be violated. Katul et al. (2008) lists five reasons why dissimilarity occurs: active roles of temperature (and water vapour), advective conditions, modulations from the outer layer (and unsteadiness), dissimilarity in ground sources and sinks, and entrainment processes. Consequently, many expressions of $f_\varepsilon(\zeta)$ and $f_T(\zeta)$ co-exist (Hartogensis and De Bruin, 2005; Hill, 1997; Li et al., 2012; Moene et al., 2004; Savage, 2009).

By selecting the proper functions of $f_\varepsilon(\zeta)$ and $f_T(\zeta)$ the fluxes can be derived. From a scintillometer that can estimate C_T^2 and ε , H and u_* can be derived by iterating Eqs. (2.62), (2.64), (2.73), and (2.75). Thereby it is assumed that the sensible-heat flux represents the buoyancy flux. In case C_q^2 is measured as well, $L_v E$ can be solved by adding Eq. (2.65) and Eq. (2.74) to the iteration procedure, see chapter 4. In that case the buoyancy effect on L_O can be estimated by (Kohsiek, 1982)

$$L_O = \frac{-\rho c_p \bar{\theta}_v}{k_{kar} g} \frac{u_*^3}{H + 0.61 c_p \bar{\theta}_v E}, \quad (2.76)$$

Neglecting the humidity effect on buoyancy under wet conditions leads to an underestimation of about 1% in u_* , 2% in H , and 3% in $L_v E$, see chapter 4.

For scintillometers that only can estimate C_T^2 a slightly different approach is required to estimate H and u_* . Some authors have looked at the free convection limit ($-\zeta > 0.2$), for which the fluxes get independent of u_* (De Bruin et al., 1995; Green et al., 2000; Kohsiek, 1982; Li et al., 2012). The free convection approximation works best under warm and dry conditions with little wind, or higher in the atmosphere where z and thus $-\zeta$ is large (De Bruin et al., 1995). For values of $-\zeta > 0.5$ the error in the free convection method is negligible (De Bruin et al., 1995; Li et al., 2012).

Nevertheless, the free convection method is not applicable during stable or near neutral conditions. To avoid this restriction u_* must be estimated and this can be done in two ways. One, with Eq. (2.77), by using wind-speed measurements at two heights, $z_{eff,ul}$ and

$z_{eff,u2}$. Second, with Eq. (2.78), by using the wind speed at one height and an estimate for the roughness length, z_0 (the height at which the wind speed is zero) (Businger et al., 1971; De Bruin et al., 1995; Moene et al., 2004; Paulson, 1970)

$$u_* = \frac{k_{kar} (\overline{u_{z_{eff,u1}}} - \overline{u_{z_{eff,u2}}})}{\ln\left(\frac{z_{eff,u1}}{z_{eff,u2}}\right) - \Psi_m\left(\frac{z_{eff,u1}}{L_O}\right) + \Psi_m\left(\frac{z_{eff,u2}}{L_O}\right)} \quad (2.77)$$

$$u_* = \frac{k_{kar} \overline{u_{z_{eff,u1}}}}{\ln\left(\frac{z_{eff,u1}}{z_0}\right) - \Psi_m\left(\frac{z_{eff,u1}}{L_O}\right) + \Psi_m\left(\frac{z_0}{L_O}\right)}, \quad (2.78)$$

where Ψ_m is the Businger-Dyer equation for momentum. Using Eq. (2.77) or Eq. (2.78), H can be iteratively solved in combination with Eqs. (2.62), (2.64), and (2.73).

2.2. Scintillometry

A scintillometer is an instrument that emits a monochromatic electromagnetic-wave signal with a constant intensity (irradiance). Theoretically, this can be a signal of any wavelength. One or more transmitters emit a wave signal, which travels through the atmosphere and then is recorded by the receiver(s). On its travel through the atmosphere, turbulent eddies slightly scatter the wave signal and consequently the measured signal intensity fluctuates. The strength of these fluctuations is expressed by the (co)variance of the receiver(s) measurements and depends on the atmospheric conditions, the wavelength of the emitted signal, and the travelling distance through the atmosphere.

How these scattered electromagnetic waves relate exactly to C_T^2 and ε , and thus H and u_* , is explained in this section. To that purpose, we introduce the wave-propagation theory. This theory describes how electromagnetic waves propagate through the turbulent atmosphere and how they are affected by it. The physics behind the theory have a significant influence on the interpretation of the scintillometer measurements and therefore the theoretical section is followed by a section in which we describe the consequences for the interpretation of the measurements. Finally, we end the chapter by discussing how to infer C_T^2 and ε from the scintillometer measurements.

2.2.1. Wave-propagation through the turbulent atmosphere

How do the scattered electromagnetic waves relate to the atmospheric turbulence? Wave-propagation theory provides an answer to this question. In the following, we will start with a descriptive picture of wave-propagation and scattering concepts in the atmosphere that are relevant to scintillometry. In addition, we quantify the scattering of the propagated waves. This will be done by showing the derivation of a solution to the wave-propagation problem. There are multiple approaches to get to a solution. However, all start with the same set of equations, the Maxwell equations. Thus, the Maxwell equations are introduced and from them the wave equation is deduced. Subsequently, by combining the wave equation and atmospheric-turbulence theory, we derive a solution of the wave equation for waves that are scattered by atmospheric turbulence. It is with this solution that we attain the key equation for scintillometry.

2.2.1.1. Wave propagation and scattering

Electromagnetic waves that travel through the atmosphere undergo scattering and/or absorption. In the application of scintillometry, we limit ourselves to scattering caused by differences in air density and assume that further scattering/absorption by aerosols, CO₂, H₂O, etc. can either be neglected or discriminated from this scattering (see section 2.2.2 on how this can be done).

The density differences in the atmosphere occur, because turbulent eddies each have different densities as a result of their particular heat and humidity characteristics. Consequently, these eddies have different refractive indices, n , as well, causing them to act like small lenses through which and around which the electromagnetic waves are bended. The refractive index is defined as the factor with which the speed of an electromagnetic wave (speed of light, c) in a medium, m , is reduced as compared to that in vacuum, 0 ,

$$n = \frac{c_0}{c_m} = \sqrt{\frac{\epsilon_m \mu_m}{\epsilon_0 \mu_0}} = \sqrt{\epsilon_{rel} \mu_{rel}} \quad (2.79)$$

where μ is the magnetic permeability, ϵ is the dielectric constant, and the subscript *rel* denotes relative values (Hecht, 1998; Stull, 2000).

In the atmosphere, \bar{n} is near unity (1.000277 at standard pressure) and refractive index fluctuations are very small ($\sim 10^{-6}$) (Hecht, 1998). Hence, the scattering is weak, but since

eddies are moved through the atmosphere both horizontally and vertically, the refractive-index field continuously changes. These changes cause fluctuations in the amount of scatter, which as we will show in section 2.2.1.3 relate to the turbulence. Note, that the refractive index does not only depend on the fluid (the eddies), but also on the wavelength of the electromagnetic wave. This dependence on the wavelength is called dispersion (Hecht, 1998) and to avoid complications caused by dispersion a scintillometer signal is set to be nearly monochromatic.

Within scintillometry two scattering concepts are relevant, namely refraction and diffraction. Refraction is a change in direction and/or speed of the wave, i.e. bending (Hecht, 1998; Stull, 2000). It is known best by the example of a prism. A prism bends light, but one individual colour more than the other. Consequently, the white light is dispersed in the well-known rainbow pattern. Refraction occurs when the smallest eddies are still larger than the beam, so that they can only focus and defocus the signal like a lens. The conditions for which refraction dominates is quantified by $\sqrt{\lambda L} \ll l_0$, where L is the travelling-path length and λ the wavelength (Tatarskii, 1961). In practice this means that refraction occurs for an optical-wave signal when $L \ll (10^{-2})^2/10^{-6} = 100$ m and when $L \ll (10^{-2})^2/10^{-3} = 0.1$ m for a millimetre-wave signal.

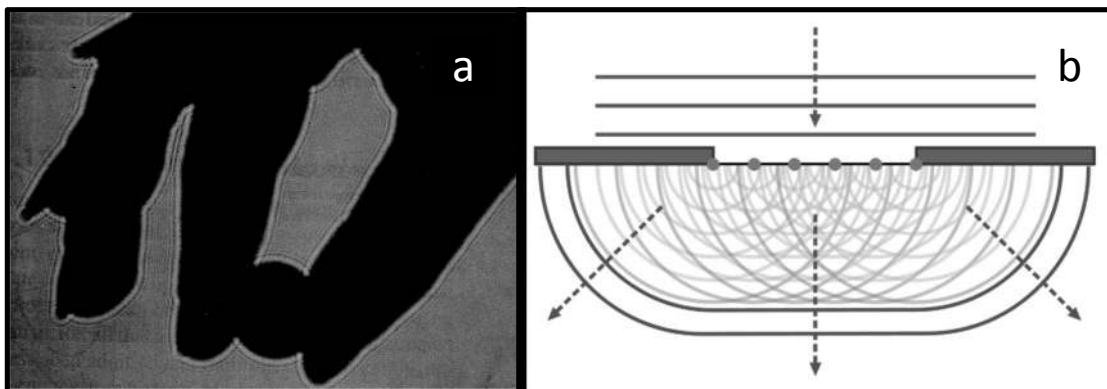


Figure 2.3: Effect of diffraction for (a) a shadow on a wall (Hecht, 1998), and (b) for plane waves passing a small opening using the Huygens-Fresnel principle to explain the curvature.

Diffraction is “the bending or spreading of a wave around an object” (Kapralos et al., 2005). In colliding with and bending around the object, part of the wave front changes and when propagating beyond the object there are two possibilities. Firstly, interference with other parts of the wave front can occur, so that the typical diffraction patterns occur. This is illustrated by e.g. a shadow on the wall, of which the edges between light and dark are not sharp (Figure

2.3a). Secondly, part of the wave front can be blocked, so that the undisturbed part has to redistribute its density (Hecht, 1998). This is illustrated by e.g. plane waves approaching a small inlet. A part of the wave front goes through the inlet and travels further, but now as circular waves (Figure 2.3b). Diffraction is explained by the Huygens-Fresnel principle: “every point on the primary wave front can be thought of as a continuous emitter of secondary wavelets (sources) and these secondary wavelets combine to produce a new wave front in the direction of propagation” (Kapralos et al., 2005); cf. (Hecht, 1998). Diffraction occurs when the beam is larger than the smallest eddies, so that the waves can bend around them (Strohbehn, 1968), i.e. for $\sqrt{\lambda L} \gg l_0$.

Scattering always affects the electromagnetic wave on its travel through the atmosphere. When diffraction occurs, the wave starts to widen in all directions as is explained by the Huygens-Fresnel principle. Therefore, at the receiver, a part of the beam comes directly from the transmitter, but other parts have travelled further and arrive therefore (partly) out of phase.

The concept that describes which secondary waves arrive at the receiver in or out of phase is the Fresnel zone concept. More Fresnel zones exist, all being concentric with the first one, ring shaped and with less influence than the previous one. Waves from odd numbered Fresnel zones do not interfere at the receiver with waves that come straight from the transmitter, whereas waves from even numbered Fresnel zones interfere destructively.

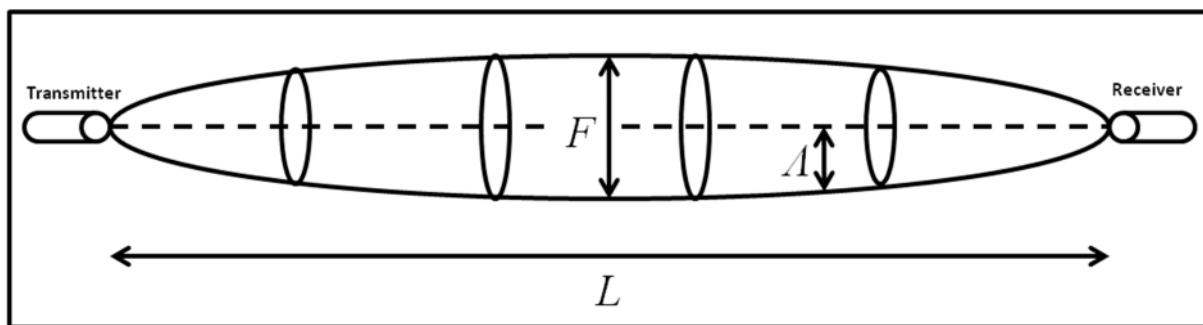


Figure 2.4: Schematic drawing of the first Fresnel zone. L is the distance between the transmitter and the receiver, A is the local radius of the first Fresnel zone, and F is the maximum diameter of the first Fresnel zone.

The first Fresnel zone takes a special position. It is a theoretical ellipsoid that is smallest at the ends, largest in the middle and has circular cross sections (Figure 2.4). The radius of the first Fresnel zone, A , changes along the path and is given by $A = \sqrt{\lambda x(L-x)/L}$, where $0 \leq x \leq L$

(Tatarskii, 1961). In order to distinguish it from the maximal diameter of the first Fresnel zone, F , A is also called the local radius of the first Fresnel zone. F is found at $x = 0.5L$ and is given by $F = \sqrt{\lambda L} = 2\sqrt{\lambda 0.5L(L - 0.5L)/L}$. In case $x \neq 0.5L$, $F > 2A$. To the application of scintillometry the first Fresnel zone is the most important of all Fresnel zones, because eddies of these sizes scatter most efficiently. Furthermore, the first Fresnel zone must always be free of objects to get a signal at the receiver (Kapralos et al., 2005).

2.2.1.2. The wave equation

The above description of scattering seems simple, but to quantify the scattering of waves travelling through the turbulent atmosphere is complex. Therefore, more theoretical approaches/frameworks for solving the propagation problem co-exist. Yet, the starting point of all these approaches is the same, the Maxwell equations. Tatarskii (1961) makes four assumptions to simplify the Maxwell equations and hence formulates the wave equation. The first assumption is that the refractive index field is a random function of the coordinates and does not depend on time, i.e. all the time changes are actually different realizations of the random field. The second assumption is that the conductivity of the atmosphere is zero (and thus free of charges, \vec{j}) and $\mu_{rel} = 1$. The third assumption is that the time dependence of the electromagnetic field is sinusoidal, $e^{-i\omega t}$, so that every field has the form $H = H_0 e^{-i\omega t}$.

This leads to the following set of simplified Maxwell equations (Tatarskii, 1961)

$$\begin{aligned}\nabla \times \vec{E} &= i\kappa \vec{H} \\ \nabla \times \vec{H} &= -i\kappa \varepsilon_{rel} \vec{E} \\ \nabla \cdot \varepsilon_{rel} \vec{E} &= \varepsilon_{rel} \nabla \cdot \vec{E} + \vec{E} \cdot \nabla \varepsilon_{rel} = 0\end{aligned}\tag{2.80}$$

where $\kappa = \omega/c$ is the wave number of the electromagnetic wave and E and H are the amplitudes of the electric and magnetic fields.

In order to derive the wave equation from the Maxwell equations, H is eliminated by taking the curl of the first equation and using the right hand side of the second equation with the equality $\nabla \times (\nabla \times \vec{E}) = \Delta \vec{E} - \nabla(\nabla \cdot \vec{E})$. Subsequently, the third Maxwell equation is used to express the latter term of this equality as

$$\nabla \cdot \vec{E} = -\vec{E} \cdot (\nabla \varepsilon_{rel}) / \varepsilon_{rel} = -\vec{E} \cdot \nabla \log \varepsilon_{rel}. \quad (2.81)$$

This leads to the full expression of the wave equation

$$\Delta \vec{E} + \kappa^2 \varepsilon_{rel} \vec{E} - \nabla (\nabla \cdot \vec{E}) = \Delta \vec{E} + \kappa^2 \varepsilon_{rel} \vec{E} + \nabla (\vec{E} \cdot \nabla \log \varepsilon_{rel}) = 0 \quad (2.82)$$

where $\Delta = \nabla^2 = \partial^2 / \partial x^2 + \partial^2 / \partial y^2 + \partial^2 / \partial z^2$.

Then, the fourth assumption is that depolarization effects are negligible. Together with the fact that $\varepsilon_{rel} = n^2$ (Eq. (2.79)) this leads to the final form of the wave equation, also known as the Helmholtz equation (Lawrence and Strohbehn, 1970; Tatarskii, 1961)

$$\Delta \vec{E}(\vec{r}) + \kappa^2 n^2(\vec{r}) \vec{E}(\vec{r}) = 0. \quad (2.83)$$

To neglect polarization effects (the third term from Eq. (2.82)), Tatarskii (1961) assumes that only small-angle scattering occurs, i.e. $\lambda \ll l_0$, hence excluding electromagnetic waves in the millimetre/centimetre region. However, Lee and Harp (1969) show that this assumption is irrelevant, because for large waves the influence of inhomogeneities on the order of l_0 is negligible compared to the optically most active inhomogeneities that affect large waves. Furthermore, the use of a finite receiver aperture results in a cone from which scattered light is recorded and thus prevents wide-angle scattering (Lee and Harp, 1969). Consequently, also for millimetre/centimetre waves depolarisation effects can safely be ignored.

2.2.1.3. Solution to the wave equation

The wave equation is non-linear and therefore impossible to solve without more assumptions. To derive a solution to the wave equation for an electromagnetic wave scattered by atmospheric turbulence multiple approaches and thus multiple solutions exist. In the following, we will shortly introduce three common methods and show the derivation for the most comprehensive method, which is required for scintillometry.

The first method is called the method of geometrical optics. This method neglects diffraction and explains the scattering of the signal with refraction. The geometrical optics method is applicable only over short path lengths ($L \ll 100$ m), because as shown in section 2.2.1.1 for longer path lengths diffraction is dominant (Strohbehn, 1968).

The second method is called the method of “small” perturbations or Born approximation. This approximation assumes perturbations to the wave to be small and “assumes that the field at the receiver can be calculated as the sum of the original field plus the field scattered one time” by a turbulent eddy (Strohbehn, 1968).

The third method is called the method of “smooth” perturbations, better known as the Rytov method. This method does not apply the perturbation technique to the wave, but to the logarithm of the wave, $\psi = \ln(E)$ (Obukhov, 1953; Tatarskii, 1961). This method describes scattering of the signal with diffraction as does the Born approximation, but because perturbations are applied to the logarithm of the wave the requirement of small perturbations is not so stringent anymore (Monin and Yaglom, 1975). Furthermore, by applying perturbation theory to the logarithm of the wave field instead of to the wave field itself, it is assumed that the probability distribution of the amplitude fluctuations follow the lognormal distribution instead of the so-called Rayleigh distribution (Monin and Yaglom, 1975; Strohbehn, 1968).

In the following, we show the derivation of the solution of the wave equation for the Rytov method only. However, both the geometrical optics method and the Born approximation result as a limiting case of the Rytov method (Lawrence and Strohbehn, 1970; Strohbehn, 1968). Furthermore, in describing the turbulent n field, Tatarskii (1961) makes two assumptions, namely that $\bar{n} = 1$ and that $n' \ll 1$. He thereby uses n_l instead of n' , so henceforth we follow this convention.

The Rytov method assumes that the wave has the form $E = Ae^{iS}$, with A the amplitude and S the phase. Consequently, the logarithm can be written as $\Psi = \chi + iS$, where $\chi \equiv \ln(A)$. Hence, the logarithmic amplitude, χ , is the real part of Ψ and the phase, S , is the imaginary part (Obukhov, 1953; Strohbehn, 1968). Substituting the logarithm into the wave equation (Eq. (2.83)), leads to the Riccati equation

$$\Delta \vec{\psi}(\vec{r}) + \nabla \vec{\psi}(\vec{r}) \cdot \nabla \vec{\psi}(\vec{r}) + \kappa^2 n^2(\vec{r}) = 0. \quad (2.84)$$

To get a solution of Eq. (2.84) Tatarskii (1961) applies the method of perturbations whereby $\vec{\psi}$ is expanded into a linear series $\vec{\psi} = \vec{\psi}_0 + \vec{\psi}_1 + \vec{\psi}_2 + \vec{\psi}_3 + \dots + \vec{\psi}_\infty$. Tatarskii (1961) assumes that single scattering occurs, i.e. he neglects the higher order terms Ψ_2 , Ψ_3 , etc. This assumption is valid in many cases, but as will be shown it limits the validity of the obtained

solution under conditions of strong turbulence, when multiple scattering occurs (Monin and Yaglom, 1975; Strohbehn, 1968).

By neglecting the higher order terms, the following expression is obtained

$$\Delta \psi_1(\vec{r}) + 2\nabla \psi_0(\vec{r}) \cdot \nabla \psi_1(\vec{r}) + 2\kappa^2 n_1^2(\vec{r}) = 0. \quad (2.85)$$

The solution of this differential equation for a scattered wave is (Monin and Yaglom, 1975; Tatarskii, 1961)

$$\psi_1(\vec{r}) = \frac{\kappa^2}{2\pi u_0(\vec{r})} \int_V n_1(\vec{r}') u_0(\vec{r}') \frac{e^{ik|\vec{r}-\vec{r}'|}}{|\vec{r}-\vec{r}'|} dV', \quad (2.86)$$

in which u_0 describes the wave and \vec{r}' is a variable vector with components x' , y' and z' ranging over the volume V' , the scattering volume i.e. the region in which $n_1(\vec{r})$ is non-zero (Tatarskii, 1961).

Subsequently, Tatarskii (1961) expands the radius, r , into Cartesian coordinates and assumes that the perturbed-refractive-index field $n_1(r') = n_1(x', y', z')$ and the perturbed-wave field $\psi_1(r') = \psi_1(x', y', z')$ are homogeneous and isotropic random fields that can be represented by a stochastic Fourier-Stieltjes integral. In addition he assumes that the wave form is spherical.

Applying these assumptions to Eq. (2.86) leads to an expression connecting the spectral amplitudes of the perturbed-wave field, $d\phi$, to the spectral amplitudes of the perturbed-refractive-index field, $d\nu$

$$d\phi(k_2, k_3, L) = -i\kappa \int_0^L e^{\frac{-iL(L-x)(k_2^2+k_3^2)}{2\kappa x}} d\nu\left(k_2 \frac{L}{x}, k_3 \frac{L}{x}, x\right) dx, \quad (2.87)$$

with k the eddy wavenumber and k_2 and k_3 its components in the y and z direction.

Tatarskii (1961) states that this equation has a simple physical meaning: "Field inhomogeneities characterized by the wave number k (i.e. by the dimension $l = 2\pi/k$) owe their origin to inhomogeneities of the medium with characteristic wave number kL/x , or with dimensions $l' = lx/L$. These inhomogeneities are at the distance x from the wave source. The

factor x/L takes into account the magnification of the dimensions of the image due to illumination by a divergent ray bundle.”

In addition to $n_I(x', y', z')$ and $\psi_I(x', y', z')$, also the amplitude of the perturbed-wave field, $\chi'(L, y, z)$, with $\chi' = \ln(A_1)/\ln(A_0)$ can be expanded in a Fourier-Stieltjes integral

$$\chi'(L, y, z) = \iint e^{i(k_2 y + k_3 z)} da(k_2, k_3, L) \quad (2.88)$$

where da is the spectral amplitude of the amplitude of the perturbed-wave field. As y and z equal zero, the variance of the logarithmic-amplitude fluctuations is represented by

$$\overline{\chi'^2} = \overline{\chi'(L, 0, 0)\chi'^*(L, 0, 0)} = \iiint \overline{da(k_2, k_3, L)da^*(k'_2, k'_3, L)}. \quad (2.89)$$

Furthermore, da is connected to $d\varphi$ by

$$da(k_2, k_3, L) = \frac{d\varphi(k_2, k_3, L) + d\varphi^*(-k_2, -k_3, L)}{2}, \quad (2.90)$$

and therefore, by substituting Eq. (2.87) into Eq. (2.90), an expression that connects da to $d\nu$ can be obtained

$$da(k_2, k_3, L) = -\kappa \int_0^L \sin\left(\frac{L(L-x)(k_2^2 + k_3^2)}{2\kappa x}\right) d\nu\left(k_2 \frac{L}{x}, k_3 \frac{L}{x}, x\right) dx. \quad (2.91)$$

Finally, substitution of Eq. (2.91) into Eq. (2.89) leads to an expression that connects the amplitude fluctuations of the perturbed wave to the spectral amplitudes of the perturbed-refractive-index field, $d\nu$, and thus to the refractive-index spectrum (cf. Eq. (2.22)).

To solve this complex equation Tatarskii (1961) assumes that the turbulent field has no influence on the scattered wave for sizes larger than the Fresnel zone. Together with the already applied assumption of local isotropy, this leads to the scintillometer equation for a point-source scintillometer (a scintillometer with an aperture much smaller than F)

$$\overline{\chi'^2} = 4\pi^2 \kappa^2 L \int_0^\infty \Phi_{nn}(k, C_{n^2}, l_0) dk \int_0^k \sin^2\left(\frac{Lk'(k-k')}{2\kappa}\right) dk' \quad (2.92)$$

Wang et al. (1978) substitute the wave number and path length in Eq. (2.92), which leads to the more common form

$$\overline{\chi'^2} = 4\pi^2 \kappa^2 \int_0^L \int_0^\infty k \Phi_{nn}(k, C_{n^2}, l_0) \cdot \sin^2\left(\frac{k^2 x(L-x)}{2\kappa L}\right) dx dk. \quad (2.93)$$

Eq. (2.93) links both turbulence and wave propagation theory. Solutions to this equation can be obtained for the case of diffraction or refraction, i.e. long and short path lengths. For that it is essential that the refractive-index spectrum is correctly prescribed. Thus, Tatarskii (1961) assumes that the Kolmogorov spectrum applies (Eq. (2.50)) and consequently, the solution for the condition $\sqrt{\lambda L} \gg l_0$ is

$$\overline{\chi'^2} = 0.13 \cdot C_{n^2} \kappa^{7/6} L^{11/6} \quad (2.94)$$

and the solution for the condition $\sqrt{\lambda L} \ll l_0$ is

$$\overline{\chi'^2} = 0.246 \cdot C_{n^2} L^3 l_0^{-7/3}. \quad (2.95)$$

2.2.2. Scintillometer measurements

The detector in the receiver of the scintillometer measures the intensity or irradiance, I , of the propagated wave and returns a voltage such that the signal strength is equal to the measured intensity. Since $I = A^2$, the variance of the logarithmic intensity of the wave equals four times the variance of the logarithmic amplitude of the wave, i.e. $\overline{(\ln(I))^2} = 4\overline{\chi'^2}$ (Lawrence and Strohbehn, 1970). This section shows the implications of the theory on the measurements and the method to derive C_{n^2} and l_0 from the scintillometer measurements $\text{var}(\ln(I))$ and $\text{covar}(\ln(I_1), \ln(I_2))$.

Ideally, only scattering induces $\text{var}(\ln(I))$, but in practice absorption or electronic noise can induce additional variance as well (Nieveen et al., 1998a). Most commercially available

scintillometers apply a band-pass filter to remove high-frequent noise or absorption fluctuations, so usually there is no need to bother about it. However, in chapter 3, we show possible consequences when this filtering fails.

Once $\text{var}(\ln(I))$ is properly obtained, we can acquire C_n^2 . However, it is not evident how the spatial distribution of eddies influences $\text{var}(\ln(I))$. To shed some light on this issue we introduce Figure 2.5. Figure 2.5 shows the spatial contribution of turbulent eddies (expressed in terms of their wavenumbers) to the intensity fluctuations, for each position on the path of a point-source scintillometer.

Three important implications of scintillometer theory on the measurements can be readily deduced from this. First, not all eddies at a given position x contribute to the intensity fluctuations (the graph goes to zero frequently). Second, smaller eddies (eddies with higher wavenumbers) cause less intensity fluctuations than larger eddies at a position x , i.e. the secondary peaks are smaller than the primary peak. Third, eddies at the centre of the scintillometer path cause larger intensity fluctuations than eddies at the edges of the scintillometer path (Meijninger, 2003; Ward et al., 2011).

Furthermore, Figure 2.5a shows a curvature in the intensity fluctuations with respect to the eddy wavenumber. Towards the edges of the scintillometer path, the primary contribution to the intensity fluctuations is caused by eddies with higher wavenumbers than at the centre of the path. At first instance, this distribution over the eddy wave-numbers looks rather arbitrary. However, the curvature relates to the diameter of the local first Fresnel zone, 2λ . When the eddy wavenumber is normalized with 2λ , the curvature disappears (Figure 2.5b). This stresses that the importance of an eddy (refractive-index inhomogeneity) depends on the relation between its dimensions and the dimensions of the local first Fresnel zone (Tatarskii, 1961). Eddies with eddy wavelengths of 2λ scatter most efficient, whereas eddies with wavelengths different from 2λ scatter less efficient. This conclusion holds for $F \gg l_0$, i.e. when diffraction is the important scattering mechanism.

Also the scintillometer formula confirms the importance of the first Fresnel zone. When we rewrite the sine term in Eq. (2.93) in terms of the radius of the local first Fresnel zone, λ , and the eddy wavelength, $l = 2\pi/k$, the equation becomes

$$\overline{(\ln(I))^2} = \pi^2 \kappa^2 \int_0^{L_\infty} \int_0^\infty k \Phi_{mn}(k, C_n^2, l_0) \cdot \sin^2\left(\pi \frac{\lambda^2}{l^2}\right) dx dk. \quad (2.96)$$

Thus, it can be seen that the Fresnel zone concept is an important concept in scintillometry.

For situations when $2A \ll l_0$, refraction is the most important scattering mechanism. Regardless of the wavelength of the scintillometer, eddies with eddy wavelengths $2l_0$ scatter most efficiently (Figure 2.5c). The scattering has become independent of the wavelength, because “there is no significant energy in the turbulence for eddy sizes smaller than l_0 ” (Strohbehn, 1968). Furthermore, also the secondary peaks do not exist anymore.

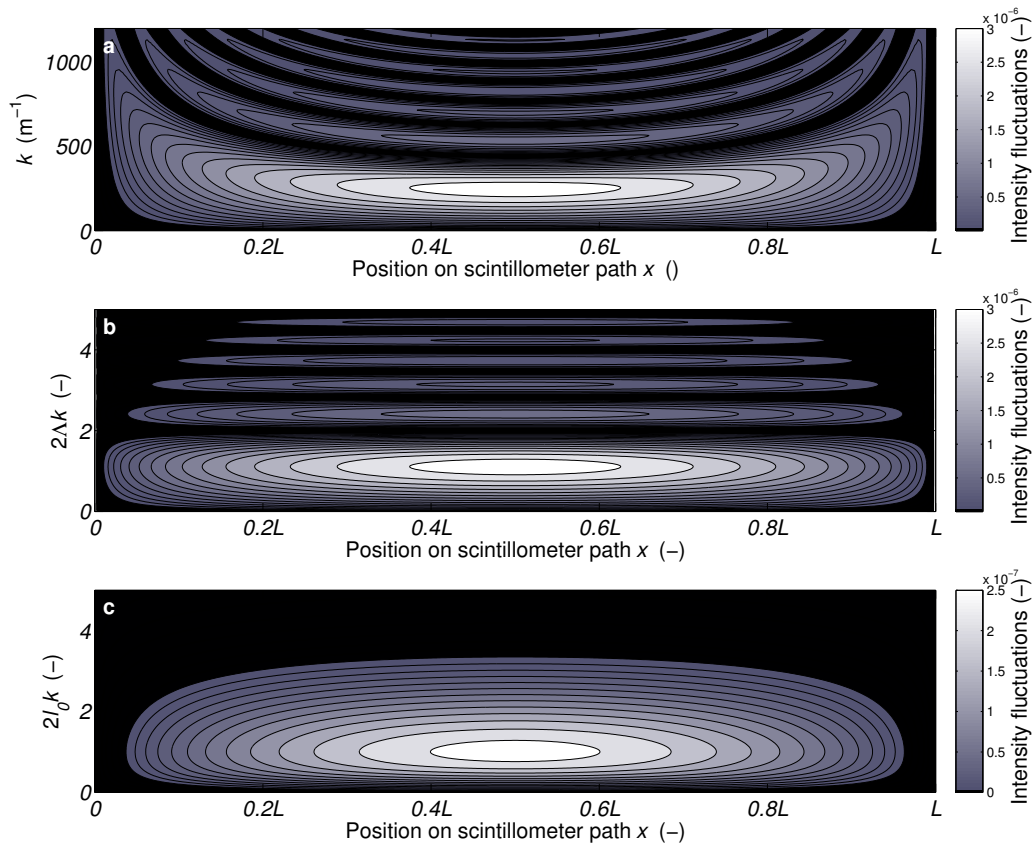


Figure 2.5: Relative contribution to the intensity fluctuations of eddies with wavenumber k on position x on the scintillometer path, (a) not normalized, (b) eddy wavenumbers are normalized with respect to the local radius of the first Fresnel zone, A , and (c) eddy wavenumbers are normalized with respect to l_0

The above-mentioned shows the contribution to the intensity fluctuations from individual eddies with a given wavenumber on a specific position on the scintillometer path. However, the overall effect on $\text{var}(\log(I))$ of all eddies on the scintillometer path only becomes clear by integrating Eq. (2.96) over k or x . The resulting path-weighting function and eddy-weighting function are introduced in Figure 2.6 for a theoretical point-source scintillometer and two commercial available scintillometers, which we will introduce and discuss below.

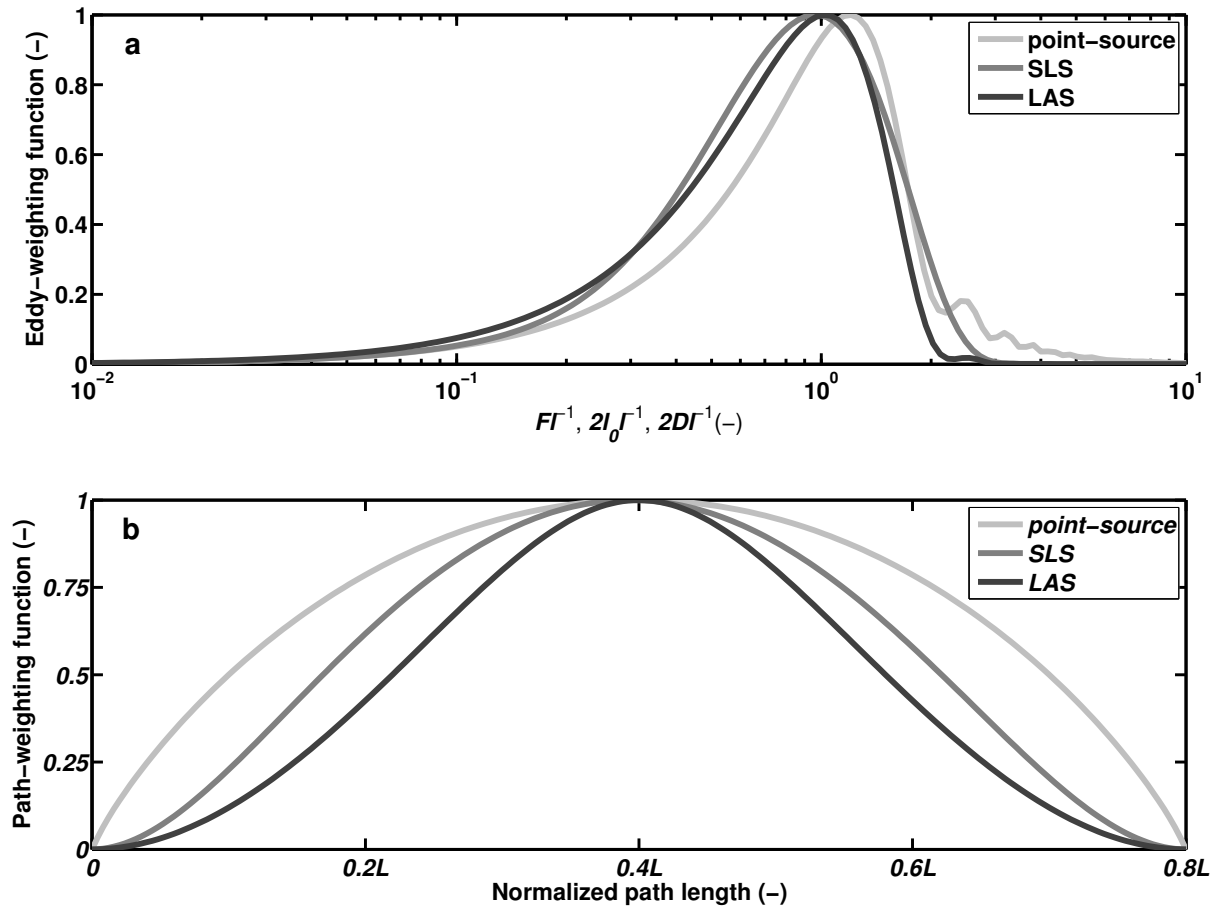


Figure 2.6: (a) Eddy-weighting function and (b) path-weighting function for a point-source scintillometer, a displaced-beam laser scintillometer (SLS), and a large-aperture scintillometer (LAS). The eddy-weighting function for each scintillometer is normalized with the eddy wavelength, l , which spans the physical size of two eddies.

The point-source scintillometer (with $F \gg l_0$) is clearly sensitive to eddies with eddy wavelengths slightly smaller than F (peak is located at $F/l = 1.2$). Furthermore, the scintillometer is most sensitive at the centre of the path and insensitive at the edges of the path. Thus, the scintillometer path averaging is not equal over the whole path. On the one hand this causes the scintillometer measurement to lose some spatial representativeness, but on the other hand flow distortion by the structures on which the scintillometer is mounted is negligible (Thiermann and Grassl, 1992).

Finally, note that the intensity fluctuations observed by the scintillometer do not necessarily come from straight below the scintillometer. The area from which these eddies origin is called the footprint area and depends on scintillometer height above the ground, stability, wind speed, and wind direction (Meijninger et al., 2002b). The real area over which is averaged, thus depends on more factors than the path-weighting function only.

Until now, we considered a virtual point-source scintillometer. However, the scintillometer equation can be extended to account for multiple beams with or without different wavelengths, transmitters and receivers with different apertures etc. The scintillometer equation then becomes

$$\overline{(\ln(I))}^2 = \pi^2 \kappa^2 \int_0^L \int_0^\infty k \Phi_{nm}(k, C_{n^2}, l_0) \cdot \sin\left(\pi \frac{\Lambda_1^2}{l^2}\right) \sin\left(\pi \frac{\Lambda_2^2}{l^2}\right) f_{avTr} f_{avRc} f_{cov} dx dk \quad (2.97)$$

where f_{avTr} describes the aperture averaging for the transmitter, f_{avRc} describes the aperture averaging for the receiver, f_{cov} describes the covariance of two beams, and Λ_1 and Λ_2 reflect the different wavelengths of the beams (Hill and Lataitis, 1989; Wang et al., 1978),

$$f_{avTr} = 2 \frac{J_1\left(0.5kD_{Tr1}\left(1-\frac{x}{L}\right)\right)}{0.5kD_{Tr1}\left(1-\frac{x}{L}\right)} \cdot 2 \frac{J_1\left(0.5kD_{Tr2}\left(1-\frac{x}{L}\right)\right)}{0.5kD_{Tr2}\left(1-\frac{x}{L}\right)} \quad (2.98)$$

$$f_{avRc} = 2 \frac{J_1\left(0.5kD_{Rc1}\frac{x}{L}\right)}{0.5kD_{Rc1}\frac{x}{L}} \cdot 2 \frac{J_1\left(0.5kD_{Rc2}\frac{x}{L}\right)}{0.5kD_{Rc2}\frac{x}{L}} \quad (2.99)$$

$$f_{cov} = J_0\left(k\left|d_T\left(1-\frac{x}{L}\right) + d_R\left(\frac{x}{L}\right)\right|\right) \quad (2.100)$$

where, J_0 and J_1 are Bessel functions of the first kind and zeroth and first order, D_{Tr1} and D_{Tr2} are the diameters of transmitter one and two, D_{Rc1} and D_{Rc2} are the diameters of receiver one and two, and d_T and d_R are the separation distances between the centre of the transmitters and the receivers respectively.

From the theoretical basis of Eq. (2.97) many possible types of scintillometers can be and have been developed: large-aperture scintillometers, microwave scintillometers, bi- and monochromatic displaced-beam scintillometers, the boundary-layer scintillometer etc. (De Bruin et al., 1995; Green et al., 2001; Green et al., 1997; Hill, 1992; Hill and Ochs, 1978; Hill et al., 1992; Kleissl et al., 2009; Meijninger et al., 2006; Meijninger et al., 2002a; Thiermann and Grassl, 1992; Wang et al., 1978). Depending on the type or combination of scintillometers, these scintillometers can estimate different variables, like $L_v E$, H , and u^* , from

C_q^2 , C_T^2 , and l_0 , or in some cases also crosswind and visibility. Discussing all these scintillometer types falls outside the scope of this thesis and in the following two sections we will limit ourselves to the two commercially available scintillometers that have been used in experiments as a part of this PhD project.

2.2.2.1. Large aperture scintillometer

Tatarskii (1961) derived the theory described above under the assumption of weak scattering. As a result, this theory fails under conditions of strong turbulence and is only valid for $\overline{(\ln(I))^2} \leq 1.2$ (Clifford et al., 1974; Monin and Yaglom, 1975; Strohbehm, 1968). If the value of 1.2 is crossed $\overline{(\ln(I))^2}$ increases no longer when C_n^2 increases, i.e. additional eddy-fluctuations do not cause larger amplitude fluctuations. This process is called saturation. Especially optical scintillometers are susceptible to this, because their Fresnel zone is relatively small. In order to prevent saturation one must either increase the wavelength (seeing bigger eddies, which there are fewer) or shorten the path length (seeing less eddies).

However, optical scintillometers can resolve C_T^2 and H , which in itself are already much desired measurable quantities over long paths. However, what is more, a large-aperture scintillometer is an essential part of an optical-microwave scintillometer system, which can resolve H and $L_v E$. Thus, there are good reasons why people do want to operate optical scintillometers over long paths (5-10 km) and therefore Wang et al. (1978) developed a large-aperture scintillometer (LAS) to prevent saturation. This scintillometer is based on the theory of Clifford et al. (1974) and emits a beam of near-infrared light (940nm). The corresponding equation is

$$\overline{(\ln(I))^2} = \pi^2 \kappa^2 \int_0^L \int_0^\infty k \Phi_{nn}(k, C_{n^2}) \cdot \sin^2\left(\pi \frac{\Lambda^2}{l^2}\right) \cdot \left(\frac{2 \cdot J_1\left(0.5kD \frac{x}{L}\right)}{0.5kD \frac{x}{L}} \cdot \frac{2 \cdot J_1\left(0.5kD \left(1 - \frac{x}{L}\right)\right)}{0.5kD \left(1 - \frac{x}{L}\right)} \right)^2 dx dk \quad (2.101)$$

where $D = D_{Tr1} = D_{Tr2} = D_{Rc1} = D_{Rc2}$ is the aperture diameter of the scintillometer (0.15 m). Note that Eq. (2.101) is only valid for $D \geq 20l_0$, because it neglects the dissipation-range of the turbulence spectrum (Hill, 1981). The solution differs from Eq. (2.96) and is given by

$$\overline{(\ln(I))^2} = 4 \cdot 0.223 C_n^2 D^{-7/3} L^3. \quad (2.102)$$

Figure 2.6 shows the result of aperture averaging. The most important eddy sizes are not those with Fresnel-zone wavelengths anymore, but those that have an eddy wavelength of about $2D$ (eddies with a physical size that equals D). Eddies smaller than the diameter of the aperture are averaged out over the aperture (Meijninger, 2003; Wang et al., 1978). Therefore, fewer eddies contribute to the intensity fluctuations, which reduces the scatter. Also the path averaging changes. The path averaging is more pronounced in the centre of the path than it is for a point-source scintillometer. To give an indication, for a point-source scintillometer 70% of the averaging is done in the area $0.23L - 0.77L$, i.e. 54% of the path. For a large-aperture scintillometer this is done in the area $0.3L - 0.7L$, i.e. 40% of the path. Thus, the advantage of obtaining C_n^2 over a certain path length is still present, but the actual path averaging has a stronger accent on the middle of the path.

2.2.2.2. Displaced-beam laser scintillometer

The large-aperture scintillometer has the advantage that an optical scintillometer can be operated over large paths, the advantage of the displaced-beam laser scintillometer is that it can resolve both C_n^2 and l_0 , i.e. H and u^* . Basically, this scintillometer consists of two point-source scintillometers operated parallel to each other and displaced in the horizontal plane by about 2.7 mm. The transmitters of the displaced-beam laser scintillometer emit two beams of laser light (wavelength 670 nm). The light intensities are measured by two receivers that are typically 100 m – 300 m away from the transmitter. For the displaced-beam laser scintillometer the equation is given by (Hartogensis et al., 2002; Thiermann and Grassl, 1992)

$$\overline{\ln(I_1)\ln(I_2)} = \pi^2 \kappa^2 \int_0^L \int_0^\infty \Phi_{nm}(k, C_n^2, l_0) J_0(kd) \sin^2 \left(\pi \frac{\Lambda^2}{l^2} \left(\frac{2J_1\left(\frac{kD_{Rc}x}{2L}\right)}{\frac{kD_{Rc}x}{2L}} \right)^2 \right) dk dx, \quad (2.103)$$

where $d = d_T = d_R$ and $D_{Rc} = D_{Rc1} = D_{Rc2}$. When $d = 0$ Eq. (2.103) provides the variance of one detector. For a given displacement distance and path length a unique relation exists between the correlation coefficient of the two beams and l_0 (Frehlich, 1992; Hartogensis, 2006)

$$\frac{\overline{\ln(I_1)\ln(I_2)}}{(\ln(I_1))^2} = \frac{\pi^2 \kappa^2 C_n^2 \int_0^L \int_0^\infty \Phi_m(k, l_0) J_0(kd) \sin^2\left(\pi \frac{\Lambda^2}{l^2}\right) \left(\frac{2J_1\left(\frac{kD_{Rc}x}{2L}\right)}{\frac{kD_{Rc}x}{2L}}\right)^2 dk dx}{\pi^2 \kappa^2 C_n^2 \int_0^L \int_0^\infty \Phi_m(k, l_0) \sin^2\left(\pi \frac{\Lambda^2}{l^2}\right) \left(\frac{2J_1\left(\frac{kD_{Rc}x}{2L}\right)}{\frac{kD_{Rc}x}{2L}}\right)^2 dk dx} \quad (2.104)$$

In this equation C_n^2 can be taken outside the integrals, because it does not depend on k or x and thus cancels out. Hence, by measuring the covariance of $\ln(I_1)$ with $\ln(I_2)$ and the variance of $\ln(I_1)$ or $\ln(I_2)$ l_0 can be obtained. Subsequently, with the obtained l_0 , C_n^2 can be determined with Eq. (2.103) for $d = 0$.

Figure 2.6 shows the path-weighting and eddy-weighting functions for this scintillometer. The most important eddies are those with eddy wavelengths of $2l_0$ (corresponding to a physical size of eddies that equals l_0) and refraction usually is the most important scattering mechanism for this scintillometer. Hartogensis (2006) shows that in contrast to the large-aperture scintillometer, the exact form of the high-wavenumber spectrum is important for displaced-beam laser scintillometers. As there is still some ambiguity about the exact form of the spectrum at these high wavenumbers, the prescribed form of the spectrum can be a potential source of errors, see section 2.1.3.2.

Lastly, also the path weighting is different from the virtual point-source and large-aperture scintillometer. The path averaging is more pronounced in the centre of the path than that it is for a point-source scintillometer, albeit not as pronounced as the path averaging of the large-aperture scintillometer.

2.2.3. From C_n^2 and l_0 to C_T^2 and ε

We have shown that scintillometers can determine C_n^2 and sometimes also l_0 averaged over big parts of their paths. Depending on the type of scintillometer, the eddies that scatter most efficiently have wavelengths of about F , $2D$, or $2l_0$. This section discusses how these scintillometer signals, C_n^2 and l_0 , relate to C_T^2 and ε , with which we can resolve H and u^* .

We begin with the relation between C_n^2 and C_T^2 . Under (local) isotropic conditions, the structure function is connected to the structure parameter by (cf. Eq. (2.15) and Eq. (2.46))

$$D_{n^2}(r) = C_{n^2} r^{2/3} = \overline{(n(x) - n(x+r))^2} = 2(\overline{n'(0)n'(0)} - \overline{n'(x)n'(x+r)}). \quad (2.105)$$

Moene et al. (2004) present several empirical formulas that give the refractive index fluctuations as a function of the scintillometer wavelength, λ , pressure, P , water vapour pressure, e , specific humidity, q , and temperature, T . For wavelengths in the visible light and near-infrared (360 – 3000 nm) these formulas all have the general form

$$n = m_1(\lambda) \frac{P}{T} + m_2(\lambda) \frac{e}{T} + 1 = m_1(\lambda) \frac{P}{T} + m_2(\lambda) \frac{P}{T} \frac{1}{(1-\varepsilon) + \frac{\varepsilon}{q}} + 1 \quad (2.106)$$

where m_1 and m_2 are functions that depend on the scintillometer wavelength and ε is the molecule-mass ratio of water vapour and dry air ($\varepsilon = M_v/M_d$). Applying Reynolds decomposition and expanding n to a first order with a Taylor series, n' can be expressed as (Andreas, 1988; Moene et al., 2004)

$$n' = \frac{\partial n}{\partial p} p' + \frac{\partial n}{\partial q} q' + \frac{\partial n}{\partial T} T'. \quad (2.107)$$

This expression can be rewritten as

$$n' = A_p \frac{p'}{p} + A_q \frac{q'}{q} + A_T \frac{T'}{T}, \quad (2.108)$$

in which $A_x = \frac{\partial n}{\partial x}$ are functions that through Eq. (2.106) depends on the wavelength by m_1 and m_2 , but also on p , q , and T . Inserting Eq. (2.108) into Eq. (2.105) leads to (Moene et al., 2004)

$$C_{n^2} = \frac{A_T^2}{\bar{T}^2} C_{T^2} + \frac{2A_T A_q}{\bar{T} q} C_{Tq} + \frac{A_q^2}{q^2} C_{q^2}. \quad (2.109)$$

The pressure fluctuations are assumed negligible and therefore terms containing C_p^2 , C_{pT} , or C_{pq} do not appear anymore. The values of A_T and A_q are recently reviewed by Ward et al. (2012), who contrary to Hill et al. (1980), Andreas (1988; 1989) and Kohsiek and Herben (1983) evaluate Eq. (2.106) in terms of specific humidity and thus account for adiabatic effects.

Green et al. (2001) measured the contribution of C_T^2 , C_q^2 and C_{Tq} to C_n^2 for an optical and a microwave scintillometer. They find that an optical scintillometer is most sensitive to C_T^2 , whereas a microwave scintillometer is most sensitive to C_q^2 and that in both cases C_{Tq} cannot be neglected. Consequently, when using only an optical scintillometer a correction is necessary to correct for the effect of C_q^2 and C_{Tq} on C_n^2 .

Moene (2003) shows the derivation of the Bowen correction, using increasing levels of approximation. The first step in the derivation of the Bowen correction leads to the following, most comprehensive correction, the Moene correction (Moene, 2003)

$$C_{n^2} = \frac{A_T^2}{\bar{T}^2} C_{T^2} \left(1 + 2 \frac{A_q}{q} \frac{\bar{T}}{A_T} r_{Tq} \frac{\sigma_q}{\sigma_T} + \frac{A_q^2}{q^2} \frac{\bar{T}^2}{A_T^2} \left(\frac{\sigma_q}{\sigma_T} \right)^2 \right), \quad (2.110)$$

in which r_{Tq} is the correlation coefficient between T and q , and σ_T and σ_q are the standard deviations of T and q . Using this approximation, Moene (2003) finds the error to be less than 3%, even for small (<1) Bowen-ratio values.

Eq. (2.110) is derived from the following two expressions

$$C_{q^2} = C_{T^2} \left(\frac{\sigma_q}{\sigma_T} \right)^2 \left(\frac{1 - R_{qq}(r)}{1 - R_{TT}(r)} \right) \quad (2.111)$$

$$C_{Tq} \approx C_{T^2} r_{Tq} \left(\frac{\sigma_q}{\sigma_T} \right)^2 \left(\frac{1 - \sqrt{R_{TT}(r) R_{qq}(r)}}{1 - R_{TT}(r)} \right) \quad (2.112)$$

where $R_{TT}(r)$ and $R_{qq}(r)$ are the autocorrelation functions of T and q as a function of the separation distance r . The underlying assumption is that the cross-correlation function $R_{Tq}(r)$ can be estimated from $R_{TT}(r)$ and $R_{qq}(r)$, which must therefore be approximately equal.

To start simplifying Eq. (2.110) it must be noted that the Bowen ratio, β , can be expressed in terms of σ_T and σ_q

$$\beta = \frac{c_p \overline{w'T'}}{L_v \overline{w'q'}} \equiv \frac{c_p \sigma_T R_{wT}}{L_v \sigma_q R_{wq}}. \quad (2.113)$$

Subsequently, Moene (2003) makes a second assumption, namely that $|R_{wT}| = |R_{wq}|$, and inserts Eq. (2.113) into Eq. (2.110), which leads to the Bowen- r_{Tq} correction

$$C_{n^2} = \frac{A_T^2}{\bar{T}^2} C_{T^2} \left(1 + 2 \frac{A_q}{q} \frac{\bar{T}}{A_T} r_{Tq} \frac{c_p}{L_v} |\beta|^{-1} + \frac{A_q^2}{q^2} \frac{\bar{T}^2}{A_T^2} \left(\frac{c_p}{L_v} \right)^2 |\beta|^{-2} \right). \quad (2.114)$$

The third and last assumption Moene (2003) makes is $|r_{Tq}| = 1$. With the sign of r_{Tq} taken from β , this leads to the Bowen correction

$$C_{n^2} = \frac{A_T^2}{\bar{T}^2} C_{T^2} \left(1 + \frac{A_q}{q} \frac{\bar{T}}{A_T} \frac{c_p}{L_v} \beta^{-1} \right)^2. \quad (2.115)$$

For standard atmospheric conditions ($p = 10^5$ Pa, $T = 300$ K) the term before the β^{-1} equals 0.031, which was found by Wesely (1976) and is often used in literature, see for example Meijninger et al. (2002b) and Moene et al. (2004). Moene (2003) showed that the simplification used in Eq. (2.115) gives good results for $|\beta| > 1$.

It is important to realize that this relation is derived for optical scintillometers and cannot be used for microwave scintillometers, because the contribution of C_T^2 and C_{Tq} to C_n^2 is not necessarily small for microwave scintillometers. Microwave scintillometers can therefore only be usefully operated in addition with an optical scintillometer, which results in a so-called optical-microwave system (Lüdi et al., 2005; Meijninger et al., 2002a). On the other hand, under homogeneous conditions Eq. (2.111) can be used to estimate C_q^2 . For that only additional measurements of σ_T and σ_q are required (Nakaya et al., 2006), see chapter 4.

The derivation of ε from l_0 is much easier than the derivation of C_T^2 from C_n^2 . Unfortunately, the favour of measuring l_0 in addition to C_n^2 is granted to only some scintillometers. The inner scale, l_0 , is related to the dissipation rate of turbulent kinetic energy, ε , by Eq. (2.30) and Eq. (2.48), which results in

$$\varepsilon = \nu^3 \left(\frac{7.4}{l_0} \right)^4, \quad (2.116)$$

where ν is the kinematic viscosity of air. ν can be calculated from measurements of T and ρ by (Scintec, 2006; Weiss, 2002)

$$\nu = \frac{1.718 + 0.0049(T - 273.15)}{\rho} 10^{-5}. \quad (2.117)$$

Hence, with the above described equations C_T^2 and ε can be obtained from scintillometer measurements and thus the surface fluxes H and u_* can be estimated with Monin-Obukhov similarity theory, see section 2.1.4. The only thing that rests is estimating the stability and the direction of the fluxes, because through the assumption of local isotropy this information has been lost. Fortunately, there are several methods to estimate the flux direction and stability, which we discuss in Appendix A of chapter 4.

With this, we close the discussion on estimating surface fluxes with scintillometry. We have shown that many assumptions have been made regarding atmospheric flows in the boundary layer, regarding the nature of the turbulence and the turbulent fields, and regarding the wave-propagation. At the end it all comes together in a complex theory that in fact is amazingly easy in its application. In the following chapters, we discuss the application of the theory and measurement errors that occur in some commercially available scintillometers, followed by a discussion on the extension of the scintillometer application for estimating 1-minute fluxes of evapotranspiration and CO₂ over short paths (< 500m).

3. Analysis of the systematic errors found in the Kipp & Zonen large-aperture scintillometer¹

3.1. Introduction

Many applications in meteorology and hydrology rely on accurate estimates of the area-averaged sensible heat flux, H . The large-aperture scintillometer (LAS) yields this property from area-averaged measurements of the refractive index structure parameter, C_n^2 . Initially, only prototype large-aperture scintillometers were employed and research focussed on theoretical and practical issues regarding the method (De Bruin et al., 1995; Meijninger and De Bruin, 2000; Nieveen et al., 1998a; Ochs and Wang, 1978; Wang et al., 1978). Based on this research the large-aperture scintillometer was made commercially available and has been widely used since (Asanuma and Iemoto, 2007; Hartogensis, 2007; Kleissl et al., 2008). This inspired two studies to investigate the instrument variability of two large-aperture scintillometer types that are commercially available, namely the Kipp & Zonen large-aperture scintillometer (Kipp & Zonen, Delft, the Netherlands) and the boundary-layer scintillometer (Scintec, Rottenburg, Germany) (Kleissl et al., 2008; Kleissl et al., 2009).

In the first study Kleissl et al. (2008) conducted two field experiments with six Kipp & Zonen large-aperture scintillometers using horizontal and slant paths. During the first experiment the instruments stood on two slopes that overlook relatively flat grassland. The scintillometer path was horizontal, had a length of 2 km and an average effective height, z_{eff} , of 43 m. The distance between the outermost scintillometers was 54 m at one side and 26 m at the other. An eddy-covariance system installed at a height of 2.93 m, 1.3 km south of the transect served as an independent reference for H . During the second experiment over arid shrubland the transmitters were located on an 80 m high ridge and the receivers almost at surface level in the plains below. The scintillometer path was slanted, had a length of 1.3 – 2.8 km, and z_{eff} varied between 15 - 24 m. The lateral distance between any two receivers was 30 m. An eddy-covariance system installed at a height of 2.85 m at the centre of the scintillometer path served as an independent reference for H .

In comparing the scintillometers with each other, Kleissl et al. (2008) chose to evaluate the more common variable H rather than a rescaled C_n^2 to account for differences in

¹ This chapter has been published as **Van Kesteren, B.** and Hartogensis, O.K., 2011, *Analysis of the systematic errors found in the Kipp & Zonen large-aperture scintillometer*, *Boundary-Layer Meteorol.*, 138: 493-509

z_{eff} between the scintillometers. They showed that the scintillometers correlate very well with each other ($r > 0.98$), which is superior to that reported for eddy-covariance flux intercomparisons (Kleissl et al., 2008). However, the magnitude of H varied considerably between the different sensors. Overall H_{LAS} overestimated H_{EC} by 2 – 17% and regression-slope differences between the instruments were typically 6% with a maximum of up to 21%. One of the scintillometers was sent back to Kipp & Zonen to repair a photodiode detector that was out of focus. Kleissl et al. (2008) observed that H from this scintillometer was on average 18% larger than that of another scintillometer before the repair and on average 18% smaller than that of the same scintillometer after the repair. They therefore considered uncertainties in the effective aperture size, which is related to the detector alignment, as the prime suspect for the observed differences in regression slope (Kleissl et al., 2008).

In the second study Kleissl et al. (2009) extended and improved on the first study. Firstly, they made improvements by making the scintillometer footprints closer and better defined through measurements along a path of 635 m over a homogeneous peanut field. The measurement height varied between 1.50 m – 1.66 m above ground level and the lateral distances between 0.62 m – 2.19 m at one side and 4.5 m on the other side. Secondly they extended by comparing two types of large-aperture scintillometers instead of one, namely one Kipp & Zonen large-aperture scintillometer (K&ZLAS) with three boundary layer scintillometers (BLSs). In this way they could determine whether the differences in the regression slope that were observed in the previous study are specific to the K&ZLAS or typical of other types as well. Unfortunately independent flux measurements for comparison were not available in this experiment. Kleissl et al. (2009) again compared H and found correlation coefficients were greater than 0.97 for all scintillometer comparisons and a BLS inter-instrument variability of the regression slope less than 3%. The difference, however, in the regression slope with the K&ZLAS was more than 20%. This suggested that, indeed, the observed differences are due to problems in the K&ZLAS (Kleissl et al., 2009).

The goal of the present study is to perform a more detailed and systematic analysis of the differences that were observed by Kleissl et al. (2008; 2009). To achieve this we conducted an experiment under more controlled conditions, compared the scintillometer fluxes with independent flux measurements, and did a spectral analysis of the raw scintillometer signal. From August 2007 until November 2008 we deployed four Kipp & Zonen large-aperture scintillometers and one Wageningen large-aperture scintillometer at the Chilbolton Observatory, UK. Unlike Kleissl et al. (2008; 2009) we installed all transmitters and receivers at exactly the same height of 4.37 m above ground level. We could therefore

compare the more direct scintillometer output, C_n^2 , rather than H , since we did not have to consider the height dependency of C_n^2 . A vibration free installation was ensured by locating the scintillometers on the special benches available in the research cabins. At approximately the same height as the scintillometers (4.46 m above ground level) we placed an eddy-covariance system halfway along the scintillometer paths to measure H as an independent reference. In addition to the more controlled set-up our experiment has the advantage over the two Kleissl studies (2008; 2009) in that we sampled the raw scintillometer signal with a 500-Hz sampling frequency. This sampling frequency allowed us to do spectral data analysis and so investigate the reasons behind the systematic differences and propose, at least partly, solutions for them.

3.2. Theory

A large-aperture scintillometer consists of a transmitter that emits a beam of electromagnetic radiation at near-infrared wavelength and a receiver that registers the beam intensity, I , over distances of typically 500 - 5000 m. On the way to the receiver the emitted electromagnetic wave is diffracted by turbulent eddies. These eddies all have different air densities and thus different refractive indices, n . Since eddies move, the refractive-index field continuously changes, causing the measured intensity to fluctuate. If the aperture of the scintillometer is much smaller than the outer scale of turbulence, yet much larger than the inner scale of turbulence the intensity fluctuations can be directly related to the refractive-index structure parameter, C_n^2 (Wang et al., 1978):

$$C_n^2 = 1.12 \sigma_{\ln I}^2 D^{7/3} L^{-3}. \quad (3.1)$$

where $\sigma_{\ln I}^2$ is the variance of the logarithmic intensity, D is the aperture size, and L is the path length.

The procedure to estimate the sensible heat flux, H , from C_n^2 consists of two steps and needs additional standard measurements of pressure, temperature, humidity, and wind speed. The first step is to derive the structure parameter of temperature, C_T^2 , from C_n^2 , and we use Eq. (12) from (Moene, 2003) and the values of A_t and A_q as given in (Andreas, 1988; Andreas, 1989). The second step is to iteratively solve H from C_T^2 using Monin-Obukhov similarity theory (MOST). In our study the similarity relations of (Andreas, 1988) are used with the constants $c_1 = 4.9$ and $c_2 = 6.1$ (Moene et al., 2004); The friction velocity, u_* , is obtained from

the standard MOST flux-profile relationship (see Eqs. (12) – (15) in De Bruin et al., (1995)). The wind speed was measured at 10 m above the ground and the roughness length, z_0 , was estimated as 0.01 m. A more elaborate description of the flux calculations can be found in (Meijninger et al., 2002b; Moene et al., 2004; Van Kesteren, 2008).

3.3. Experiment and instrumentation

This section describes the set-up of the field experiment that consisted of two parts: the first, most comprehensive, part (Experiment 1) took place from 23 July until 10 September 2007. The second part (Experiment 2) took place from 17 October until 19 November 2008.

3.3.1. Description of the field site

The experiment was performed at the Chilbolton Observatory, UK (51.1445° N and 1.437° W), which is operated by the Radio Communications Research Unit (RCRU) of the Space Science and Technology Department at the Rutherford Appleton Laboratory (RAL). Measurements were made at their so-called test range, a nearly horizontal strip of grassland (grass <0.1 m tall), approximately 15 m wide and 500 m long with identical research cabins at each end (see Figure 3.1).

The research cabins were equipped with benches that stood independent of the cabins on large concrete pillars anchored deep into the ground. The benches provided the necessary space to place all the scintillometers at the same height (4.37 m). Consequently we could ignore the height dependency of C_n^2 and directly compare the instruments without any additional measurements. Furthermore the benches ensured a vibration-free installation so that intensity fluctuations induced by vibrations of the instrument itself did not disturb the measurements.

To account for the small height differences in the topography along the test range we determined the effective height of the scintillometers following Hartogensis et al. (2003). In addition we used their Eq. (15) to give a stability independent effective height formulation, which is appropriate for this case. The topographical data are obtained from a survey carried out in 1980 by J.A. Storey and Partners. The topographic levels of the area around the test range were sampled at 50-m intervals. The resulting effective height is 3.90 m.

At the east side of the range an eddy-covariance mast was placed halfway between the cabins at approximately the same height (4.46 m) as the scintillometers to obtain independent flux measurements. The height, together with the relatively short scintillometer path length of

500 m, ensured similar footprints for scintillometer and eddy-covariance systems. Consequently we could compare the fluxes estimated by the two methods.

The standard additional meteorological measurements were made on site and obtained from the British Atmospheric Data Centre (Wrench, 2003-2010).



Figure 3.1 (a) K&ZLAS receiver cabin – the scintillometers are visible behind the two encircled windows. (b) View from the K&ZLAS transmitter to the receiver cabin – the eddy-covariance tower is encircled

3.3.2. Specification of the scintillometers

Two large-aperture scintillometer types were used in our study: the first, a prototype built by the Meteorology and Air Quality group of Wageningen University, is based on the work of Ochs and Wang at NOAA and called the Wageningen large-aperture scintillometer (WagLAS) (Ochs and Wang, 1978; Wang et al., 1978). The second is a commercial large-aperture scintillometer from Kipp & Zonen (K&ZLAS) that has been developed based on the WagLAS (De Bruin et al., 1995; Meijninger, 2003).

There are several differences between the WagLAS and the K&ZLAS. First of all, the K&ZLAS uses Fresnel lenses and the WagLAS spherical concave mirrors to collimate the beam and focus it onto the detector. Secondly, in the K&ZLAS the transmitting light-emitting diode and receiving detector are connected to the housing with only limited adjusting possibilities, whereas the light-emitting diode and detector in the WagLAS are mounted on high-precision positioning devices. Thirdly, the K&ZLAS has an additional circuit on the board of the receiver electronics to calibrate the signal (Meijninger, 2003; Van Kesteren, 2008), which the WagLAS does not have. Less important differences are the wavelength used ($0.88 \mu\text{m}$ for the K&ZLAS versus $0.94 \mu\text{m}$ for the WagLAS) and the shape of their housing (round for the KippLAS versus square for the WagLAS).

Table 3.1: Overview of the large-aperture scintillometers (LAS) by abbreviation, type, serial number (S/N), owner, deployment time, and Experiment number (Exp.).

LAS	Type	S/N	Owner	Deployment (dd-mm-year)	Exp.
WagLAS	Wageningen LAS	99004	MAQ	08/08/2007 – 10/09/2007	1
K&ZLAS09	Kipp & Zonen LAS	040009	CEH	08/08/2007 – 19/11/2008	1 + 2
K&ZLAS01	Kipp & Zonen LAS	030001	CEH	17/10/2008 – 21/10/2008	2
K&ZLAS30	Kipp & Zonen LAS	060030	King's College	21/10/2008 – 03/11/2008	2
K&ZLAS29	Kipp & Zonen LAS	060029	King's College	03/11/2008 – 19/11/2008	2

In total five large-aperture scintillometers from the Meteorology and Air Quality group (MAQ), the Centre for Ecology and Hydrology (CEH) from Wallingford, UK, and King's College London, UK, were deployed in this study (Table 3.1). The K&ZLAS09 was the only scintillometer present during both Experiment 1 and 2.

3.3.3. Design of the experiment

During Experiment 1 the scintillometers were separated 1.5 m and their beams crossed to match their footprints as much as possible. To prevent crosstalk the transmitters were directed in opposite direction (see Figure 3.2). A CSAT3 sonic anemometer (Campbell Sci., Logan, USA) and a LiCor-7500 fast response H₂O-CO₂ sensor (LiCor, Lincoln, USA) placed directly below it were installed on the eddy-covariance mast. A CR23X datalogger (Campbell Sci., UK) recorded raw 20-Hz data. The fluxes from the eddy-covariance system were determined using the processing package (ECPack) from Wageningen University (Van Dijk et al., 2004). The following corrections and rotations were applied: the Schotanus correction, linear detrending of the data, the planar-fit rotation, and the frequency response correction (Kaimal and Finnigan, 1994; Moore, 1986; Schotanus et al., 1983).

Experiment 2 had a different set-up to Experiment 1. The scintillometers were now separated by 7 m and were directed in the same direction with their beams crossing. Despite the fact that this separation distance exceeded the beam width of 5 m ($\approx 1\%$ of the path length) we verified that the receivers only observed their corresponding transmitter. Verification was made by switching off one transmitter at a time; when its corresponding receiver signal fell to zero, the separation distance was confirmed as large enough. Furthermore the set-up was different because the eddy-covariance system was no longer

present and the data-logger settings were changed (see following section). Otherwise everything remained the same.

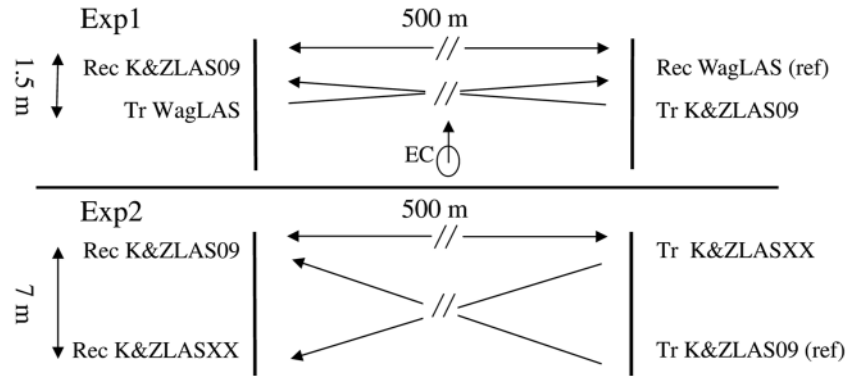


Figure 3.2 Experimental set-up at the Chilbolton Observatory during Experiment 1 and Experiment 2

3.3.4. Logging and filtering of the scintillometer data

The large-aperture scintillometers are designed to provide two signal outputs both of which were recorded. The first signal is the received signal intensity, I , the so-called demodulated signal, which is related to C_n^2 as shown in Eq. (3.1). During our experiment we recorded the demodulated-signal variance, but for use in Eq. (3.1) the variance first had to be converted to a lognormal variance. Furthermore we logged 1-min variances from which we generated longer-term (30-min) variances for comparison of scintillometer data with eddy-covariance data.

Generating N -min variances from m -min variances uses (Oncley, 2007)

$$\left(\sigma_I^2\right)^N = \overline{I I}^N = \frac{1}{m} \sum_{j=1}^m \left(\overline{I I}^j + \bar{I}^j \bar{I}^j \right) - \frac{1}{m} \sum_{j=1}^m \bar{I}^j \frac{1}{m} \sum_{j=1}^m \bar{I}^j, \quad (3.2)$$

where $\left(\sigma_I^2\right)^N$ is the variance of I over the time interval N . That is, the squared mean over the sub-intervals is subtracted from the mean of the sums of the sub-interval variances and the squared sub-interval means. Transforming from normal distributed variance to log-normal distributed variance is done using

$$\sigma_{\ln I}^2 = \ln \left(1 + \frac{\sigma_I^2}{\bar{I}^2} \right), \quad (3.3)$$

which is valid only when the fluctuations are small compared to the mean value, as is the case for the intensity fluctuations.

The second signal that is recorded from the large-aperture scintillometer is the V_{Cn2} signal, which is related to C_n^2 by

$$C_n^2 = 10^{-12+V_{Cn2}}, \quad (3.4)$$

where V_{Cn2} is the signal obtained from the demodulated signal after being processed by the receiver analogue electronics following Eq. (3.1). It is important to note that part of this analogue processing is to filter the demodulated signal with a band-pass filter between 0.01 – 400 Hz. In this filter the lower limit is set to exclude absorption fluctuations of I (Nieveen et al, 1998), whereas the upper limit is set to exclude electronics noise.

In Experiment 1 two CR9000 dataloggers (Campbell Sci., Inc.) differentially sampled and stored the demodulated signal with 500-Hz sampling frequency and an integration time of 40 μ s. Also a CR23X and a CR10 (both Campbell Sci., Inc.) differentially sampled the demodulated signal and V_{Cn2} signal with 1-Hz sampling frequency and an integration time of 250 μ s. Subsequently the CR23X and CR10 stored the 1-min mean and standard deviation of these two signals. Thus, for Experiment 1 C_n^2 can be calculated from the demodulated raw signal as well as from the statistics of both scintillometer signals. In Experiment 2 a CR9000 datalogger differentially sampled and stored the demodulated signal with a 500-Hz sampling frequency and an integration time of 40 μ s. Also the CR9000 differentially sampled the demodulated signal and V_{Cn2} signal with 500-Hz sampling frequency and an integration time of 40 μ s. Subsequently the CR9000 stored the 1-min mean and standard deviation of these two signals. Thus, for Experiment 2 C_n^2 can be calculated from the demodulated raw signal as well as from the statistics of both scintillometer signals.

To check on and improve data quality in Experiment 1 we applied data filters. Data were excluded when the signal variance was not solely determined by refractive index fluctuations, which happened during rain, fog, and dust/smoke events. Furthermore the flux comparison was limited to unstable daytime data. The exact data filters for each variable are described in (Van Kesteren, 2008). In Experiment 2 data filters were different. We only excluded data when the mean modulated signal became too low (indicating fog) or when it rained.

3.4. Results

3.4.1. Comparison of H_{EC} with H_{WagLAS} and $H_{K\&ZLAS09}$

Firstly, we compare the WagLAS and the K&ZLAS09 with the independent eddy-covariance (EC) system, and to this end we present in Figure 3.3 H_{WagLAS} and $H_{K\&ZLAS09}$ (derived from the V_{Cn2} signal) plotted against H_{EC} . Figure 3.3 shows that the scatter is small, resulting in high correlation coefficients, r , of 0.97 and 0.96 respectively. However, both scintillometers estimate a greater H than the eddy-covariance method. The regression fit of H_{WagLAS} has an offset of 4.8 W m^{-2} and the slope is 1.07 and that of $H_{K\&ZLAS09}$ has an offset of 21 W m^{-2} and the slope is 1.37.

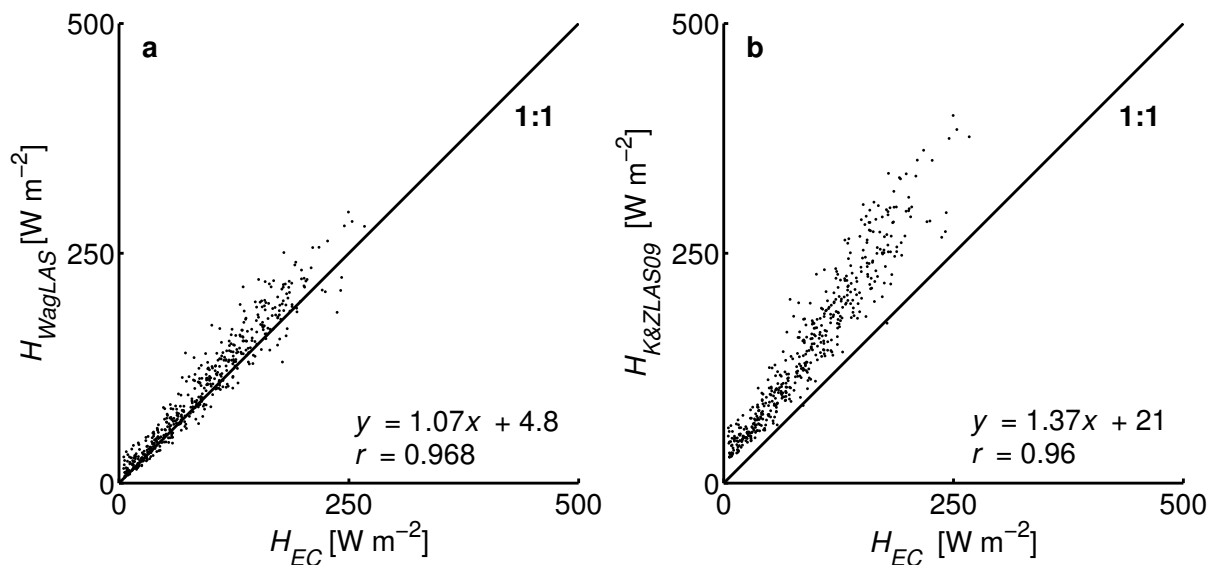


Figure 3.3 (a) Comparison of the sensible heat flux from the Wageningen LAS with eddy covariance, and (b) the sensible heat flux from the Kipp & Zonen LAS with eddy covariance. Each data point is derived from 30-min statistics

The most striking characteristic from these regression data is the difference in regression slope between the two scintillometers. As the effective height of both scintillometers and their footprints are identical we expect their regression slopes to be similar. Instead, $H_{K\&ZLAS09}$ is 28% greater than H_{WagLAS} and 37% greater than H_{EC} . Furthermore Figure 3.3 shows that the relative difference between $H_{K\&ZLAS09}$ and H_{EC} is dependent on the magnitude of the flux. There is a different regression slope for $H_{EC} < 50 \text{ W m}^{-2}$ than for $H_{EC} > 50 \text{ W m}^{-2}$, whereas for H_{WagLAS} no such difference in the regression slope can be observed. This is even clearer when plotted on a logarithmic scale (not shown).

Figure 3.3, thus, corroborates the performance of the WagLAS and K&ZLAS09 found in the literature: the WagLAS has been shown to give accurate flux estimates (Beyrich et al., 2002; De Bruin et al., 1995; Green, 2001; Meijninger et al., 2006; Meijninger et al., 2002b), whereas the K&ZLAS has been shown to have systematic errors of up to 20% (Kleissl et al., 2008; Kleissl et al., 2009). In the following we therefore use the WagLAS as the reference scintillometer.

3.4.2. Comparison C_n^2 between WagLAS and K&ZLASs

To investigate the systematic differences between the scintillometers we will compare the scintillometers directly with each other by looking at C_n^2 instead of H . For consistency, for C_n^2 derived from the V_{Cn2} signal, we use the same collection of data points as in Figure 3.3.

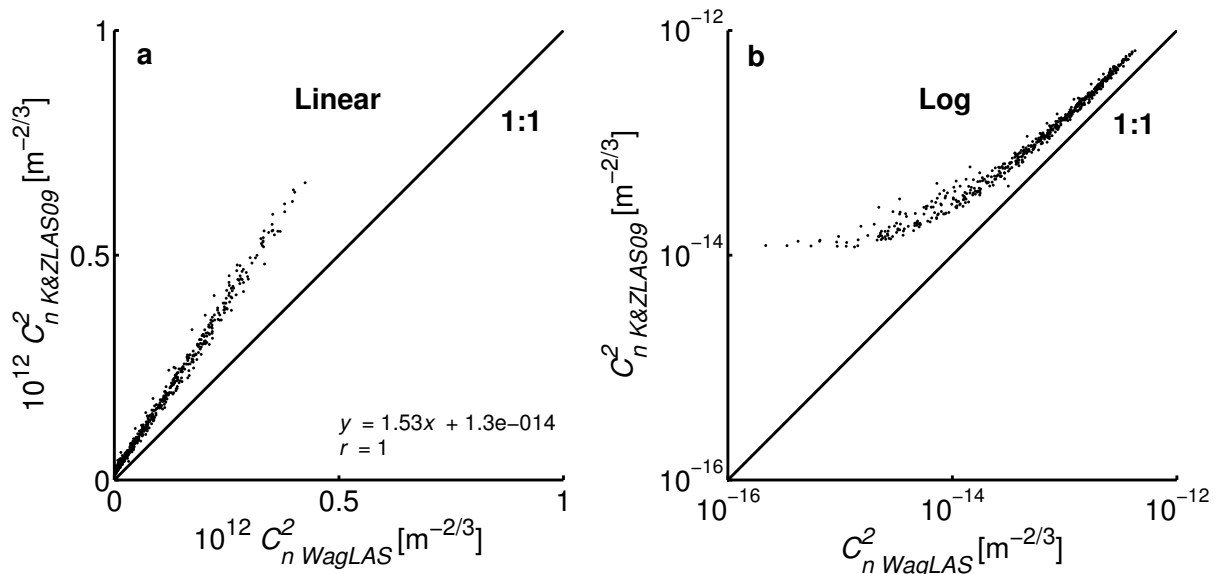


Figure 3.4 Comparison of C_n^2 from the Wageningen LAS with Kipp & Zonen LAS on (a) a linear scale and (b) on a logarithmic scale. Each data point is derived from 30-min statistics²

As can be seen in Figure 3.4 the correlation between the scintillometers is 0.997, a high correlation that underlines that indeed the differences are systematic and not random. Furthermore, it can be seen that the K&ZLAS09 overestimates C_n^2 in two ways. Firstly, Figure 3.4a shows a linear overestimation affecting high values of C_n^2 . It is this overestimation that leads to the large regression slope that can be observed in Figure 3.3b, and

² The formulation of C_n^2 in this figure/chapter differs from that in other chapters. Multiple formulations exist in literature next to each other. Important to realize is that the 2 refers to the n , not to the C . The correct formulation of the structure parameter thus is C_m , see also chapter 2.1.2.3 on statistical moments.

from here on we refer to this overestimation as the high- C_n^2 error. Secondly, Figure 3.4b shows a non-linear overestimation affecting low values of C_n^2 . It is this overestimation that leads to the bending that can be observed in Figure 3.3b, and from here on we refer to this overestimation as the low- C_n^2 error.

To gain insight into what time scales contribute to the variance of the demodulated, raw signal and thus to C_n^2 we present typical frequency spectra in Figure 3.5. Figure 3.5a shows the spectrum for a strong turbulence case (high C_n^2) and Figure 3.5b shows the spectrum for a weak turbulence case (low C_n^2). We scaled the spectra such that the area below the curves is proportional to the variance and that the axes of both spectra are the same.

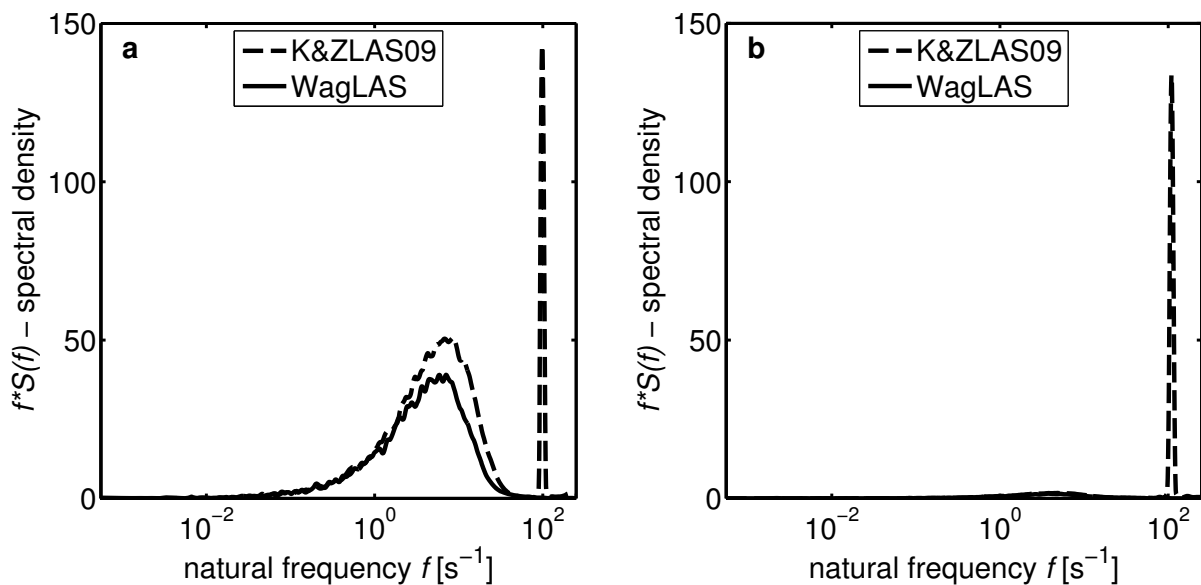


Figure 3.5 Frequency spectra of the Kipp & Zonen LAS (S/N 040009) and the Wageningen LAS demodulated signal, plotted such that the area below the curve is proportional to the variance. Spectra are for 26 August 2007 for the interval (a) 13:00 – 13:30 UTC and (b) 17:30 – 18:00 UTC

Figure 3.5a illustrates the linear high- C_n^2 error. The frequencies lower than 100 Hz represent signal-intensity fluctuations due to refractive-index fluctuations, i.e. scintillations. It is in this region that the K&ZLAS09 spectral density is greater than the WagLAS spectral density. At about 100 Hz a distinct peak contaminates the frequency spectrum. For strong turbulence the peak has a negligible contribution to the overall signal-intensity variance and thus to C_n^2 . Consequently, for strong turbulence the K&ZLAS09 C_n^2 overestimation is dominated by its elevated spectral density at frequencies smaller than 100 Hz. Apparently the K&ZLAS09 elevated spectral density has a fixed ratio with the WagLAS spectral density given the linear relationship between their resulting C_n^2 values as observed in Figure 3.4a.

Figure 3.5b illustrates the non-linear low- C_n^2 error. For this weak-turbulent case the spectral densities caused by scintillations are considerably lower than those for the strong-turbulent case. Although not distinguishable with the applied axis scaling the K&ZLAS09 spectral density caused by scintillations is still systemically greater than that of the WagLAS. However, at 100 Hz, the non-scintillation peak is still present with roughly the same magnitude. Since the magnitude of the peak remains the same, regardless of the turbulent intensity, the contribution of the peak to the overall signal-intensity variance becomes less significant with increasing turbulent intensity. This explains the non-linear behaviour for low C_n^2 observed in Figure 3.4b.

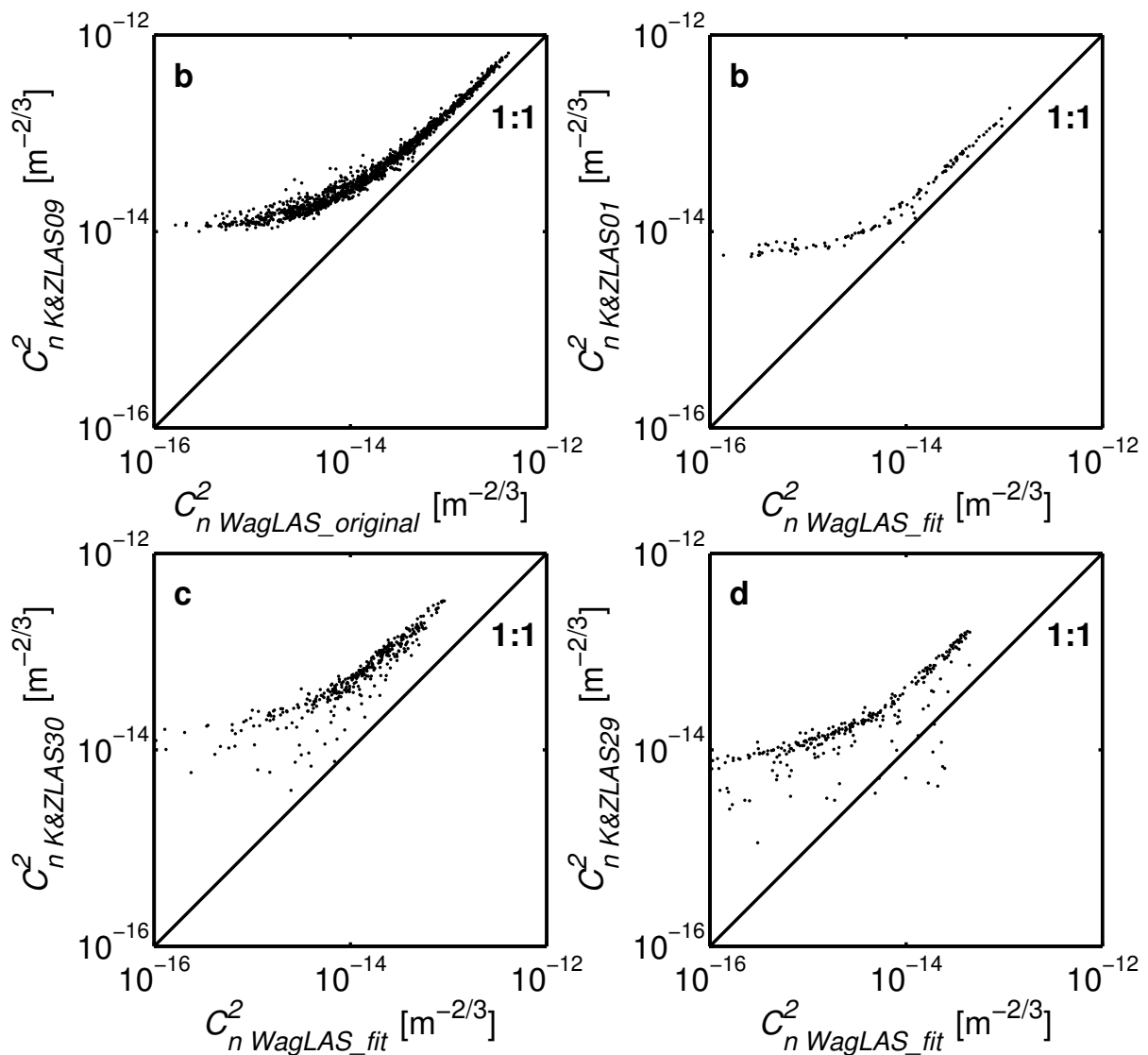


Figure 3.6 C_n^2 comparison of K&ZLAS09 against (a) the reference WagLAS, (b) K&ZLAS01, (c) K&ZLAS30, (d) K&ZLAS29. See text for further explanation on the difference between $C_{n,WagLAS_original}^2$ and $C_{n,WagLAS_fit}^2$. Each data point is derived from 30-min statistics

To show that the two systematic errors incurred by the K&ZLAS09 are not an exception we introduce Figure 3.6, which combines results of Experiment 1 and 2 for comparing the WagLAS with the K&ZLASs. Note that in Experiment 2 the WagLAS was not available and the K&ZLAS09 was the only scintillometer available during both Experiment 1 and 2. We therefore fitted a curve to the WagLAS-K&ZLAS09 comparison and applied that to the K&ZLAS09 measurements during Experiment 2. This explains the terms $C_n^2,_{WagLAS_original}$ in Figure 3.6a and $C_n^2,_{WagLAS_fit}$ in Figure 3.6b-d. As in Figure 3.4, C_n^2 was calculated from the V_{Cn2} signal.

The main conclusion that can be drawn from Figure 3.6 is that indeed all four K&ZLAS instruments have the systematic high- and low- C_n^2 errors. In addition, it can be seen that the magnitude of the high- and low- C_n^2 errors differ for each scintillometer.

3.4.3. Discussion and solutions of the K&ZLAS systematic errors

In the previous section we showed that the systematic error in the K&ZLAS09 is present in all K&ZLASs, that it is different for each K&ZLAS, and that it consists of two parts: the low- C_n^2 error and the high- C_n^2 error. These two parts we more closely consider in the next. In section 3.4.3.1 we deal with the low- C_n^2 error and subsequently with the high- C_n^2 error in section 3.4.3.2.

3.4.3.1. Discussion and solution of the low- C_n^2 error

The low- C_n^2 error was already noted on site during Experiment 1, and for that reason we did three tests to investigate the source of this error. Firstly, we connected the direct-current power supply to batteries to exclude possible interference from the mains power supply. Secondly, we turned off the WagLAS, located the transmitter and receiver in the same cabin, and sampled with the WagLAS CR9000. Thus we could check whether external interference in the K&ZLAS09 receiver cabin or measurements in the K&ZLAS09 CR9000 were the source of errors. Lastly, we used the WagLAS transmitter instead of the K&ZLAS09 transmitter to check whether the transmitter was the source. In all spectra created from these test data the peak amplitude and position remained unchanged. Consequently we concluded that the low- C_n^2 error was generated by an internal source within the K&ZLAS09 receiver.

To investigate what source in the receiver causes the low- C_n^2 error, we consider the different output signals of the scintillometer, see section 3.3.4. In section 3.4.2 we implicitly neglected any difference between the two signals and linked the low- C_n^2 error observed in

Figure 3.4 with the spectral peak observed in Figure 3.5. However, to learn about the source of the low- C_n^2 error we consider below in more detail the C_n^2 estimates from the V_{Cn2} signal and the demodulated signal. Furthermore we look at the datalogger's influence on these signals by considering the logger's signal integration times.

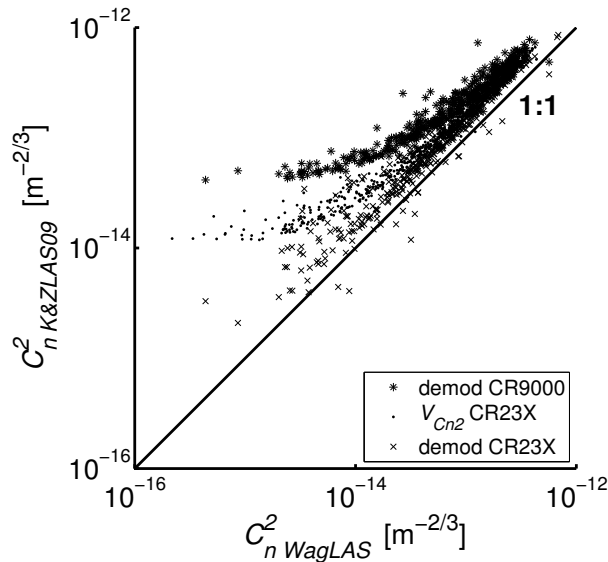


Figure 3.7 Comparison of 30-min averaged C_n^2 measured with the K&ZLAS09 and the WagLAS. C_n^2 was evaluated in three different ways. Firstly, C_n^2 derived from the demodulated signal sampled with an integration time of 40 μ s. Secondly, C_n^2 derived from the V_{Cn2} signal sampled with an integration time of 250 μ s. Thirdly, C_n^2 derived from the demodulated signal sampled with an integration time of 250 μ s.

Figure 3.7 depicts the 30-min C_n^2 comparison between the K&ZLAS09 and WagLAS, where C_n^2 is evaluated in three different ways. Firstly, C_n^2 is derived from the V_{Cn2} signal sampled on the CR23X with a frequency of 1 Hz and an integration time of 250 μ s. Most users evaluate C_n^2 in this way. Secondly, C_n^2 is derived from the demodulated signal sampled on the CR23X with a frequency of 1 Hz and an integration time of 250 μ s. The 1-min statistics from this signal are averaged and transformed to C_n^2 using Eqs. (3.2), (3.3), and (3.1). Since Kipp & Zonen recommends users to store the variance of the demodulated signal, most users can evaluate C_n^2 in this way. Thirdly, C_n^2 is derived from the demodulated signal sampled on the CR9000 with a frequency of 500 Hz and an integration time of 40 μ s. These are more specialist measurements and most users cannot evaluate C_n^2 in this way.

Figure 3.7 shows that the low- C_n^2 error depends on the way in which C_n^2 is evaluated. The low- C_n^2 error is the largest for C_n^2 derived from the demodulated signal with 40 μ s integration time, for C_n^2 derived from the V_{Cn2} signal the error is smaller, whereas for C_n^2 derived from the demodulated signal with 250 μ s integration time the error has been reduced

to zero. As can be seen, a key aspect in this is the signal integration time of the datalogger. Looking at the C_n^2 estimates derived from the demodulated signal we observe that increasing the integration time removes the low- C_n^2 error.

However, for C_n^2 derived from the V_{Cn2} signal this observation is only partly true. The reason for this is that there is noise on the demodulated signal when it is processed. Apparently, the high-frequency noise is not completely filtered out by the filter in the Kipp & Zonen LAS analogue electronics, or the noise is again introduced after that filter, which leads to an overestimated V_{Cn2} signal and thus C_n^2 .

Figure 3.7 also shows that the spectral peak associated with the low- C_n^2 error is aliased from higher frequencies. It would show up as a 100-Hz peak in the frequency spectrum derived from measurements with a 40- μ s integration time, but it is averaged out by an integration time of 250 μ s. Hence we conclude that the low- C_n^2 error is caused by noise with a frequency that is greater than 4 kHz (250 μ s). Together with the points discussed above, and considering that the main difference between the K&ZLAS and WagLAS electronics is the inclusion of a calibration unit in the K&ZLAS receiver, leads us to the conclusion that the calibration unit is the most likely noise source.

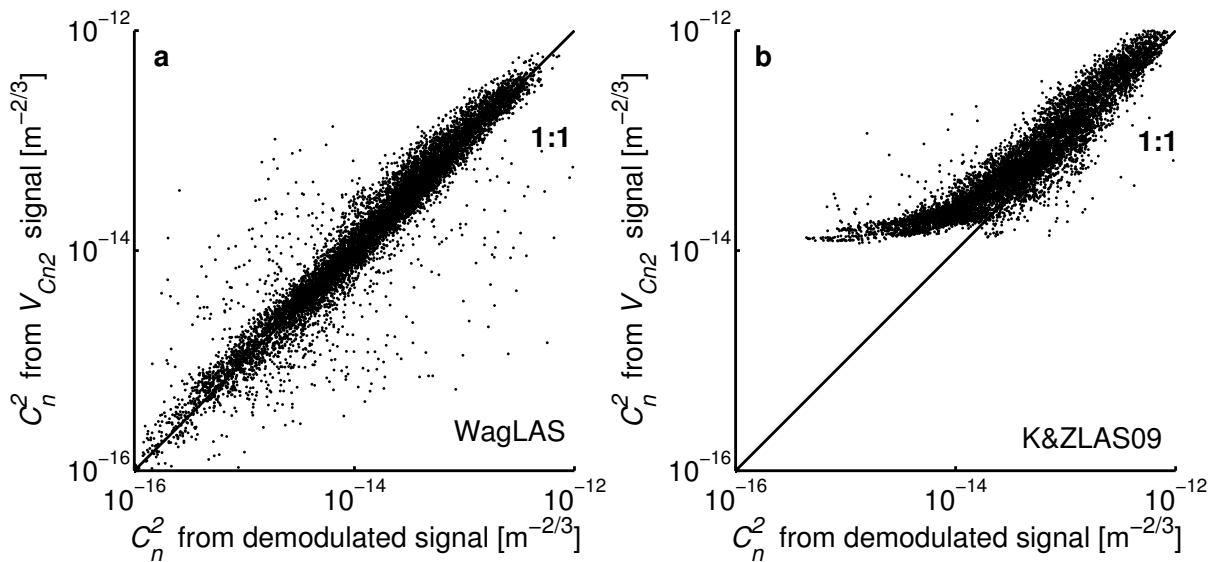


Figure 3.8 LAS signal comparison of C_n^2 from the demodulated signal sampled with an integration time of 250 μ s and from the V_{Cn2} signal. (a) for the WagLAS and (b) the K&ZLAS09. Each data point is derived from 1-min statistics, and only limited data filtering was done for them

As a solution for the problem of the low- C_n^2 error we recommend users to evaluate C_n^2 derived from the variance and average of the demodulated signal, using Eqs. (3.3) and (3.1).

Note that in doing so, we ignore the band-pass filtering included in the C_n^2 derived from V_{Cn2} . For path lengths greater than 500 m the effect of ignoring this filter is limited, especially when absorption fluctuations are small. As a result, and depending on the humidity, our solution will still somewhat overestimate C_n^2 , but this is only a fraction compared to the effect of the low- C_n^2 error, which is corrected for by this procedure.

To check the quality of C_n^2 thus obtained one can compare with C_n^2 derived from the V_{Cn2} signal. Figure 3.8 shows this comparison and it can be observed that the WagLAS is indeed free of the low- C_n^2 error, whereas the K&ZLAS09 is not free of this error. Furthermore, in this way one can also identify whether the calibration of the potentiometer setting to set the path length is still valid or if the potentiometer was set to an incorrect value. If not valid or incorrect, this would show that the scatter in Figure 3.8 would have a constant offset from the 1:1 line. Of course also a reference scintillometer can be used to validate these results.

The magnitude of the low- C_n^2 error is different for each K&ZLAS. Its effect on the resulting heat flux for neutral to near-neutral conditions is:

$$\frac{H \pm dH}{H} \propto \left(\frac{C_n^2 \pm dC_n^2}{C_n^2} \right)^{0.5}, \quad (3.5)$$

where dH and dC_n^2 are the errors in H and C_n^2 respectively. Of all K&ZLASs the K&ZLAS09 suffers most from the low- C_n^2 error. For this scintillometer, with C_n^2 derived from the V_{Cn2} signal, the error is typically $\approx 20 \text{ W m}^{-2}$ for $H < 10 \text{ W m}^{-2}$, $\approx 5 \text{ W m}^{-2}$ for $H \approx 50 \text{ W m}^{-2}$, and it is negligible for $H > 100 \text{ W m}^{-2}$. Hence, for this instrument the low- C_n^2 error is significant for $H \leq 50 \text{ W m}^{-2}$.

To put this into perspective: the uncertainty in estimating H for neutral to near-neutral conditions is typically $10\text{-}20 \text{ W m}^{-2}$ due to e.g. choice of MOST functions and estimated effective parameters as roughness length and effective height. Whether the low- C_n^2 error significantly contributes to the overall error in H therefore depends on each K&ZLAS instrument.

3.4.3.2. Discussion and solution of the high- C_n^2 error

In this section we continue with the high- C_n^2 error introduced in section 3.4.2. To this end we present Table 3.2, where we show for C_n^2 derived from the V_{Cn2} signal the comparison of all

K&ZLASs against the WagLAS. Note that, similar to Figure 3.6, for Experiment 2 H_{WagLAS} was reconstructed using the $H_{K\&ZLAS09}$ versus H_{WagLAS} regression of Experiment 1.

Table 3.2: Comparison of the K&ZLASs with the WagLAS: r is the correlation coefficient, a is the regression slope, b is the regression intercept and n is the number of samples used. D_{eff} is the effective aperture diameter determined from Eq. (3.1) with C_n^2 from the WagLAS. All statistics are determined using a 95% confidence interval and derived from 30-min statistics.

Scintillometer	r (-)	a (-)	b ($m^{-2/3}$)	n (-)	D_{eff} (m)
K&ZLAS09	0.998	1.53x	1.3×10^{-14}	549	0.127
K&ZLAS01	0.999	1.35x	8.8×10^{-15}	115	0.134
K&ZLAS30	0.990	3.40x	3.4×10^{-15}	307	0.090
K&ZLAS29	0.996	3.12x	1.4×10^{-14}	303	0.093

Table 3.2 shows that all the scintillometers correlate very well with correlation coefficients of at least 0.99. This confirms the results of (Kleissl et al., 2008; Kleissl et al., 2009) and shows the high quality of the scintillometer measurements. The high- C_n^2 error, however, is large: the Kipp & Zonen LASs overestimate C_n^2 by at least 35% and up to 240%.

The magnitude of the high- C_n^2 error is different for each Kipp & Zonen LAS. Its effect on the resulting heat flux under free convection conditions is:

$$\frac{H \pm dH}{H} \propto \left(\frac{C_n^2 \pm dC_n^2}{C_n^2} \right)^{0.75}. \quad (3.6)$$

Since the offsets, b , in the regression equations are small we can assume that the multiplication factor, a , is a good approximation to the high- C_n^2 error. For the K&ZLAS09 this would suppose a relative error of 53% in C_n^2 ($a = 1.53$) and consequently a relative error of 37% in H . To show that this is a fair approximation we take the regression equations from Figure 3.3. For $H_{EC} = 250 \text{ W m}^{-2}$ we find that the relative error in H is $\approx 33\%$. One has to realize that the accuracy of Eqs. (3.5) and (3.6) is determined by the validity of the neutral or the free-convection assumption on which they are based. The true error, however, is always between these two limits.

One suspect for the high- C_n^2 error is the optical quality of the Fresnel lenses in the K&ZLASs. The quality of these is known to be less than that of the concave mirror used in the WagLAS. As a result the effective diameter, D_{eff} , seems to be smaller than the geometrical

diameter of 0.152 m. From Eq. (3.1) it follows that overestimating D leads to overestimating C_n^2 . This is consistent with what we observe.

However, Kipp & Zonen did several tests to determine D_{eff} by measuring the mean demodulated signal using a range of aperture sizes. They determined D_{eff} by extrapolating the linear relationship between the aperture diameter and the square root of the mean demodulated signal. Kipp & Zonen found typical values for D_{eff} that were smaller than the physical lens diameter but were larger than 0.14 m (Martin Veenstra, Kipp & Zonen, personal communication, 2010; Kleissl et al., 2008). We also conducted this test using a K&ZLAS instrument that was not part of the Chilbolton experiment and found D_{eff} to be $0.141 \text{ m} \pm 0.001 \text{ m}$.

To test whether these values of D_{eff} explain the observed difference in H we apply an alternative approach to determining D_{eff} , and derive this from the comparison between the K&ZLAS and our reference scintillometer, the WagLAS. From Eq. (3.1) D_{eff} of the K&ZLAS can be determined using C_n^2 from the WagLAS, and σ_{inL}^2 and L from the K&ZLAS. D_{eff} thus determined is listed in Table 3.2. It can be seen that the largest D_{eff} is 0.134 m, which is smaller than the typical values found by Kipp & Zonen and ourselves in the test with the smaller apertures. Moreover, the values of 0.093 m and 0.090 m are so low that it is very unlikely a problem of the Fresnel-lens quality only.

Another contribution to the high- C_n^2 error could be poor alignment of the detector in the focal point of the lens. Recall that Kleissl et al. (2008) reported that the effect of a misaligned photodiode detector resulted in a 35% error in H , poor alignment causes the detector to be lit by a part of the lens only. Two design issues enhance the K&ZLAS sensitivity to poor detector alignment: firstly, the fact that the detector is mounted on a large metal block (Kipp & Zonen refer to this block as the bullet (Kipp&Zonen, 2007)), which because of its bulkiness makes accurate alignment difficult. Secondly, the focal length of the Fresnel lens is 0.152 m whereas the WagLAS mirror has a focal length of 0.30 m (Kipp&Zonen, 2007; Meijninger, 2003). This implies that for the K&ZLAS instrument a displacement away from the focal point in the lens-detector plane has a larger impact on the alignment than a similar displacement has on the alignment of the WagLAS. Poor focal-point alignment affects both the transmitter and the receiver. We did not test which of the two has a stronger influence on the high- C_n^2 error. Kipp & Zonen found D_{eff} to be 0.148 m for the receiver and D_{eff} to be 0.145 for the transmitter (Kipp&Zonen, 2007).

The high- C_n^2 is a linear error and consequently affects the whole range of H . We cannot offer a solution for the high- C_n^2 error other than checking the focal-point alignment or, if this cannot be done with sufficient accuracy, comparing the K&ZLAS in the field against a reference scintillometer. The fact that the four K&ZLASs all have a different high- C_n^2 error, and that their corresponding D_{eff} is lower than can be expected from Fresnel-lens quality, supports our hypothesis that the main cause for this error is the focal-point alignment of the detector.

3.5. Conclusions

Kleissl et al. (2008; 2009) showed that there is a systematic error in the K&ZLAS measurements of H . Although these studies clearly allowed this general conclusion, the measurement conditions were not ideal, nor did they study the characteristics of the systematic error.

We conducted two experiments at the Chilbolton Observatory, where we compared four K&ZLASs with a reference scintillometer, the WagLAS. This experiment was conducted under highly controlled conditions and we analysed the characteristics of the error. We improved on the Kleissl experiments by installing all scintillometers close together (lateral spacing of 1.5 m in Experiment 1 and 7 m in Experiment 2) at exactly the same height, and over a path of 500 m length. This ensured the footprints to be the same, making a good comparison possible. To validate the scintillometer measurements an eddy-covariance system measured the sensible heat flux, H , halfway along the path at approximately the same height as the scintillometers. In addition, the scintillometers were placed in special research cabins on tables that stood independently from the cabins on large concrete pillars to avoid instrument-movement induced noise on the scintillometer signals.

Furthermore high-frequent sampling was done to enable spectral analysis of the data. From our comparison between the four K&ZLASs with the WagLAS we draw two main conclusions. Firstly, our study shows that the scatter between the scintillometers is very low with correlation coefficients ≥ 0.99 . This confirms the results of previous studies, shows the robustness of the scintillometer method, and that the large-aperture scintillometer outperforms any other measurement system that obtains H . Secondly, unlike the Kleissl studies (2008; 2009), we found two systematic errors in the K&ZLAS measurements, namely a high- C_n^2 error and a low- C_n^2 error that both result in an overestimation of C_n^2 and thus H .

The low- C_n^2 error is a non-linear error that is significant for $H \leq 50 \text{ W m}^{-2}$ and varies significantly between each scintillometer. Typical values for the K&ZLAS09, which suffers most from this error, are $\approx 20 \text{ W m}^{-2}$ for $H < 10 \text{ W m}^{-2}$. The low- C_n^2 error has its origin in the receiver and was detected by spectral analysis of the demodulated raw signal. The error shows up as a peak in the spectrum at frequencies of 100 Hz or higher. We suspect that the calibration circuit within the receiver is the source of this error. We showed that the low- C_n^2 error does affect the V_{Cn2} signal, which is the output most users use. To remove this error we provided a procedure that estimates C_n^2 using the variance of the demodulated signal.

The high- C_n^2 error is a linear error that also varies significantly between each K&ZLAS (overestimation from 35% up to 240%), and it is the same error as that was observed by Kleissl et al. (2008; 2009). A high- C_n^2 error of 53% in the K&ZLAS09 measurements of C_n^2 resulted in a 33% error in H . As this is a linear error it affects the whole range of H . We suspect poor focal-point alignment of the receiver detector and the transmitter light-emitting diode, which leads to ineffective use of the Fresnel lens, to be the cause. Unfortunately there is no correction for the high- C_n^2 error other than to calibrate the K&ZLAS against a reference scintillometer in the field.

4. Instrument development: Revisiting a scintillometer design

The results of the research presented in the previous chapter were communicated with Kipp&Zonen. Based on these results and some other issues, they completely redesigned their large-aperture scintillometer, which recently (2011) became available. This chapter continues with the displaced-beam laser scintillometer (SLS20/SLS40) from Scintec, which also suffers from systematic errors in its measurements.

The SLS20/SLS40 displaced-beam laser scintillometer, DBLS, is a small-aperture scintillometer with $D < F$, see section 2.2.2.2. It is sensitive to eddy sizes of the order of the inner scale length, l_0 . The DBLS typically provides fluxes at field scales. Heat fluxes derived from the DBLS have been shown to compare well with local eddy-covariance measurements (e.g. (De Bruin et al., 2002; Green et al., 1994; Green et al., 1997; Hartogensis et al., 2002; Hoedjes et al., 2002; Thiermann and Grassl, 1992)). However, studies showed that individual measurements of C_T^2 and u_* systematically differ from local eddy-covariance measurements (Hartogensis et al., 2002; Van Kesteren et al., 2012a), although these systematic differences could not always be confirmed (Lüers and Bareiss, 2011; Savage, 2009).

Therefore, part of this PhD research focuses on improving the measurement technique. The first part of this chapter focusses on experiments that have been conducted as part of the LITFASS-2009 experiment. During these experiments the variability among five different DBLSs has been studied (Beyrich et al., 2012). As Hartogensis (2006) already indicated, the proposed solutions for the errors in these measurements are merely working hypotheses, rather than final solutions and the variability among the DBLSs confirms this. Consequently, we decided to revisit an old scintillometer design for determining C_T^2 and u_* at field scales. This technique was first suggested by Hill and Ochs (1978) and successfully applied thereafter (Hill et al., 1992). As such, the second part focusses on experiments within the LITFASS-2012 project during which this design was applied.

4.1. DBLS inter-comparison experiment³

One of the aims of LITFASS 2009 was to compare C_T^2 measurements over different agricultural fields (Beyrich et al., 2012). As a pre-requisite for the interpretation of possible

³ This section, 4.1, has been published as Beyrich, F., Bange, J., Hartogensis, O.K., Raasch, S., Braam, M., van Dinter, D., Gräf, D., **Van Kesteren**, B., Van den Kroonenberg, A.C., Maronga, B., Martin, S., and Moene, A.F., 2012, *Towards a validation of scintillometer measurements: The LITFASS-2009 experiment*, *Boundary-Layer Meteorol.*, 144:83-112

differences in the C_T^2 measurements at field scale, derived from DBLS measurements over different surface types, a quantification of the instrumental uncertainty (i.e., the differences obtained when operating the systems over the same type of surface) is necessary. So far, only a few scintillometer comparison results have been published in the scientific literature (e.g. (Kleissl et al., 2008; Kleissl et al., 2009; Van Kesteren and Hartogensis, 2011). These mainly consider the commercially available LAS systems from Scintec and Kipp & Zonen. Moreover, published results generally focus on the derived fluxes. We are not aware of any publication on the comparison of a number of DBLS with respect to the basic turbulence variables, namely C_n^2 and l_0 . Before installing the SLS-20/40 systems at the agricultural fields we therefore performed a 3-day inter-comparison experiment at the GM Falkenberg grassland site. The five DBLS were set up over a path length of 145 m and at a measurement height of 2.15 m. The orientation of the paths was roughly E-W with prevailing northerly winds predicted for the period of the comparison experiment. The lateral distance between four of the paths was 8-10 m, for logistic reasons the 5th path was about 40 m to the north of the 4th path. The diagnosis-data period was set to 6 seconds and the basic averaging interval was set to 10 minutes for the measurements during this experiment. All five paths “saw” the grass at GM Falkenberg over a fetch of at least 150 m. Since the upstream, along-wind footprint area of a measurement system installed at 2 m or higher extends over several tens of metres, the source areas for the different paths largely overlap for the lateral distance we have used in this set-up.

4.1.1. Structure parameters from the DBLS data

Determination of the structure parameters from the DBLS data was based on the SLSRun / SRun system software provided by the manufacturer. This software determines the C_n^2 from the variances and from the covariance of the logarithmic intensity of the received signals of two parallel laser beams. The inner scale length of turbulence l_0 is derived from the correlation of the signal intensity between the two beams. Internal analysis of the signal is performed over so-called diagnosis intervals (the length of which was set as 6 s). A series of statistical tests is internally applied to the signals during one diagnosis interval, and an error code is assigned to the 6 s dataset based on the results of these tests (where `error_code = 0` indicates that all tests have been passed). Statistics from the single sampling periods are then aggregated to 10 min averages of the derived parameters whereby only data from sampling intervals without an error message are considered.

4.1.2. SLS-20 / 40 instrumental uncertainty

A statistical analysis has been performed of the data collected during the DBLS inter-comparison experiment. The Wageningen SLS-20 (SN221) has been chosen as the reference for this analysis (System 1). Only those 10 min averaging intervals were considered for the comparison for which more than 70 % of the diagnosis data periods were available without error messages from the internal data quality checks. The results are summarized in Table 4.

Table 4 – Results of the statistical inter-comparison of the C_n^2 measurements with five DBLS SLS-20 / 40 (reference: Wageningen instrument SN221, Firmware version SLSRun 2.24)

Parameter	System 2	System 3	System 4	System 5
SLS type	SLS-20	SLS-40	SLS-40	SLS-20
Serial number	148	191 / 192	261	165 / 166
Firmware version	SLSRun 2.03	SLSRun 2.33	SRun1.05	SLSRun 2.25
Number of data points	272	281	145	136
Correlation coefficient	0.997	0.996	0.984	0.999
Slope of linear regression line	0.94	1.27	1.23	1.05
Mean ($C_n^2(X) / C_n^2(WUR221)$)	0.89	1.23	1.03	0.94
Median ($C_n^2(X) / C_n^2(WUR221)$)	0.91	1.25	1.04	0.95

The number of data points available for the comparison was considerably reduced in case of the systems 4 and 5. While a configuration error resulted in a one-day data loss in case of system 5, system 4 runs on a completely revised hardware and software basis with an increased internal sampling rate that is higher by more than a factor of 10 when compared to all the other systems. This makes the internal statistical data quality tests more sensitive to any irregularities in the signal characteristics resulting in an increased number of flagged diagnosis data. The correlation coefficient is very high for all systems showing that the data from the different instruments follow the same variations (mainly the pronounced diurnal cycle). The other three scores vary between about 0.89 and 1.28. This indicates a deviation of up to about 25 % in the C_n^2 values measured by the different systems. The slope of the regression line tells that the different instruments do not give the same values; this might be interpreted as a certain percentage of underestimation or overestimation. But the slope is dominated by the high values; possible problems at low values might remain hidden. The mean relative value indicates how large – in the mean – the relative deviation is for each sample, but it is not a very robust measure (especially when looking at relative numbers). That

is why we also determined the median relative deviation that gives a more robust indication of the overall relative deviation between the instruments. To look at these relative measures is particularly useful in the case of C_n^2 since it has such a large variation in values. If one would only look at the absolute errors the possible problems at low C_n^2 would completely disappear. While the different measures are consistent for system 2 and system 3 and still show the same tendency for system 4 they provide a different message for system 5 for which apparently the larger values of C_n^2 are overestimated but the lower ones are underestimated (not sufficient to change the slope, but visible in the relative deviations).

It should be noticed that deviations of comparable relative magnitude were found for the inner scale length, l_0 . Since errors in C_n^2 and errors in l_0 partially cancel out when calculating the turbulent fluxes, the differences in the sensible heat fluxes are smaller than 5%. The reasons for these differences are not completely clear. We repeated the inter-comparison exercise in 2010 with three of the five systems over a longer time period (more than one month). Two of the three systems had been sent to the manufacturer for technical inspection and maintenance before this second experiment. Again, we found deviations of roughly the same magnitude. One possible reason could be the differences in the firmware version. For future experiments we therefore recommend a harmonization of the firmware used with the different laser scintillometers. In any case, the uncertainty has to be taken into account when interpreting the measurements at the different sites.

4.2. A new field-scale scintillometer for measuring u^* and H

The above section concluded that there is great variety among the DBLSs from Scintec in the C_n^2 and l_0 measurements. Hartogensis et al.(2002) suggested that these differences are related to varying displacement distances between the two beams among the DBLSs. From this it follows that the calibration of each instrument would be required to avoid uncertainties in the displacement distance and hence in l_0 and C_n^2 – a solution that Scintec by now (2012) has implemented in its production process. Another way of determining l_0 and C_n^2 and thus u^* and H is by using a scintillometer that emits two beams with different aperture sizes. One smaller aperture that is more sensitive to l_0 and one larger aperture that is more sensitive to C_n^2 . In the scope of the STW project, we explored the application of such a scintillometer.

4.2.1. Theoretical considerations

Hill and Ochs (1978) developed a method for determining u^* and H from measurements of scintillometers with two different aperture sizes. This method has the advantage that saturation of the scintillometer can be prevented by choosing the diameters sufficiently large, so that operation over paths longer than 300 m is feasible. With the correlation technique that has been adapted by Scintec in their current DBLS design, the maximum path length advised is 300 m (Scintec, 2006). This technique works only for lasers, which saturate under conditions of strong turbulence or when applied over long paths. To give an idea, for path lengths of 300 m saturation will occur for $H > 200 \text{ W m}^{-2}$. On the other hand, for this distance the sensitivity to l_0 deteriorates, because the Fresnel zones of the beams increase and start to overlap each other. The separation distance of the two lasers within the DBLS is only 2.5 mm, whereas $F = 14 \text{ mm}$ for this distance. Consequently the minimum of the correlation coefficient is 0.4 instead of 0. For the two-aperture method the separation distance of the two beams is irrelevant, as long as they sample the same turbulence. The crucial parameters with this set-up are the aperture sizes, these must be exactly known.

With the two-aperture method, l_0 and C_n^2 can be obtained by the merit of the unequal sensitivity of the beams to the inner scale. Ideally, this can be done by choosing one aperture such that the beam is insensitive to l_0 , $D > 20l_0$, in combination with another aperture such that the beam is sensitive to l_0 . Unfortunately, the signal-to-noise ratio of available large-aperture scintillometers with $D > 20l_0$ is insufficient for operation over short paths ($L < 150\text{m}$). However, for the application of this method it is not required that one beam is insensitive to l_0 . It is sufficient when the sensitivity of the beams to l_0 are sufficiently different from each other. Thus adapting Eq. (2.97) to the present design, we obtain the following expression

$$\frac{B_{11}}{B_{22}} = \frac{\overline{(\ln(I_1))^2}}{\overline{(\ln(I_2))^2}} = \frac{\pi^2 \kappa^2 C_n^2 \int_0^L \int_0^\infty k \Phi_{mm}(k, l_0) \cdot \sin^2\left(\pi \frac{\Lambda^2}{l^2}\right) f_{avTr1} f_{avRc1} dx dk}{\pi^2 \kappa^2 C_n^2 \int_0^L \int_0^\infty k \Phi_{mm}(k, l_0) \cdot \sin^2\left(\pi \frac{\Lambda^2}{l^2}\right) f_{avTr2} f_{avRc2} dx dk} \quad (4.1)$$

where C_n^2 is taken outside the integrals, because it does not depend on x or k (cf. Eq. (2.52)). As the beams sample the same turbulence, C_n^2 is equal for both beams and hence everything outside the integrals cancels out. Hence, l_0 is the only unknown in the equation and from the measured ratio, B_{11}/B_{22} , l_0 can be solved, because for each combination of aperture sizes a

unique relation between l_0 and B_{11}/B_{22} exists. Subsequently, C_n^2 can be solved with the obtained l_0 , either via the numerators or the denominators of Eq. (4.1).

Figure 4.1 shows the theoretical relationships of the measured ratio vs. l_0 , for three different designs. The apertures in the numerator are a laser beam (infinite small aperture), a 1-cm aperture, and a 2-cm aperture. The reference aperture in the denominator is 10 cm.

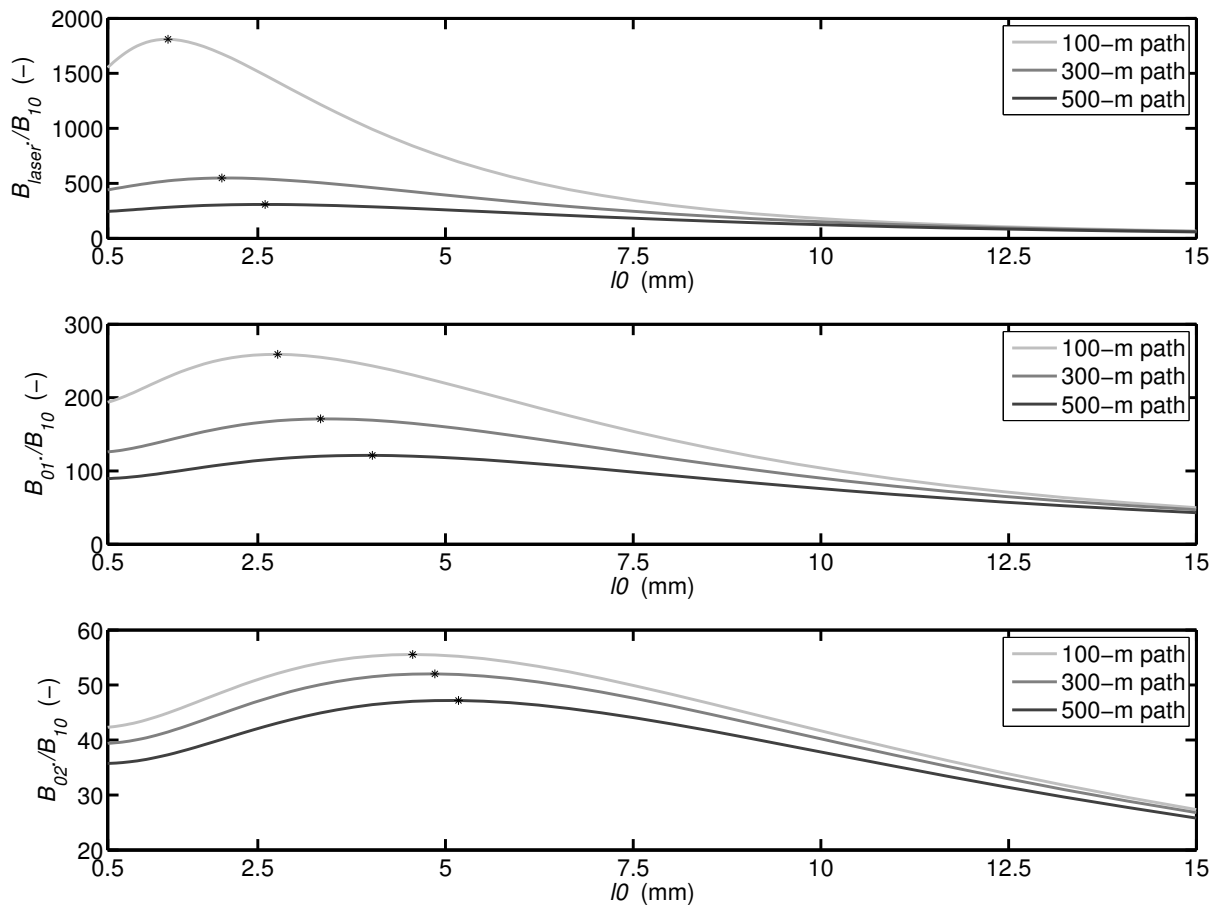


Figure 4.1: Relationships of the ratio vs. l_0 for the two-aperture method. B_{laser} denotes the variance of the logarithmic amplitude from the laser beam. B_{01} , B_{02} , and B_{10} denote the same variance for the beams with apertures of 1 cm, 2 cm and 10 cm respectively. The stars indicate the peak of the ratio.

Figure 4.1 shows that the more different the apertures are, the greater the sensitivity of their ratio is to l_0 . Increasing the path lengths deteriorates the sensitivity to l_0 , because the size of the Fresnel zone increases. Furthermore, it is important to realize that close to the surface l_0 falls in a range of 2 – 10 mm, under natural conditions. This indicates that the ratio B_{02}/B_{10} is probably unsuitable for determining l_0 , because its peak makes it almost insensitive to l_0 in the range of 4 – 6 mm. Theoretically, the combination of the laser with the 10-cm aperture is most suitable for determining l_0 . However, the theory does not take saturation effects into account,

which makes the laser unsuitable for application over distances longer than 300 m. Choosing the 1-cm aperture instead of the laser, significantly reduces the chance of saturation, but as can be seen the peak moves already to 4 mm, which makes the sensitivity of the ratio to $l_0 < 5$ mm insufficient for paths of 500 m. For these long paths (speaking in terms of field scales), the sensitivity to $l_0 > 5$ mm can be improved by using a 15-cm aperture instead of a 10-cm aperture. Nevertheless, the sensitivity of the ratio to $l_0 < 5$ mm will remain insufficient, which implies that the scintillometer height must be increased in order to encounter conditions with large l_0 .

4.2.2. Design and experiment

For practical purposes, we preferred a design that is easily accessible to scintillometer users. Therefore, we choose a set-up that is based on some simple modification to the apertures of two large-aperture scintillometers from Wageningen university. Based on the theoretical considerations, we concluded that a 1-cm aperture in combination with a 10-cm aperture gives the optimal sensitivity of the ratio to l_0 . Hence, one large-aperture scintillometer was modified such that the Plexiglas sheets were replaced by black sheets containing a hole with a 10-cm diameter in it. The other scintillometer was modified such that the Plexiglas sheets were replaced with black sheets with a hole in it that contains a diaphragm. With this diaphragm, we can modify the aperture and optimize the aperture for sensitivity to l_0 and yet secure that the signal strength is large enough. One of the challenges, of reducing the aperture size is that the signal intensity decreases quadratically with the radius. Unfortunately, the detector was not sensitive enough to measure the intensity corresponding to an aperture of 1.00 cm. Therefore, we had to enlarge the aperture to 1.75 cm and decided to operate the modified scintillometers with apertures of 1.75 cm and 10 cm, see Figure 4.2.

The experiment has been conducted as part of the LITFASS-2012 field campaign. During May and June 2012, we measured over short grass on the measurement field from the German meteorological service (DWD) in Falkenberg. The two modified scintillometers were installed at a height of 2.10 m, together with a DBLS (type SLS-20, Scintec, Germany). Figure 4.2 shows the field set-up. The scintillometers were operated with crossed beams, whereby the middle one was directed in opposite direction compared to the other two. Their orientation was approximately north-south and their path lengths were 113 m. Furthermore, each scintillometer was separated from the other ones by at least 1.25 m.



Figure 4.2: Field set-up of the scintillometer experiment in Falkenberg with a close-up of the modified large-aperture scintillometers from Wageningen University.

Additional standard measurements of temperature, pressure, humidity, wind speed etc. were performed as routine measurements by the German meteorological service, as well as eddy-covariance measurements. The eddy-covariance measurements were performed with an USA-1 sonic anemometer (METEK, Germany). All these measurements are routinely obtained within the data acquisition system of the German meteorological service and processed and checked on quality as such (Beyrich et al., 2012; Beyrich et al., 2006). The raw SLS-20 data were measured with an internal datalogger and processed by SLS-run 2.24, as provided by the manufacturer. This processing routine gives estimates of B_{laser} as well as $C_n^2_{SLS}$ and $l_{0,SLS}$, of which the latter is estimated with the correlation method. The raw modified-scintillometer data were measured with a CR9000 datalogger (Campbell sci., UK) and stored as $B_{1.75}$ and B_{10} . To calculate the fluxes, two changes in the data processing were made compared to Scintec's standard processing. We used the humidity correction, Eq. (11), from Moene (2003) to calculate C_T^2 from C_n^2 , using an estimated value for $|r_{Tq}|$ of 0.8. Furthermore, we used the

following MOST functions: f_ε , from Hartogensis and de Bruin (2005) to estimate u^* and f_T from Andreas (1988) to estimate H .

During the experiment, the temperature was on average 15.1 °C and minima and maxima varied between 0.2 °C and 30.9 °C. Precipitation occurred regularly and the total sum of precipitation was 96 mm, of which most was obtained during short, intensive thunderstorms. The grass was green all the time and the Bowen ratio was generally smaller than 0.8, but on some days it was about 1.5.

4.2.3. Results

The main aim of this section is to validate the l_0 estimates that are estimated with the dual-aperture method as part of the LITFASS2012 campaign. As references will serve $l_{0,SLS}$ and $C_n^2_{SLS}$. In section 4.1 it was shown that the accuracy of these measurements varies among the scintillometers and therefore we will start this section by making an estimation of the accuracy of these reference measurements. To this purpose we introduce Figure 4.3, which shows the comparison of u^* and H estimated with the displaced-beam laser scintillometer (SLS) and estimated with the eddy-covariance method (EC). For the analysis 10-min averaging intervals are considered, of which only those intervals are included in the comparison for which more than 90 % of data within the data period was available without error messages from the internal data-quality checks.

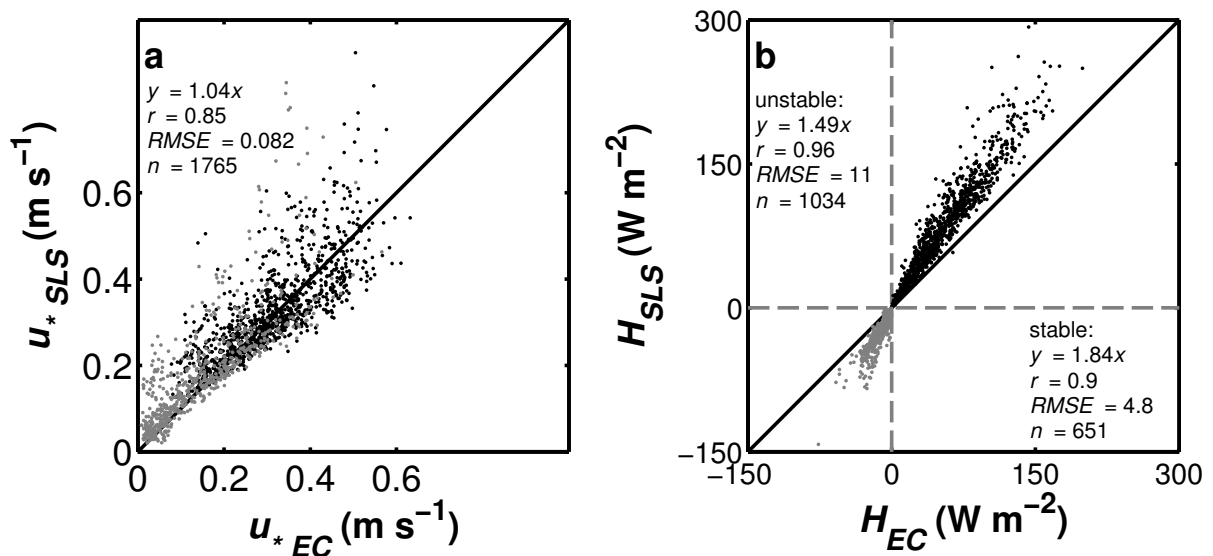


Figure 4.3: Comparison between scintillometer and eddy-covariance measurements for (a) u^* and (b) H . Each data point consists of 10-min statistics. The grey dots denote stable conditions and the black dots denote unstable conditions.

The comparison shows that the scintillometer estimate agrees well with that of the eddy-covariance method for u^* . The data are scattered around the 1:1 line and no systematic difference is observed. This is surprising, because in previous studies the same scintillometer has been shown to underestimate u^* (chapter 5). Furthermore, the scatter is small, with a correlation coefficient, r , of 0.85.

For H the results are slightly different. The scintillometer clearly overestimates H with at least a factor 1.5. On the other hand, the scatter is smaller than it was for u^* . During unstable conditions $r = 0.95$ and during stable conditions $r = 0.90$. All in all, we conclude from the large correlation coefficients that $l_{0,SLS}$ and $C_{n^2,SLS}$ can serve as a reference for the validation of the dual-aperture method.

However, before proceeding to the validation of the l_0 estimates, the accuracy of the measurements from the modified scintillometers is estimated by considering their time spectra. Figure 4.4 shows representative frequency spectra of the two modified scintillometers for a situation during the night and a situation during the day. The axes are scaled such that the area below the graph is proportional to the variance, i.e. to $B_{1.75}$ and B_{10} .

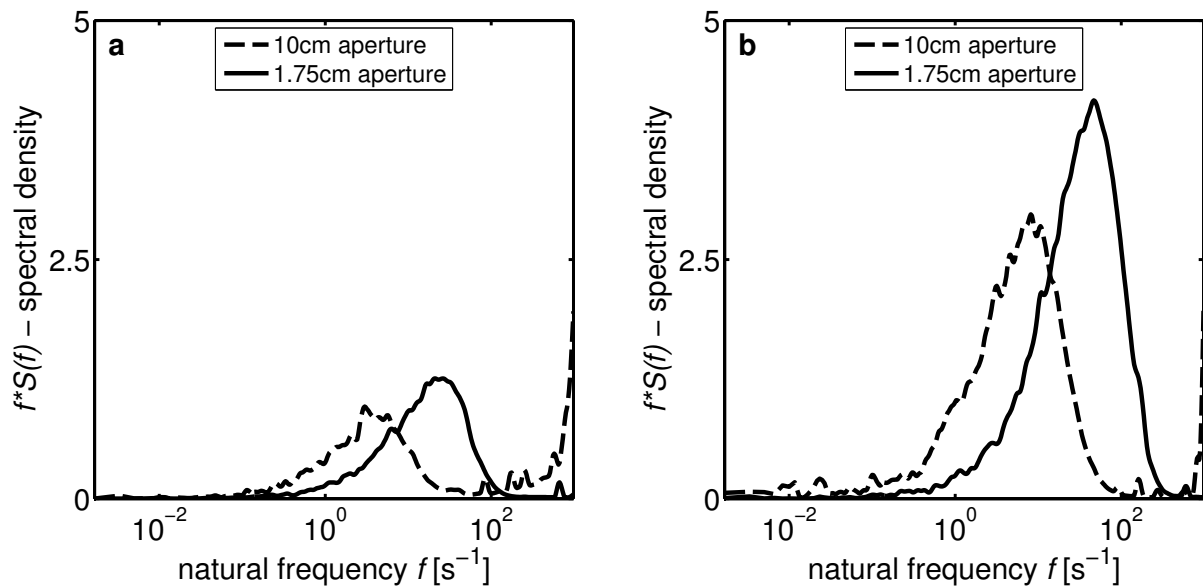


Figure 4.4: Frequency spectra of the scintillometer demodulated signal, plotted such that the area below the curve is proportional to the variance. Shown are a scintillometer with a 1.75-cm aperture and one with a 10-cm aperture. Spectra are from 24 May 2012 for the interval (a) 00:00 – 00:10 UTC and (b) 13:50 – 14:00 UTC.

As expected, the peak in the spectra of the 1.75cm-aperture scintillometer is more elevated and located at higher time frequencies than the peak in the spectra of the 10cm-aperture

scintillometer. For both scintillometers applies that $D > F$ and consequently they are most sensitive to eddies of size D . Smaller eddies have shorter time scales and hence larger frequencies, which is reflected in the spectra. Furthermore, over the 10-cm aperture more eddies are averaged out than over the 1.75-cm aperture, which explains why the peak of the spectrum of the 1.75cm aperture scintillometer is more elevated than that of the 10cm-aperture scintillometer.

Another, pronounced difference between the two scintillometers is that the spectra of the 1.75cm-aperture scintillometer are smooth and show only one peak, whereas the spectra of the 10-cm-aperture scintillometer are less smooth and have a second peak at frequencies larger than 100 Hz. This is noise that is induced on the scintillometer signal. Similar as in chapter 3, where we called it the low- C_n^2 error, this noise mainly affects the measurements for low C_n^2 . In this case the noise is caused by the fact that we used an unshielded measurement cable of 130 m long. Unfortunately, this cable functioned as a long antenna, which easily picked up noise.

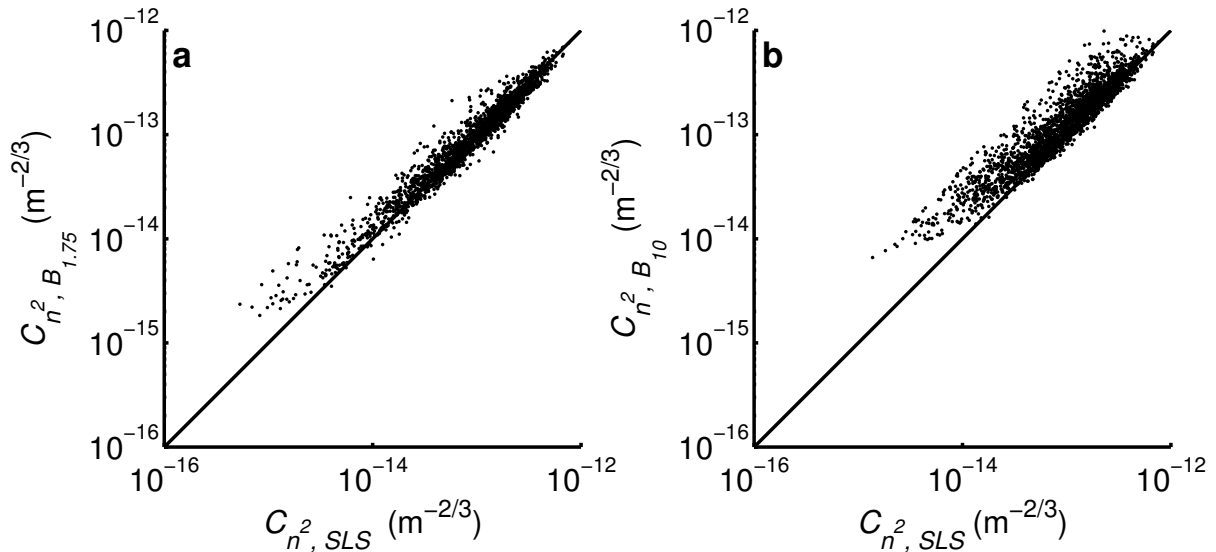


Figure 4.5: Comparison of C_n^2 from the displaced-beam laser scintillometer (SLS) and (a) the 1.75cm-aperture scintillometer and (b) the 10cm-aperture scintillometer. All C_n^2 are estimated with l_0 from the displaced-beam laser scintillometer. Each data point is derived from 10-min statistics

Figure 4.5 confirms this. The figure shows the comparison of C_n^2 estimated via $B_{1.75}$ and B_{10} with $C_n^2,_{SLS}$. Each C_n^2 has been determined with $l_{0,SLS}$, so that the three scintillometer can be compared. The 1.75cm-aperture scintillometer compares well to the displaced-beam laser scintillometer. The scatter is small and only for $C_n^2 < 2 \times 10^{-15} \text{ m}^{-2/3}$, the 1.75cm-aperture scintillometer overestimates C_n^2 . For the 10cm-aperture scintillometer the scatter is larger and

C_n^2 is overestimated for values of $C_n^2 < 3 \times 10^{-14} \text{ m}^{-2/3}$. Both the larger scatter and the overestimation are caused by the cable noise. Consequently, we conclude that B_{10} cannot be used for determining l_0 during conditions with low C_n^2 and hence B_{10} corresponding to $C_n^2 < 3 \times 10^{-14} \text{ m}^{-2/3}$ will be omitted in the subsequent validation of l_0 .

For the validation of the l_0 estimates, we introduce Figure 4.6, in which l_0 is obtained from three combinations of dual apertures. Figure 4.6a shows l_0 estimated from the ratio $B_{1.75}/B_{10}$, Figure 4.6b shows l_0 estimated from the ratio $B_{laser}/B_{1.75}$, and Figure 4.6c shows l_0 estimated from the ratio B_{laser}/B_{10} . In all cases, $l_{0,SLS}$ serves as the reference.

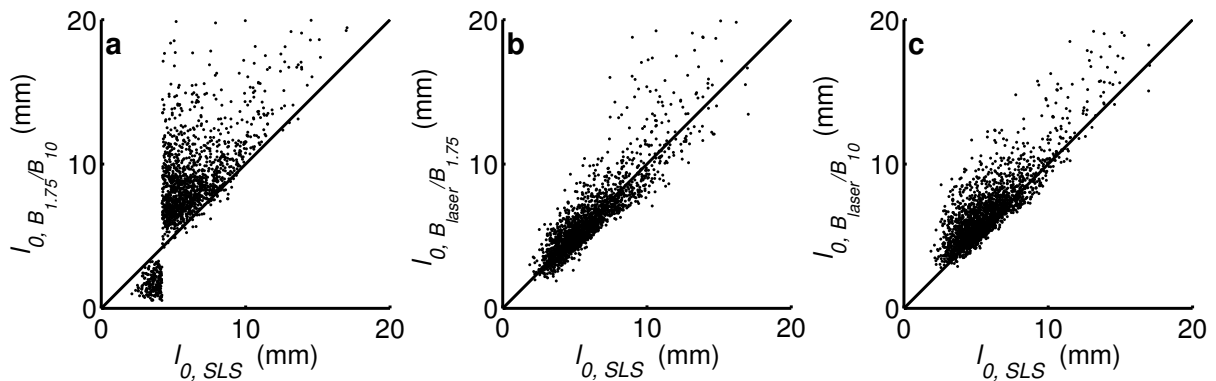


Figure 4.6: Comparison of l_0 from the displaced-beam laser scintillometer (SLS) and (a) estimated from the ratio $B_{1.75}/B_{10}$, (b) estimated from the ratio $B_{laser}/B_{1.75}$, and (c) estimated from the ratio B_{laser}/B_{10} . Each data point is derived from 10-min statistics

From Figure 4.6 it can be readily seen that the two estimates of l_0 that are estimated with B_{laser} agree well with $l_{0,SLS}$. In both cases the scatter is relatively small and the data scatters around the 1:1 line. It appears that the scatter is slightly less when l_0 is estimated from the ratio $B_{laser}/B_{1.75}$ than when it is estimated from the ratio B_{laser}/B_{10} (root-mean-squared error for $l_0 < 13$ mm equals 1.1 mm vs. 1.4 mm). On the other hand, l_0 estimated from the ratio $B_{1.75}/B_{10}$ yields bad estimates. The peak of the ratio $B_{1.75}/B_{10}$ is located at 4.2 mm and consequently, for l_0 in the range 2 mm – 6 mm the ratio $B_{1.75}/B_{10}$ is approximately constant with increasing l_0 . Therefore, small errors in the measured ratio cause large errors in the l_0 estimate, which is reflected in the large scatter that is displayed in the figure.

The above results agree with the work of Hill et al. (1992), who show that the dual-aperture method works well for a combination of a laser and a scintillometer with an aperture.

Unfortunately, with our present set-up, we were not able to estimate l_0 accurately from the ratio measurements of the two modified large-aperture scintillometers.

4.3. Conclusions for scintillometer development

Based on the results from section 4.1 and 4.2 and based on the theoretical discussion, we conclude that it is possible to modify existing large-aperture scintillometers such that a combination of two of them can be operated as a field-scale scintillometer, provided that the ratio $B_{1.00}/B_{10}$ is used. In this way it is ensured that the measured ratio is sensitive enough to l_0 for l_0 in the range 2 mm – 6 mm. For paths of 500 m this is questionable, but the method will in any case work for paths shorter than 150 m. In order that a modified large-aperture scintillometer works also with a 1.00-cm aperture, the detector in the receiver must be sensitive enough for measuring the weak signal intensity corresponding to the 1.00-cm aperture. In our case, either the sensitivity of the square-law detector was not large enough (it was about 5000 kV W^{-1}), or the emissivity of the light-emitting diode was too weak (it is about 100-150 mW). Our estimation is that the sensitivity or the emissivity should be improved by at least a factor 3 to make this set-up work.

Furthermore, to prevent deterioration of the measurements by cable noise the scintillometers must be pointed in the same direction, so that the measurement-cable length remains small, or shielded cables must be used. Even when pointing the scintillometers in the same direction, crosstalk is not likely to occur, because the beam of 1.00cm-aperture scintillometer is very narrow.

Related to the narrow beam are two practical aspects. First, it is a challenge of aligning a scintillometer with such a small aperture. The displaced-beam laser scintillometers operate in the visible light domain, but the modified large-aperture scintillometers do not do so. By enlarging the aperture with the diaphragm the alignment could be found and reducing the aperture after the first alignment and then do a final optimization of the alignment with the narrow beam. Another practical aspect is determining the aperture size. Especially for the small aperture knowing the exact diameter (up to an accuracy of 0.1 mm) is crucial. Using diaphragms this is not an easy procedure, unless they can be fixed while setting the exact diameter with a pair of callipers. Probably it would be easier to use a set of aperture reducers, for which the aperture sizes are exactly known.

5. Measuring H₂O and CO₂ fluxes at field scales with scintillometry: Part I – introduction and validation of four methods⁴

5.1. Introduction

Due to increased water scarcity and the presumed role of carbon dioxide on climate and climate change, interest in understanding the cycles of water and carbon has increased over the past decades. Much effort has been put on assessing the exchange between the different compartments that are involved in these cycles, with a special focus on the exchange between the land surface and the atmosphere. Methods to assess the fluxes of water vapour (evapotranspiration) and carbon dioxide were developed and networks to monitor these fluxes were set up worldwide (Baldocchi et al., 2001).

The eddy-covariance method, ideally, measures these fluxes in a straight forward manner and its set-up is relatively easy in maintenance. Therefore, the eddy-covariance method is extensively used to do these measurements (Baldocchi, 2003; Shuttleworth, 2007). However, the use of the eddy-covariance method is limited in four ways. Firstly, flow distortion (by the mast or instrument itself) is not negligible for unfavourable wind directions. Secondly, the eddy-covariance method needs to sample all eddy scales relevant to the turbulent flux (Finnigan et al., 2003). Thirdly, as a point-sampling measurement technique it requires time to adequately sample the largest eddy scales and during the whole flux-averaging interval turbulence needs to be stationary. Fourthly, point-sampling measurements only represent a small area, which especially in heterogeneous conditions limits their applicability as a reference in e.g. numerical models or water/carbon-balance estimates (Aubinet, 2008; Foken, 2008; Hartogensis et al., 2002; Mahrt, 2010; Vickers et al., 2009).

Scintillometry is an indirect flux estimation method that overcomes these four limitations. Scintillometers spatially average fluxes over field scales (100 m - 500 m) to kilometre scales (up to 10 km). Therefore, flow distortion of the instrument is negligible (Thiermann and Grassl, 1992) and the obtained fluxes represent larger areas than fluxes obtained with eddy-covariance (Wyngaard and Clifford, 1978). Furthermore, scintillometers sample only one eddy scale. The advantage is that the larger measurement path enhances the number of independent samples of eddies to which the scintillometers are sensitive.

⁴ This chapter has been published as **Van Kesteren, B.**, Hartogensis, O.K., van Dinter, D., Moene, A.F., and De Bruin, H.A.R., 2012, *Measuring H₂O and CO₂ fluxes at field scales with scintillometry: Part I – introduction and validation of four methods*, Agric. Forest Meteorol., doi 10.1016/j.agrformet.2012.09.013

Therefore, statistically stable fluxes can rapidly (< 1 min) be obtained. Research has confirmed these results and shows that optical large-aperture scintillometers yield accurate estimates of the area-averaged sensible-heat flux over moderately heterogeneous terrain. (Meijninger et al., 2006; Meijninger et al., 2002b). Furthermore, area-averaged latent-heat fluxes have been determined accurately on kilometre scales over heterogeneous terrain, by combining an optical large-aperture and microwave scintillometer (Green et al., 2001; Green et al., 2000; Lüdi et al., 2005; Meijninger et al., 2006; Meijninger et al., 2002a). Finally, for field scales (< 500 m) it has been shown that accurate estimates of both the sensible-heat flux and momentum flux can be obtained with a displaced-beam laser scintillometer for averaging intervals shorter than one minute (Hartogensis et al., 2002; Wyngaard and Clifford, 1978). Unfortunately, scintillometers cannot determine the fluxes of all scalar quantities.

The goal of this study is to test four methods that in principle are able to obtain fluxes of every passive-scalar quantity. By combining displaced-beam laser scintillometer measurements with turbulence measurements of the passive scalar, these methods have the potential to obtain fluxes with a similar time averaging as the above described scintillometers. To realise this short averaging time, homogeneous conditions are required, which is ensured by limiting the application of the methods to single crop fields.

All methods have been described in the literature already, but as far as the authors know only the Bowen-variance and the energy-balance method have been applied in combination with scintillometer measurements so far. The four combined methods are: the flux-variance method (De Bruin et al., 1993; Hill, 1989; Lamaud and Irvine, 2006), the Bowen-variance method (De Bruin et al., 1999; Guo et al., 2009; Lamaud and Irvine, 2006; Moene and Schüttemeyer, 2008; Nakaya et al., 2006), the structure-parameter method (De Bruin et al., 1993; Hill, 1989), and the energy-balance method, which only gives evapotranspiration (Ezzahar et al., 2007; Green et al., 1997; Meijninger et al., 2002a; Savage, 2009).

The essence of these combined methods is that the scintillometer measures the area-averaged parameters of the atmospheric turbulence (the transport mechanism) and that the additional measurements provide a turbulence statistic of the scalar quantity that is transported. As such, the water-vapour flux density or evapotranspiration, presented in this chapter in terms of latent heat, and the carbon dioxide flux density, presented as CO₂ flux serve as illustrations for any other passive-scalar quantity that is transported by turbulence. The difference in footprint of the combined measurement techniques is another reason for the requirement of homogeneity. That is, the different footprints must represent areas with similar

conditions. Furthermore, homogeneity is required, because all the combined methods rely on the application of Monin-Obukhov similarity theory.

We divide this study in three parts, in which we show that these combined methods can acquire latent-heat and CO₂ fluxes over short averaging intervals and during non-stationary conditions, e.g. intermittent or cloudy conditions (see chapter 6 and 7). This chapter (part I) discusses the reliability of the combined methods. Firstly, the results of the sensitivity analysis of the methods are discussed in section 5.4. Secondly, the results of the methods are validated with eddy-covariance fluxes in section 5.5. Finally, as scintillometry is an indirect method, scintillometers cannot decide on stability or flux direction, so Appendix A discusses the issue on how to obtain stability and the flux direction from the measurements that are done already for the combined methods.

5.2. Theory

5.2.1. Eddy-covariance method

The eddy-covariance method derives turbulent fluxes using high-frequency point-sampling measurements. With a sonic anemometer, the wind components are measured in three directions u , v , and w , as well as the temperature, T . Furthermore, an open-path gas analyser measures the specific humidity, q , and CO₂ concentration, q_{CO_2} . In this study, we consider the fluxes of sensible-heat, H , latent-heat, $L_v E$ and CO₂, FCO_2 . In the framework of eddy covariance the fluxes of quantity x are defined by

$$F_x = \overline{\rho w' x'} = \overline{\rho} \text{cov}(w, x), \quad (5.1)$$

where F_x is the flux of quantity x ($\text{kg m}^{-2} \text{s}^{-1}$), ρ the density of air (kg m^{-3}), w' the turbulent part of the vertical wind speed (m s^{-1}) and x' the turbulent part of scalar quantity x (Stull, 1988; Webb et al., 1980). Furthermore, quantity x represents $c_p T$ (J kg^{-1}), $L_v q$ (J kg^{-1}), and q_{CO_2} (kg kg^{-1}), with c_p the heat capacity of air at constant pressure ($\text{J kg}^{-1} \text{K}^{-1}$) and L_v the latent heat of vaporization (J kg^{-1}). In this study, both c_p and L_v are modelled by taking into account their temperature dependence (Garratt, 1992; Stull, 1988). To reduce the random error in the covariances, high-frequency measurements of the wind speed, temperature, humidity, and CO₂ are needed to limit the averaging time (Bosveld and Beljaars, 2001; Lenschow et al., 1994). At the same time, however, the averaging time must be long enough to include the

largest turbulent eddies and short enough to exclude non-turbulent motions (Lenschow et al., 1994; Mahrt, 2010). This results in an averaging time of at least 10, but typically 30 minutes (Aubinet, 2008; Finnigan, 2008; Foken, 2008; Hartogensis et al., 2002; Mahrt, 2010; Sun et al., 2005; Vickers et al., 2009). During these 10-30 minutes, stationarity is required, a condition that is not always met, e.g. in cloudy conditions or intermittent boundary layers (Hartogensis et al., 2002). Consequently, under these circumstances the eddy-covariance method has limited application.

5.2.2. Scintillometer method

Scintillometers provide line measurements that improve on eddy-covariance measurements, not only regarding spatial representativeness, but also regarding the requirements of stationarity. The displaced-beam laser scintillometer used in this study emits two parallel laser beams (wavelength 670 nm), displaced by about 2.7 mm. Two detectors that are typically 100 m – 300 m away from the transmitter measure the light intensities, I_1 and I_2 .

Wave propagation and turbulence theory describes how the correlation coefficient of $\ln(I_1)$ with $\ln(I_2)$ is related to the inner-scale length of the refractive index, l_0 (m), which we assume to equal the inner scale of temperature (Hartogensis et al., 2002; Hill, 1982; Thiermann and Grassl, 1992). Once l_0 is obtained, the structure parameter of the refractive index, C_n^2 ($\text{m}^{-2/3}$), can be obtained from the variance of $\ln(I_1)$ or $\ln(I_2)$. For the displaced-beam laser scintillometer the relation is given by

$$B_{12} = 4\pi^2 \kappa^2 \int_0^L \int_0^\infty \Phi_{nn}(k, C_n^2, l_0) J_0(kd) \sin^2 \left(\pi \frac{\Lambda^2}{l^2} \right) \left(\frac{2J_1 \left(\frac{kDx}{2L} \right)}{\frac{kDx}{2L}} \right)^2 dk dx, \quad (5.2)$$

where $B_{12} = 0.25 \text{cov}(\ln(I_1), \ln(I_2))$ is the covariance of the logarithmic amplitude of the beam intensities, $\kappa = 2\pi/\lambda$ is the wave number of the emitted radiation, L is the path length between transmitter and receiver, $\Phi_{nn}(k, C_n^2, l_0)$ is the three-dimensional spectrum of the refractive index, $k = 2\pi/l$ is the eddy wave number, J_0 and J_1 are Bessel function of the first kind (zeroth and first order respectively), d is the displacement between the two beams (2.7 mm), D is the aperture size of the receiver (2.5 mm), and $\Lambda^2 = \lambda x(L-x)/L$ is the square of the radius of the first Fresnel zone at position x . When $d = 0$, Eq. (5.2) provides the variance of one detector. In

Eq. (5.2) the J_0 term describes the covariance between the beams, the sine term describes the wavelength of the eddies to which the scintillometer is sensitive, and the last term describes the aperture averaging. $\Phi_{nn}(k, C_n^2, l_0)$ is described by

$$\Phi_{nn}(k, C_n^2, l_0) = 0.033 C_n^2 k^{-11/3} f(k, l_0), \quad (5.3)$$

where $f(k, l_0)$ is a function describing the dissipation range of the turbulence spectrum (Hill and Clifford, 1978). By determining B_{12} and B_{11} with the scintillometer, C_n^2 and l_0 are obtained from Eq. (5.2) and Eq. (5.3). Subsequently the structure parameter of temperature, C_T^2 ($\text{K}^2 \text{m}^{-2/3}$), is derived from C_n^2 (Moene, 2003). Finally, with C_T^2 and l_0 the area-averaged friction velocity, u^* , and area-averaged flux of sensible heat are iteratively solved, using Monin-Obukhov similarity theory (MOST) Eqs. (5.4) – (5.6).

$$u_* = \nu \left(\frac{7.4}{l_0} \right)^{4/3} (k_{kar} z_{eff})^{1/3} f_\varepsilon \left(\frac{z_{eff}}{L_O} \right)^{-1/3}, \quad (5.4)$$

$$\theta_* = (C_T^2)^{1/2} (k_{kar} z_{eff})^{1/3} f_T \left(\frac{z_{eff}}{L_O} \right)^{-1/2}, \quad (5.5)$$

where, θ_* is the turbulent scale of temperature, ν is the kinematic viscosity of air, $k_{kar} = 0.4$ is the von-Kármán constant, z_{eff} is the effective measurement height of the scintillometer, L_O is the Obukhov length, and f_T and f_ε are MOST functions for temperature and the dissipation rate of turbulent kinetic energy that depend on z_{eff}/L_O . Then, in the framework of MOST the fluxes of quantity x are defined by

$$F_x = -\rho u_* x_*, \quad (5.6)$$

where x_* is the turbulent scale of quantity x ($c_p \theta_*$, $L_v q_*$, and q_{CO_2*}). In determining L_O , we took into account the influence of humidity on buoyancy (Kohsiek, 1982). For that $L_v E$ estimates are required, which are obtained from the combined methods themselves. Therefore, the combined methods are included in the iteration procedure to calculate H and u^* . The effect of including humidity in buoyancy on H and u^* is small, about 2% and 1% respectively.

5.2.3. Combined methods

The displaced-beam laser scintillometer provides u^* and H , but neither L_vE nor FCO_2 . Therefore, we propose to combine the scintillometer measurements with turbulence measurements of these scalar quantities in order to obtain L_vE and FCO_2 . As such four combined methods are discussed, namely the flux-variance method, the Bowen-variance method, the structure-parameter method, and the energy-balance method.

5.2.3.1. Flux-variance method

The flux-variance method uses the standard deviation of humidity or CO_2 , σ_q or σ_{qCO_2} , to estimate L_vE or FCO_2 . In the framework of MOST the scale of the specific humidity or CO_2 concentration, q^*_{*x} , is derived using (De Bruin et al., 1993; Hill, 1989)

$$\frac{\sigma_x}{q^*_{*x}} = f_{xx} \left(\frac{z_{eff}}{L_O} \right), \quad (5.7)$$

where $f_{xx}(z_{eff}/L_O)$ is a MOST function (see section 5.3.2 for the exact f_{xx} used in this study). Note that here z_{eff} is the effective height of the fast-response hygrometer, which in our set-up is identical to the effective height of the scintillometer.

In the flux-variance method, L_vE and FCO_2 are obtained using

$$F_x = -\rho u_* q^*_{*x} = -\rho \frac{u_*}{f_{xx}(z_{eff}/L_O)} \sigma_x = -\rho K_{x,std} \sigma_x, \quad (5.8)$$

where $K_{x,std}$ is the turbulence transport efficiency of the flux-variance method. L_O and u_* , and thus $K_{x,std}$, are obtained from the scintillometer and σ_q and σ_{qCO_2} are obtained from turbulence measurements of the scalar quantities.

5.2.3.2. Bowen-variance method

The Bowen-variance method uses the variances of temperature and humidity to estimate the Bowen ratio. Nakaya et al. (2006), based on Moene (2003), used this estimated Bowen ratio together with scintillometer measurements of H to obtain L_vE . Thus, the Bowen ratio, β , is defined as the ratio between H and L_vE , and can be written in terms of the standard deviations

of temperature, σ_T , and humidity, σ_q , (De Bruin et al., 1999; Guo et al., 2009; Lamaud and Irvine, 2006; Moene and Schüttemeyer, 2008):

$$\beta \equiv \frac{H}{L_v E} \equiv \frac{r_{wT}}{r_{wq}} \frac{c_p}{L_v} \frac{\sigma_T}{\sigma_q}, \quad (5.9)$$

where r_{wT} is the correlation coefficient between vertical velocity and temperature, and r_{wq} the correlation coefficient between vertical velocity and humidity (Lamaud and Irvine, 2006). The ratio r_{wT}/r_{wq} is known as the relative transport efficiency, λ_{Tq} , and accounts for the dissimilarity of temperature and/or humidity. For perfect similarity the MOST functions of heat and humidity are identical and $\lambda_{Tq} = 1$ (Hill, 1989). However, typically, λ_{Tq} approximates r_{Tq} for large β (> 1) and $1/r_{Tq}$ for small β (< 0.1) (Guo et al., 2009; Lamaud and Irvine, 2006; Moene and Schüttemeyer, 2008). Depending on the cause of the dissimilarity (Katul et al., 2008), MOST requirements can be violated for one variable, but not necessarily for the other (Andreas et al., 1998; Moene and Schüttemeyer, 2008). The Bowen-variance method, however, requires simultaneous similarity of heat and humidity.

As for $L_v E$ a similar method exists to estimate FCO_2 . The CO_2 Bowen ratio, α , is defined as the ratio between H and FCO_2 and can be written in terms of σ_T and σ_{qCO_2} (Guo et al., 2009; van Dinter, 2009):

$$\alpha \equiv \frac{H}{\varepsilon_p F_{CO_2}} \equiv \frac{r_{wT}}{r_{wqCO_2}} \frac{c_p}{\varepsilon_p} \frac{\sigma_T}{\sigma_{qCO_2}}, \quad (5.10)$$

where ε_p is the photosynthetic efficiency, $11 \times 10^6 \text{ J kg}^{-1}$ (Jacobs et al., 2008), which cancels out in the flux calculation, Eq. (5.11), but is introduced here to arrive at a dimensionless Bowen ratio.

In this study we follow the method given by Guo et al. (2009) and use r_{Tq} and r_{TqCO_2} to parameterize the relative transport efficiency as described in their section 2.2.2. The exceptions are that we follow Lamaud and Irvine (2006) in the intermediate regime and use $k = (-1 - 2 \log(\beta))$ to parameterize $\lambda_{Tq} = r_{Tq}^k$. Furthermore, we determined M from our own eddy-covariance data and use $M = (0.9 - 1.33 \log(\alpha))$ for $1 \leq \alpha \leq 24$ to parameterize $\lambda_{TqCO_2} = r_{TqCO_2}^M$. Note, that all these parameterizations are empirical.

In the Bowen-variance method, $L_v E$ and FCO_2 are obtained using

$$F_x = \frac{\rho}{\lambda_{Tx}} \frac{H}{\rho c_p} \frac{\sigma_x}{\sigma_T} = \rho K_{x,Bowen} \sigma_x. \quad (5.11)$$

H is obtained from the scintillometer and r_{Tq} , r_{TqCO_2} , σ_T , σ_q , and σ_{qCO_2} are obtained from turbulence measurements of the scalar quantities.

5.2.3.3. Structure-parameter method

The structure-parameter method uses the structure parameter of humidity or CO_2 , C_q^2 or $C_{qCO_2}^2$, to estimate $L_v E$ or FCO_2 . The structure parameter is defined as (Tatarskii, 1961):

$$C_{x^2} = \frac{D_{x^2}}{r^{2/3}} = \frac{\overline{[x(y) - x(y+r)]^2}}{r^{2/3}}, \quad (5.12)$$

where the over-bar denotes the averaging time, T_{av} , D_x^2 is the structure function of a quantity x , $\Delta x = x(y) - x(y+r)$ is the difference in concentration of quantity x between position y and $y+r$ (r is a distance that must lie in the inertial sub-range of the turbulence spectrum). Assuming frozen turbulence, the structure parameter is derived from a time series of one sensor by replacing r by $U\Delta t$, with U the mean wind speed and Δt the time difference between two measurements (Hartogensis, 2006; Tatarskii, 1961). To determine C_x^2 , we chose a separation distance of 1 m. However, when deriving C_x^2 from a time series, C_x^2 is underestimated, because of path averaging over the sensor. Following Hartogensis (2006), we estimated the path-averaging error and corrected for the corresponding underestimation of 12.6%.

In the framework of MOST, q_{*x} is derived using (De Bruin et al., 1993; Hill, 1989)

$$\frac{C_{x^2} z_{eff}^{2/3}}{q_{*x}^2} = f_x(z_{eff}/L_O), \quad (5.13)$$

where $f_x(z_{eff}/L_O)$ is a MOST function (see section 5.3.2 for the exact f_x used in this study). Note that here z_{eff} is the effective height of the fast-response hygrometer, which in our set-up is identical to the effective height of the scintillometer.

In the structure-parameter method, $L_v E$ and FCO_2 are obtained using

$$F_x = -\rho u_* q_{*x} = -\rho z_{eff}^{1/3} \frac{u_*}{\sqrt{f_x(z_{eff}/L_O)}} \sqrt{C_{x^2}} = -\rho K_{x, strpar} \sqrt{C_{x^2}}, \quad (5.14)$$

where $K_{x, strpar}$ is the turbulence transport efficiency of the structure-parameter method. L_O and u_* , and thus $K_{x, strpar}$, are obtained from the scintillometer and C_q^2 or $C_{qCO_2}^2$ are obtained from turbulence measurements of the scalar quantities.

5.2.3.4. Energy-balance method

The energy-balance method uses the energy balance to estimate $L_v E$ and has been successfully applied before in combination with scintillometry (Ezzahar et al., 2007; Green et al., 1997; Meijninger et al., 2002b; Savage, 2009). The method assumes that all the net radiation, Q_{net} , is transferred into fluxes of sensible heat, latent heat, and soil heat, G :

$$Q_{net} \equiv H + L_v E + G, \quad (5.15)$$

In the energy-balance method H is obtained from the scintillometer, and Q_{net} and G from additional measurements. Note that contrary to the other combined methods, the additional measurements of the energy-balance method are non-turbulent and that the method only yields $L_v E$.

5.3. Material and methods

5.3.1. Experimental set-up

Data used in this study are gathered in the framework of Transregio32 project. The Transregio 32 focusses on exchange processes between the soil, vegetation, and adjacent atmospheric boundary layer (Graf et al., 2010).

The measurements took place in a winter-wheat field near Merken, Germany (50° 50' 53.92" N, 6° 24' 1.99" E) between 7 May and 10 June 2009. The dimensions of the field were 350 m by 150 m. In the middle of the field, an eddy-covariance system was installed 2.40m above ground level. The system consisted of a CSAT3 sonic anemometer (Campbell Scientific, Logan, USA) and a LiCor7500 H₂O/CO₂ sensor (LiCor, Lincoln, USA). A

CR3000 datalogger (Campbell Sci., UK) recorded the raw 20-Hz data. Furthermore, we installed a displaced-beam laser scintillometer (SLS-20, Scintec, Rottenburg, Germany) with the middle of its path 20 m west from the eddy-covariance tower. The scintillometer was installed at 2.40 m above ground level as well. Its path was directed NW to SE and had a length of 120 m. The effective height of the scintillometer linearly decreased from 2.11 m at the beginning of the experiment to 1.84 m at the end of the experiment, due to the growing crop. We estimated the effective height by subtracting the displacement height, i.e. 2/3 of the crop height (Green et al., 1994). For that reason, the crop height was measured four times during the experiment and found to increase linearly from 0.33 m at the beginning to 0.85 m at the end of the experiment. The empirical expression for the displacement height is a good approximation for the humid and densely vegetated conditions as encountered in our experiment (Brutsaert, 1982; Verhoef et al., 1997).

In addition to the turbulence measurements, long-wave and short-wave radiation were measured at 2 m height in the EC tower with a four component net-radiation meter, NR01 (Hukseflux, Delft, the Netherlands). Also a soil heat flux plate, HFP01SC (Hukseflux, Delft, the Netherlands), measured the soil-heat flux at a depth of 0.01 m. Furthermore, standard measurements of temperature, air pressure, p , humidity, and precipitation were performed on site.

During the measurement period the average temperature was about 15 °C, with minima and maxima usually between 10 °C and 21 °C. The amount of precipitation was 60 mm. Only from the 20th of May until the 6th of June it was relatively dry with 3.1 mm of precipitation on the 24th-28th of May. Furthermore, during daytime β generally was smaller than 0.6 and z/L_0 typically varied between -0.4 and 0.1. Consequently, the wheat was well watered and green during the whole measurement period.

5.3.2. Data processing

The eddy-covariance data were processed using the software package ECpack from Wageningen University (Van Dijk et al., 2004). The following corrections and rotations were applied: correction for humidity effects on the sonic temperature; linear detrending of the data; the planar-fit rotation; and the frequency response correction, path-averaging correction and sensor-separation correction (Kaimal and Finnigan, 1994; Moore, 1986; Schotanus et al., 1983).

The SLS measurements were obtained with SLSrun 2.24, which is provided by Scintec (Scintec, 2006). The flux calculations of scintillometer techniques are more straightforward than eddy-covariance in the sense that there are no additional, and debatable, corrections needed, such as axes-rotation corrections, corrections for under sampled eddy sizes etc. However, some data processing is still involved to obtain H and u^* from B_{11} and B_{12} . To calculate the fluxes, three changes were made to the data processing as compared to Scintec's standard processing. Firstly, De Bruin et al. (2002) and Hartogensis et al. (2002) found two systematic errors in the SLS measurements, B_{11} and B_{12} , for which we applied corrections. To this end, we estimated l_0 from eddy-covariance data in two ways. First, from wind-velocity spectra (Hartogensis and De Bruin, 2005) and second, from u^* by applying Eq. (5.4). When estimating u^* with the new l_0 , both methods yielded identical regression statistics as those given in Figure 5.3a, except that the spectral method underestimates u^* by 8%. As we want to focus on the methodology of the combined methods and not on the quality of the MOST functions for u^* in Eq. (5.4), we decided to correct the systematic error with l_0 estimated from Eq. (5.4). Thus, we applied a linear correction to make the inner scale of the scintillometer fit the inner scale calculated from eddy-covariance data ($l_{0\text{new}} = 1.25l_{0\text{old}} - 1.72 \times 10^{-3}$). Subsequently, with this new l_0 we recalculated C_n^2 and linearly corrected its overestimation ($C_n^2_{\text{new}} = 0.6C_n^2_{\text{recalculated}}$). Secondly, we used the humidity correction, Eq. 8 from Moene (2003), which is most comprehensive to calculate C_T^2 from C_n^2 . Thirdly, we used the following MOST functions: f_ε from Hartogensis and De Bruin (2005) to estimate u^* , and f_T from Andreas (1988) to estimate H . In addition, for the structure-parameter method $f_x = f_T$ from Andreas (1988) was used. For the flux-variance method, we used $f_{xx} = f_{TT}$ from De Bruin et al. (1993) for unstable conditions and $f_{xx} = f_{TT}$ from Pahlow et al. (2001) for stable conditions (a constant value of 3).

Neither scintillometers can distinguish stable from unstable conditions, nor can the combined methods distinguish the flux direction. Therefore, we chose to use eddy-covariance data to decide on stability and flux direction. We refer to Appendix A for a more elaborate discussion about possible methods to decide on stability and flux direction without eddy-covariance measurements. The appendix shows that by using the correlation coefficients good estimates can be made of the flux direction. Only in about 5% of the cases a different flux-sign estimation than from eddy-covariance data is obtained.

All data were filtered to remove unreliable data. Data were excluded when it rained, when the percentage of valid data samples from the eddy-covariance system was less than 98%, when the percentage of valid data samples from the scintillometer was less than 90%,

when the wind direction was $15^\circ - 100^\circ$ (mast obstruction). Furthermore data were rejected when the iteration process to obtain H or u^* did not converge to a solution. For the Bowen-variance method data were also rejected when $|r_{Tq}| < 0.2$ and when $|\beta| < 0.1$ or $|\alpha| < 1$.

5.3.3. Sensitivity analysis

We apply a data-based sensitivity analysis to see to which variables each method is sensitive. As the focus of the sensitivity analysis is on the combined methods and not on the measurements, we focus on the variables that serve as input for the combined methods. In doing so, we can readily see which variables are important in estimating the flux for each method and besides that, see which variables need to be estimated accurately.

Thus, we divide the variables in three groups. First, mean-state variables, i.e. variables not representing turbulence. Second, method-specific turbulence variables, i.e. variables that represent the turbulence behaviour of the scalar quantity for a specific method. Third, turbulence variables associated with scintillometry. Note that depending on the combined method, a variable can act for one method as a mean-state variable, whereas for another method it acts as a method-specific turbulence variable.

Table 5.1: Perturbation applied to variables in sensitivity analysis

<i>Variable</i>	<i>Perturbation</i>	<i>Variable</i>	<i>Perturbation</i>
z_{eff}	20%	σ_q	20%
T	2 K	C_q^2	20%
p	5 hPa	Q_{net}	20%
q	$5 \times 10^{-3} \text{ kg kg}^{-1}$	G	20%
r_{Tq}	20%	C_n^2	20%
σ_T	20%	l_0	20%

The mean state variables T , p , q , all get a fixed perturbation (Table 5.1). The perturbations of these variables are set relatively large compared to the measurement accuracy, in order to test whether they impact the flux. A relative perturbation of 20% was set for all other variables, so that we can see the relative impact of the different variables and can compare them. Furthermore, all variables are treated as being independent from each other in order to separately study the influence of each variable. Finally, in our discussion we limit

ourselves to $L_v E$, because the results for FCO_2 or flux of any other scalar quantity are identical, except for the absolute value of the root-mean-square error (RMSE).

We perturbed the input variables of the combined methods and in the analysis compare the unperturbed situation with the perturbed situation by means of the regression slope (forced through origin) and the root-mean-square error (RMSE). The RMSE is a measure for the non-linearity of the response. An increased RMSE can happen for two reasons, first when the response is linear, but slightly scattered; second, when the response is not linear, but for example exponential.

5.4. Sensitivity analysis of the combined methods

This section presents the results of the sensitivity analysis. Figure 5.1 and Figure 5.2 show the sensitivity of the flux to each variable. On the x-axis the perturbed variables are shown in four groups. First, z_{eff} is coloured black. Second, the mean-state variables are coloured grey. Third, the method-specific turbulence variables are coloured black. Fourth, the turbulence variables associated with scintillometry are coloured grey again. Note, that when a method does not use a variable, it is not plotted on the x-axis.

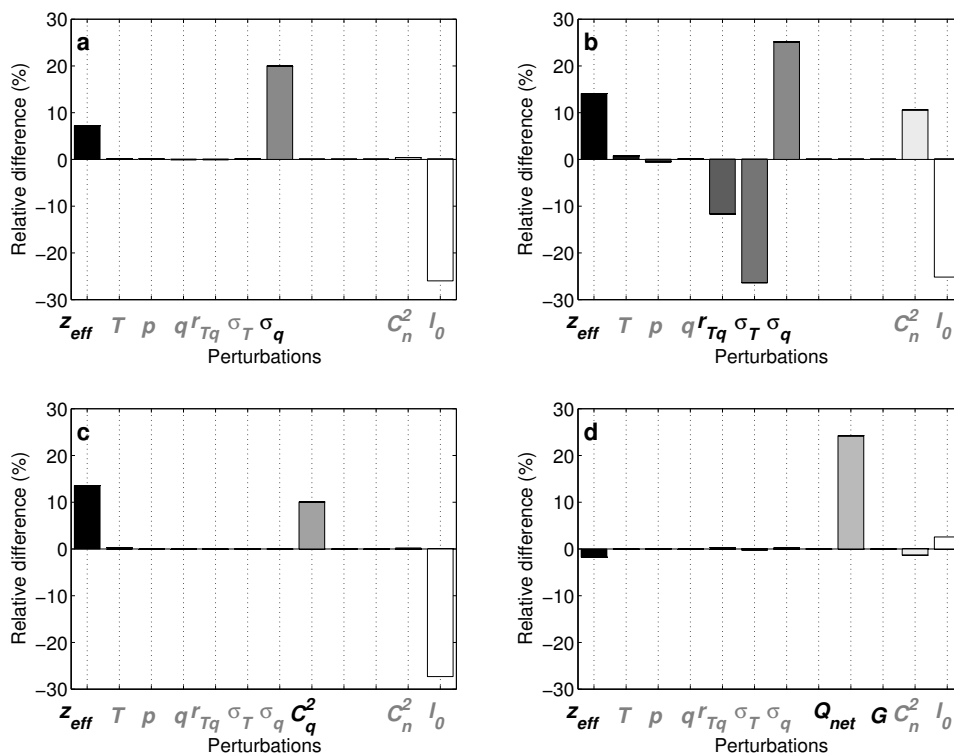


Figure 5.1: Systematic differences caused by 12 data-based perturbations for (a) the flux-variance method, (b) the Bowen-variance method, (c) the structure-parameter method, and (d) the energy-balance method. The greyscales depict a specific variable and are the same for each method.

First of all, we want to mention that the sensitivity to the choice of a specific MOST function is large. Savage (2009) showed that the variability in H , resulting from choosing different MOST functions, is about 35% for unstable conditions. For stable conditions this variability is even greater. $L_v E$ and FCO_2 experience a similar variability as H (not shown), because these fluxes are estimated with the same MOST functions by the combined methods.

Then, as can be seen in Figure 5.1 and Figure 5.2, all methods are sensitive to z_{eff} . The large sensitivity arises from their dependence on MOST. Consequently, having a correct estimation of z_{eff} is essential for obtaining accurate flux estimates (Hartogensis et al., 2003). Similarly, it can be seen that no method is sensitive to its mean-state variables. Turbulence variables like C_T^2 and u_* do depend on them, but as they are mean-state variables their influence is of minor importance. Furthermore, it can be seen that each method is sensitive to its method-specific turbulence variables and the turbulence variables associated with scintillometry. The combined methods are especially sensitive to l_0 and thus u_* , because we measured close to the surface. This emphasizes the importance of accurate estimates of u_* . In the following, we discuss each method more in detail.

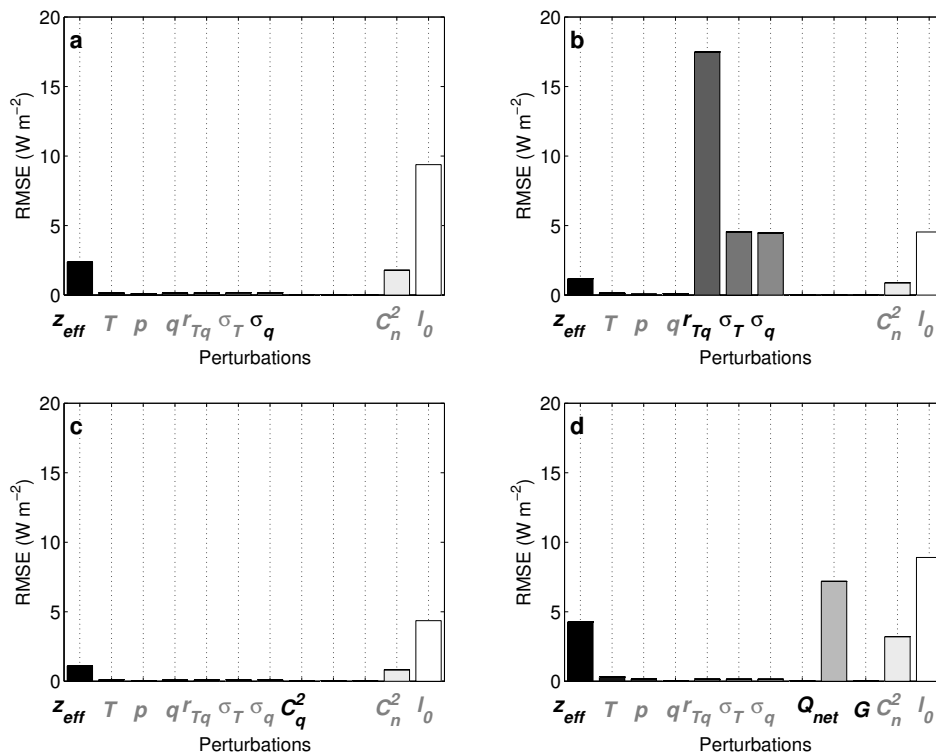


Figure 5.2: Root mean-squared error caused by 12 data-based perturbations for (a) the flux-variance method, (b) the Bowen-variance method, (c) the structure-parameter method, and (d) the energy-balance method. The greyscales depict a specific variable and are the same for each method.

5.4.1. Flux-variance method

To start with, the flux-variance method is considered. This method is sensitive to a 20% perturbation in z_{eff} , but the corresponding 8% perturbation in the flux is less than those for the Bowen-variance and the structure-parameter method, which are both 13%. The flux-variance method is less sensitive to z_{eff} than the other two methods, which has to do with the shape of its MOST functions. In addition to z_{eff} , the flux-variance method is sensitive to its method-specific turbulence variable. A 20% perturbation in σ_q leads to a 20% perturbation in the flux. Finally, to the variables that are associated with the scintillometer measurements, the flux-variance method shows divergent responses. The method is almost insensitive to C_n^2 . C_n^2 enters the flux-variance method through the stability and close to the surface stability is only weakly dependent on buoyancy, which C_n^2 represents. The sensitivity to l_0 is far greater: a 20% positive perturbation in l_0 leads to a 27% smaller flux ($-27\% \approx (-4/3 \cdot 0.2)$), because l_0 relates to u^* with a $-4/3$ power, Eq. (5.4)). For this method the RMSE of l_0 (RMSE $\approx 9 \text{ W m}^{-2}$) is largest. This occurs, because the flux relates partly non-linearly to u^* through L_O in the MOST functions and l_0 relates non-linearly to u^* .

5.4.2. Bowen-variance method

The second method that is considered is the Bowen-variance method. Through MOST, this method is sensitive to z_{eff} . The sensitivity to z_{eff} , however, is greater than for the flux-variance method, because different MOST functions are used. Furthermore, the method is sensitive to its method-specific turbulence variables. r_{Tq} appears to cause a negative response, but actually this is only true for large fluxes. When β is large (≥ 1), λ_{Tq} approximates r_{Tq} , but when β is small (≤ 0.1) λ_{Tq} approximates $1/r_{Tq}$. Hence, r_{Tq} causes a non-linear response and consequently the RMSE depicted in Figure 5.2 is large (18 W m^{-2}). For σ_T and σ_q the response is more straight-forward. A positive perturbation in σ_T leads to a smaller flux, whereas a positive perturbation in σ_q leads to a larger flux. In both cases the effect is somewhat enhanced and the response slightly scattered (RMSE $\approx 4 \text{ W m}^{-2}$) through the influence of λ_{Tq} on the Bowen ratio in the flux estimate. Finally, the Bowen-variance method is sensitive to both variables that are associated with the scintillometer measurements. A 20% perturbation on C_n^2 leads to an 11% perturbation in the flux. In fact, this reflects the influence of H ($11\% \approx 0.5 \cdot 0.2$, because C_n^2 relates to H with a $1/2$ power, Eq. (5.5)). The sensitivity to l_0 is larger: a 20% positive perturbation in l_0 leads to a 27% smaller flux ($-27\% \approx (-4/3 \cdot 0.2)$), because l_0 relates to u^* with a $-4/3$ power, Eq. (5.4)). The RMSE of 4 W m^{-2} in l_0 occurs, because the flux

relates partly non-linearly to u^* through L_O in the MOST functions and l_0 relates non-linearly to u^* .

5.4.3. Structure-parameter method

The third method that is considered is the structure-parameter method. Through MOST, also this method is sensitive to z_{eff} . This sensitivity is almost identical to the Bowen-variance method, because the same MOST functions are used. Furthermore, the method is sensitive to its method-specific turbulence variables. A 20% perturbation in C_q^2 leads to a 10% perturbation in the flux. The structure-parameter method seems less sensitive to its method-specific turbulence variable than the other three methods are to theirs. However, for the flux-variance method we applied the perturbation to the standard deviation instead of to the variance. Applying a 20% perturbation to $\sqrt{C_q^2}$, yields a 20% perturbation in the flux (not shown). Finally, to the variables that are associated with the scintillometer measurements, the structure-parameter method shows divergent responses. It is almost insensitive to C_n^2 . As for the flux-variance method, C_n^2 represents buoyancy, which is weak close to the surface. The sensitivity to l_0 is far greater: a 20% positive perturbation in l_0 leads to a 27% smaller ($-27\% \approx (-4/3 \cdot 0.2)$), because l_0 relates to u^* with a $-4/3$ power, Eq. (5.4)). The method shows a similar, scattered response of l_0 (RMSE $\approx 4 \text{ W m}^{-2}$) as the Bowen-variance method, because the same MOST functions are used and l_0 relates non-linearly to u^* .

5.4.4. Energy-balance method

The fourth and final method that is considered is the energy-balance method. Through MOST, also this method is sensitive to z_{eff} . However, the sensitivity is clearly lower than for the other three methods, because H is small compared to Q_{net} . Furthermore, the method shows divergent responses to the method-specific turbulence variables. A 20% positive perturbation in Q_{net} leads to a 23% increase in the flux. However, a 20% positive perturbation in G leads to a 0% difference in the flux. This happens, because G is small compared to Q_{net} and H . Finally, the energy-balance method is hardly sensitive to the variables that are associated with the scintillometer measurements. A perturbation of 20% in C_n^2 leads to a 1% perturbation in the flux. Also the sensitivity to l_0 is smaller than in the other methods: a 20% perturbation in l_0 leads to a 2% perturbation in the flux (l_0 is inversely related to u^* , but $L_\gamma E$ also to H). In fact, the weak sensitivity of C_n^2 and l_0 , reflects the weak influence of H on the flux.

An aspect that stands out in Figure 5.2 is that for the energy balance method the RMSE is typically not zero for the variables it is sensitive to. L_vE is the sum of three fluxes that vary in sign and phase. Therefore, an increase in H leads to a larger L_vE during the late afternoon, but a smaller L_vE during the day. Furthermore, during the transition time of a flux the influence of a perturbation on this flux will be negligible. The energy-balance method, thus, is sensitive to Q_{net} , H , and G , but their relative importance differs in time.

5.5. Validation of the combined methods with experimental data

This section discusses the flux validation results of the combined methods. We used averaging intervals of 30 min, so that we can assume that we can trust the eddy-covariance fluxes. Section 5.5.1 starts with an evaluation of the scintillometer input of the combined methods. That is, the area-averaged measurements of u^* and H . Then, in section 5.5.2, we evaluate the output of the combined methods. That is, L_vE and FCO_2 . Firstly, however, we make some general comments on the results.

The results in this study are obtained under conditions during which z/L_O typically varied between -0.4 and 0.1. These results are in principle valid for conditions with greater $|z/L_O|$ as well (Li et al., 2012). However, there are some exceptions. In case $|z/L_O|$ is large because of a large H , i.e. when $|\beta|$ or $|\alpha| \gg 1$, the methods will have difficulties in resolving L_vE and FCO_2 (Moene and Schüttemeyer, 2008), see also section 5.5.2. Furthermore, under dry, high H conditions saturation of the scintillometer signal can occur, i.e. when $B_{11} > \sim 0.3$ (Beyrich et al., 2012). To avoid saturation of the SLS signal, the path length should be sufficiently short or the measurement height sufficiently large. That is, with $z_{eff} = 2.0$ m saturation virtually will not happen for path lengths shorter than 150, whereas for path lengths of 300 m saturation can occur already when $H \geq 200 \text{ W m}^{-2}$.

5.5.1. Scintillometer u^* and H

Figure 5.3 shows the comparison between the scintillometer and the eddy-covariance system for u^* and H , after having corrected for the systematic errors. It can be seen that the scintillometer compares well with the eddy-covariance measurements. For u^* the data is on the 1:1 line, but more important, the correlation coefficient is 0.97.

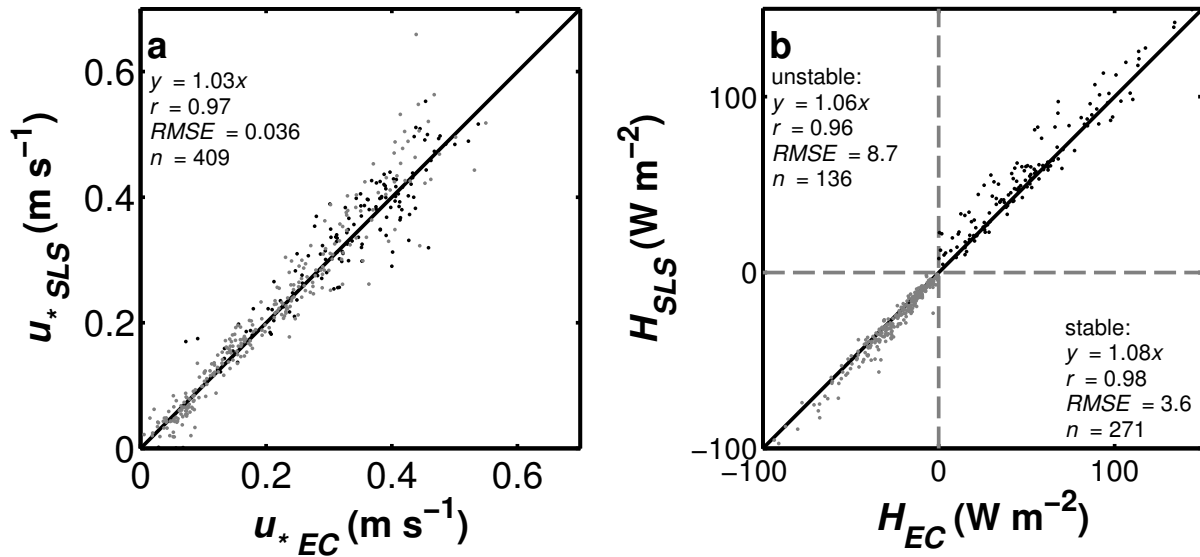


Figure 5.3: Comparison between scintillometer and eddy-covariance measurements for (a) u_* and (b) H . Each data point consists of 30-min statistics. The grey dots denote stable conditions and the black dots denote unstable conditions.

For H in unstable conditions the relationship is given by $H_{SLS} = 1.06H_{EC}$ and has a correlation coefficient of 0.96. For H in stable conditions the relationship is given by $H_{SLS} = 1.08H_{EC}$ and has a correlation coefficient of 0.98. For both u_* and H , the correlation coefficients are similar to De Bruin et al. (2002) and Rotach et al. (2004), who measured under similar circumstances, and better than Nakaya et al. (2006), Savage (2009), and Lüers and Bareiss (2011), who measured under more difficult circumstances. Moreover, these correlation coefficients are within the range of variability between eddy-covariance systems (Loescher et al., 2005; Mauder et al., 2006). Thus, for both u_* and H the scatter is low, which confirms that the scintillometer agrees excellently with the eddy-covariance method. Therefore, we conclude that after correcting for the systematic errors, the scintillometer measurements are suitable as input for the combined methods.

5.5.2. Fluxes of the combined methods

After having evaluated the scintillometer input of the combined methods in section 5.5.1, this section continues with the evaluation of the output. In Figure 5.4 and Figure 5.5 the fluxes from the combined methods are compared to the eddy-covariance fluxes. As such, Figure 5.4 depicts the results for $L_v E$ and Figure 5.5 depicts the results for FCO_2 .

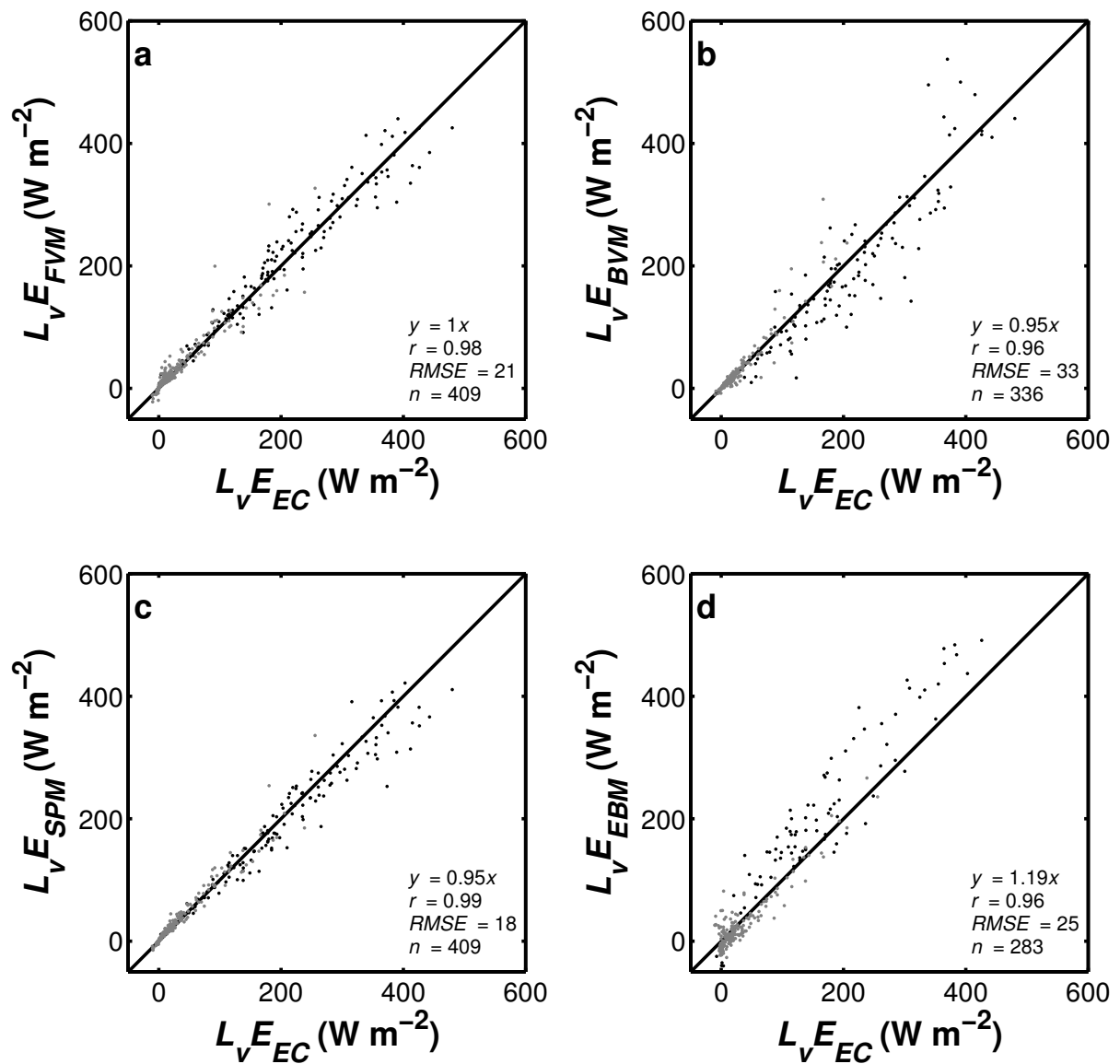


Figure 5.4: Comparison between combined methods $L_v E$ and eddy-covariance $L_v E$. (a) the flux-variance method (FVM), (b) the Bowen-variance method (BVM), (c) the structure-parameter method (SPM), and (d) the energy-balance method (EBM) for 30-min averaging intervals. The grey dots denote stable conditions and the black dots denote unstable conditions.

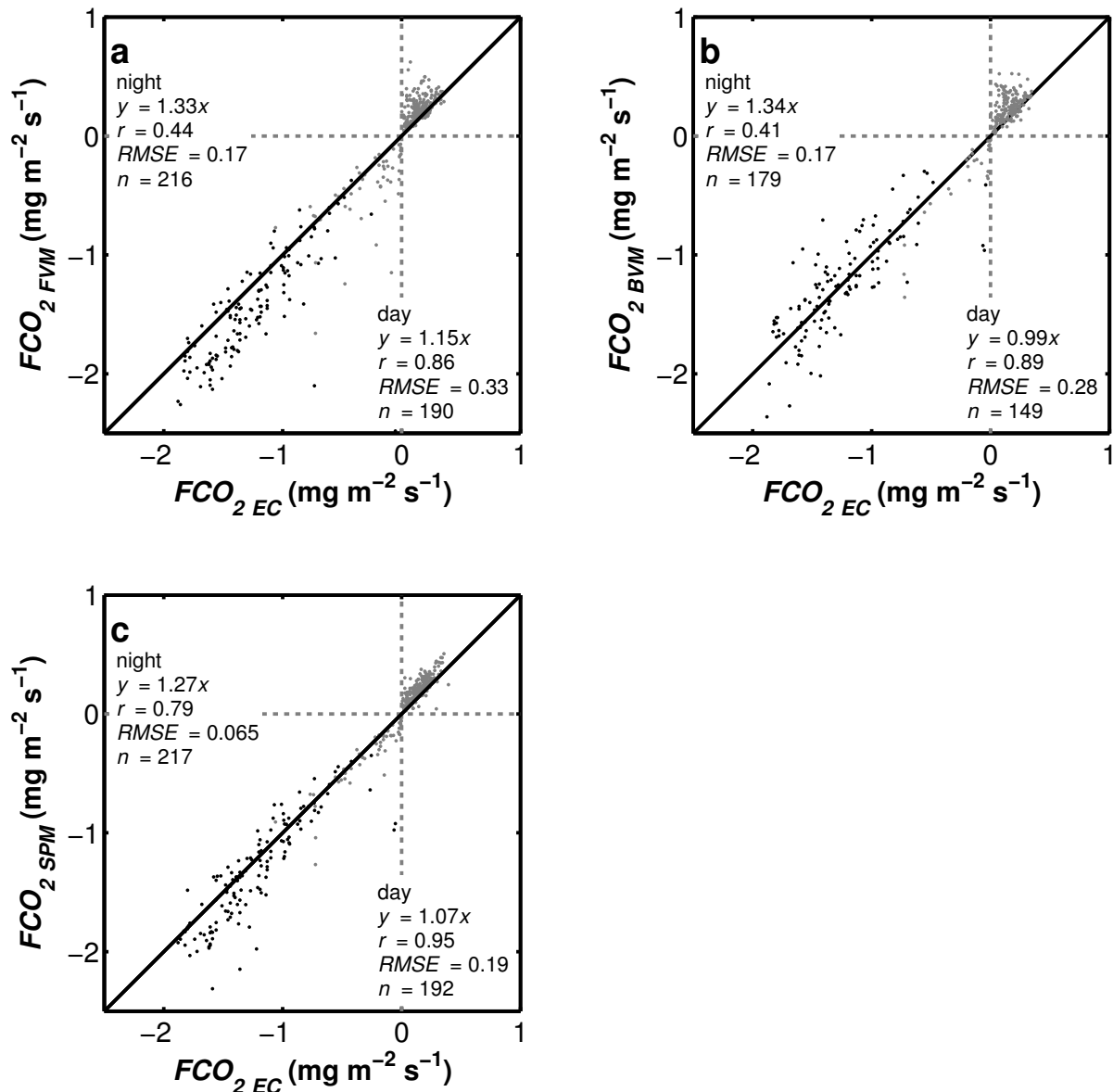


Figure 5.5: Comparison between combined methods FCO_2 and eddy-covariance FCO_2 . (a) The flux-variance method (FVM), (b) the Bowen-variance method (BVM), and (c) the structure-parameter method (SPM) for 30-min averaging intervals. The grey dots denote stable conditions and the black dots denote unstable conditions.

5.5.2.1. Flux-variance method

The first method that is considered is the flux-variance method: $L_v E$ is well reproduced by this method. The scatter is low, $r = 0.98$ and $RMSE = 21\ W\ m^{-2}$, and $L_v E$ is accurately estimated (the regression slope, $a = 1.00$). This comparison is excellent when compared with examples from the literature (Choi et al., 2004; De Bruin et al., 1993; Guo et al., 2009). Regarding FCO_2 , results are comparable with $L_v E$ for the daytime and the flux-variance method agrees well with the eddy-covariance method (Guo et al., 2009). The scatter is slightly larger than for

L_vE ($r_{day} = 0.86$ and $RMSE = 0.33 \text{ mg m}^{-2} \text{ s}^{-1}$) and FCO_2 is slightly overestimated ($a = 1.15$). The effect of humidity on L_O was found to be the largest for this method. Without the humidity correction both L_vE and FCO_2 are 5% smaller (not shown). For the night the method performs worse than for the daytime. The scatter is large ($r_{night} = 0.44$ and $RMSE = 0.17 \text{ mg m}^{-2} \text{ s}^{-1}$) and eddy-covariance FCO_2 is a factor, a , 1.33 smaller. To ensure that not a few outliers determine the regression statistics we take a confidence interval of 95%, which changes the regression statistics to $r_{night} = 0.68$ and $a = 1.22$. Hence, this method does not reproduce FCO_2 well for nighttime conditions.

This bad nocturnal performance occurs, because the CO_2 concentrations are not stationary for periods of 30 minutes, but rather for periods of 5 or 10 minutes (Foken et al., 2001). When taking 5-min averaging intervals, which subsequently are averaged (arithmetically) to 30-min means improves the regression statistics to (again with a confidence interval of 95%) $r_{night} = 0.80$ and $a = 0.95$. Hence, non-stationarity of the CO_2 signal negatively influences the flux-variance method for the nighttime.

Yet, when on the one hand considering nighttime data of the flux-variance method for H (derived similarly as for L_vE , results not shown), we find that the method performs much better than it did for FCO_2 , and even L_vE , for the nighttime. The correlation is high ($r = 0.92$ and $RMSE = 7.2 \text{ W m}^{-2}$, cf. Figure 5.3). So, for the night it appears that similarity theory for humidity and CO_2 is violated, whereas for heat it is not (Andreas et al., 1998; Moene and Schüttemeyer, 2008).

On the other hand, when considering daytime data of the flux-variance method for H (not shown), we find that the method performs slightly worse than for FCO_2 or L_vE . The correlation is lower ($r = 0.87$ and the $RMSE = 18 \text{ W m}^{-2}$). Moreover, the deteriorated regression statistics are caused by only 20% of the data points. In fact, these data points consist only of positive outliers and these outliers are caused by too large σ_T . So, it appears that during the day similarity sometimes is violated for σ_T , whereas for σ_q and σ_{qCO_2} it is not. This is exactly opposite to what we observe for the night. Nevertheless, the main conclusion is that the flux-variance method reproduces L_vE and FCO_2 well.

5.5.2.2. Bowen-variance method

The second method that is considered is the Bowen-variance method. This method has fewer samples than the flux-variance method, because we omitted data for $|r_{Tqx}| < 0.2$, and $|\beta| < 0.1$ and $|\alpha| < 1$.

L_vE is well estimated by this method. The scatter is low, $r = 0.96$ and $RMSE = 33 \text{ W m}^{-2}$, and the data is scattered around the 1:1 line. Although, the comparison is slightly worse than for the flux-variance method, it is a good comparison compared to examples from the literature (De Bruin et al., 1999; Nakaya et al., 2006). Regarding FCO_2 , results are comparable with L_vE for the daytime. The scatter is slightly larger ($r_{day} = 0.89$ and $RMSE = 0.28 \text{ mg m}^2 \text{ s}^{-1}$), but the data are scattered around the 1:1 line. The effect of humidity on L_O was found to be negligible for this method. Again, for the night the situation is worse. The scatter is large ($r_{night} = 0.41$ and $RMSE = 0.17 \text{ mg m}^2 \text{ s}^{-1}$) and FCO_2 is a factor 1.34 larger than eddy-covariance FCO_2 . To ensure that not a few outliers determine the regression statistics in Figure 5.5b, we take a confidence interval of 95%, which changes the regression statistics to $r_{night} = 0.67$ and $a = 1.27$. Similarly as the flux-variance method, taking 5-min averaging intervals, which subsequently are averaged to 30-min means improves the regression statistics to (again with a confidence interval of 95%) $r_{night} = 0.82$ and $a = 1.11$. Hence, non-stationarity negatively influences the Bowen-variance method too, which is similar to the flux-variance method, because they both use σ_q or σ_{qCO_2} .

Furthermore, non-stationarity slightly influences the daytime results of the Bowen-variance method. Using 10-min averaging intervals, which subsequently are averaged to 30-min means improves the regression statistics for both L_vE and FCO_2 . For L_vE the scatter reduces ($r = 0.98$ and $RMSE = 21 \text{ W m}^{-2}$) and the data scatters exactly around the 1:1 line ($a = 1.01$). Also for FCO_2 the scatter reduces ($r_{day} = 0.93$ and $RMSE = 0.21 \text{ mg m}^2 \text{ s}^{-1}$) and the data scatters around the 1:1 line ($a = 1.04$). Here, we see how important it is that similarity theory holds for both heat and the transported scalar. Non-stationarity of the temperature signal deteriorates the results for L_vE and FCO_2 for the Bowen-variance method, whereas for the flux-variance method heat is not of influence. Nevertheless, despite the small effects of non-stationarity, the Bowen-variance method reproduces L_vE and FCO_2 well.

Finally, a correct parameterization of the relative transport efficiency, λ_{Tqx} , proved to be important. Under ideal MOST conditions $\lambda_{Tqx} = 1$ (De Bruin et al., 1999; Hill, 1989), but this assumption did not hold for our dataset and led to a deviation in the order of 8% on both L_vE and FCO_2 . However, although we applied the (empirical) parameterizations, results still were improved by removing effects of non-stationarity. Improvements on good, theoretically based parameterizations would thus greatly help. Katul et al. (2008) lists five different reasons why dissimilarity occurs and the authors suspect that the success of a certain parameterization differs among the five causes for dissimilarity.

5.5.2.3. Structure-parameter method

The third method that is considered is the structure-parameter method. This method reproduces L_vE very well (cf. C_T^2 in De Bruin et al. (1999)) and improves even on the already excellent results of the flux-variance method. The scatter is low ($r = 0.99$ and $RMSE = 18 \text{ W m}^{-2}$) and L_vE is slightly underestimated ($a = 0.95$). Also FCO_2 is very well reproduced. The scatter is slightly larger than for L_vE ($r_{day} = 0.95$ and $r_{night} = 0.79$) and FCO_2 is slightly higher ($a_{day} = 1.07$ and $a_{night} = 1.27$). The effect of humidity on L_O was found to be smaller for this method than for the flux-variance method. Without the humidity correction both L_vE and FCO_2 are 2% and 3% smaller (not shown).

The big difference with the previous two methods is that the 30-min structure parameter still represents the turbulence well for the night. In this, we confirm Tatarskii (1961), that the structure parameter is less sensitive to non-stationarity than the variance or standard deviation. This is so because the structure parameter is defined for the inertial sub-range and observes only eddies up to the size for which it is evaluated (1 m in our case). By averaging 30 minutes at night, the flux-variance method and Bowen-variance method also observe the production range of the spectrum, i.e. the part of the spectrum that does not contribute to the flux in the surface layer. Hence, we conclude that the structure-parameter method works the best, because it is not affected by the non-stationarity that affects the results of the two variance methods.

5.5.2.4. Energy-balance method

The fourth and last method that is considered is the energy-balance method. It should be noted that this method has few data points, because the radiometers did not work for two weeks. This method performs slightly better than the Bowen-variance method. The scatter is low, $r = 0.96$ and $RMSE = 25 \text{ W m}^{-2}$, a rather good result compared to those in the literature (Ezzahar et al., 2007; Green et al., 1997; Savage, 2009). L_vE is overestimated by 19%, which is a typical value for the non-closure of the energy balance (Foken, 2008; Wilson et al., 2002). The effect of humidity on L_O was found to be negligible for this method.

Three aspects contribute to this non-closure. Firstly, that is the inaccuracy of the measured G . The plate was installed at 1 cm depth below the wheat. As we did not have additional soil-temperature measurements above the heat-flux plate we could neither correct G to its surface value, nor account for energy storage (heat) in the soil and vegetation (Jacobs et al., 2008; Liebenthal et al., 2005; Savage, 2009). Our data seem to indicate this as well. In

analysing the data, we found hysteresis. Morning values of L_vE from the energy-balance method were typically higher than afternoon values for a given value of L_vE from the eddy-covariance method. These afternoon data (measured after 14:00 UTC) fit the 1:1 line (not shown). So, probably, in the afternoon the plants and soil are already heated up and storage changes above the heat-flux plate are expected to be minimal.

The second aspect considers footprint issues. It is questionable whether the measured G at one location is representative for the whole field, given the variability of soil-thermal properties (Ezzahar et al., 2007; Liebethal et al., 2005; Savage, 2009). Even though a 20% error in G has hardly any effect on L_vE for most time of the day (see error analysis), it can affect the closure, especially when Q_{net} and H are small (Liebethal et al., 2005). In a similar way it is challenging to obtain a spatially reliable average of the radiation (Savage, 2009). However, because the radiometers were installed at 2 m above the ground, the footprint is already more representative for the whole field than that of G .

A final aspect we want to mention is that FCO_2 is small, but not completely negligible. Figure 5.5 shows that daytime FCO_2 typically is $-1.5 \times 10^{-6} \text{ kg m}^{-2} \text{ s}^{-1}$. By applying the photosynthetic efficiency of $11 \times 10^6 \text{ J kg}^{-1}$ (Guo et al., 2009; Jacobs et al., 2008) we find that this typical value corresponds to an energy flux of -16.5 W m^{-2} . That is approximately 5% of the measured L_vE ($\approx 400 \text{ W m}^{-2}$). These aspects underline that even though the method in itself is simple, the method is challenged by the fact that not all energy-balance terms are taken into account and that there are large differences in footprint between Q_{net} , H , and G .

5.6. Conclusions

This chapter discussed the performance of four combined methods for estimating L_vE and FCO_2 . The essence of these combined methods is that the scintillometer measures the area-averaged parameters of the atmospheric turbulence (the transport mechanism) and that the additional measurements provide a turbulence statistic of the scalar quantity that is transported. The combined methods that were discussed were the flux-variance, Bowen-variance, the structure-parameter, and the energy-balance methods. Data were gathered in the framework of the Transregio32 project in a wheat field near Merken (Germany) and scintillometer and eddy-covariance measurements were performed. Furthermore, the scintillometer measurements were corrected for systematic errors in both C_n^2 and l_0 .

Based on the measured data, we performed a sensitivity analysis that showed four things. Firstly, large RMSE for the Bowen-variance method and the energy-balance method

shows that the relative importance of some of the turbulence variables varies strongly during the day. Secondly, it is important to accurately determine the effective measurement height of the scintillometer, as well as the height of the turbulence measurements of the scalar quantities (in this study they are equal). Thirdly, fluxes hardly showed any response when perturbations were made on the mean-state variables, whereas fluxes showed a clear response when perturbations were made on the turbulence variables. So, the combined methods accurately estimate the flux, because they correctly represent the atmospheric turbulence. Fourthly, all the methods are most sensitive to u_* , rather than to C_n^2 . This illustrates the importance of shear over buoyancy close to the surface and emphasizes the importance of accurate measurements of u_* .

Subsequently, the combined-methods were validated with eddy-covariance fluxes, having 30-min averaging intervals in order that we could trust the eddy-covariance fluxes. Firstly, the energy-balance method reproduces L_vE reasonably well (large correlation). However, the method fails in predicting the correct magnitude of L_vE , because the energy balance does not close. Likely, the non-closure is caused by neglecting FCO_2 , the storage above the heat-flux plate, and the storage in the vegetation. In principle the energy-balance method is a simple method, but the method is challenged by the fact that not all energy-balance terms are taken into account and that there are large differences in footprint between Q_{net} , H , and G .

Secondly, the flux-variance method and Bowen-variance method reproduce the fluxes well. Both methods are similar in that they use the standard deviation of the scalar quantity to represent the turbulence. Both methods suffered from non-stationarity during the night. The comparison to eddy-covariance fluxes was improved by shortening the averaging time to 5 min. Furthermore, the Bowen-variance method suffered also from non-stationarity in the temperature signal for 20% of the daytime. Here too, shortening the averaging interval (to 10 min) improved the comparison to eddy-covariance fluxes. Generally, however, both methods reproduce L_vE and FCO_2 well.

Thirdly, the structure parameter method performs best of all combined methods. The method reproduces the fluxes excellently, both for day and night. The structure parameter is not sensitive to the non-stationarity from which the variance methods suffered, making this method more robust than the two variance methods.

Finally, in this study we used the eddy-covariance fluxes to determine the sign in order to prevent getting distracted from the methodology. However, in Appendix A it is shown that

by using the correlation coefficients good estimates can be made of the flux direction and stability. Only in about 5% of the cases this leads to different flux or stability estimations.

Appendix A: Estimating stability and the sign of the flux

One of the challenges when using scintillometry is to obtain the direction of the flux. Scintillometry uses the assumption of local isotropy, which eliminates all the information about the direction of the flux. To overcome this challenge the surface-layer scintillometer can be extended with temperature measurements to estimate the temperature gradient, from which the sign of H can be deduced (Lüers and Bareiss, 2011; Scintec, 2006). However, when using the combined methods one also has to determine the sign of L_vE and FCO_2 .

We therefore introduce a method that can be used with only one additional thermocouple next to the measurements of humidity and CO_2 that are already done. This method uses the correlation between temperature and humidity or CO_2 concentration (r_{Tq} and r_{TqCO_2}) to derive the sign of the flux.

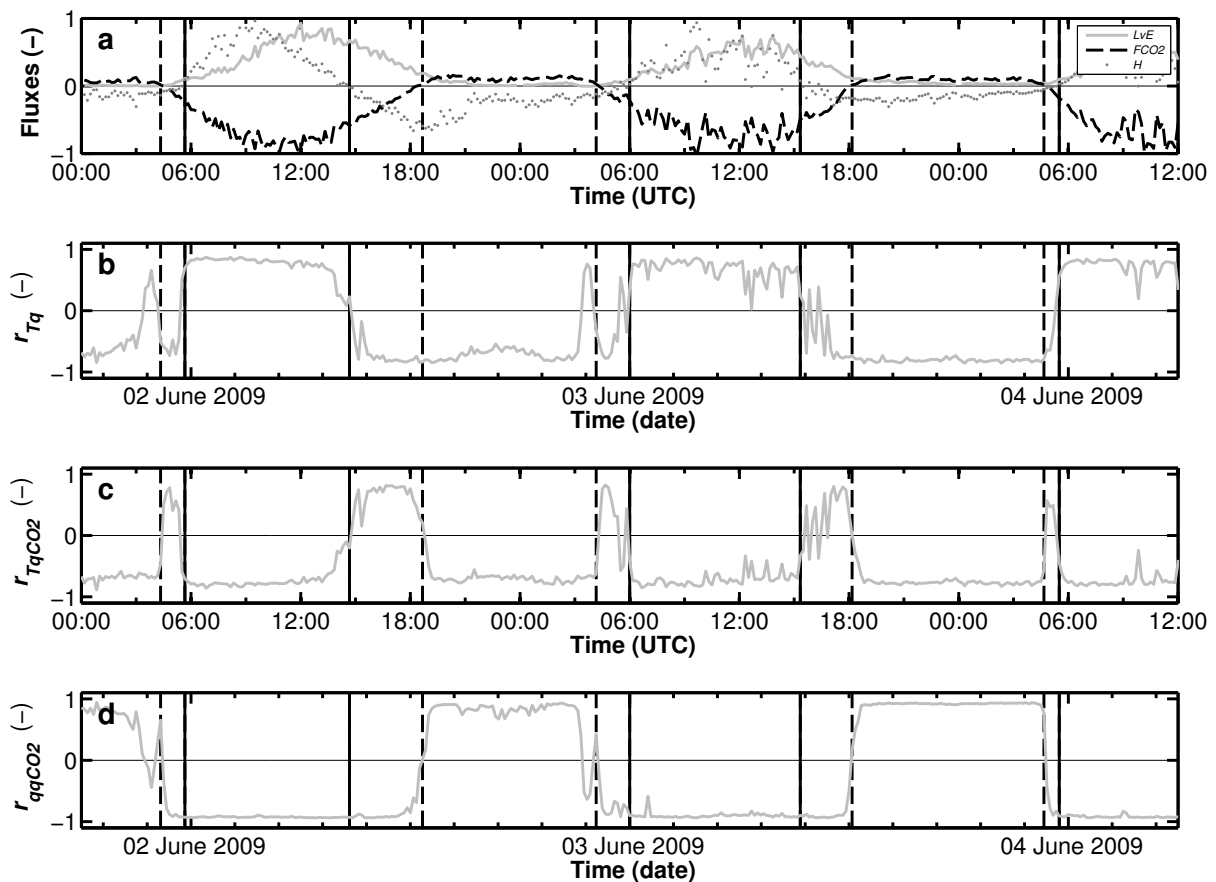


Figure 5.6: Normalized eddy-covariance fluxes compared with r_{Tq} , r_{TqCO_2} , and r_{qqCO_2} for 10-min averaging intervals. Fluxes were normalized with respect to their maximum value during the observed period.

Figure 5.6 illustrates how it works. The upper panel shows H , L_vE , and FCO_2 from the eddy-covariance measurements. L_vE is positive most of the time, except for some cases of dewfall. During stable conditions H is negative, whereas during unstable conditions H is positive. For FCO_2 it is exactly the other way around. During the night FCO_2 is positive (respiration), whereas during the day it is negative (photosynthesis). The thick lines indicate the moments at which H changes sign and the dashed lines indicate the moments at which FCO_2 changes sign.

In the second pane r_{Tq} is shown. As can be seen r_{Tq} is positive during the day and negative during the night, assuming that L_vE always is positive implies that H is positive during the day and negative during the night. However there are also two short events that occur on the 2nd and 3rd of June around 4:00 UTC during which r_{Tq} becomes positive. During both events H does not change sign, but L_vE changes sign, i.e. dewfall occurs. As this downward flux is very small ($L_vE \approx -3 \text{ W m}^{-2}$) it is hardly noticeable, but this sign change leads to a wrong sign estimation of H . Dewfall is the only situation during which L_vE becomes negative and can easily be filtered out. We use an algorithm that considers the solar elevation (Stull, 2000) and r_{qqCO_2} . When the sun's elevation angle is lower than 7 degrees H usually is not positive (Holtslag and Van Ulden, 1983). Therefore, before the elevation angle of the sun is higher than 7 degrees, dew fall must occur when positive r_{Tq} occurs simultaneously with negative r_{TqCO_2} and r_{qqCO_2} .

After determining the sign of H and L_vE , the sign of FCO_2 can be determined as well. In principle FCO_2 and H are always opposing each other. However, in the third pane there are some moments where r_{TqCO_2} is positive. If, H and FCO_2 were in the same phase, then r_{TqCO_2} would never be positive, making the sign determination more difficult. In that case, information about r_{qqCO_2} must be used. Of course, one can also use radiation measurements to determine the sign of FCO_2 , but then radiometers are required.

We applied the sign determining method to the data for 30-min averaging intervals and 1-min averaging intervals and subsequently compared it with the sign of the eddy-covariance fluxes. Firstly, for H , 21 out of 400 data points (5%) and 454 out of 14764 data points (3%) were estimated differently. Secondly, for L_vE 24 out of 409 data points (6%) and 560 out of 15172 data points (4%) were estimated differently. Thirdly, for FCO_2 31 out of 406 data points (7%) and 580 out of 15150 data points (4%) were estimated differently. These results show that by using the correlation coefficients of variables that are already measured, the sign of the fluxes can be estimated.

6. Measuring H₂O and CO₂ fluxes at field scales with scintillometry: Part II – evapotranspiration for 1-30 minute averaging intervals⁵

6.1. Introduction

The eddy-covariance method is used worldwide for measuring evapotranspiration (Baldocchi, 2003; Shuttleworth, 2007). This method, which uses point-sampling measurements, typically measures evapotranspiration on field scales (50 m – 200 m). Furthermore, the eddy-covariance method obtains flux information over averaging intervals as short as 10 minutes, but typically 30-60 minutes (Hartogensis et al., 2002; Mahrt, 2010; Sun et al., 2005). During the averaging period, the turbulence is required to be stationary. This condition is violated for several common events such as rapidly changing cloud cover or intermittent turbulence.

Scintillometers estimate spatially averaged fluxes (100 m – 5000 m) and literature shows that displaced-beam laser scintillometers can accurately determine fluxes for averaging intervals shorter than 1 minute (Hartogensis et al., 2002; Wyngaard and Clifford, 1978). Consequently, scintillometry does not require turbulence to be stationary over periods of 10-30 minutes. Scintillometer systems that measure evapotranspiration on large scales (> 1 km) are available (Evans, 2009; Green et al., 2001; Meijninger et al., 2006), but unfortunately these systems cannot be operated on field scales (< 500m), i.e. over single crop fields.

In part I of this study (Van Kesteren et al., 2012a), we introduced and validated four methods for averaging intervals of 30 minutes, which can determine evapotranspiration and other passive-scalar fluxes on field scales. They combine estimates of stability and friction velocity from the displaced-beam laser scintillometer with additional turbulence measurements of humidity or CO₂ to estimate the fluxes. These so-called combined methods are called the flux-variance method, the Bowen-variance method, the structure-parameter method, and the energy-balance method.

The aim of this part, part II, is to apply the spatial-averaging advantages of scintillometry to the four combined methods, so to evaluate evapotranspiration over short averaging intervals (~ 1 min). Therefore homogeneous conditions are required, which is ensured by limiting the application of the methods to single crop fields. The motivation to

⁵ This chapter is part of **Van Kesteren, B.**, Hartogensis, O.K., van Dinter, D., Moene, A.F., De Bruin, H.A.R., and Holtslag, A.A.M., 2012, *Measuring H₂O and CO₂ fluxes at field scales with scintillometry: Part II – application and validation of 1-min flux estimates*, Agric. Forest Meteorol., conditionally accepted

explore these relatively short flux-averaging intervals is that it provides us with a detailed mass-flux description in non-stationary circumstances. Consequently, with methods that can measure 1-min fluxes, turbulent exchange of vegetation with the atmosphere can be studied under natural, often non-stationary conditions (e.g. (Foken et al., 2001)). Furthermore, detailed, short-interval mass fluxes will teach us about plant behaviour in a natural environment and thus add to the highly controlled laboratory experiments that are usually performed on plants (e.g. (Cardon et al., 1994)). Moreover, by reducing the averaging time the flux comparison with snap-shot remote-sensing estimates can be improved. This improvement can especially be achieved in non-stationary conditions, when the snapshot of the satellite does not represent the 15-30 minute flux data (Bastiaanssen et al., 1997). A similar argument holds for the validation and performance of hydrological/meteorological models. Models with fine horizontal or vertical resolution need to be operated with small time steps in order to keep the models stable. At present, these models are confronted with 15-30 minute averaged fluxes, which partly conceals the qualities of/uncertainties in the models.

This chapter elaborates on part I and explores the possibilities of studying evapotranspiration, presented in terms of latent heat, on time intervals as short as 1 minute. At present, there are no direct flux-validation methods for 1-min averaging intervals. So, to evaluate the performance of the combined methods on these short averaging intervals, we will follow two alternative approaches. First, we will test the accuracy of the 1-min flux estimates with an extensive error analysis. The error analysis is based on the error concepts of Lenschow et al. (1994), who show that the estimated fluxes differ systematically and randomly from the “ideal” ensemble average of a flux, when the averaging time is not “long enough”. We will determine these random and systematic errors for averaging intervals varying from 1 to 30 minutes. Second, we will estimate the accuracy of the 1-min averaged flux estimates by evaluating their reaction to rapid changes in the forcing of the latent-heat flux. Net radiation is the energy available for the latent-heat flux and therefore is suitable to serve as a reference variable. In theory, the Penman-Monteith model (Monteith, 1965) would be the ideal validation method. However, in practice this model is limited because it assumes a closed energy balance, and requires an accurate description of the canopy resistance and of the roughness length for heat. Nevertheless, the Penman-Monteith model still is a more comprehensive validation method than net radiation.

Two more aspects need to be considered in this study. First, Andreas et al. (2003) question the averaging advantage of scintillometers over point-sampling measurement techniques and the applicability of Monin-Obukhov similarity functions on short averaging

intervals. Wyngaard and Clifford (1978) and Hartogensis et al. (2002) show that scintillometers do have an averaging advantage over point-sampling measurement techniques. Nevertheless, in the error analysis we will address both questions of Andreas et al. (2003) and show that accurate estimates of the latent-heat flux can be obtained, even over short averaging intervals. The second aspect considers the question of plant physiology. Can plants (in our case wheat) physiologically react as fast as 1 minute to changes in external forcings? In the flux validation, we will address this question and discuss the influence of a variable stomatal size on the latent-heat flux.

6.2. Theory and methods

6.2.1. Eddy covariance and scintillometry

The eddy-covariance method estimates the flux from high-frequency measurements of vertical wind speed and scalar concentration. Scintillometers determine the friction velocity and sensible-heat flux via turbulence induced scattering of their beams, using wave-propagation theory and Monin-Obukhov similarity theory, see section 5.2. In the introduction, we argued that scintillometers perform better than the eddy-covariance method in estimating the ensemble-averaged fluxes over shorter averaging intervals. There are two reasons for this. First, contrary to the eddy-covariance method, scintillometers do not need to capture all flux-transporting scales of the co-spectrum of scalar and vertical wind speed. The displaced-beam laser scintillometer only observes eddies that are of similar size as its first Fresnel zone (for the current set-up ~ 9 mm). Turbulence theory describes how these eddies relate to the other eddies in the turbulence spectrum (Hartogensis et al., 2002; Thiermann and Grassl, 1992; Van Kesteren et al., 2012a). Second, the number of independent samples per unit time observed by the scintillometer is larger than that of a point-sampling measurement, because scintillometers average both over space and time, whereas the point-sampling measurements only average over time. Therefore, provided the conditions are homogenous, scintillometers require significantly less averaging time (only $\sim 1\%$) than eddy-covariance systems for acquiring accurate measurements (Hartogensis et al., 2002; Wyngaard and Clifford, 1978) (cf. section 6.4.1).

6.2.2. Combined methods

The displaced-beam laser scintillometer can determine u^* and H , but not the latent-heat flux, $L_v E$. To extend the optical-scintillometer application to mass fluxes Van Kesteren et al. (2012a) proposed four methods that combine scintillometer measurements with additional turbulence measurements of humidity or CO_2 . These methods are called the flux-variance method, the Bowen-variance method, the structure-parameter method, and the energy-balance method. For a detailed description of the combined methods, we refer to Part I. Here, we only give an overview of the turbulent variables used in the methods (see Table 6.1)

Table 6.1: The turbulence variables of the scintillometer and additional turbulence measurements to calculate $L_v E$ with the four combined methods.

Method	Scintillometer measurements	Additional point-measurements
Bowen-variance	H	σ_T, σ_q and r_{Tq}
Flux-variance	u^* and L_O	σ_q
Structure-parameter	u^* and L_O	C_q^2
Energy-balance	H	Q_{net} and G

* L_O is the Obukhov length, σ_T is the standard deviation of temperature, σ_q is the standard deviation of humidity, r_{Tq} is the correlation coefficient of temperature and humidity, C_q^2 is the structure parameter of humidity, Q_{net} is the net radiation and G is the soil-heat flux.

6.2.3. Validation methods

It is a challenge to come up with a proper validation method for 1-min averaged fluxes. Direct methods that accurately measure $L_v E$ over 1-min averaging intervals are lacking. Here, we propose two methods to validate the combined methods. The first method uses error analysis for validation and the second method uses a reference variable for validation, i.e. net radiation. Both methods are described below.

6.2.3.1. Error analysis

Measurement errors are quality parameters that specify the accuracy of a measurement and consequently they can serve to validate the combined methods. The error analysis we apply uses the error concept of Lenschow et al. (1994), who show that the estimated fluxes differ systematically and randomly from the “ideal” ensemble average of a flux, when the averaging time of the flux is not “long enough”. This error applies to statistical moments of any order,

but for our application only second order moments are important, i.e. fluxes (covariance between vertical wind speed and a given variable) and variances (a covariance of a variable with itself).

Figure 6.1 shows a theoretical time spectrum of a (co)variance. For the systematic error (Figure 6.1a), averaging not “long enough” results in the exclusion of some larger relevant eddy scales from the record (as indicated by the hatched area in Figure 6.1a). Consequently, the (co)variance is systematically underestimated. For the random error (Figure 6.1b), averaging not “long enough” results in too few independent samples to accurately determine the spectral intensity (the uncertainty is indicated by the thin lines). Consequently, the (co)variance has a random error.

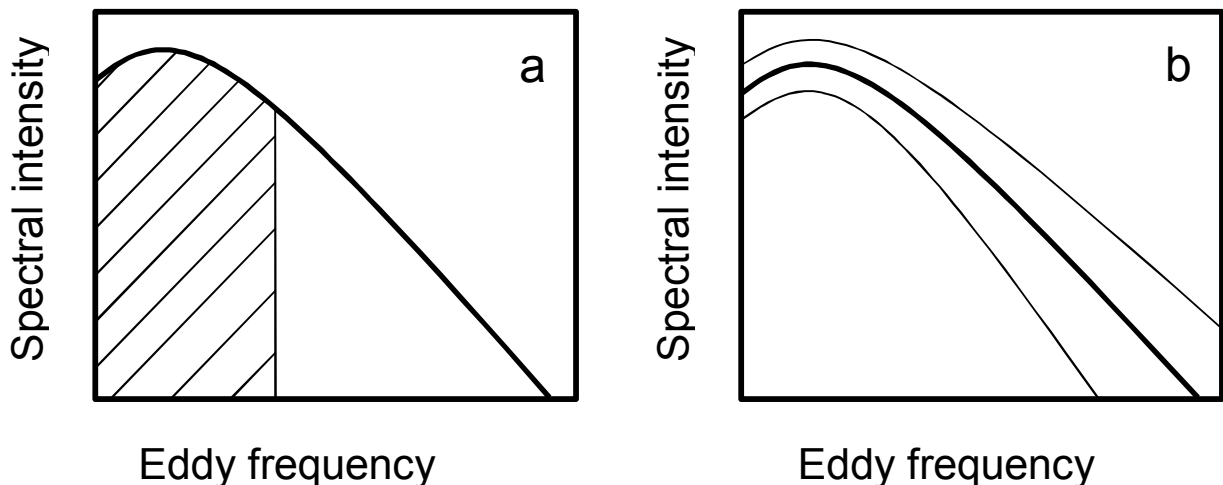


Figure 6.1: Theoretical spectrum to indicate (a) the systematic error and (b) the random error. The errors occur, because in both cases the averaging time is not long enough. For the systematic error this results in missing large eddies (the hatched area) and an underestimation of the (co)variance. For the random error this results in having too few independent samples and a larger uncertainty (thin lines). All figure axes are logarithmic.

Systematic errors

To determine the systematic error in $L_v E$ from the combined methods and eddy-covariance method, we use an averaging method similar to Sun et al. (2005). This method gives an estimate of the systematic error by comparing 30-min arithmetic means from $L_v E$ with averaging intervals shorter than 30 minutes to their corresponding $L_v E$ with 30-min averaging interval. We introduce the relative systematic error

$$SE_i = \frac{\bar{x}_i^{-30}}{x_{30}} - 1, \quad (6.1)$$

where SE_i is the systematic error for a given averaging interval i , x_i is the flux with averaging interval i ($i = 1, 2, 3, 4, 6, 20$, or 15 min), x_{30} is the flux with 30-min averaging interval, and \bar{x}_i^{-30} the 30-min arithmetic mean of $30/i$ x_i 's. From rewriting Eq. (6.1) to $\bar{x}_i^{-30} = (SE_i + 1)x_{30}$, it follows that the relative systematic error can be obtained from the regression slope of x_{30} with their corresponding \bar{x}_i^{-30} .

The method described above considers discrete averaging intervals. A comparable, but continuous approach is the Ogive technique (Foken et al., 2006; Oncley et al., 1996). An Ogive is a cumulative integral of a time (co)spectrum and can be used for studying the systematic error in a (co)variance as a function of the continuous averaging interval. This follows from the fact that the integral of a (co)spectrum equals the (co)variance (Stull, 1988). With the Ogive approach, the systematic error is defined as

$$SE_i = \frac{\int_{f_{av}}^{\infty} S df}{\int_{f_{30}}^{\infty} S df} - 1, \quad (6.2)$$

where S denotes the (co)spectrum, f is the frequency, f_{av} is the frequency corresponding to a given averaging interval $f_{av} = 1/T_{av}$, and f_{30} is the frequency corresponding to an averaging interval of 30 min.

The Ogive approach cannot be used for determining the systematic error in $L_v E$ estimated with the combined methods. However, the approach can be used for determining the systematic error in the (co)variances that serve as additional measurements for the combined methods (Table 6.1). For most input variables the application of the Ogive technique is obvious, but for C_q^2 it is not. In the following, we will therefore explain more about C_q^2 .

C_q^2 , is a spatial statistic, denoting fluctuations between two fixed points in space, and relates to the structure function by (Tatarskii, 1961)

$$C_{q^2} = D_q^2 r^{-2/3} = \overline{[q(y) - q(y+r)]^2} r^{-2/3}, \quad (6.3)$$

where D_q^2 is the structure function of humidity, $\Delta q = q(y) - q(y+r)$ is the difference in humidity between position y and $y+r$, and the over-bar represents an average over the averaging time, T_{av} . The structure parameter can be determined from one time series by using Taylor's frozen turbulence approximation, so that $r = U\Delta t$, with U the mean wind speed and Δt the time difference between two measurements. When applying Reynolds decomposition to Eq. (6.3) it is important to realize that if $T_{av} \gg U\Delta t$, i.e. when the assumption of local isotropy holds, then $\overline{q(Ut)} = \overline{q(Ut + U\Delta t)}$. In that case, D_q^2 for a given r can be written as

$$D_q^2 = \overline{[q(Ut) - q(Ut + U\Delta t)]^2} = \overline{[q(Ut) - q(Ut + U\Delta t)]^2} = \overline{[\Delta q(Ut)]^2}, \quad (6.4)$$

where Δq now denotes the temporal difference in humidity. To understand the application of the Ogive technique to C_q^2 , it is important to note that $\overline{[\Delta q(Ut)]^2}$ is the variance of Δq . Therefore, applying the Ogive technique on Δq is to D_q^2 and hence C_q^2 , as applying the Ogive technique on q is to σ_q . This will allow us to determine also the systematic error of C_q^2 .

Random errors

To determine the random error in $L_v E$ from the combined methods and eddy-covariance method, we use a method that considers discrete intervals. This method gives an estimate of the random error, by determining the fluctuations in $L_v E$ with averaging intervals shorter than 30 minutes normalized to their corresponding 30-min arithmetic mean. By normalizing to the 30-min arithmetic mean, we avoid the influence of the systematic error on the random error estimate. The random error is determined for cloud free conditions only. As long as the plants are not stressed and the stomata fully open, we can expect $L_v E$ (and also H) to perfectly follow the sine pattern of the diurnal cycle, so that any observed fluctuation can be attributed to the random error.

We introduce the relative random error

$$RE_i = \sqrt{\frac{1}{N} \sum_{i=1}^N \left(\frac{x_i}{x_i^{-30}} - 1 \right)^2}, \quad (6.5)$$

where RE_i is the random error for a given averaging interval i , x_i is the flux with averaging time i , x_i^{-30} the 30-min mean of 30/ i x_i 's to normalize x_i , and N the number of flux samples.

With the combined methods, we calculate L_vE from measured variables that each has a random error. These variables are $K_{q, meth}$, which is the turbulent exchange coefficient of the method, and the statistical humidity variable, $st(q)$, which is σ_q for the Bowen-variance and flux-variance methods, and C_q^2 for the structure parameter method (Van Kesteren et al., 2012a). The relative random error in L_vE is determined by the relative random error in $K_{q, meth}$ and $st(q)$ as

$$\frac{\Delta L_vE}{|L_vE|} = \sqrt{\left(\frac{\Delta K_{q, meth}}{|K_{q, meth}|} \right)^2 + \left(0.5 \frac{\Delta st(q)}{|st(q)|} \right)^2}. \quad (6.6)$$

For the energy-balance method, absolute errors need to be considered

$$\Delta L_vE = \Delta Q_{net} - \Delta H - \Delta G. \quad (6.7)$$

We want to reduce the random error in L_vE by using the highly accurate measurements of the scintillometer, which define $K_{q, meth}$ in Eq. (6.6) and H in Eq. (6.7). In section 6.4.1.2, we discuss the effects of the errors in the measurements on the random error in L_vE .

6.2.3.2. Radiative forcing

The second validation method is an evaluation with Q_{net} . Over well watered crops, fully covering the soil, Q_{net} is the main variable driving L_vE (De Bruin, 1987; Priestley and Taylor, 1972), since under these conditions H and G are relatively small. The radiometers have a time response of typically 5-10 seconds and they can therefore accurately resolve variations in Q_{net} with time scales of one minute.

Thus, Q_{net} can be used as a reference for validating the 1-min L_vE from the combined methods. Q_{net} itself is of course not an absolute measure of L_vE , but it can be seen as a relative

reference in the sense that changes in Q_{net} should be followed by changes in L_vE , also on short, 1-min time scales. We will use the correlation coefficient of Q_{net} against L_vE to quantify the response of L_vE to changes in Q_{net} .

The Penman-Monteith method is a more comprehensive model to approximate the fluctuations in L_vE than Q_{net} , because fluctuations in L_vE are not only determined by Q_{net} , but also by G , vegetation, and the water-vapour deficit (Monteith, 1965). The model is given by

$$L_vE_{PM} = \frac{s(Q_{net} - G) + \frac{\rho c_p (\overline{e_{sat}} - \overline{e_a})}{r_a}}{s + \gamma \left(1 + \frac{r_c}{r_a}\right)}, \quad (6.8)$$

where s , is the slope of the saturated water-vapour pressure curve, e_{sat} is the saturated water-vapour pressure for a given temperature, e_a is the actual water-vapour pressure, γ is the psychrometric constant, r_a is the aerodynamic resistance, and r_c the canopy resistance. The water-vapour deficit is $\overline{e_{sat}} - \overline{e_a}$ and $r_a = [\ln(z_{eff} / z_{0\theta}) - \Psi(z_{eff} / L_0) + \Psi(z_{0\theta} / L_0)] / k_{kar} u^*$, with the Ψ -functions for heat from Businger-Dyer (Businger et al., 1971; Paulson, 1970) and $z_{0\theta}$ the roughness length of heat. $z_{0\theta}$ is estimated as 1/10 of the roughness length of momentum, which in turn is estimated as 1/8 of the vegetation height (Green et al., 1994).

The Penman-Monteith model provides a direct estimate of L_vE , but for our study where we look at 1-min L_vE estimates, it cannot be used as an absolute reference. Instead, we will use it only as a relative measure, as we did with Q_{net} .

The reason why the model can only be used as relative measure of L_vE is that two assumptions embedded in the model are violated in this study. First, the model assumes the energy balance to close on H , G , and L_vE . However, in part I we show a non-closure of 19% of the energy balance, because the carbon dioxide flux and storage terms that account for the height differences of the measurements are not taken into account (Van Kesteren et al., 2012a). Moreover, these storage terms are not constant throughout the day, but can vary greatly. Second, the model requires a detailed description of the canopy resistance, r_c , and of the roughness length for heat. Especially the dynamic behaviour of r_c on 1-min time-scales is not well parameterised and we therefore used a constant value of 50 s m^{-1} (Kelliher et al., 1995).

6.3. Experimental set-up and data treatment

Data used in this study were gathered in the framework of Transregio32 project (Graf et al., 2010). The measurements took place in a winter-wheat field near Merken, Germany (50° 50' 53.92" N, 6° 24' 1.99" E) between 7 May and 10 June 2009. The dimensions of the field were 350 m by 150 m. In the middle of the field, an eddy-covariance system, consisting of a CSAT3 sonic anemometer (Campbell Scientific, Logan, USA) and a LiCor7500 H₂O/CO₂ sensor (LiCor, Lincoln, USA), were installed 2.40 m above ground level. Approximately 20 m west of the eddy-covariance tower, we installed a displaced-beam laser scintillometer (SLS-20, Scintec, Rottenburg Germany) at exactly the same height as the eddy-covariance system, with the middle of the scintillometer path centred at the tower. The scintillometer was installed at 2.40 m above ground level as well and had a path length of 120 m. The effective height of the scintillometer linearly decreased from 2.11 m at the beginning of the experiment to 1.84 m at the end of the experiment, due to the growing crop. Long-wave and short-wave radiation were measured at 2 m height in the EC tower with a four component net-radiation meter, NR01 (Hukseflux, Delft, the Netherlands). During the measurement period, the average temperature was about 15 °C. The amount of precipitation was 60 mm. Furthermore, during daytime the Bowen ratio, β , was generally smaller than 0.6 and z/L_0 typically varied between -0.4 and 0.1. Consequently, the wheat was well watered and green during the whole measurement period. For more details about the other measurements and specific set-up features we refer to part I of this study (Van Kesteren et al., 2012a).

All data were processed in the same way as described in part I of this study (Van Kesteren et al., 2012a), with two differences. Firstly, the eddy-covariance data were processed using the processing package ECPack from Wageningen University (Van Dijk et al., 2004), for averaging intervals of 1, 2, 3, 4, 6, 20, 15, and 30 minutes. Secondly, the scintillometer measurements were processed for the same averaging intervals.

The data for the validation with the error analysis is obtained in the following way. To estimate the relative systematic error, we first determine \bar{x}_i^{-30} and x_{30} for each half hour in the data set and subsequently apply linear-regression analysis to determine the regression slope (forced through origin and with a confidence interval of 95%). In addition, the root-mean-squared error (RMSE) of the regression is determined to indicate the accuracy of the error estimate. The larger the RMSE, the less representative the slope is for the systematic error.

To determine the systematic error with the Ogive technique, we used the raw, high-frequency eddy-covariance data to which no corrections have been applied yet. Therefore, we

corrected these data for the humidity influence on sonic temperature in order to determine the specific humidity from the absolute humidity (Schotanus et al., 1983). Other corrections were not applied, because they only affect the small scales (high frequencies) or wind measurements. This is an adequate approach, because small scale errors cancel out when considering the relative errors and for the wind we only need an estimate of its mean value. Furthermore, these corrected data were divided in data blocks of four hours instead of 30 minutes, to improve the estimate of the spectral intensity at 30 minutes (Foken et al., 2006). Finally, we determined the systematic error for all four-hour blocks in the whole data set.

To estimate the relative random error, we determine $\overline{x_i^{-30}}$ and x_i for all cloudless conditions. $\overline{x_i^{-30}}$ is determined such that the corresponding x_i is located at the centre of this 30-minute interval. Furthermore, for this analysis data were omitted when $L_v E$ of the method in question was lower than 30 W m^{-2} .

The data for the validation with the Penman-Monteith model is obtained in the following way. This validation is done for the complete data set. To avoid the situation that the diurnal cycle primarily determines the regressions statistics, we divide the data set into periods of two hours and omit some of the data. Data are omitted when Q_{net} was not affected by clouds during a period of two hours, when $L_v E_{PM} < 10 \text{ W m}^{-2}$, or when for a 2-hour period 60% or more of its data is missing. For the remaining data, we determine the correlation and RMSE over each 2-hour period. Subsequently, the correlations and RMSEs obtained from the 2-hour periods are averaged in order to get one value for the whole data set.

6.4. Results and discussion

6.4.1. Error analysis

Lenschow et al. (1994) showed that averaging not “long enough” results in an averaging-time-dependent systematic error (underestimation) because of missing larger eddies and a random error (uncertainty) because of having too few independent samples. In this section, we show the results of an error analysis to investigate how well each method approaches the ensemble averaged $L_v E$, as estimated by its 30-min averaged $L_v E$, for short averaging intervals.

6.4.1.1. Systematic errors

This section shows the results of the systematic error analysis. Firstly, the results of the systematic error in $L_v E$ are shown for all methods. Subsequently, it is discussed that the methods achieve their accuracy by using scintillometer (scinti) estimates of H , u^* and L_O instead of eddy-covariance (EC) estimates of H , u^* and L_O . Building on that conclusion, we discuss each method individually and show to what extent the additional point-source measurements (Table 6.1) are of importance as well for estimating the ensemble averaged $L_v E$ accurately. Finally, we discuss the applicability of Monin-Obukhov Similarity Theory on 1-min averaging intervals.

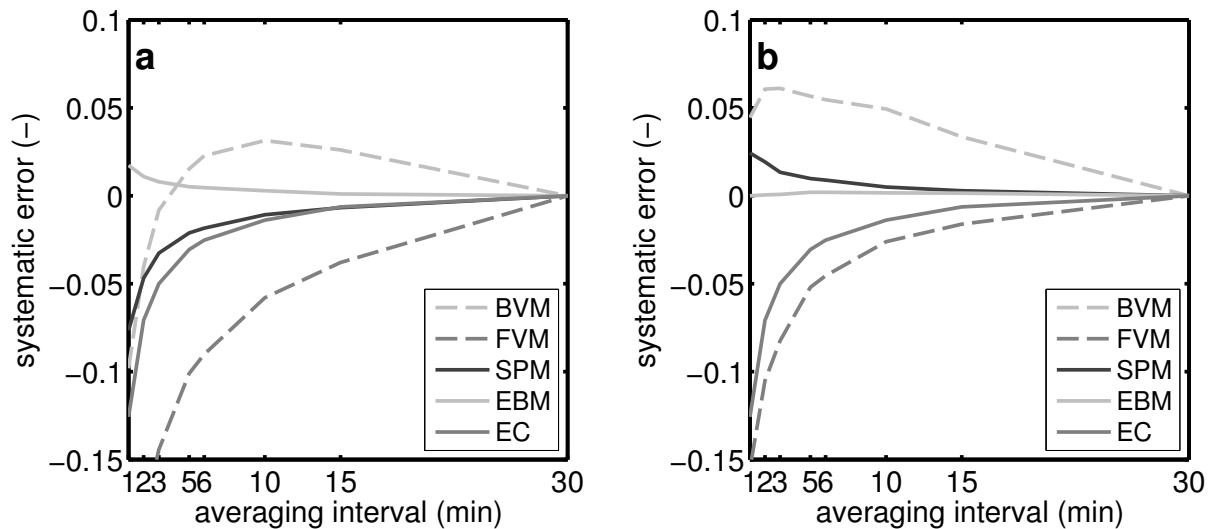


Figure 6.2: Systematic measurement errors in $L_v E$ related to averaging interval, (a) using eddy-covariance data and (b) using scintillometer data. In the legend BVM is the Bowen-variance method, FVM is the flux-variance method, SPM is the structure-parameter method, EBM is the energy-balance method, and EC is the eddy-covariance method.

We start with Figure 6.2, which shows the systematic errors in $L_v E$ estimated with the combined methods, as a function of averaging time. The combined methods in Figure 6.2a use H_{EC} , u^*_{EC} , and $L_{O,EC}$ as “scintillometer” input, whereas in Figure 6.2b they use H_{scinti} , u^*_{scinti} , and $L_{O,scinti}$ (for input variables used per method, see Table 6.1). $L_v E_{EC}$ is added as a reference and is identical in both subfigures. The systematic error estimates of the eddy-covariance system are based on ~ 350 hours of data, whereas those of the scintillometer are based on only ~ 150 hours of data, because of instrument malfunctioning during two weeks of the measurement campaign. In addition, the systematic errors in $L_v E$ for 1-min averages are shown in Table 6.2 together with the RMSE of the regression analysis that is used to quantify

the uncertainty in the mean-error estimate. Furthermore, the table shows the systematic error and the corresponding RMSE for the reference method and the “scintillometer” input variables, i.e. $L_v E_{EC}$, H_{EC} , H_{scinti} , u^*_{EC} , and u^*_{scinti} .

Table 6.2: Systematic errors (SE) in $L_v E$ for the combined methods and the eddy-covariance method and the systematic errors in H and u^* for the scintillometer method and the eddy-covariance method. All error estimates are for 1-min averaging intervals. In addition the root-mean square error (RMSE) is given to indicate the accuracy of the error estimate. For $L_v E$ from the combined methods, the error is estimated with H_{scinti} , u^*_{scinti} , and $L_{O,scinti}$ and with H_{EC} , u^*_{EC} , and $L_{O,EC}$. All regression is based on a 95% confidence interval. Shorthand notations of the methods are the same as in Figure 6.2.

	Sonic-anemometer data (EC)		Scintillometer data (scinti)	
	SE	RMSE	SE	RMSE
$L_v E$ BVM	-0.10	5 W m ⁻²	+0.05	7 W m ⁻²
$L_v E$ FVM	-0.26	15 W m ⁻²	-0.16	7 W m ⁻²
$L_v E$ SPM	-0.08	5 W m ⁻²	+0.02	2 W m ⁻²
$L_v E$ EBM	+0.02	4 W m ⁻²	0.00	2 W m ⁻²
$L_v E$ EC	-0.13	10 W m ⁻²		
H	-0.21	7 W m ⁻²	+0.01	2 W m ⁻²
u^*	-0.08	1.6x10 ⁻² m s ⁻¹	+0.02	0.6x10 ⁻² m s ⁻¹

Before considering each method specifically, we will first look at two general issues of Figure 6.2. First, note that the systematic errors for some of the combined methods are positive, i.e. $\overline{L_v E_{1min}}^{30}$ overestimates $L_v E_{30min}$. This counterintuitive overestimation is related to the fact that in the Bowen-variance method σ_T is inversely related to $L_v E$, as is H in the energy-balance method, and as is l_0 (through u^*) in the structure-parameter method.

Another issue that plays a role is that u^* non-linearly depends on l_0 by a $-4/3$ power, see Eq. (5.4). As a result, in determining a 30-min interval u^* , u^* based on 1-min l_0 will be larger than u^* based on 30-min l_0 , i.e. $\overline{u^*(l_{0,1min})}^{30} > u^*(l_{0,30min})$. This effect is enhanced due to the log-normal distribution of l_0 . As $L_v E$ and H depend linearly on u^* they are affected in a similar way, i.e. $\overline{L_v E(l_{0,1min})}^{30} > L_v E(l_{0,30min})$.

Second, comparison of Figure 6.2a with Figure 6.2b shows that the scintillometer outperforms the eddy-covariance method and greatly benefits the accuracy of the $L_v E$ estimate. The obvious reason is that the systematic errors found in the scintillometer H and u^* estimates are much lower than those in the eddy-covariance estimates. For the data considered in Figure 6.2, the systematic errors in the scintillometer H and u^* are +0.01 and +0.02, whereas for the eddy-covariance system the errors are -0.21 and -0.08 respectively (see Table

6.2). The error of -0.21 we found in H_{EC} is particularly large, when compared to values found in the literature (Sun et al., 2005). The high accuracy of the scintillometer is in agreement with previous results of Hartogensis et al. (2002), who conclude that the scintillometer is “superior” to eddy-covariance flux estimates when using short averaging intervals.

With these conclusions in mind, we now proceed to discuss the results of the systematic error in $L_v E$ for each combined method. We will focus on the 1-min averaging intervals, unless stated otherwise. As we wish to improve upon the results of the eddy-covariance method, this method serves as a reference. The error in eddy-covariance $L_v E$ is -0.12, which is similar to the error in $L_v E$ reported by Sun et al. (2005).

The energy-balance method is the combined method with the smallest systematic error. For this method, Q_{net} is the most significant input and the only turbulence variable that suffers from the systematic error is H (Van Kesteren et al., 2012a). This error in H results in a systemic error in $L_v E$ of +0.02 when H_{EC} is used and a zero error when H_{scinti} is used.

The flux-variance and Bowen-variance method have larger systematic errors than the energy-balance method, i.e. -0.27 and -0.10 when H_{EC} , u^*_{EC} , and $L_{O,EC}$ are used and -0.15 and +0.05 when H_{scinti} , u^*_{scinti} , and $L_{O,scinti}$ are used. Unlike the systematic error in the energy-balance method, the systematic error in the flux-variance method and the Bowen-variance method are not eliminated by using the scintillometer. This happens, because the additional measurements of both these methods are σ_T and/or σ_q (Table 6.1), which suffer from a systematic error, see below. The flux-variance method only gets as accurate as the eddy-covariance method, whereas the Bowen-variance method seems to perform better. Ideally, when $r_{Tq} = 1$, the underestimations in σ_T and σ_q cancel out against each other, but unfortunately this is only partly the case in our experiment. Note, that the error for 1-min values is probably slightly larger than 0.05, when considering the curves of the other methods. Finally, the RMSE is low for these methods, yet larger than for the other two combined methods (Table 6.2). For both methods applies that the magnitude of the relative error for an individual interval can differ from the mean error estimate and in case of the Bowen-variance method even can change sign sometimes (especially at night).

The structure-parameter method does improve upon the eddy-covariance method and the two variance-based methods. The systematic error in $L_v E$ is virtually eliminated by using the scintillometer measurements. With the scintillometer H , u^* , and L_O the error is only +0.02 (RMSE = 2 W m⁻²), which is brought about by the small systematic error in the scintillometer u^* and to a lesser extent by the small systematic error in L_O . Furthermore, the “additional variable” C_q^2 does not have a systematic error (see below).

To clarify how the errors in the additional variables propagate in the flux estimates, we will discuss the systematic errors in the additional variables of the combined methods. We determined the systematic errors, by applying the Ogive technique to high-frequency data of q , T , and Δq (section 6.2.3.1). As such, we obtained the systematic errors for σ_q , σ_T , and C_q^2 . Figure 6.3 shows a representative example of the systematic error for these three variables during daytime. Also the systematic difference of the ratio of σ_q and σ_T , i.e. $\sigma_q/\sigma_T = 1/\beta_\sigma$, is shown, as this ratio directly shows how the errors in σ_q and σ_T propagate into $L_v E$ for the Bowen-variance method. For the other methods, the relation between the structure parameter or variance and $L_v E$ is direct.

For 1-min averaging intervals, the systematic error in σ_q is approximately -0.15, diminishing rapidly with increasing averaging interval, whereas the error in σ_T (-0.23) is larger and more persistent. Consequently, the systematic difference in $1/\beta_\sigma$, is positive and equals the difference between the error in σ_T and σ_q , i.e. a +0.10 error for 1 min averaging intervals. Apparently, σ_T , like H_{EC} , is influenced more strongly by larger time scales than σ_q , causing $|r_{Tq}| < 1$ and the error in $1/\beta_\sigma > 0$.

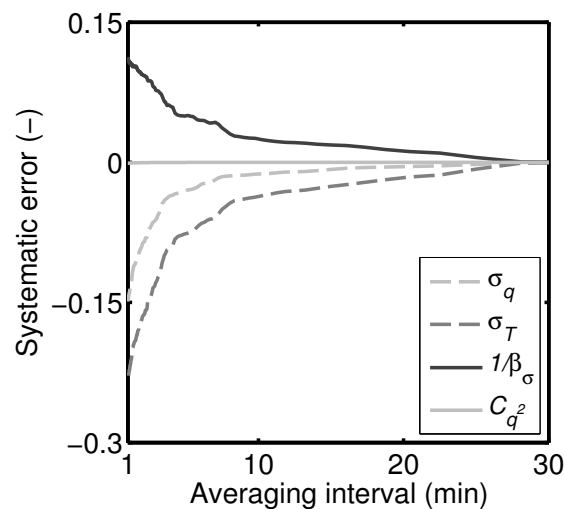


Figure 6.3: Systematic error obtained with Ogive technique, 23rd of May 2009 10:00 UTC – 14:00 UTC.

As σ_q and σ_T need a minimum averaging time (cf. Figure 6.1a) $L_v E$ will always have a systematic error when estimated with the flux-variance method. Also, $L_v E$ estimated with the Bowen-variance method will have a systematic error, except for “ideal” conditions when $|r_{Tq}| = 1$. However, often the conditions are not ideal. The structure-parameter method is a method that does not suffer from a systematic error, even when $|r_{Tq}| < 1$. C_q^2 is only defined for eddies of a size that falls in the inertial sub-range (Tatarskii, 1961) and is evaluated for one particular

size, in our case 1 m. Simply because of how C_q^2 is defined, it is only sensitive to time scales corresponding to length scales of 1 m or smaller. Consequently, C_q^2 is insensitive to larger time scales, which are associated with the systematic error for variances (Figure 6.1a).

Figure 6.3 shows that, indeed, C_q^2 has no systematic error. Note, that the fact that the systematic error in C_q^2 equals zero for all averaging intervals does not imply that a 1-min averaged C_q^2 will correctly represent a 30-min averaged C_q^2 . However, it does imply that taking the arithmetic mean of thirty 1-min averaged C_q^2 results in a correct estimate of the 30-min averaged C_q^2 .

Moreover, with its high accuracy the structure-parameter method confirms that the application of Monin-Obukhov similarity theory (MOST) is justified even for these short averaging intervals. This contradicts the conclusion of Andreas et al. (2003), who argue that for non-stationary conditions 1-min averaged values of C_n^2 and l_0 do not represent the 30-min averaged value of C_n^2 and l_0 . They base this argument on the observation that individual 1-min averages differ from the 30-min average. Then, they continue their argument in stating that because of the non-stationarity observed in the 1-min averaged fluxes, MOST functions, which are based on averaging intervals of 30-60 minutes may not be applied. However, 1-min averages may differ from 30-min averages. Essential for MOST is that for the dimensionless groups, y , $\overline{y_i}^{-30} = y_{30}$, i.e. the ensemble average must be accurately estimated. Under homogeneous conditions, the scintillometer achieves this by a combination of spatial and temporal averaging, whereas the eddy-covariance method relies on temporal averaging only. Using spatial averaging to estimate the ensemble average is a technique that is also applied in large-eddy-simulation (LES) studies. In these studies it is standard practice to estimate the ensemble average at a given time by averaging over all grid points in homogeneous directions (e.g. horizontal slabs) (Cheinet and Siebesma, 2009). In contrast to LES models, a scintillometer always requires some temporal averaging as C_n^2 is determined from a time-series of $\ln(J)$. However, the results above confirm that a 1-min averaging time is sufficient, since the scintillometer $\overline{u_{*1\min}}^{-30} = u_{*30\min}$, $\overline{H_{1\min}}^{-30} = H_{30\min}$ and for the structure-parameter method $\overline{L_v E_{1\min}}^{-30} = L_v E_{30\min}$.

6.4.1.2. Random errors

Similarly to the previous section, we will evaluate the random error in $L_v E_{EC}$ as well as in $L_v E$ for all combined methods using the scintillometer- and the eddy-covariance H , u_* and L_0 . We

recall that we estimate the random error based on all cloudless data (520 samples). We will consider relative random errors and will use only the 1-min averaging results in the discussion. The results are given in Figure 6.4 and the random error in $L_v E_{EC}$ (~ 0.32) serves as the reference.

Comparing Figure 6.4a with Figure 6.4b shows that, as for the systematic error, using the scintillometer greatly reduces the random error in $L_v E$ for all the combined methods that make use of additional turbulence humidity measurements. The random errors in the combined methods using H_{EC} , u^*_{EC} , and $L_{O,EC}$ are ~ 0.25 and these reduce to random errors of ~ 0.17 when the combined methods are evaluated with H_{scinti} , u^*_{scinti} , and $L_{O,scinti}$. The reason that the combined methods yield a smaller random error than the eddy-covariance method is twofold.

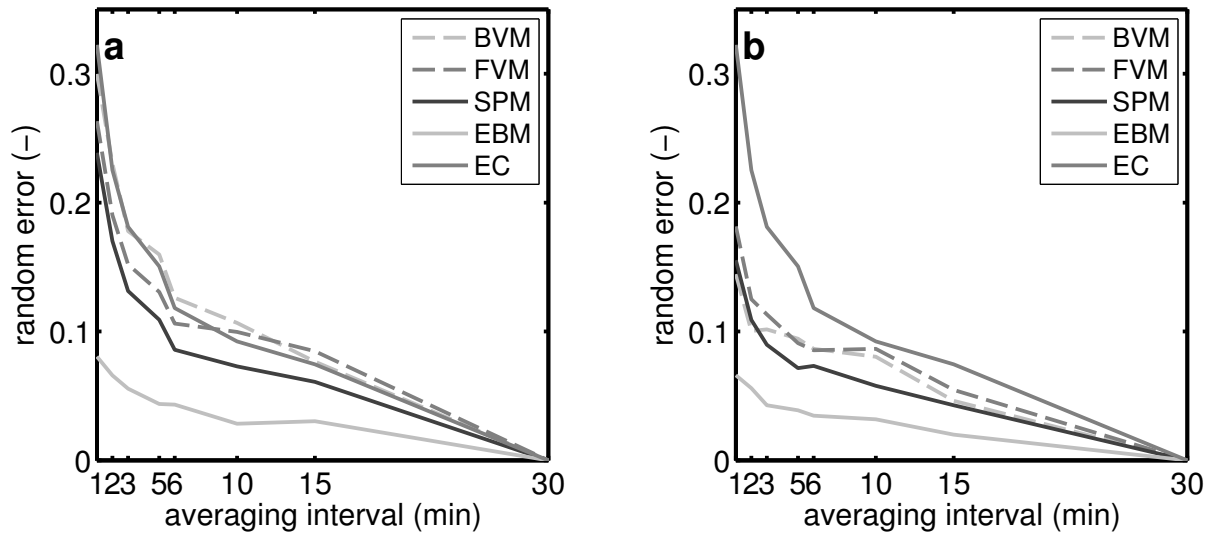


Figure 6.4: Random measurement errors for $L_v E$ related to averaging interval, (a) using eddy-covariance data and (b) using scintillometer data. In the legend BVM is the Bowen-variance method, FVM is the flux-variance method, SPM is the structure-parameter method, EBM is the energy-balance method, and EC is the eddy-covariance method.

The first reason is that the scintillometer acquires more independent samples than the sonic anemometer, by sampling small eddies with the size of its first Fresnel zone (in this set-up ~ 9 mm) (Wyngaard and Clifford, 1978). As a result the random error in $K_{q, meth}$ is greatly reduced, see Eq. (6.6). For the data shown in Figure 6.4, the random error in e.g. scintillometer H is 0.11, whereas for the eddy-covariance system the error in H is 0.3. This is in line with Hartogensis et al. (2002), who found that the random error in H_{EC} was about twice the error in H_{scinti} .

The second reason is that the random error in the humidity variable is small. The error in L_vE for the combined methods is determined by the decorrelation time of q , whereas the error in L_vE_{EC} is determined by the decorrelation time of w . Two advantages follow from not using $\text{cov}(w,q)$, but $\sqrt{\text{var}(q)}$ or $\sqrt{C_q^2}$. Firstly, Eq. (49) of Lenschow et al. (1994) shows that a low r_{wq} (in our case $r_{wq} \approx 0.3$) increases the time to acquire enough independent samples for a covariance as compared to a variance (in our case with a factor ten). Hence, as long as the decorrelation time of q is less than ten times longer than that of w , the resulting random error in $\text{var}(q)$ still is smaller than that in $\text{cov}(w,q)$. Secondly, using $\sqrt{\text{var}(q)}$ or $\sqrt{C_q^2}$ ensures that the relative error in $\text{var}(q)$ or C_q^2 propagates with a factor 0.5 to L_vE , see Eq. (6.6). Thus, the net effect is that as long as the decorrelation time of q is less than twenty times larger than the decorrelation time of w , the random error in L_vE estimated with the combined methods is smaller than the random error in L_vE_{EC} . Even close to the surface, where the decorrelation time of w is much smaller than that of q this is guaranteed.

In the analysis above, the energy-balance method was not taken into account because its estimate of L_vE depends mostly on an accurate estimate of Q_{net} . As for the systematic error, the energy-balance method has the lowest random error of all methods. The random error in L_vE is about 0.06 for 1-min averaging intervals when estimated with this method. However, data were excluded for $L_vE < 70 \text{ W m}^{-2}$, otherwise the error was dominated by data from the transition from $Q_{net} > 0$ to $Q_{net} < 0$. If these data are included, the random error increases to 0.17. This increase happens, because during the transition time, H is large compared to L_vE and its magnitude is similar to the sum of Q_{net} and G . Consequently, even though the relative random error in H is small, the absolute random error is large compared to the small L_vE . The resulting relative random error in L_vE is relatively large, because the large absolute error in H propagates to L_vE , see Eq. (6.7).

6.4.2. Validation of 1-minute evapotranspiration

In the previous section we showed that the systematic and random errors of the combined methods using scintillometer H , u^* , and L_O outperform the eddy-covariance estimates of L_vE for 1-min averaging intervals. From hereon we will therefore only apply the combined methods with the scintillometer H , u^* , and L_O .

In this section, we will attempt to validate the L_vE estimates for the 1-min combined methods. We will do so in three ways. Firstly, we single out two situations and evaluate L_vE with Q_{net} . Secondly, we validate the data from the whole experiment with the Penman-

Monteith model. Thirdly, we address the question of whether plants are physiologically capable of causing the fluctuations we observe, with the method that performs the best.

6.4.2.1. Validating the combined methods with Q_{net}

The validation of the combined methods with Q_{net} is done by considering the correlation between Q_{net} and L_vE as described in section 6.2.3.1. Figure 6.5 shows the time series of 1-min averaged Q_{net} and L_vE between 7:00 and 12:00 UTC on 4 June 2009 with time steps of one minute for all the combined methods and the eddy-covariance method. The figure depicts a situation during which cloudy and sunny spells rapidly succeed each other, so that Q_{net} fluctuates abundantly. Consequently, we expect L_vE to fluctuate as well. Note, that even though Q_{net} drives L_vE we do not expect a perfect correlation between the two variables, because the available energy (represented by Q_{net}) is not only distributed to L_vE , but also over other surface fluxes.

The first impression from Figure 6.5 is that the eddy-covariance and Bowen-variance methods (Figure 6.5a,b) perform worse than the flux-variance, structure-parameter, and energy-balance methods (Figure 6.5c,d,e). In the following, we examine all five methods in detail.

Starting with the eddy-covariance method, we see many fluctuations in L_vE . The random error is so large that the radiation-driven fluctuations in L_vE tend to disappear in the random noise. The corresponding correlation with zero time lag, r_0 , between L_vE and Q_{net} is 0.34. For the combined methods, we see that the Bowen-variance method correlates better with Q_{net} than was the case for the eddy-covariance method. However, 24% of data are missing, because data were omitted when $|r_{Tq}| < 0.2$ or $|\beta| < 0.1$. The flux-variance method and structure-parameter method perform better than the Bowen-variance method. They both resolve the variations in L_vE well, have a higher data availability, and r_0 is higher, i.e. 0.60 and 0.59 respectively.

Note that Figure 6.5a-d besides r_0 also shows the correlation with one or two minutes time lag, r_1 , r_2 , i.e. the correlation of $Q_{net}(t)$ with $L_vE(t+1)$ or $L_vE(t+2)$. We determined the optimal time lag, so that r_{lag} is maximal. For all four methods, r_{lag} is significantly larger than r_0 . All methods, except the Bowen-variance method ($r_1 = 0.59$ and $r_2 = 0.58$) agree with each other on the time lag of two minutes. Thus, it seems likely that the inertia of the system is about two minutes.

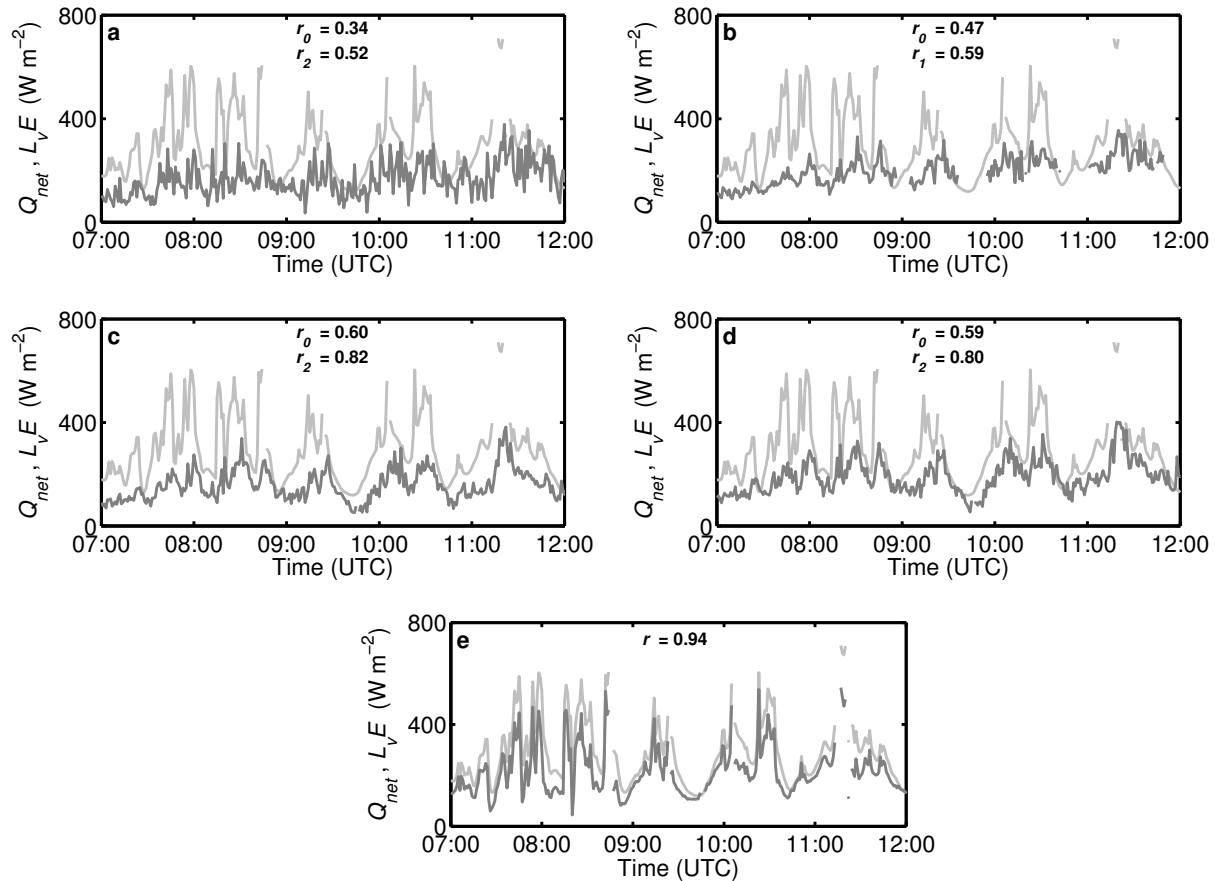


Figure 6.5: 1-minute L_vE and net radiation on 4 June 2009, (a) eddy-covariance method, (b) Bowen-variance method, (c) flux-variance method, (d) structure-parameter method, and (e) energy-balance method. In all graphs r is the correlation between the net radiation and L_vE . In all the graphs Q_{net} is light grey and L_vE grey.

Finally, the energy-balance method is added for completeness. The energy-balance method clearly overestimates L_vE as a result of the non-closure of the energy balance (Van Keulen et al., 2012a). Furthermore, the phase of L_vE is biased to that of Q_{net} , which makes that the method is not capable of capturing the two minute inertia of the system. More in general, Q_{net} is unsuitable as a validation method for the energy-balance method, because of the strong cross-correlation between method and reference through Q_{net} . This is especially true for the conditions encountered in this experiment, where H and G are relatively small compared to Q_{net} and the storage terms and the energy equivalent of the CO_2 flux are neglected. Therefore, the large correlation coefficient ($r = 0.94$) cannot be considered to be an indication of accuracy.

From the above result we can conclude that the assumption of a closed energy balance does not hold for 1-min averaging intervals. Consequently, we expect that the Penman-Monteith model, our second validation method, is affected by the invalidity of this

assumption as well. In the following, we will discuss the accuracy of the energy-balance method and the Penman-Monteith model. Figure 6.6 shows Q_{net} together with L_vE estimated with the energy-balance method, the Penman-Monteith model, and the structure-parameter method, which we added for comparison. Furthermore, we highlighted and numbered three events with distinct changes in radiation to guide the discussion.

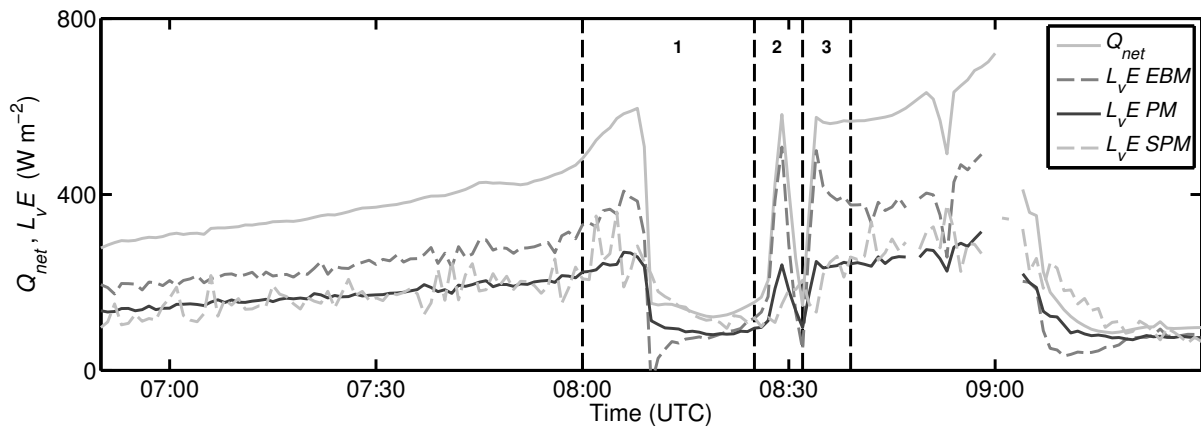


Figure 6.6: Responses of L_vE to variable radiation, 5 June 2009 from 7:00 UTC to 10:30 UTC. L_vE for 1-min averaging intervals is shown for the energy-balance method, the Penman-Monteith model, and the structure-parameter method.

From the error analysis and Q_{net} validation, we know that the structure-parameter method resolves L_vE accurately for each of these three events. As in Figure 6.5, the abrupt changes in Q_{net} are followed by delayed and slightly damped (event 2) changes in L_vE . The energy-balance method and the Penman-Monteith model are not able to resolve this inertia.

Moreover, the energy-balance method response on changes in Q_{net} is extreme. During the first event, the method shortly estimates a negative L_vE , immediately followed by an increase in L_vE , even though Q_{net} remains constant. During the third event a similar thing happens, but now mirrored as compared to the first event. This is not a physical response of L_vE upon changing Q_{net} , but it reflects the inertia in H . Hence, given the local circumstances, we conclude that the energy-balance method is unsuitable for measuring 1-min averaged fluxes.

Finally, the Penman-Monteith model yields better L_vE estimates than the energy-balance method, but the phase of its L_vE estimate is biased to Q_{net} as well. Both the assumption of a closed energy balance and constant r_c contribute to this. Despite these limitations in our model set-up, the Penman-Monteith model still gives a more comprehensive approach to fluctuations in L_vE than Q_{net} only. Especially during the late afternoon and early

night, when the second term in Eq. (6.8) (water-vapour demand) dominates over the first term (the radiation term), the model is an improvement on Q_{net} .

Before we proceed to the validation of the combined methods with the Penman-Monteith model, we first want to give some more attention to the inertia of the system. Figure 6.5 showed that the most optimal correlation between Q_{net} and L_vE is achieved for a two-minute time lag. However, from Figure 6.6 it follows that for reaching a new equilibrium upon a change in Q_{net} more time is required. When considering the first event, it follows that L_vE needs 10-15 minutes to adapt fully to the new radiation regime. However, 67% of the change in L_vE is accomplished in the first five minutes after the drop in Q_{net} , cf. Mauder et al. (2007), who found shorter response times, and Foken et al. (2001). In our situation L_vE remains so large, because heat-storage changes in the soil above the heat-flux plate and heat-storage changes in the vegetation release energy to the system that benefits L_vE . Furthermore, there is some L_vE buffering (water storage) in the lower 2 m of the atmosphere. So, apparently the time lag of two minutes is an optimum between the rapid changes in Q_{net} and the heat-storage changes and L_vE buffering of the system.

6.4.2.2. Validating the combined methods with Penman-Monteith

This section continues with the validation of the combined methods with the Penman-Monteith model based on data from the whole experiment. shows the correlation coefficient and RMSE that resulted from the regression analysis. Both statistical parameters are shown without time lag and with a two-minute time lag.

Table 6.3: Statistics of the comparison of L_vE from the combined methods and the eddy-covariance methods to L_vE from Penman-Monteith for 1-min averaging intervals. The subscript 0 denotes a 0-min time lag and the subscript 2 denotes a 2-min time lag of L_vE from the combined methods. Used are: r , the correlation coefficient, RMSE, the root mean-square error, and n the total number of 1-min samples included in the calculations.

	r_0 (-)	RMSE ₀ (W m ⁻²)	r_2 (-)	RMSE ₂ (W m ⁻²)	n (-)
Eddy covariance	0.51	74	0.58	54	2302
Bowen variance	0.71	38	0.72	34	1541
Flux variance	0.72	41	0.76	31	2181
Structure parameter	0.72	42	0.76	31	2181

For 30-minute averaging intervals, the Penman-Monteith model compares to the eddy-covariance method with a regression slope of $0.96x$, a correlation of 0.97 and a RMSE of 22 W m^{-2} . For 1-min averaging intervals, the eddy-covariance method compares worst of all methods. The method has the largest RMSE ($\text{RMSE}_0 = 74 \text{ Wm}^{-2}$ and $\text{RMSE}_2 = 54 \text{ Wm}^{-2}$) and its correlation is the lowest ($r_0 = 0.51$ and $r_2 = 0.58$). Assuming a two-minute time lag, improves the comparison, but despite the improvement, we see that the eddy-covariance method is not able to resolve rapid fluctuations in $L_v E$. Together with the fact that the method has a large systematic error, this leads to the conclusion that the method is unsuitable for measuring 1-min averaged fluxes.

The three combined methods perform better than the eddy-covariance method. All three combined methods yield good results in resolving fluctuations in $L_v E$. The Bowen-variance method, however, misses 30% of the data. These data were omitted, because like De Bruin et al. (1999) we found that the Bowen-variance method produces unreliable results when $|r_{Tq}| < 0.2$ or $|\beta| < 0.1$. The flux-variance method resolves fluctuations in $L_v E$ even slightly better than the Bowen-variance method ($r_0 = 0.72$ and $r_2 = 0.76$, and $\text{RMSE}_0 = 41 \text{ Wm}^{-2}$ and $\text{RMSE}_2 = 31 \text{ Wm}^{-2}$). Nevertheless, the method is less suitable to measure 1-min averaged $L_v E$ than the structure-parameter method, because of its large systematic error. The structure-parameter method resolves the fluctuations in $L_v E$ well ($r_0 = 0.72$ and $r_2 = 0.76$, and $\text{RMSE}_0 = 42 \text{ Wm}^{-2}$ and $\text{RMSE}_2 = 31 \text{ Wm}^{-2}$) and moreover, the method does neither suffer from a systematic error, nor misses 30% of its data. Therefore, we conclude that the structure-parameter is the best and most robust method to measure $L_v E$ for 1-min averaging intervals.

6.4.2.3. Plants versus turbulence

In this section, we investigate whether the fast response of $L_v E$ to Q_{net} is brought about by a quick adaptation of turbulence or a quick adaptation of plants. To distinguish between the two, we recall the equation of the structure-parameter method (Van Kesteren et al., 2012a)

$$L_v E = -L_v \rho u_* q_* = -\rho z^{1/3} \frac{L_v u_*}{\sqrt{f_q(z/L_0)}} \sqrt{C_q^2} = -\rho K_{q, \text{strpar}} \sqrt{C_q^2}, \quad (6.9)$$

where ρ is the density, $f_q(z/L_0)$ is a MOST function, and $K_{q, \text{strpar}}$ is the turbulence transport efficiency of the structure-parameter method. As z , L_v , and ρ are constant in time, the most variation occurs in either C_q^2 or $K_{q, \text{strpar}}$.

To check if the most variation occurs in C_q^2 or in $K_{q,strap}$ we introduce Figure 6.7, which shows Q_{net} together with C_q^2 and $K_{q,strap}$ for the same situation as Figure 6.6. Figure 6.7 shows that $K_{q,strap}$ does not correlate with Q_{net} . Through L_O , $K_{q,strap}$ is determined by u^* and H and of these two variables, Q_{net} directly influences only H . In part I, we showed that the influence of H on $K_{q,strap}$ (and thus on L_vE) is small, whereas the influence of u^* is relatively large (Van Kesteren et al., 2012a). Furthermore, u^* is sensitive to the wind speed and to adapt to changes in Q_{net} during daytime takes about 25 minutes (Foken et al., 2001). Perhaps, in this specific case $K_{q,strap}$ could also be obtained by interpolating 15-min or 30-min averaged eddy-covariance measurements. However, especially during conditions of changing wind speed, when buoyancy gets more important, or during periods of intermittent turbulence this approach does not hold.

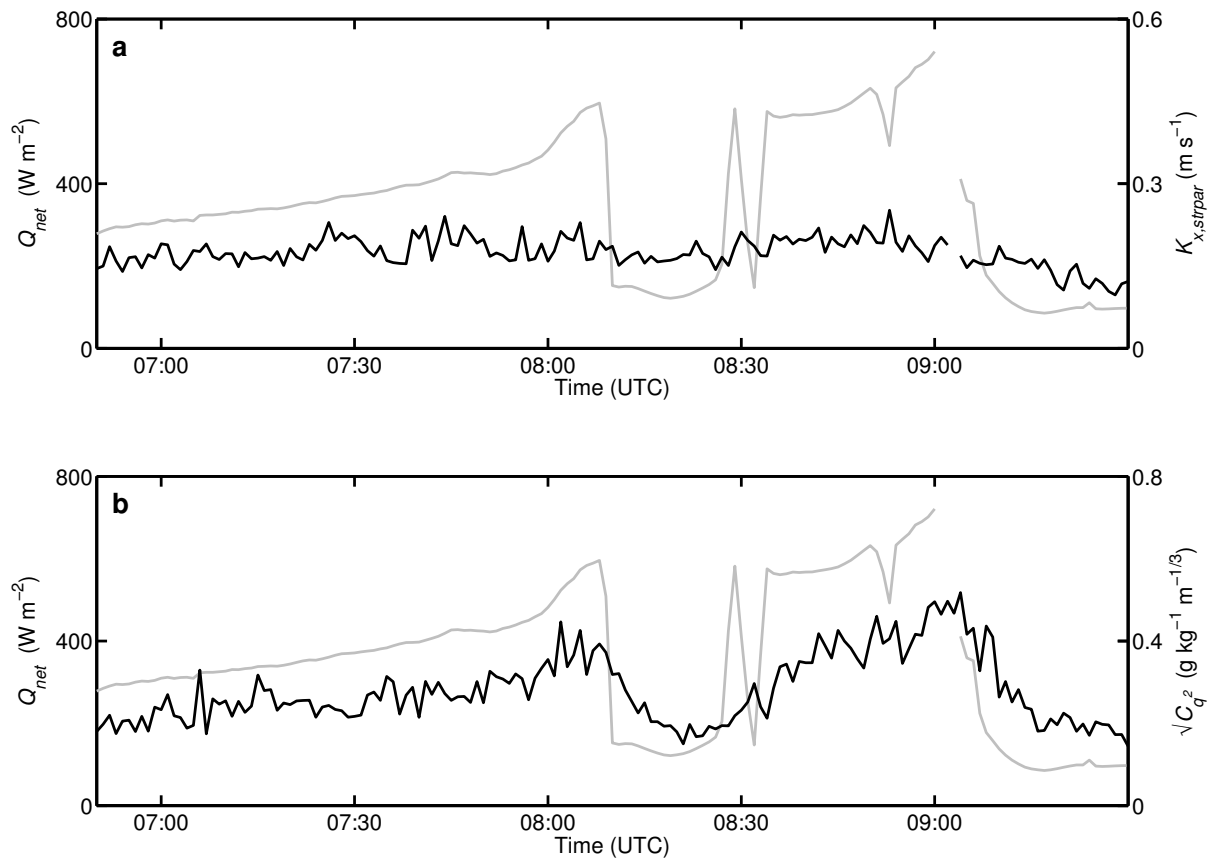


Figure 6.7: Influence of varying net radiation. The light-grey line is the net radiation and the black line (a) the turbulent transport efficiency, and (b) the structure parameter.

C_q^2 , on the other hand, does strongly correlate with Q_{net} . C_q^2 is determined by the concentration above the sensor and below it. We assume that the concentration above the sensor remains constant, whereas the concentration below the sensors (close to the canopy)

changes. This concentration changes either, because the vegetation closes its stomata or because the concentration within the stomatal cavity changes. Which of the two possibilities occurs will be investigated in section 7.5.1.

The question is whether wheat plants also control the flux by closing their stomata. Wheat belongs to the family of the Poaceae (grasses), which is characterized by its “dumb-bell-shaped” stomata (Franks and Farquhar, 2007; Hetherington and Woodward, 2003). Hetherington and Woodward (2003) state that because of the “dumb-bell design”: “Smaller changes in guard and subsidiary cell turgor lead to greater increases in stomatal aperture (...). This efficiency and speed of stomatal opening in grasses enhances photosynthesis and water-use efficiency compared with non-grass species.” Furthermore, Franks and Farquhar (2007) conclude for wheat: “(...) the capability of very rapid stomatal movements (at a substantially faster rate than perhaps any other stomatal type) (...) may be explained by the unique morphology and mechanics of its dumb-bell-shaped stomata coupled with “see-sawing” of osmotic and turgor pressure between guard and subsidiary cells during stomatal opening or closure”. With “very rapid” they mean that the stomata can fully open within 4-9 minutes, depending on humidity (Franks and Farquhar, 2007).

Figure 6.6 showed that L_vE needed 10-15 minutes to adapt to the new radiation regime in the first event, a time that will allow the stomata to close. However, they likely did not significantly close, because L_vE increases almost immediately when Q_{net} increases again. Furthermore, stomatal response strongly depends on plant type and local circumstances like water availability, heat, nutrient availability, competition with other plants, solar radiation, history, time of the year etc. (Cardon et al., 1994). Most of these local circumstances are optimized for crops, so the stomata are likely to be open during our particular conditions. Nevertheless, and this we want to underline, this example does show that the structure-parameter method is very suitable to study the influence of vegetation at field scales in a natural environment under non-stationary conditions.

6.5. Conclusions

This chapter discussed four combined methods for estimating 1-min averaged L_vE that can be used to evaluate L_vE under non-stationary conditions. The essence of these methods is that the scintillometer obtains area-averaged measurements of the atmospheric turbulence, the transport mechanism, and that the additional measurements provide turbulence measurements of humidity. The combined methods we discussed were the Bowen-variance method, the flux-

variance method, the structure-parameter method, and the energy-balance method. The methods were tested on data from a wheat field near Merken (Germany) in the framework of the Transregio32 experiment.

To evaluate the combined methods and determine their accuracy, we performed an extensive error analysis. Based on the error concepts of Lenschow et al. (1994) we determined the averaging-time-dependent systematic and random error in L_vE for averaging intervals varying from 1 to 30 minutes. Furthermore, we validated the combined methods with Q_{net} and the Penman-Monteith model. The Penman-Monteith model is a more comprehensive validation method than Q_{net} , but as we discussed, the model is limited, because it assumes a closed energy-balance and we assumed a constant canopy resistance.

The error analysis shows that the energy-balance method did not suffer from an averaging-time-dependent systematic error for 1-min averaging intervals, whereas the eddy-covariance method and flux-variance method have a large (-0.15) systematic error. Also the Bowen-variance method has a systematic error (+0.05), which results from a larger error in σ_T than in σ_q . Finally, the structure-parameter method has a negligible systematic error in L_vE . The structure parameter is defined for separation distances that fall within the inertial sub-range of the scalar spectrum. Large eddies are not observed and do not need to be sampled. Consequently, structure-parameters are more robust statistical parameters than variances. In addition, the negligible systematic error in L_vE , H , and u^* confirms that the application of Monin-Obukhov similarity theory is justified for 1-min averaging intervals. Provided the conditions are homogeneous, the scintillometer yields a local flux estimate, which estimates the ensemble average by averaging in both space and time.

Similarly, we discussed the averaging-time-dependent random error in the combined methods. For 1-min averaging intervals, the random error of the combined methods is about half the random error of the eddy-covariance method. The exception is the energy-balance method. This method has a smaller error than the other combined methods, during the time of the day when the net radiation is dominant. For all combined methods holds that the combination of measuring H and u^* with the scintillometer and using standard deviations instead of covariances as scalar turbulence variables, greatly reduces the random error in the flux estimate.

Using Q_{net} and the Penman-Monteith model, we validated the combined methods and showed that the eddy-covariance method cannot resolve 1-min fluctuations in L_vE . Together with the large systematic error this leads to the conclusion that the eddy-covariance method is unsuitable for measuring 1-min averaged fluxes. The energy-balance method has a large

autocorrelation with Q_{net} , which makes both validation methods unsuitable for a reliable validation of this method. The assumption of a closed energy balance leads to a two-fold inaccuracy, because the non-closure is fully attributed to L_vE . Firstly, the energy-balance overestimates L_vE by about 20% and secondly, the phase of L_vE is biased to the phase of Q_{net} . In one case this even led to a negative L_vE estimate during daytime. Thus, given the local circumstances, the energy-balance method is unsuitable for measuring L_vE over 1-min averaging intervals.

The three other combined methods are well able to resolve fluctuations in L_vE . Unfortunately, the Bowen-variance method has 30% less data than the other two combined methods, because data had to be omitted when $|r_{Tg}| < 0.2$ or $|\beta| < 0.1$. The flux-variance method resolved the fluctuations in L_vE better than the Bowen-variance method, but the method suffers from its systematic error for 1-min averaging intervals. The structure-parameter accurately estimates L_vE for 1-min averaging intervals and was found to be the best and most robust method of all combined methods.

Finally, it was shown that wheat plants in the field caused the rapid changes in L_vE upon changes in Q_{net} . Wheat belongs to the family of the grasses, which because of their “dumb-bell-shaped” stomata can fully open/close their stomata upon changes in Q_{net} within 4-9 minutes. However, during our experiment this has not likely happened. Nevertheless, the structure-parameter method accurately shows how changes in solar radiation affect evaporation of water out of the wheat plants. To fully adapt to the new radiation regime, the system needed a time of 10-15 minutes, whereas the optimum time between adapting to instantaneous fluctuations in Q_{net} and the heat-storage changes and L_vE buffering of the system was two minutes. These results underline that the structure-parameter method is very suitable to study the influence of vegetation at field scales in a natural environment under conditions of non-stationary turbulence.

7. Measuring H₂O and CO₂ fluxes at field scales with scintillometry: Part III – carbon-dioxide fluxes and vegetation processes for 1-30 minute averaging intervals⁶

7.1. Introduction

The eddy-covariance method is used worldwide for measuring evapotranspiration and carbon-dioxide fluxes (Baldocchi, 2003; Shuttleworth, 2007). This method, which uses point-sampling measurements, obtains fluxes typically on field scales (50 m – 200 m). Due to its nature, the eddy-covariance method obtains flux information over averaging intervals of typically 20-60 minutes (Hartogensis et al., 2002; Lenschow et al., 1994; Mahrt, 2010; Sun et al., 2005). During the averaging period, the turbulence is required to be statistically stationary. This condition is violated for several common events such as rapidly changing cloud cover or intermittent turbulence (Hartogensis et al., 2002; Van de Wiel et al., 2003). Therefore, the eddy-covariance method is unsuitable during these conditions (Sun et al., 2005; Van Kesteren et al., 2012b).

Research has shown that displaced-beam laser scintillometers can accurately determine fluxes for averaging intervals shorter than 1 minute (Hartogensis et al., 2002; Van Kesteren et al., 2012b; Wyngaard and Clifford, 1978). Consequently, these scintillometers are applicable for cases where turbulence is not statistically stationary over periods of 10-30 minutes. Unfortunately, these scintillometers cannot determine the carbon dioxide flux or evapotranspiration.

In part I of this study (Van Kesteren et al., 2012a), we introduced and validated four methods, which can determine evapotranspiration, carbon-dioxide fluxes, and fluxes of other passive scalars on field scales. They combine estimates of stability and friction velocity from the displaced-beam laser scintillometer with additional turbulence measurements of humidity and CO₂ to estimate the fluxes. These so-called combined methods are called the flux-variance method, the Bowen-variance method, the structure-parameter method, and the energy-balance method. In Part II (Van Kesteren et al., 2012b), we applied the spatial-averaging advantages of scintillometry to the four combined methods and showed that

⁶ This chapter is part of **Van Kesteren, B.**, Hartogensis, O.K., van Dinter, D, Moene, A.F., De Bruin, H.A.R., and Holtslag, A.A.M., 2012, *Measuring H₂O and CO₂ fluxes at field scales with scintillometry: Part II – validation and application of 1-minute flux estimates*, Agric. Forest Meteorol., conditionally accepted.

evapotranspiration, L_vE , can be accurately estimated for short averaging intervals (~ 1 min). In this part, Part III, we evaluate the combined methods for the carbon-dioxide flux, FCO_2 , and use the methods to study vegetation processes and flux responses. The motivation to explore these relatively short flux intervals is that we want to study the turbulent exchange of vegetation with the atmosphere under natural conditions. As turbulence is often non-stationary (e.g. (Foken et al., 2001)), methods that can determine detailed mass-flux descriptions for 1-min time intervals are required.

This chapter explores the possibilities to study FCO_2 on time intervals as short as 1 minute by analysing the Transregio-2009 dataset. As in part II, we evaluate the performance of the combined methods on these short averaging intervals following two approaches. First, we will test the accuracy of the 1-min flux estimates with an extensive error analysis, based on the error concepts of Lenschow et al. (1994). Second, we will estimate the accuracy of the 1-min averaged flux estimates by evaluating their reaction to rapid changes in the incoming short-wave radiation. The real forcing of FCO_2 is the photosynthetically active radiation (PAR), but the incoming short-wave radiation or solar irradiance is closely related to it (Papaioannou et al., 1993). Furthermore, for the structure-parameter method, estimates of both FCO_2 and L_vE will be validated for a wetter dataset than that of Transregio 2009 (i.e. Transregio 2008) and a dryer dataset (i.e. LITFASS 2009). As such, we investigate the accuracy of the method for conditions during which the similarity of sensible heat or humidity/ CO_2 can break down (Andreas et al., 1998; De Bruin and Jacobs, 1993; De Bruin and Verhoef, 1999; Moene and Schüttemeyer, 2008).

After the validation of the combined methods we will discuss three applications for which the 1-min-flux measurements are necessary. Firstly, studies of Foken et al. (2001) and Mauder et al. (2007) show that the sensible-heat flux, H , L_vE , and FCO_2 exhibit different time and amplitude responses to a decrease in solar radiation during a solar eclipse. They use wavelet analysis to investigate the fluxes, assuming that the high-frequency part of the turbulence spectrum dominates the fluxes. However, the two studies disagree with each other regarding the response times of the different fluxes. We will use our 1-min methodology and discuss the flux behaviour upon a decrease in solar radiation caused by passing clouds. This discussion will be based on the different processes that govern these three fluxes.

Secondly, we discuss light-response curves and the relevance of 1-min averaging values in determining these curves. Wolf et al. (2008) shows how the light-response curves can be used as a screening technique for erroneous data. Furthermore, light-response curves depend on atmospheric conditions such as temperature and humidity (Kim and Verma, 1990;

Nieveen et al., 1998b). Based on these notions, we will show the relevance of 1-min FCO_2 estimates for determining accurate light-response curves during conditions of non-stationary turbulence and their relevance for the comparison of light-response curves that are obtained during different atmospheric conditions.

Thirdly, we will discuss two methods for determining canopy resistances for 1-min averaging intervals. These methods are the Penman-Monteith method and the method using resistance expressions for H and $L_v E$ (Baldocchi, 1994a; de Rooy and Holtslag, 1999; Moene and Van Dam, 2012; Nieveen, 1999). Based on the 1-min averaged canopy resistance, we will discuss the accuracy of both methods and study the response of plants to changes in radiation (cloud cover) and humidity during non-stationary conditions.

7.2. Theory and methods

7.2.1. Eddy covariance and scintillometry

The eddy-covariance method estimates the flux from high-frequency measurements of vertical wind speed and scalar concentration. Scintillometers determine the friction velocity and sensible-heat flux via turbulence induced scattering of their beams, using wave-propagation theory and Monin-Obukhov similarity theory, for a complete overview of the theory, we refer to Part I and II.

7.2.2. Combined methods

Table 7.1: The turbulence variables of the scintillometer and additional turbulence measurements to calculate FCO_2 with the four combined methods.

Method	Scintillometer measurements	Additional measurements
Bowen-variance	H	σ_T , σ_{qCO_2} and r_{TqCO_2}
Flux-variance	u^* and L_O	σ_{qCO_2}
Structure-parameter	u^* and L_O	$C_{qCO_2}^2$

* L_O is the Obukhov length, σ_T is the standard deviation of temperature, σ_{qCO_2} is the standard deviation of the CO_2 concentration, r_{TqCO_2} is the correlation coefficient of temperature and CO_2 concentration, and $C_{qCO_2}^2$ is the structure parameter of the CO_2 concentration.

The double-beam laser scintillometer can determine u^* and H , but not the CO_2 flux, FCO_2 . To extend the optical-scintillometer application to mass fluxes Van Kesteren et al. (2012a)

proposed four methods of which three combine scintillometer measurements with additional turbulence measurements of humidity or CO₂. For FCO_2 , the relevant methods are the flux-variance method, the Bowen-variance method, and the structure-parameter method. For a detailed description of the combined methods, we refer to Part I. Here, we only give an overview of the turbulent variables used in the methods (see Table 7.1)

7.2.3. Validation methods

It is a challenge to come up with a proper validation method for 1-min averaged fluxes. Direct methods that accurately measure FCO_2 over 1-min averaging intervals are lacking. In Part II, we proposed two methods to validate the combined methods for these short averaging intervals, i.e. error analysis and radiative forcing. Here we will briefly repeat both methods. A more elaborate description can be found in Part II.

The first validation method is an error analysis. The error analysis we apply uses the error concept of Lenschow et al. (1994), who show that the estimated fluxes differ systematically and randomly from the “ideal” ensemble average of a flux, when the averaging time of the flux is not “long enough”.

To determine the systematic error in FCO_2 from the combined methods and eddy-covariance method, we introduce the relative systematic error

$$SE_i = \frac{\bar{x}_i^{-30}}{x_{30}} - 1, \quad (7.1)$$

where SE_i is the systematic error for a given averaging interval i , x_i is the flux with averaging interval i (1, 2, 3, 4, 6, 20, or 15 min), x_{30} is the flux with 30-min averaging interval, and \bar{x}_i^{-30} the 30-min arithmetic mean of $30/i$ x_i 's. From rewriting Eq. (7.1) to $\bar{x}_i^{-30} = (SE_i + 1)x_{30}$, it follows that the relative systematic error can be obtained from the regression slope of x_{30} with their corresponding \bar{x}_i^{-30} .

A second, continuous approach that can only be used for the input variables of the combined methods is the Ogive technique. Using this technique, the systematic error is defined as (Foken et al., 2006; Oncley et al., 1996)

$$SE_i = \frac{\int_{f_{30}}^{f_{av}} S df}{\int_{\infty}^{\infty} S df} - 1, \quad (7.2)$$

where S denotes the (co)spectrum of the input variable in question, f is the frequency, f_{av} is the frequency corresponding to a given averaging interval $f_{av} = 1/T_{av}$, T_{av} is the averaging interval, and f_{30} is the frequency corresponding to an averaging interval of 30 min.

To determine the random error in FCO_2 from the combined methods and eddy-covariance method we introduce the relative random error

$$RE_i = \sqrt{\frac{1}{N} \sum_{i=1}^N \left(\frac{x_i}{x_i^{-30}} - 1 \right)^2}, \quad (7.3)$$

where RE_i is the random error for a given averaging interval i , x_i is the flux with averaging time i , x_i^{-30} the 30-min mean of $30/i$ x_i 's to normalize x_i , and N the amount of flux samples.

The second validation method is a validation with the incoming short-wave radiation. FCO_2 is the difference between the photosynthesis and the respiration of a system, i.e. the net ecosystem exchange (Scanlon and Kustas, 2010). During daytime, photosynthesis is dominant. Photosynthesis, in turn, is mainly driven by the photosynthetic active radiation, which is a part of the incoming short-wave radiation, Q_s , and hence closely related to it (Papaioannou et al., 1993). The radiometers have a time response of typically 5-10 seconds and they can therefore accurately resolve variations in Q_s with time scales of one minute.

Thus, Q_s can be used as a reference for validating the 1-min FCO_2 from the combined methods. Q_s itself is of course not an absolute measure of FCO_2 , but it can be seen as a relative reference in the sense that changes in Q_s should be followed by changes in FCO_2 , also on short, 1-min time scales. We will use the correlation coefficient of Q_s with FCO_2 to quantify the response of FCO_2 to changes in Q_s .

7.2.4. Determining 1-min averaged values of the canopy resistance

The combined methods potentially offer a great opportunity to determine the canopy resistance, r_c , of plants for intervals as short as 1 minute. This can be done via inversion of the Penman-Monteith model or via the resistance expressions for H and L_vE .

With measurements of L_vE , r_c can be derived from the inverted Penman-Monteith model (e.g. (Baldocchi, 1994a; Nieveen, 1999)). However, this method involves several assumptions, most importantly a closed energy balance. In Part II we showed that for 1-min averaging intervals the energy balance does not close when only H , L_vE , and G are taken into account, since heat-storage changes upon quick changes in the radiation regime are important as well (Van Kesteren et al., 2012b). Hence, to obtain r_c with this method, the influence of the heat-storage changes on the L_vE estimate must be quantified. Partly, this can be circumvented by accounting for the phase differences between the different components of the energy balance (cf. Foken (2001) who concludes that using the delayed L_vE better closes the energy balance). Furthermore, this method models the atmospheric resistance, r_a , as $r_a = [\ln(z_{eff} / z_{0\theta}) - \Psi(z_{eff} / L_O) + \Psi(z_{0\theta} / L_O)] / k_{kar} u^*$, with the Ψ -functions for heat from Businger-Dyer (Businger et al., 1971; Paulson, 1970) and $z_{0\theta}$ the roughness length of heat. Here, an accurate estimate of $z_{0\theta}$ is essential. In this study, $z_{0\theta}$ is estimated as 1/10 of the roughness length of momentum, which in turn is estimated as 1/8 of the vegetation height (Green et al., 1994).

The method that uses the resistance expressions for H and L_vE is more straightforward. Deriving r_c from these expressions requires more simple additional measurements as those that are required for the previous method. The resistance expressions for H and L_vE read (de Rooy and Holtslag, 1999; Moene and Van Dam, 2012):

$$H = -\rho c_p \frac{\overline{T(z)} - \overline{T_s}}{r_a}, \quad (7.4)$$

$$L_vE = -\rho L_v \frac{\overline{q(z)} - \overline{q_{sat}(T_s)}}{r_a + r_c}, \quad (7.5)$$

where, $T(z)$ is the temperature at height z , $q(z)$ the humidity at height z , T_s the radiative-surface temperature, $q_{sat}(T_s)$ the saturated specific humidity for a given T_s , r_a the atmospheric resistance, and r_c the canopy resistance.

Eqs. (7.4) and (7.5) are based on the assumptions that the air within the stomatal cavity is saturated with water vapour at a temperature T_s (Zeiger et al., 1987) and that the canopy resistance is a resistance that governs the transport from within a hypothetical, big leaf representing the vegetation layer to the surface of that leaf (Moene and Van Dam, 2012). Hence, with measurements of T , T_s , q , the pressure, p , and accurate 1-min estimates of H and $L_v E$, r_c can be solved. Unfortunately, measurements of T_s were not available in our experiment, but we do have measurements of outgoing and incoming long-wave radiation available, so that T_s can be estimated using (de Rooy and Holtslag, 1999; Huband and Monteith, 1986)

$$L^\uparrow = \varepsilon_s \sigma T_s^4 + (1 - \varepsilon_s) L^\downarrow, \quad (7.6)$$

where L^\uparrow is the outgoing long-wave radiation, L^\downarrow is the incoming long-wave radiation, ε_s is the surface emissivity, and σ ($5.67 \times 10^{-8} \text{ W m}^{-2} \text{ K}^{-1}$) is the Stefan-Boltzmann constant. For a wheat field with a completely closed canopy that approaches the heading stage, as is the case for Transregio 2009, $\varepsilon_s = 0.98$ (Chen and Zhang, 1989; Huband and Monteith, 1986; Wittich, 1997).

7.3. Experimental set-up and data treatment

This section describes the three field experiments from which data are used in this chapter and the way the data are processed. The first and main experiment used in this chapter is the Transregio32 project in 2009 (Graf et al., 2010). The measurements took place in a wheat field near Merken, Germany ($50^\circ 50' 53.92'' \text{ N}$, $6^\circ 24' 1.99'' \text{ E}$) between 7 May and 10 June 2009. The dimensions of the field were 350 m by 150 m. In the middle of the field, an eddy-covariance (EC) system, consisting of a CSAT3 sonic anemometer (Campbell Scientific, Logan, USA) and a LiCor7500 H₂O/CO₂ sensor (LiCor, Lincoln, USA), were installed 2.40 m above ground level. Approximately 20 m west of the eddy-covariance tower, we installed a displaced-beam laser scintillometer (SLS-20, Scintec, Rottenburg Germany) at exactly the same height as the eddy-covariance system, with the middle of the scintillometer path centred at the tower. The scintillometer was installed at 2.40 m above ground level as well and had a path length of 120 m. The effective height of the scintillometer linearly decreased from 2.11 m at the beginning of the experiment to 1.84 m at the end of the experiment, due to the growing crop. Long-wave and short-wave radiation were measured at 2 m height in the EC

tower with a four component net-radiation meter, NR01 (Hukseflux, Delft, the Netherlands). During the measurement period, the average temperature was about 15 °C. The amount of precipitation was 60 mm. Furthermore, during daytime the Bowen ratio, β , generally was smaller than 0.6 and z/L_O typically varied between -0.4 and 0.1. Consequently, the wheat was well watered and green during the whole measurement period. For more details about the other measurements and specific set-up features we refer to part I of this study (Van Kesteren et al., 2012a).

The second experiment presented in this chapter is also part of the Transregio32 project. The measurements were performed near Merken (Germany), between 7 August and 30 September 2008 at a sugar-beet field (50° 50' 47.85" N, 6° 23' 50.99" E) (van Dinther, 2009). The set-up was identical to the set-up of the 2009 field experiment. The installation height of both the LiCor7500 H₂O/CO₂ sensor (LiCor, Lincoln, USA) and the scintillometer (SLS-20, Scintec, Rottenburg Germany) was 2.20 m above ground level. Long-wave radiation was measured with a two-component CG1 pyrgeometer (Kipp & Zonen, Delft, the Netherlands) and short-wave radiation was measured with a two-component CM11 pyranometer (Kipp & Zonen, Delft, the Netherlands). The sugar beets were fully grown and about 0.70 m tall. Estimating the displacement height as 2/3 of the crop height (Green et al., 1994), this results in a displacement height of 0.47 m and consequently an effective scintillometer height of 1.73 m. Rain was plentiful during this experiment and the Bowen ratio was typically smaller than 0.5. As for Transregio 2009, the systematic errors in l_o , were corrected by fitting u_{*SLS} to u_{*EC} for 30-min averaging intervals. This resulted in a correction of $u_{*corrected} = (u_{*SLS} - 0.14)/0.3$ (van Dinther, 2009).

The third experiment presented in this chapter is part of the LITFASS-2009 campaign (Beyrich et al., 2012). The aim of this experiment was to study a number of assumptions in the scintillometer data processing and interpretation that still call for a thorough evaluation, in particular over heterogeneous terrain (Beyrich et al., 2012). The LITFASS-2009 field campaign took place around the Meteorological Observatory Lindenberg-Richard-Aßmann-Observatory of the German Meteorological Service (DWD) from 29 June 2009 until 24 July 2009. The experiment used in this chapter took place over a triticale field (52° 10' 54.6" N, 14° 07' 11.0" E), with field dimensions of approximately 500 m by 400 m. The set-up of the experiment presented here was similar to the set-up of the two Transregio32 experiments. The installation height of the LiCor7500 H₂O/CO₂ sensor (LiCor, Lincoln, USA) was 2.90 m above ground level and the scintillometer (SLS-20, Scintec, Rottenburg Germany) was installed 3.15 m above ground level. Furthermore, the scintillometer path length was 110 m.

Long-wave radiation was measured with a two-component CG1 pyrgeometer (Kipp & Zonen, Delft, the Netherlands) and short-wave radiation was measured with a two-component CM11 pyranometer (Kipp & Zonen, Delft, the Netherlands). Triticale is a hybrid of wheat (*Triticum*) and rye (*Secale*). The plants were full-grown (1.2 m) and entered the senescent phase at the beginning of the experiment. Hence, estimating the displacement height as $2/3$ of the crop height, i.e. 0.8 m, the effective scintillometer height was estimated to be 2.35 m. While the triticale plants dried out during the experiment, the typical Bowen ratio increased from 0.9 at the beginning of the experiment to 4.0 at the end of the experiment. The scintillometer u^* was corrected for measurement errors in the same way as it was done for the Transregio 2009 data (wheat), as these experiments took place right after each other and we used the same SLS-20.

All data of all experiments were processed as described in part I and II of this study (Van Kesteren et al., 2012a). The eddy-covariance data were processed using the processing package ECpack from Wageningen University (Van Dijk et al., 2004), for averaging intervals of 1, 2, 3, 4, 6, 20, 15, and 30 minutes. The scintillometer measurements were processed for the same averaging intervals.

The data for the validation with the error analysis are obtained in the same way as was done in Part II. We shortly recall here that the relative systematic error was obtained based on all available data. Furthermore, the relative systematic error with the Ogive technique was determined based on intervals of 4 hours, for each 4-hour period of the whole data set. Finally, the relative random error was obtained based on all cloudless daytime data and fluxes were required to obey the condition $|FCO_2| > 0.5 \text{ mg m}^{-2} \text{ s}^{-1}$ (in total 385 1-min samples).

7.4. Validation of the combined methods

Lenschow et al. (1994) showed that averaging not “long enough” results in an averaging-time-dependent systematic error (underestimation) because of missing larger eddies and a random error (uncertainty) because of having too few independent samples. In this section, we show the results of an error analysis to investigate how well each method approaches the ensemble averaged FCO_2 , as estimated by its 30-min averaged FCO_2 , for short averaging intervals. Furthermore, we validate the combined methods by evaluating the errors in 1-min estimates of FCO_2 with the incoming short-wave radiation. For the results of $L_v E$, we refer to Part II (Van Kesteren et al., 2012b). Finally, the results of the structure-parameter method are validated in more detail with data from wetter and dryer experiments.

7.4.1. Validating the combined methods with an analysis of systematic errors

Figure 7.1 shows the systematic errors in FCO_2 estimated with the combined methods, as a function of averaging time. The combined methods in Figure 7.1a use eddy-covariance (EC) H , u^* , and L_O as “scintillometer” input, whereas in Figure 7.1b they use scintillometer (scinti) H , u^* , and L_O (for input variables used per method, see Table 7.1). $FCO_{2,EC}$ is added as a reference and is identical in both subfigures. The systematic error estimates of the eddy-covariance system are based on ~ 350 hours of data, whereas those of the scintillometer are based on only ~ 150 hours of data, because of instrument malfunctioning during two weeks of the measurement campaign. In addition, the systematic errors in FCO_2 for 1-min averages are shown in Table 7.2 together with the RMSE of the error estimate.

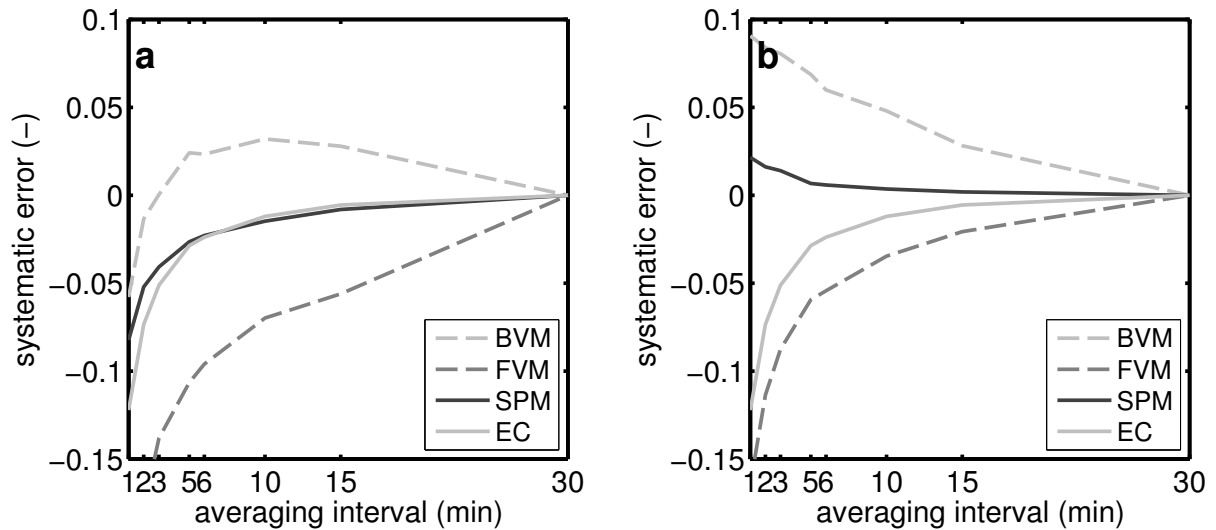


Figure 7.1: Systematic measurement errors in FCO_2 related to averaging interval, (a) using eddy-covariance data for u^* , H and L_O and (b) using scintillometer data. In the legend BVM is the Bowen-variance method, FVM is the flux-variance method, SPM is the structure-parameter method, and EC is the eddy covariance method.

Table 7.2: Systematic errors (SE) in FCO_2 for the combined methods and eddy covariance for 1-min averaging intervals based on regression analysis. In addition the root-mean square error (RMSE) is given to indicate the accuracy of the error estimate. For FCO_2 from the combined methods the error is estimated with H_{scinti} , u^*_{scinti} , and $L_{O,scinti}$ and with H_{EC} , u^*_{EC} , and $L_{O,EC}$. All regression statistics are based on a 95% confidence interval. Shorthand notations of the methods are the same as in Figure 7.1.

	Sonic-anemometer data (EC)		Scintillometer data (scinti)	
	SE (-)	RMSE ($\text{mg m}^{-2} \text{s}^{-1}$)	SE (-)	RMSE ($\text{mg m}^{-2} \text{s}^{-1}$)
FCO_2 BVM	-0.06	1.4×10^{-1}	+0.09	1.1×10^{-1}
FCO_2 FVM	-0.24	1.1×10^{-1}	-0.16	7.3×10^{-2}
FCO_2 SPM	-0.08	4.7×10^{-2}	+0.02	3.1×10^{-2}
FCO_2 EC	-0.12	7.6×10^{-2}		

Before discussing the systematic errors, note that the systematic errors for some of the combined methods are positive, i.e. $\overline{FCO_{2,1\text{min}}}$ ³⁰ overestimates $FCO_{2,30\text{min}}$, instead of negative as we would expect from our definition. This overestimation is related to the fact that in some methods turbulence variables like σ_T and l_0 are inversely and/or non-linearly related to FCO_2 (Van Kesteren et al., 2012b).

If we then proceed to the discussion of the systematic errors, it can be seen that the results for FCO_2 are similar to those in L_vE (Van Kesteren et al., 2012b). Comparing Figure 7.1a with Figure 7.1b shows that the scintillometer outperforms the eddy-covariance method and greatly benefits the accuracy of the FCO_2 estimate. That is, replacing H_{EC} , u^*_{EC} and $L_{O,EC}$ by H_{scinti} , u^*_{scinti} and $L_{O,scinti}$ reduces the systematic error for most combined methods, because H_{scinti} , u^*_{scinti} and $L_{O,scinti}$ virtually have no systematic error (Van Kesteren et al., 2012b).

Unfortunately, using the accurate estimates of the scintillometer does not eliminate the systematic errors in the Bowen-variance and flux-variance method. This happens, because the σ_T and σ_{qCO_2} in these methods have a systematic error (see below). Furthermore, contrary to what the error analysis for L_vE showed (Van Kesteren et al., 2012b), the error for the Bowen-variance method has a smaller systematic error when H_{EC} and u^*_{EC} are used than when H_{scinti} and u^*_{scinti} are used (-0.06 vs. +0.09). The differences between the error in FCO_2 and L_vE , however, indicate the same – the errors in σ_T and σ_{qCO_2} are not identical and do not cancel out against each other. Finally, both methods show some small uncertainty in their mean error estimate ($RMSE_{BVM} = 1.1 \times 10^{-1} \text{ mg m}^{-2} \text{ s}^{-1}$ and $RMSE_{FVM} = 7.3 \times 10^{-2} \text{ mg m}^{-2} \text{ s}^{-1}$). For both methods, the magnitude of the error for a single 1-min interval can differ from the mean error estimate and in case of the Bowen-variance method even can change sign sometimes (especially at night) (Van Kesteren et al., 2012b).

The structure-parameter method does improve upon the eddy-covariance method and the two variance-based methods. The systematic error in FCO_2 is virtually eliminated by using the scintillometer measurements. With the scintillometer H and u^* , the error is only +0.02 ($RMSE = 3.1 \times 10^{-2} \text{ mg m}^{-2} \text{ s}^{-1}$). This small error results from both the accuracy of the scintillometer measurements and the accuracy of the “additional variable” $C_{qCO_2}^2$ (see below).

To clarify how the errors in the additional variables propagate in the flux estimates, we will discuss the systematic errors in the additional variables of the combined methods. We determined the systematic errors, by applying the Ogive technique to high-frequency data of q_{CO_2} , T , and Δq_{CO_2} (Van Kesteren et al., 2012b). As such, we obtained the systematic errors for σ_{qCO_2} , σ_T , and $C_{qCO_2}^2$. Figure 7.2 shows a representative example of the systematic error

for these three variables during daytime. Also the systematic difference of the ratio of σ_T and σ_{qCO_2} , $\sigma_{qCO_2}/\sigma_T = 1/\alpha_\sigma$, is shown, as this ratio directly shows how the errors in σ_{qCO_2} and σ_T propagate into FCO_2 for the Bowen-variance method. For the other methods, the relation between the structure parameter or variance and FCO_2 is direct.

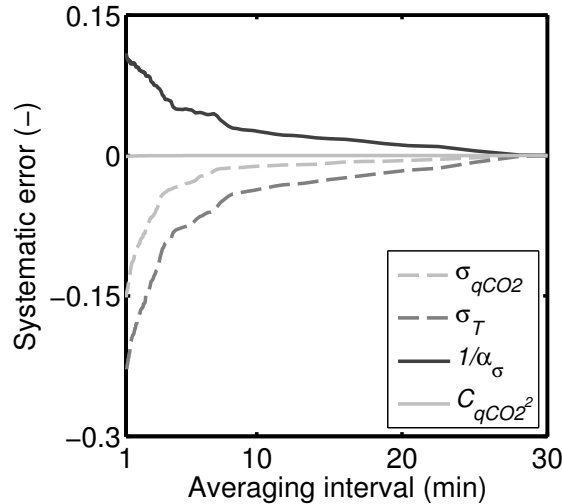


Figure 7.2: Systematic error obtained with Ogive technique, 23rd of May 2009 10:00 UTC – 14:00 UTC.

The systematic errors in the input variables confirm the idea that these variables cause the systematic error in FCO_2 . For 1-min averaging intervals, the systematic error in σ_{qCO_2} is approximately -0.15, diminishing rapidly with increasing averaging interval, whereas the error in σ_T is larger (-0.23) and more persistent. Consequently, the systematic difference in $1/\alpha_\sigma$ is positive and equals the difference between the error in σ_T and σ_{qCO_2} , i.e. a +0.10 error for 1 min averaging intervals.

As σ_{qCO_2} needs a minimum averaging time to reduce the systematic error, FCO_2 will always have a systematic error when estimated with the flux-variance method. Also FCO_2 estimated with the Bowen-variance method will have a systematic error, except for “ideal” conditions when $|r_{TqCO_2}| = 1$. In that case the systematic errors in σ_T and σ_{qCO_2} would be identical and cancel out against each other. However, often the conditions are not ideal. The structure-parameter method is a method that does not suffer from a systematic error, even when $|r_{TqCO_2}| < 1$. $C_{qCO_2}^2$ is only defined for eddies of a size that falls in the inertial sub-range (Tatarskii, 1961) and is evaluated for one particular size, in our case 1 m. Simply because of how $C_{qCO_2}^2$ is defined, it is only sensitive to time scales corresponding to length scales of 1 m or smaller. Consequently, $C_{qCO_2}^2$ is insensitive to larger time scales, which are associated with the systematic error for variances (Figure 7.2).

7.4.2. Validating the combined methods with an analysis of random errors

Similarly to the previous section, we will evaluate the random error in $FCO_{2,EC}$ and in FCO_2 for all combined methods using the scintillometer- and the eddy-covariance H , u^* and L_O . We recall that we estimate the random error based on all cloudless data and a minimum FCO_2 of $0.5 \text{ mg m}^{-2} \text{ s}^{-1}$ (385 samples). We will consider relative random errors and will only use the 1-min averaging intervals in the discussion, see Figure 7.3. The random error in $FCO_{2,EC}$ (~ 0.27) serves as the reference.

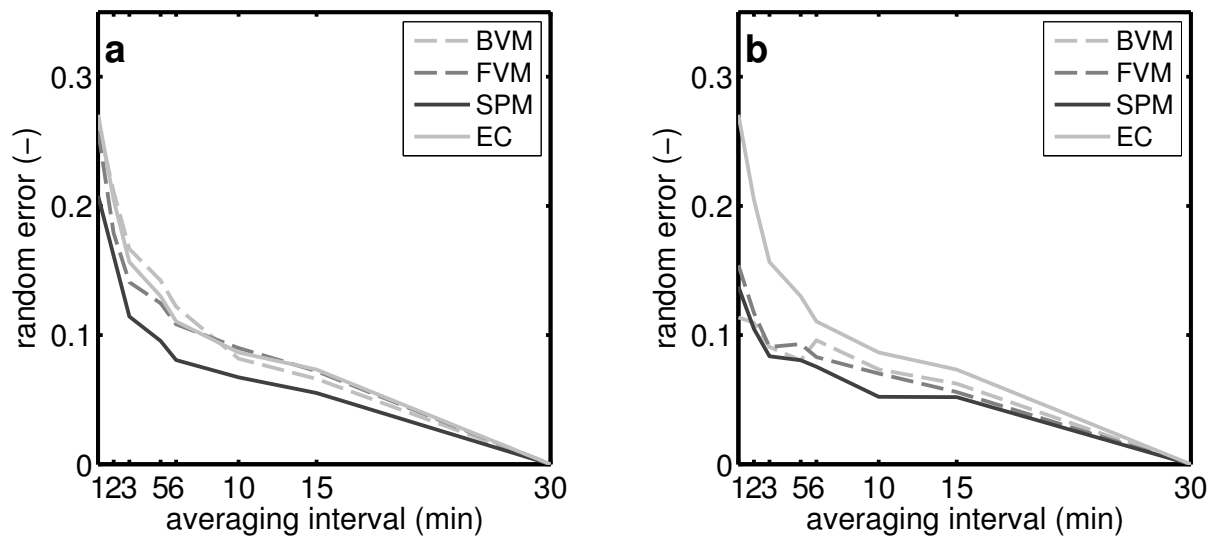


Figure 7.3: Random measurement errors for FCO_2 related to averaging interval, (a) using eddy-covariance data and (b) using scintillometer data. In the legend BVM is the Bowen-variance method, FVM is the flux-variance method, SPM is the structure-parameter method, and EC is the eddy covariance method.

When comparing Figure 7.3a with Figure 7.3b it gets clear that, as for the systematic error, using the scintillometer instead of eddy-covariance measurements greatly reduces the random error in FCO_2 . The random errors in the combined methods using H_{EC} , u^*_{EC} , and $L_{O,EC}$ are ~ 0.23 and these reduce to random errors of ~ 0.14 when the combined methods are evaluated with H_{scinti} , u^*_{scinti} , and $L_{O,scinti}$. The reason for the decreased random error is twofold and can be summarized as a combined effect of reducing the random error by measuring with the scintillometer and reducing the random error by using standard deviations instead of covariances (Lenschow et al., 1994; Van Kesteren et al., 2012b; Wyngaard and Clifford, 1978).

Finally, it should be noted that for all methods, the random errors in FCO_2 are smaller than the random errors in L_vE . The random error in L_vE_{EC} is ~ 0.32 , whereas the random error in $FCO_{2,EC}$ is ~ 0.27 . A similar difference is observed for the combined methods. This difference occurs due to the fact that different criteria for omitting data based on flux magnitude were used, i.e. $L_vE < 30 \text{ W m}^{-2}$ vs. $|FCO_2| < 0.5 \text{ mg m}^{-2} \text{ s}^{-1}$. Therefore, the lower random error of FCO_2 compared to that of L_vE is not caused by a physical difference.

7.4.3. Validating the combined methods with Q_s

In the previous section we showed that the systematic and random errors of the combined methods using scintillometer H and u^* outperform the eddy covariance estimates of FCO_2 for 1-min averaging intervals. From hereon we will therefore only apply the combined methods with the scintillometer H , u^* , and L_O . In this section, we validate the combined methods by considering the correlation between Q_s and FCO_2 as described in section 7.2.3.

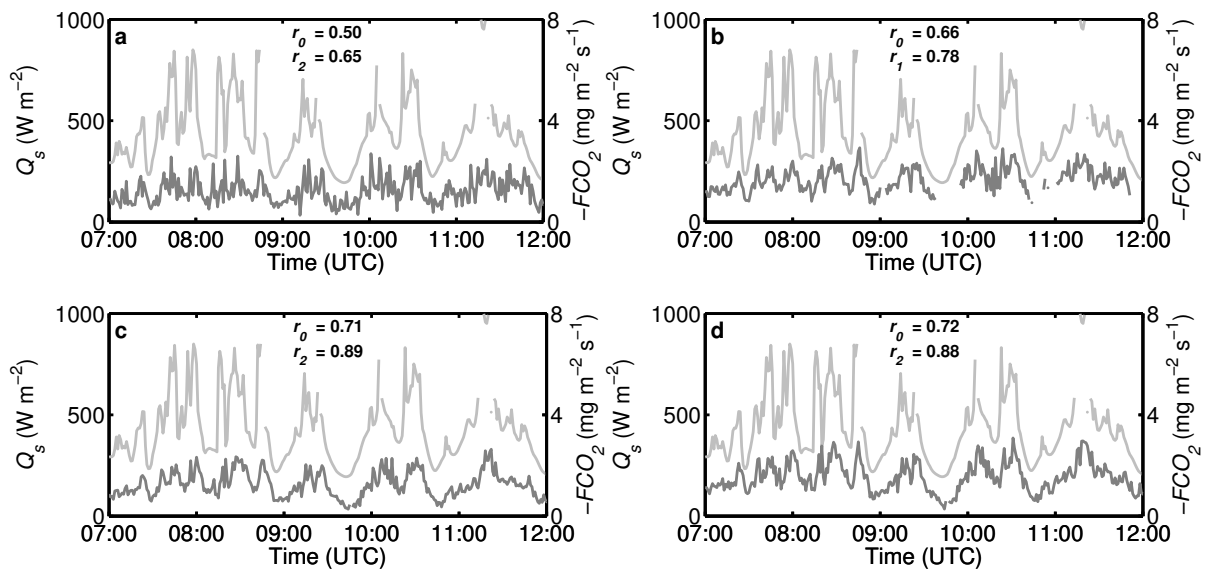


Figure 7.4: 1-minute FCO_2 and incoming short-wave radiation on 4 June 2009, (a) eddy covariance, (b) Bowen-variance method, (c) flux-variance method, and (d) structure-parameter method. In all graphs r is the correlation between the incoming short-wave radiation and FCO_2 . In the figure Q_s is light grey and $-FCO_2$ is grey.

Figure 7.4 shows the time series of 1-min averaged Q_s and $-FCO_2$ between 7:00 and 12:00 UTC on 4 June 2009 with time steps of one minute. Each subfigure represents a different combined method or the eddy-covariance method. The figure depicts a situation during which cloudy and sunny spells rapidly alternate. As a result Q_s fluctuates abundantly and we expect

FCO_2 to follow these sudden fluctuations. Note, that even though Q_s drives FCO_2 we do not expect a perfect correlation between the two variables, because Q_s does not exactly equal the photosynthetically active radiation and light saturation occurs for $Q_s > 300 \text{ W m}^{-2}$ (not shown).

The first impression from Figure 7.4 is that the eddy-covariance and Bowen-variance methods (Figure 7.4a,b) perform worse than the flux-variance and structure-parameter methods (Figure 7.4c,d). In the following, we examine all four methods in detail.

Starting with the eddy covariance method, we see many fluctuations in FCO_2 . The random error is large, but the correlation with zero time lag (r_0) between $-FCO_2$ and Q_s is with 0.50 larger than the correlation between L_vE and Q_{net} (0.34) (Van Keesteren et al., 2012b).

The Bowen-variance method FCO_2 correlates better with Q_s than was the case for the eddy-covariance method. However, 24% of data are missing, because data were omitted when $|r_{TqCO_2}| < 0.2$ or $|\alpha| < 1$. The flux-variance method and structure parameter method perform better than the Bowen-variance method. They both resolve the variations in FCO_2 well, have a higher data availability, and r_0 is higher, i.e. 0.71 and 0.72 respectively.

Note that Figure 7.4a-d besides r_0 , also shows the correlation with a one or two minute time lag (r_1, r_2), i.e. the correlation of $Q_s(t)$ with $FCO_2(t+1)$ or $FCO_2(t+2)$. We determined the optimal time lag, where r_{lag} is maximal. For all four methods, r_{lag} is significantly larger than r_0 , even as large as 0.89 and 0.88 for the flux-variance and structure-parameter methods. In addition, the fact that $r_{lag} > r_0$ implies that the fluxes respond with a delay to changes in Q_s . For each method, except the Bowen-variance method the optimal time lag is two minutes, which therefore likely is the real inertia of the system. The reason why FCO_2 shows a time lag too is discussed in section 7.5.1, here it suffices to say that it is related to the storage capacity of the system.

The above-mentioned results from the validation with the error analysis and the validation with Q_s are in clear agreement with the results from Part II for L_vE . Both FCO_2 and L_vE represent the surface fluxes of a passive scalar, so that we may conclude that the methodology of the combined methods holds for all passive scalars. Furthermore, we conclude that for a given passive scalar in the surface layer the structure-parameter method is the most robust method for measuring the passive-scalar fluxes over 1-min averaging intervals. Unlike the Bowen-variance and flux-variance methods the method does neither suffer from a systematic error, nor requires data to be omitted. Consequently, in the following we will apply the structure-parameter method to extend the final validation to conditions that were wetter and dryer than the conditions used for the previous validation.

7.4.4. Validating the structure-parameter method with Transregio2008 and LITFASS2009 data

In the previous section we validated the combined methods for FCO_2 with data from the Transregio 2009 experiment. In this section, we will do a final validation in which we regard L_vE and FCO_2 . The data used in this section come from Transregio 2008 and LITFASS2009, i.e. for sugar beets under relatively wet conditions and for triticale under relatively dry conditions.

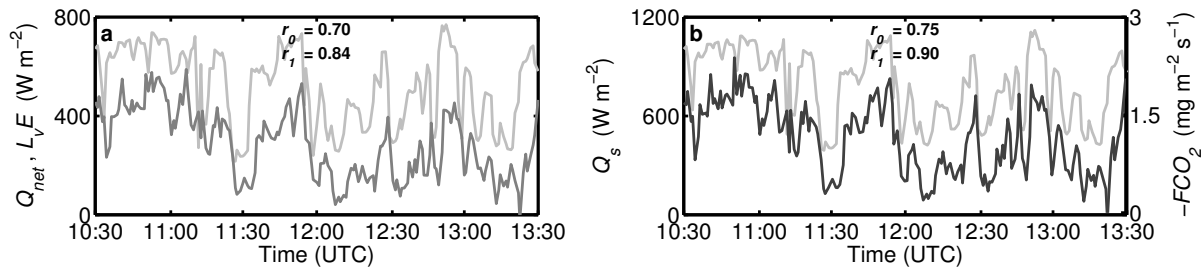


Figure 7.5: Influence of (a) varying net radiation on L_vE and (b) incoming short-wave radiation on FCO_2 for a situation on 14 August 2008 from 10:30 UTC to 13:30 UTC. Measurements were made over sugar beets, the Bowen ratio was about 0.2. In (a) Q_{net} is light grey and L_vE is grey. In (b) Q_s is light grey and $-FCO_2$ dark grey.

Figure 7.5 shows Q_{net} with L_vE (a) and Q_s with FCO_2 (b) over the sugar beets on the 14th of August 2008. Both fluxes show a comparable, high correlation with the radiation ($r_l = 0.84$ and $r_l = 0.90$ for L_vE and FCO_2 respectively). This is similar as to what was observed over the wheat field in the 2009 experiment ($r_2 = 0.80$ for L_vE and $r_2 = 0.89$ for FCO_2). Precipitation characterized the 2008 experiment and the conditions were wetter ($\beta \approx 0.2$) than during the 2009 experiment ($\beta \approx 0.3$). The optimal time lag for the correlation over the sugar beets is one minute, which is one minute faster than was observed over the wheat in the 2009 experiment. Probably this is related to the lower crop density of the sugar beets compared to the wheat. Wheat has a large crop density (in terms of dry and wet matter as well as leaf-area index) and the leafs and the stems form a dense canopy compared to the canopy of sugar beets. Consequently, less storage is possible in sugar beets than in the wheat.

Figure 7.6 shows Q_{net} with L_vE (a) and Q_s with FCO_2 (b) over the triticale on the 9th of July 2009 during the LITFASS-2009 experiment. The triticale was in its senescence phase and slowly dried out during the experiment. Furthermore, the Bowen ratio fluctuated and reached values of about 2.5 during the sunny spells and 0.3 during the cloudy periods. These conditions are drier than during the two Transregio32 experiments. Just as for the sugar beets,

the optimal time lag is one minute. Triticale is a grain, as is wheat, but it has dried out and hence lost some of its storage capacity.

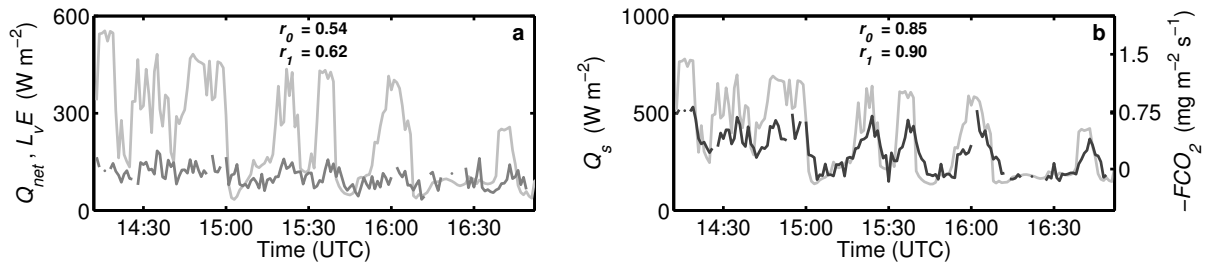


Figure 7.6: Influence of (a) varying net radiation on L_vE and (b) incoming short-wave radiation on FCO_2 for a situation on 9 July 2009 from 14:00 UTC to 17:00 UTC. Measurements were made over triticale, the Bowen ratio varied between 0.3 and 2.5. In (a) Q_{net} is light grey and L_vE is grey. In (b) Q_s is light grey and $-FCO_2$ dark grey.

For L_vE , the correlation is clearly lower than in the previous experiments, $r_l = 0.62$. Also when using the flux-variance method, $r_l = 0.70$ (not shown). However, FCO_2 still has a large correlation with Q_s ($r_l = 0.90$), even though FCO_2 is much smaller than in the previous two experiments (during the cloudy situations respiration dominates over photosynthesis). Also C_q^2 hardly correlates with Q_{net} , whereas $C_{qCO_2}^2$ does correlate with Q_s (not shown). Thus, it seems that in contrast to the CO₂ availability, the water availability is limited, causing the decorrelation of L_vE and Q_{net} . Note, that the different correlations do not indicate that L_vE and FCO_2 have become dissimilar (the combined methods assumes similarity). Similarity only concerns the way the scalars are transported through the atmosphere and it does not require the fluxes to be identical. This will be illustrated in the next section.

7.5. Applications of 1-min evapotranspiration and CO₂ fluxes

In this section, we will apply the structure-parameter method to study flux responses and vegetation responses under non-stationary conditions. From here onward, we will use the Transregio-2009 data again (winter wheat) and consider 1-min averaging intervals. We will start with using the method to discuss the different responses of L_vE and FCO_2 upon decreased radiation. Then, we will discuss the relevance of determining light-response curves based on 1-min averaging intervals. Finally, we will determine 1-min averaged canopy resistances and discuss plant behaviour for two days with significantly different atmospheric conditions.

7.5.1. Exploring mechanisms that drive L_vE and FCO_2

Section 6.4.2.3 shows that close to the surface, the flux forcings mainly affect the variations in humidity, but not the atmospheric turbulence, i.e. the transport mechanism. This is in line with findings in literature, which show different responses of the surface fluxes to changes in radiation (Foken et al., 2001; Mauder et al., 2007). In the following, we will use the 1-min fluxes to study the flux responses upon an almost instantaneous change in radiation (a step response). The 1-min fluxes enable us to do a detailed study of the flux response and discuss the mechanisms that cause L_vE and FCO_2 to respond differently upon changes in radiation.

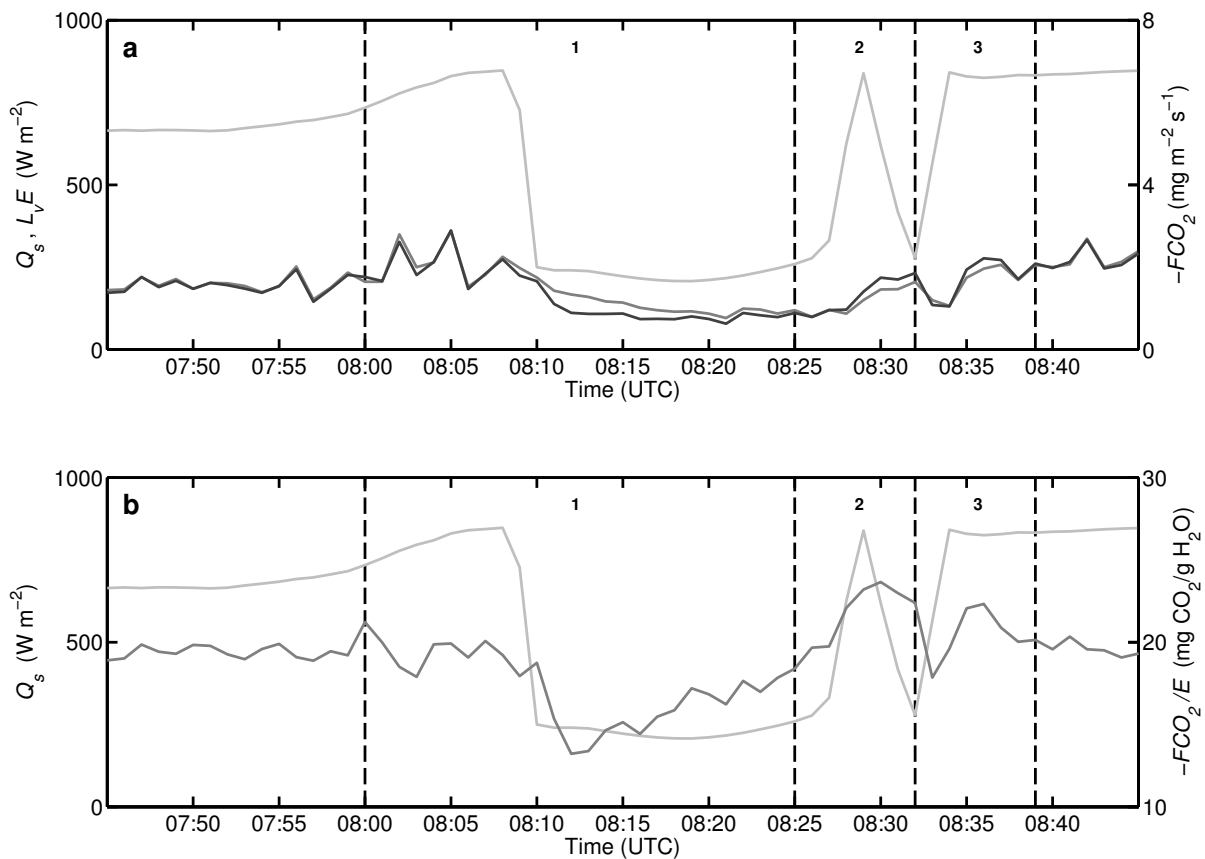


Figure 7.7: Influence of varying incoming short-wave radiation on L_vE and FCO_2 for a situation on 5 June 2009 from 7:00 UTC to 10:30 UTC. (a) showing both L_vE and FCO_2 (b) showing the ratio of FCO_2 and E . In (a) Q_s is light grey, L_vE is grey, and $-FCO_2$ is dark grey. In (b) Q_s is light grey and $-FCO_2/E$ is grey.

To this end, we introduce Figure 7.7, which compares L_vE and FCO_2 with Q_s for the same situation as in the previous section. Figure 7.7a shows Q_s with L_vE and $-FCO_2$ plotted such that they overlap and Figure 7.7b shows Q_s with the ratio of $-FCO_2$ and E ($E = L_vE/L_v$). This ratio is similar to the water-use efficiency, but we did not correct for the respiration flux (in

this case $\sim 0.3 \text{ mg m}^{-2} \text{ s}^{-1}$). Finally, three specific events are marked in order to guide the analysis.

During the first event, Q_s suddenly drops (8:08 UTC) and Figure 7.7a shows that after 8:10 UTC FCO_2 drops more rapidly than L_vE . FCO_2 collapses in four minutes (including the time lag of 2 min), whereas L_vE requires 10-15 minutes to adapt to the new radiation regime. Also during event 2 and 3 FCO_2 reacts more pronounced on changes in Q_s than L_vE . The same is reflected in Figure 7.7b. Already from 6:30 UTC onward the ratio FCO_2/E fluctuates around $19 \text{ mg CO}_2/\text{g H}_2\text{O}$ (cf. Baldocchi (1994b) who found $11 \text{ mg CO}_2/\text{g H}_2\text{O}$) and when FCO_2 and L_vE respond to the changed radiative forcing the ratio clearly deviates from this mean (from 8:10 UTC onward). From this we can conclude that it are not the plant stomata that cause the change in C_q^2 and $C_{qCO_2}^2$. Otherwise, both structure parameters would react identically and the fluxes would change in a similar way. We checked this by determining the canopy resistance as described in section 7.2.4 and found that the canopy resistance remained constant during these events (not shown).

For FCO_2 , these results are similar to Foken et al. (2001) over maize and Mauder et al. (2007) over cotton, who upon a solar eclipse estimated the delay of FCO_2 to be $<5 \text{ min}$ and $<3 \text{ min}$, i.e. almost immediate. The 2-min time lag (delay) in FCO_2 is probably caused by the CO₂-storage changes in the lower two meters of the atmosphere and in the vegetation.

For L_vE , our results are neither as long as the 25 min delay found by Foken et al. (2001), nor as short as the immediate response found by Mauder et al. (2007). For H a similar pattern as for L_vE is observed (not shown). First there is a 2-min time lag, which is caused by flux-storage changes. This time lag is followed by a drop of H in 3 minutes, which accomplishes 67% of the total change in the flux. Finally, the response ends with a gradual decrease of H and L_vE in 6-7 minutes. This brings the total response time at 11-12 minutes. For H , Foken et al. (2001) found a response time of 5 minutes and Mauder et al. (2007) found a response time of 8-13 minutes, of which the latter is more in agreement with our observations.

However, we do not expect identical response times. Firstly, note that in our case the radiation decreases in less than 2 minutes (causing a step response), whereas in case of the solar eclipse it takes about one to one-and-a-half hour to get a similar decrease (causing a sine response). Furthermore, the heat capacity of systems differ, depending on the crop in question, development stage of the crops, atmospheric conditions, drought etc. In our case, storage of heat in the soil, the wheat plants, and in the air, makes that the energy for H and L_vE remains available even though Q_s dropped. Slowly, this energy is released (the surface

temperature slowly decreases), so that H and L_vE gradually decrease during the 5-12 minutes after the initial drop in Q_s . In the case of Mauder et al. (2007) the eclipse causes that this stored energy is already partly released during the different stages of the eclipse. In case of Foken et al. (2001), the delay he determines is related to a dip in the wind speed, rather than being related to the eclipse. In considering their Figure 2b it can be seen that L_vE peaks about 5 minutes after a peak in radiation caused by clouds, which is more similar to what we find.

Summarizing the above, it is clear that solar radiation plays a more active role in determining FCO_2 than in determining L_vE . The photosynthesis rate, a bio-chemical rate, is directly affected by the solar radiation. As this rate determines the amount of CO_2 taken up by the plant, and with that FCO_2 , there is a direct link between Q_s and FCO_2 . The effect of CO_2 -storage changes on FCO_2 is small, but large enough to cause the 2-minute time lag in FCO_2 . For L_vE the link with Q_s is less direct, because L_vE is passively lost through the open plant stomata. The effect of L_vE -storage changes causes a 2-minute time lag in L_vE as well. However, as long as there is energy available, through heat-storage release, L_vE will not decrease as fast as FCO_2 .

7.5.2. Light-response curves

Light-response or radiation-response curves are plots of Q_s with $-FCO_2$. They are a measure of how efficient plants can photosynthesise for a given light intensity. These curves differ among crops and depend on atmospheric conditions (Gilmanov et al., 2003; Kim and Verma, 1990; Moene and Van Dam, 2012; Nieveen et al., 1998b). The advantage of determining these curves based on 1-min data is that only one morning is required to accurately determine a light response curve instead of one month. During one morning the development stage of the crop and atmospheric conditions are more constant than during one month and as such it becomes easier to study light response curves for specific conditions.

This is illustrated in Figure 7.8. Figure 7.8 shows the light-response curves based on 1-min measurements of FCO_2 for two mornings early in June 2009 over wheat, i.e. a cloudless morning on 1 June 2009 from 3:15 UTC until 10:00 UTC and a cloudy morning on 3 June from 3:15 UTC until 10:30 UTC. On the cloudless day the temperature increased from 11 °C to 22 °C and the water-vapour deficit, wvd , increased from $wvd \approx 0$ hPa to $wvd \approx 10$ hPa, whereas on the cloudy day the temperature increased from 10 °C to 15 °C and wvd increased from $wvd \approx 0$ hPa to $wvd \approx 5$ hPa. As can be seen the light saturation is higher for the cloudy morning with the lower wvd (cf. Kim and Verma (1990) and Nieveen et al. (1998b)). This is

related to the fact that the lower the wvd the better the water-use efficiency of crops (e.g. (Baldocchi, 1994b; Nieveen, 1999). As L_vE had a similar magnitude on both days, and the water-use efficiency was higher on the cloudy day with the low wvd , the light saturation is higher for that day. Note, that a low wvd and cloudy conditions are closely related, because the temperature usually remains low during cloudy conditions. In addition, cloudy conditions benefit the light-use efficiency of vegetation, because there is more diffuse radiation than during unclouded conditions (Gu et al., 2002).

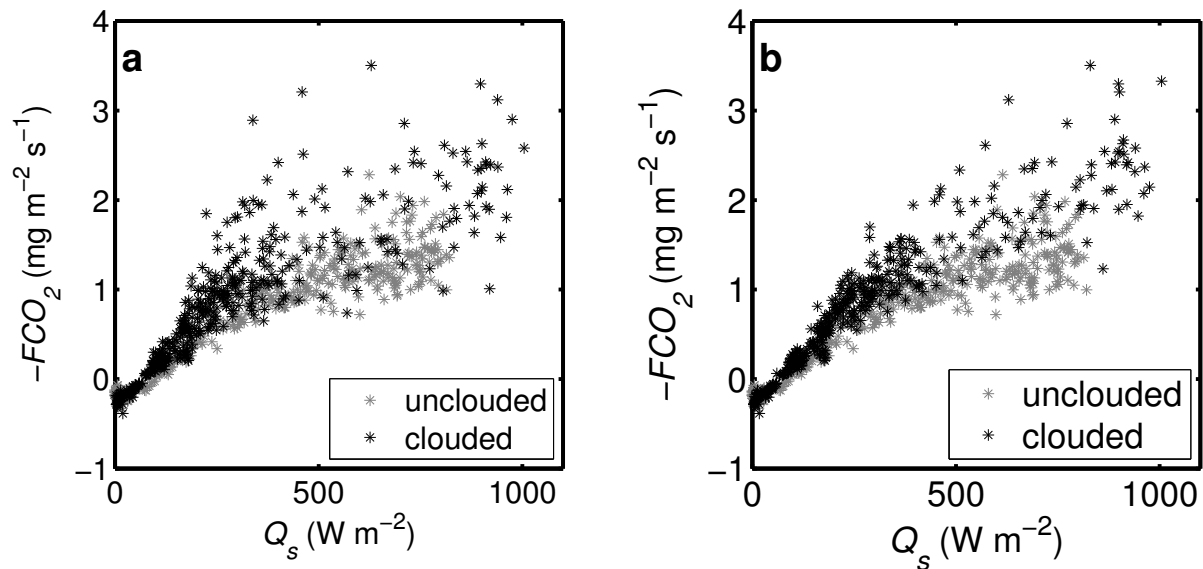


Figure 7.8: Light-response curves for wheat on a cloudy morning (3 June 2009) and on a cloudless morning (1 June 2009), (a) without time-lag correction and (b) with time-lag correction.

Another aspect that is shown by Figure 7.8 is the importance of taking account the 2-min time lag of $-FCO_2$ compared to the radiation, i.e. plotting $Q_s(t)$ vs. $FCO_2(t+2)$. Figure 7.8a shows the light-response curves for which the time-lag has not been taken into account and Figure 7.8b shows the light-response curves for which the time-lag has been taken into account. Clearly, the scatter of the response curve from the cloudy situation is reduced by taking into account the time lag. Taking into account this time lag is not only relevant for working with 1-min fluxes, but also for determining light-response curves based on 30-min averaging intervals. For the cloudy conditions, the differences between $\overline{FCO_2(t)}^{30}$ and $\overline{FCO_2(t+2)}^{30}$ randomly varies between -3% and +7%.

7.5.3. Canopy resistance on 1-min time scales

This section discusses the results of the 1-min averaged canopy resistance. Figure 7.9a1 and Figure 7.9b1 show Q_s , together with L_vE and H , whereas Figure 7.9a2 and Figure 7.9b2 show r_c . For this discussion, we selected two events. A day that was almost cloudless, 2 June 2009 (Figure 7.9a), and a day that had a variable cloud cover, 4 June 2009 (Figure 7.9b). To estimate r_c , we followed the procedure outlined in section 7.2.4, using the resistance expressions for H and L_vE .

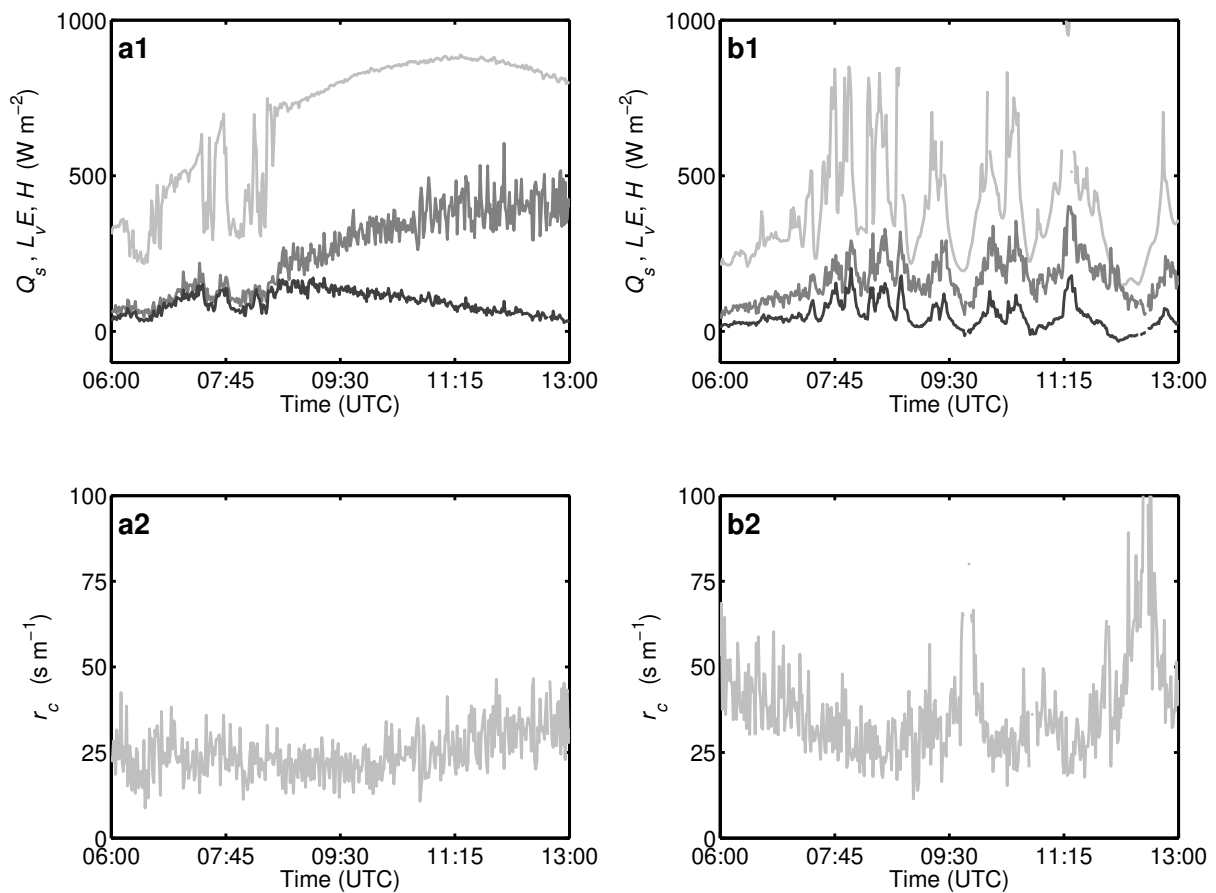


Figure 7.9: 1-min values for the canopy resistance of wheat for (a) 2 June 2009 and (b) 4 June 2009. (a1) and (b1) show the incoming short-wave radiation, Q_s , together with the fluxes H and L_vE , (a2) and (b2) show the canopy resistance, r_c , for the corresponding time. In (a1) and (b1) Q_s is light grey, L_vE is grey and H is dark grey.

Starting with 2 June 2009, it can be seen that L_vE increases until 12:15 UTC and then slowly levels off, whereas H decreases from about 8:30 UTC. On the other hand, r_c is more or less constant. It fluctuates slightly during the clouded periods, reaches a minimum around 9:30 UTC and increases afterwards. Furthermore, r_c shows some noise, which is mainly caused by the noise in the L_vE measurements. These estimated values for r_c are slightly lower than found

by Baldocchi (1994a), who found values typically between 50 and 100 s m⁻¹, and more comparable to Hatfield (1985) who found typical afternoon values of less than 30 s m⁻¹ in the shade. However, r_c strongly depends on the atmospheric conditions, soil and crop properties like the leaf-area index (Baldocchi, 1994a; Hatfield, 1985). Hence, we can safely assume that r_c is accurately resolved by this method.

Probably, r_c increases after 9:30 UTC, because plants reduce their stomatal aperture on large water loss (large L_vE) (Monteith, 1995; Mott and Parkhurst, 1991). The air gets drier and $wvd \approx 10$ hPa, corresponding to a relative humidity, RH , of about 50%-60%. When plotting r_c against wvd a clear relation was observed (not shown), whereas no clear relation was observed between r_c and Q_s (not shown).

On the cloudy day both L_vE and H correlate well with Q_s . Note, that before 13:00 UTC H is negative for a while, which is a sign that warm air is advected. The response of r_c differs from that in the previous situation. First, r_c decreases and then from 9:30 UTC on r_c starts to fluctuate. The peaks in r_c coincide with dips in Q_s , albeit that the peaks lag approximately 5 minutes behind. Estimating the elapsed time between the base and top of the peaks leads to the conclusion that the wheat vegetation achieves the maximum change in r_c in about 20 minutes. In section 6.4.2.3 we show that this is a feasible stomatal response time from a plant-physiological point of view, but also that the factual vegetation response strongly depends on many aspects. In contrast to the situation in Figure 7.9a, the air is more humid ($RH > 75\%$) during the situation in Figure 7.9b and no clear relation between r_c and wvd is observed (not shown), whereas a relation between r_c and Q_s is clearly observed (not shown).

Finally, we want to mention that with the inverted Penman-Monteith method, by taking into account the time-lags of H , L_vE , and G , we could reproduce r_c for the cloudy day, albeit with more scatter (not shown). During this day, $H(t+2)+L_vE(t+2)$ scattered around the 1:1 line when plotted against $Q_{net}(t) - G(t+4)$, indicating a closure of the energy balance. For the cloudless day, we could not reproduce these results, because $Q_{net}(t) - G(t+4) > H(t+2)+L_vE(t+2)$, i.e. the energy balance did not close. Non-closure of the energy balance occurs in many experiments, so great care must be taken when using the inverted Penman-Monteith Method. Thus, we conclude that through the resistance expressions for H and L_vE , the structure-parameter method most accurately solves 1-min averaged r_c and can be usefully applied to study vegetation responses in the field.

7.6. Conclusions

This chapter discussed three combined methods for estimating 1-min averaged FCO_2 and L_vE that can be used to evaluate these fluxes under non-stationary conditions. To validate the combined methods and determine their accuracy, we performed an extensive error analysis. Based on the error concepts of Lenschow et al., (1994), we determined the averaging-time-dependent systematic and random error in FCO_2 for averaging intervals varying from 1 to 30 minutes. Furthermore, we evaluated the combined methods with Q_s . Finally, we used the structure-parameter method to study flux responses and vegetation responses under non-stationary conditions.

The validation was based on the data from a wheat field near Merken (Germany), gathered in the framework of the Transregio32 experiment in 2009. Furthermore, an additional validation of the structure-parameter method was based on data from a wet sugar beet field near Merken gathered in the framework of Transregio32 in 2008 and data from a dry triticale field near Lindenberg (Germany) gathered in the framework of the LITFASS-2009 experiment.

The validation results of the FCO_2 estimates are in agreement with those of L_vE as shown in Part II. The error analysis shows that the eddy-covariance method suffers from an averaging-time-dependent systematic error (-0.12 for 1-min averaging intervals). Similarly, the errors in the flux-variance method and the Bowen-variance method are -0.16 and +0.09, respectively. The structure-parameter method, however, has a negligible systematic error in FCO_2 (+0.02). Similarly, we discussed the averaging-time-dependent random error in FCO_2 estimated with the combined methods. For 1-min averaging intervals, the random error of the combined methods is about half the random error of the eddy-covariance method.

The evaluation with Q_s showed that the flux-variance method and structure-parameter method resolve the fluctuations in FCO_2 better than the Bowen-variance method and eddy-covariance method. Based on these results for FCO_2 and the previous results in Part II for L_vE , we conclude that the results obtained with these methods should be valid for any passive scalar. Furthermore, we conclude that the structure-parameter performs best in resolving the fluxes of these passive scalars.

For a final, more extensive evaluation, we therefore applied the structure-parameter method to other experiments as well. It was shown that over sugar beets during wet conditions ($\beta \approx 0.2$), the method performed equally well in determining L_vE and FCO_2 as over the wheat field. During dryer conditions (β fluctuating between 0.3-2.5) L_vE did not correlate well with Q_{net} , because C_q^2 did not correlate with Q_{net} . L_vE was small and thus sensitive to disturbances.

FCO_2 , however, correlated as well with Q_s as during the other experiments and $C_{qCO_2}^2$ did do so too.

Having finished the validation, we investigated the relevance of 1-min fluxes under non-stationary conditions, for several applications. First, we showed that L_vE and FCO_2 respond differently to abrupt changes in solar radiation. Both fluxes lag 2 minutes behind the radiation, because of storage of water vapour and CO_2 in the vegetation and atmosphere below our sensors. After these two minutes, FCO_2 almost immediately responds to a change in radiation, because the available radiation directly affects the chemical rate of photosynthesis and with that the CO_2 uptake. L_vE on the other hand shows a more dampened response, because stored (heat) energy still benefits L_vE (through the surface temperature) and the canopy resistance did not change. Therefore, L_vE (and H) change more gradually upon changes in the radiation than FCO_2 . Of course these findings depend strongly on the data set, because for the two other datasets, the time lag for example was found to be 1 minute instead of 2 minutes.

Second, we studied light-response curves of the wheat canopy for a cloudy and unclouded morning and showed that the light-saturation level was significantly higher during the cloudy morning (as expected). This happened, because during the cloudy morning the water-vapour deficit was higher and with that the water-use efficiency. Furthermore, there was more diffuse radiation, all factors that benefit the light efficiency of the vegetation. In addition, we showed that especially during cloudy conditions it is crucial to take into account the possible time-lag between FCO_2 and Q_s . Even when determining curves based on 30-min Q_s and FCO_2 not taking into account the time lag can lead to errors that in our case randomly varied between -3% and +7%.

Third, we applied the structure-parameter method to study the 1-min averaged values of the canopy resistance. It was shown that via the resistance expressions for H and L_vE , the structure-parameter method accurately resolves 1-min r_c . Depending on the atmospheric conditions, r_c was driven by either the radiation or by the magnitude of L_vE (water-vapour deficit). Thus, it was shown that plants indeed modify their canopy resistance and thus modify turbulent fluxes on time intervals shorter than 30 minutes. By taking into account the time lags in H , L_vE and G compared to Q_{net} , the inverted Penman-Monteith method could also be used to resolve 1-min r_c , but the accuracy of this method is very sensitive to non-closure of the energy balance.

8. General discussion and perspective

Exploring the borders of Monin-Obukhov similarity theory

Monin-Obukhov similarity theory (MOST) is a key part in deriving the surface fluxes from the structure parameters that are measured with the scintillometers. The theory has been extensively described in this thesis (section 2.1.4). There, it has been shown that by assuming quasi-steady state, horizontal homogeneity, no flux divergence, no radiation divergence, and no pressure flux, the atmospheric flow equations can be simplified to a balance between the production and destruction terms (Wyngaard and Kosovic, 1994). Subsequently, when made dimensionless, dimensionless groups can be formed from these equations, which relate the structure parameter of a given quantity to its surface flux. Once this relation is accurately determined (a so-called MOST function) it should be universally applicable. A similar approach holds for variances, which is shown by the flux-variance method and Bowen-variance method in chapter 5. In determining the evapotranspiration or fluxes of other scalars, there is an extra assumption involved: temperature is assumed to be transported passively by the turbulence and any other passive scalar should thus behave similar as temperature.

Unfortunately, the validity of the assumptions behind this theory is often neglected, which in the literature leads to a “cacophony” of MOST-functions. The errors, depending on the cause of dissimilarity greatly vary (<20% up to >200%). Katul et al. (2008) lists five reasons why dissimilarity occurs:

1. Active roles of temperature and water vapour
2. Advective conditions
3. Modulations from the outer layer (and unsteadiness)
4. Dissimilarity in ground sources and sinks
5. Entrainment processes

Here we want to add one extra in case we are talking about chemical quantities (Vilà-Guerau de Arellano et al., 1995):

6. chemical reactions

It may appear obvious that systematic approaches have a great benefit here. However, until now such studies are rare. Most studies that deal with this subject qualitatively describe

possible reasons for their observed dissimilarity (for references see Katul et al. (2008)), but hardly any of them has been able to do any quantification of e.g. advection or entrainment and their influence on the MOST-functions. Our suggestion is to take the dimensionless groups that are derived from the gradient functions, i.e. Eqs. (2.72), (2.73), and (2.74), as a starting point. With for example large-eddy simulation models (high resolution needed) it is possible to quantify the effect of simple heterogeneity or entrainment. Also by doing a systematic analysis of data from for example the FLUXNET database, it is possible to do a systematic analysis of the MOST functions through site selection, e.g. ideal sites, or sites with advection etc. Finally, we see the need of a similar systematic approach for studying the applicability of MOST under heterogeneous conditions. The research presented in this thesis was limited to field scales, for which terrain is usually homogeneous. However, the other part of the STW project focussed on the applicability of scintillometry over kilometre scales, for which terrain is almost always heterogeneous. Studies of Meijninger et al. (2006; 2002a; 2002b) showed promising results of the applicability of MOST under slightly and moderately heterogeneous conditions, but we feel that a more systematic approach still is required.

Measuring scalar fluxes over heterogeneous terrain

The combined methods that we introduced for measuring evapotranspiration, the CO₂ flux, or fluxes of any other passive scalar work only for homogeneous conditions. Future work could go in the direction of measuring fluxes also over heterogeneous terrain. One possible solution for that lays in the combination of scintillometer measurements and differential optical absorption spectroscopy (DOAS) measurements or tuneable diode-laser absorption spectroscopy (TDLAS) measurements. The advantage of the scintillometers is that they can measure over the same path as the DOAS/TDLAS systems. By measuring a gradient with two DOASs/TDLASs and determining turbulence characteristics with the scintillometer, it is possible to infer fluxes of e.g. CO₂, NH₃, NO₂, SO₂ even over heterogeneous landscapes.

Further development of the scintillometer technique

In his thesis (2006) Hartogensis suggests the use of photosensitive chips for improving measurements of the inner scale, l_0 . When determining l_0 with a displaced-beam scintillometer or with a scintillometer that has two beams with different apertures as presented in this thesis, saturation and sensitivity issues will always limit the scintillometer application to scintillometer paths shorter than 500 m. Based on the work of Hill (1982) and Frehlich

(1992), the problem could be circumvented by using an array of scintillometers. Nowadays, mirrors or high-quality lenses are used to focus a beam on a small detector, making the application of this technique difficult. However, with e.g. CCD cameras or CMOS cameras, single pixels could serve as infinite small apertures, while at the same time aperture averaging can be performed over a multitude of pixels. In this way all kind of scintillometer combinations can be made, including arrays of scintillometers. Furthermore, the angle-of-arrival could also be determined with these cameras. The technical requirements for such a technique are high, but the work of Flach (2000) and Cheon et al. (2007) showed promising results for the application of CCD cameras.

Exploring the high-frequency part of the turbulence spectrum

Since the first high-frequency measurements of temperature were published in the late 1970s it is clear that the turbulence spectrum does not simply decay with an r^2 law as was predicted by the famous theory of Kolmogorov, but displays a bump (see section 2.1.3.2). For scintillometry, research from Hill (Hill, 1978a) and colleagues (Hill, 1978b; Hill and Clifford, 1978) showed the relevance of taking this spectral bump into account. However, in many other areas of science the existence of this spectral bump was unnoticed until Falkovich (Falkovich, 1994) published his paper on bottleneck phenomena, denoting the same feature with it. Since then direct-numerical-simulation (DNS) models have been more frequently used to study this phenomenon and a good overview of what is known at this time can be found in (Coantic and Lasserre, 1999; Donzis and Sreenivasan, 2010; Verma and Donzis, 2007).

However, it seems that until now both communities (scintillometer- and DNS communities) have proceeded mainly unaware of each other and many questions regarding this bump still remain open. First of all, many physical explanations have been suggested (Donzis and Sreenivasan, 2010; Verma and Donzis, 2007; Williams and Paulson, 1977), but up to the present day no consensus has been reached. This indicates that the bump is in fact not yet really understood. Second, back in the 1970s tremendous efforts have been made to make these measurements possible. Unfortunately, because of the technique of that time they were neither able to store long periods of these high-frequency data, nor had the computer power to extensively analyse these data. We, however, do have the computer storage and power, but lack the accurate measurement devices. Furthermore, DNS models can simulate flows for Reynolds numbers up to say 1000, but this is still far away from the turbulence that occurs in the real atmosphere. Hence, we see possibilities for progress, first by getting the two

communities into contact and sharing expertise and second, by doing high precision temperature and velocity measurements for more extended periods of time. These measurements are not only possible via hot and cold wires, but indirectly also by using scintillometers. Hartogensis (2006) showed that laser and small-aperture scintillometers are highly sensitive to this bump, so that feature can be used.

The energy-balance closure

Much has been said about this theme and equally much research has been done in this field. Foken (2008) gives an overview of the problem and concludes that exchange processes on the larger heterogeneous scale cause the non-closure. Large-eddy-simulation modelling has confirmed this and shown that turbulent organized structures can be responsible for this (Kanda et al., 2004). However, Heusinkveld et al. (2004) showed that the closure was very good over a desert area. Of course this area has a homogeneous surface, but still these turbulent organized structures are expected to exist there as well. In the evaluation of the energy balance in chapters 5, 6, and 7 we found that taking heat-storage terms into account, accurately measuring the soil-heat flux, and taking into account the energy equivalent of the carbon-dioxide flux already greatly improved the closure. A similar conclusion was drawn by Jacobs et al. (2008). Franssen et al. (2010) conclude that storage is only important for nighttime closure and that the non-closure is greatest for convective circumstances, which supports again the hypothesis of turbulent organized structures. However, the diversity of solutions shows that likely more than one cause lays behind the non-closure problem. Therefore, we feel that it is important to take this into account in approaching the problem, rather than trying to search for one solution. Finally, we give a short note on short time intervals. For 1-minute time intervals the whole energy-balance closure gets more complex and the assumption of closure can usually not be made. On these short time intervals, processes that are irrelevant for 30-minute time intervals can get relevant. As was shown in chapter 6 and 7, this is important to take into account in applications that assume the energy-balance closure.

9. References

- Andreas, E.L., 1988. Estimating C_n^2 over snow and sea ice from meteorological data. *J. Opt. Soc. Am.*, 5(4): 481-495.
- Andreas, E.L., 1989. Two-wavelength method of measuring path-averaged turbulent surface heat fluxes. *J. Atmos. Oceanic Technol.*, 6: 280-292.
- Andreas, E.L., Fairall, C.W., Persson, P.O.G. and Guest, P.S., 2003. Probability distributions for the inner scale and the refractive index structure parameter and their implications for flux averaging. *J. Appl. Meteorol.*, 42(9): 1316-1329.
- Andreas, E.L., Hill, R.J., Gosz, J.R., Moore, D.I., Otto, W.D. and Sarma, A.D., 1998. Statistics of surface-layer turbulence over terrain with metre-scale heterogeneity. *Boundary-Layer Meteorol.*, 86(3): 379-408.
- Andrews, L.C., 1992. An Analytical Model for the Refractive-Index Power Spectrum and Its Application to Optical Scintillations in the Atmosphere. *J. Mod. Optics*, 39(9): 1849-1853.
- Asanuma, J. and Iemoto, K., 2007. Measurements of regional sensible heat flux over Mongolian grassland using large aperture scintillometer. *J. Hydrol.*, 333(1): 58-67.
- Aubinet, M., 2008. Eddy covariance CO₂ flux measurements in nocturnal conditions: An analysis of the problem. *Ecol. Applic.*, 18(6): 1368-1378.
- Baldocchi, D., 1994a. A Comparative-Study of Mass and Energy-Exchange over a Closed C-3 (Wheat) and an Open C-4 (Corn) Canopy .1. The Partitioning of Available Energy into Latent and Sensible Heat-Exchange. *Agric. Forest Meteorol.*, 67(3-4): 191-220.
- Baldocchi, D., 1994b. A Comparative-Study of Mass and Energy-Exchange Rates over a Closed C-3 (Wheat) and an Open C-4 (Corn) Crop .2. CO₂ Exchange and Water-Use Efficiency. *Agric. Forest Meteorol.*, 67(3-4): 291-321.
- Baldocchi, D., Falge, E., Gu, L., Olson, R., Hollinger, D., Running, S., Anthoni, P., Bernhofer, C., Davis, K., Evans, R., Fuentes, J., Goldstein, A., Katul, G., Law, B., Lee, X., Malhi, Y., Meyers, T., Munger, W., Oechel, W., Paw, U.K.T., Pilegaard, K., Schmid, H.P., Valentini, R., Verma, S., Vesala, T., Wilson, K. and Wofsy, S., 2001. FLUXNET: A New Tool to Study the Temporal and Spatial Variability of Ecosystem-Scale Carbon Dioxide, Water Vapor, and Energy Flux Densities. *Bull. Am. Meteorol. Soc.*, 82(11): 2415-2434.
- Baldocchi, D.D., 2003. Assessing the eddy covariance technique for evaluating carbon dioxide exchange rates of ecosystems: Past, present and future. *Global Change Biol.*, 9(4): 479-492.
- Bastiaanssen, W.G.M., Pelgrum, H., Droogers, P., De Bruin, H.A.R. and Menenti, M., 1997. Area-average estimates of evaporation, wetness indicators and top soil moisture during two golden days in EFEDA. *Agric. Forest Meteorol.*, 87(2-3): 119-137.
- Beyrich, F., Bange, J., Hartogensis, O.K., Raasch, S., Braam, M., van Dinther, D., Gräf, D., Van Kesteren, B., Van den Kroonenberg, A.C., Maronga, B., Martin, S. and Moene, A.F., 2012. Towards a Validation of Scintillometer Measurements: The LITFASS-2009 Experiment. *Boundary-Layer Meteorol.*, 144(1): 83-112.
- Beyrich, F., De Bruin, H.A.R., Meijninger, W.M.L., Schipper, J.W. and Lohse, H., 2002. Results from one-year continuous operation of a large aperture scintillometer over a heterogeneous land surface. *Boundary-Layer Meteorol.*, 105(1): 85-97.
- Beyrich, F., Leps, J.P., Mauder, M., Bange, J., Foken, T., Huneke, S., Lohse, H., Ludi, A., Meijninger, W.M.L., Mironov, D., Weisensee, U. and Zittel, P., 2006. Area-averaged surface fluxes over the LITFASS region based on eddy-covariance measurements. *Boundary-Layer Meteorol.*, 121(1): 33-65.
- Bosveld, F.C. and Beljaars, A.C.M., 2001. The impact of sampling rate on eddy-covariance flux estimates. *Agric. Forest Meteorol.*, 109(1): 39-45.
- Brutsaert, W., 1982. *Evaporation into the atmosphere*. Kluwer academic publishers, Dordrecht, the Netherlands, 299 pp.
- Businger, J.A., Wyngaard, J.C., Izumi, Y. and Bradley, E.F., 1971. Flux-profile relationships in the atmospheric surface layer. *J. Atmos. Sci.*, 28(2): 181-189.

- Cardon, Z.G., Berry, J.A. and Woodrow, I.E., 1994. Dependence of the Extent and Direction of Average Stomatal Response in *Zea-Mays* L and *Phaseolus-Vulgaris* L on the Frequency of Fluctuations in Environmental Stimuli. *Plant Physiol.*, 105(3): 1007-1013.
- Champagne, F.H., Friehe, C.A., Larue, J.C. and Wyngaard, J.C., 1977. Flux measurements, flux estimation techniques, and fine-scale turbulence measurements in the unstable surface layer over land. *J. Atmos. Sci.*, 34: 515-530.
- Cheinet, S. and Siebesma, A.P., 2009. Variability of Local Structure Parameters in the Convective Boundary Layer. *J. Atmos. Sci.*, 66(4): 1002-1017.
- Chen, J.M. and Zhang, R.H., 1989. Studies on the Measurements of Crop Emissivity and Sky Temperature. *Agric. Forest Meteorol.*, 49(1): 23-34.
- Cheon, Y., Hohreiter, V., Behn, M. and Muschinski, A., 2007. Angle-of-arrival anemometry by means of a large-aperture Schmidt-Cassegrain telescope equipped with a CCD camera. *J. Opt. Soc. Am. A.*, 24(11): 3478-3492.
- Choi, T.J., Hong, J.K., Kim, J., Lee, H.C., Asanuma, J., Ishikawa, H., Tsukamoto, O., Gao, Z.Q., Ma, Y.M., Ueno, K., Wang, J.M., Koike, T. and Yasunari, T., 2004. Turbulent exchange of heat, water vapor, and momentum over a Tibetan prairie by eddy covariance and flux variance measurements. *J. Geophys. Res.*, 109: D21106, doi 10.1029/2004JD004767
- Churnside, J.H., 1990. A Spectrum of Refractive Turbulence in the Turbulent Atmosphere. *J. Mod. Opt.*, 37(1): 13-16.
- Clifford, S.F., Ochs, G.R. and Lawrence, R.S., 1974. Saturation of optical scintillation by strong turbulence. *J. Opt. Soc. Am.*, 64(2): 148-154.
- Coantic, M. and Lasserre, J.J., 1999. On pre-dissipative 'bumps' and a Reynolds-number-dependent spectral parameterization of turbulence. *Eur. J. Mech. B-Fluid.*, 18(6): 1027-1047.
- De Bruin, H.A.R., 1987. From Penman to Makkink. *Proceedings & Information - Committee for Hydrological Research TNO*, 39: 5-30.
- De Bruin, H.A.R. and Jacobs, C.M.J., 1993. Impact of CO₂ enrichment on the regional evapotranspiration of agro-ecosystems, a theoretical and numerical modelling study. *Vegetatio*, 104-105(1): 307-318.
- De Bruin, H.A.R., Kohsiek, W. and Van Den Hurk, B.J.J.M., 1993. A verification of some methods to determine the fluxes of momentum, sensible heat, and water vapour using standard deviation and structure parameter of scalar meteorological quantities. *Boundary-Layer Meteorol.*, 63(3): 231-257.
- De Bruin, H.A.R., Meijninger, W.M.L., Smedman, A.S. and Magnusson, M., 2002. Displaced-beam small aperture scintillometer test. Part I: The wintex data-set. *Boundary-Layer Meteorol.*, 105(1): 129-148.
- De Bruin, H.A.R., Van Den Hurk, B.J.J.M. and Kohsiek, W., 1995. The scintillation method tested over a dry vineyard area. *Boundary-Layer Meteorol.*, 76(1-2): 25-40.
- De Bruin, H.A.R., Van Den Hurk, B.J.J.M. and Kroon, L.J.M., 1999. On the temperature-humidity correlation and similarity. *Boundary-Layer Meteorol.*, 93(3): 453-468.
- De Bruin, H.A.R. and Verhoef, A., 1999. Reply to the comments on 'a new method to determine the zero-plane displacement', by Zhang and Park. *Boundary-Layer Meteorol.*, 91(1): 141-143.
- de Rooy, W.C. and Holtslag, A.A.M., 1999. Estimation of surface radiation and energy flux densities from single-level weather data. *J. Appl. Meteorol.*, 38(5): 526-540.
- Dole, J., Wilson, R., Dalaudier, E. and Sidi, C., 2001. Energetics of small scale turbulence in the lower stratosphere from high resolution radar measurements. *Ann. Geophys.*, 19(8): 945-952.
- Donzis, D.A. and Sreenivasan, K.R., 2010. The bottleneck effect and the Kolmogorov constant in isotropic turbulence. *J. Fluid Mech.*, 657: 171-188.
- Evans, J.G., 2009. Long-Path Scintillometry over Complex Terrain to Determine Areal-Averaged Sensible and Latent Heat Fluxes. PhD Thesis, The University of Reading, Reading, United Kingdom, 201 pp.
- Evans, J.G. and de Bruin, H.A.R., 2011. The Effective Height of a Two-Wavelength Scintillometer System. *Boundary-Layer Meteorol.*, 141(1): 165-177.
- Ezzahar, J., Chehbouni, A., Hoedjes, J.C.B., Er-Raki, S., Chehbouni, A., Boulet, G., Bonnefond, J.M. and De Bruin, H.A.R., 2007. The use of the scintillation technique for monitoring seasonal

- water consumption of olive orchards in a semi-arid region. *Agric. Water Manage.*, 89(3): 173-184.
- Falkovich, G., 1994. Bottleneck Phenomenon in Developed Turbulence. *Phys. Fluids*, 6(4): 1411-1414.
- Finnigan, J., 2008. An introduction to flux measurements in difficult conditions. *Ecol. Applic.*, 18(6): 1340-1350.
- Finnigan, J.J., Clement, R., Malhi, Y., Leuning, R. and Cleugh, H.A., 2003. Re-evaluation of long-term flux measurement techniques. Part I: Averaging and coordinate rotation. *Boundary-Layer Meteorol.*, 107(1): 1-48.
- Flach, P., 2000. Analysis of refraction influences in geodesy using image processing and turbulence models, ETH Zürich, Zürich, Switzerland 188 pp.
- Foken, T., 2008. The energy balance closure problem: An overview. *Ecol. Applic.*, 18(6): 1351-1367.
- Foken, T., Wichura, B., Klemm, O., Gerchau, J., Winterhalter, M. and Weidinger, T., 2001. Micrometeorological measurements during the total solar eclipse of August 11, 1999. *Meteorol. Z.*, 10(3): 171-178.
- Foken, T., Wimmer, F., Mauder, M., Thomas, C. and Liebethal, C., 2006. Some aspects of the energy balance closure problem. *Atmos. Chem. Phys.*, 6: 4395-4402.
- Franks, P.J. and Farquhar, G.D., 2007. The mechanical diversity of stomata and its significance in gas-exchange control. *Plant Physiol.*, 143(1): 78-87.
- Franssen, H.J.H., Stockli, R., Lehner, I., Rotenberg, E. and Seneviratne, S.I., 2010. Energy balance closure of eddy-covariance data: A multisite analysis for European FLUXNET stations. *Agric. Forest Meteorol.*, 150(12): 1553-1567.
- Frehlich, R., 1992. Laser Scintillation Measurements of the Temperature Spectrum in the Atmospheric Surface-Layer. *J. Atmos. Sci.*, 49(16): 1494-1509.
- Garratt, J.R., 1992. The atmospheric boundary layer. Cambridge University Press, Cambridge, United Kingdom, 316 pp.
- Gilmanov, T.G., Verma, S.B., Sims, P.L., Meyers, T.P., Bradford, J.A., Burba, G.G. and Suyker, A.E., 2003. Gross primary production and light response parameters of four Southern Plains ecosystems estimated using long-term CO₂-flux tower measurements. *Global Biogeochem. Cy.*, 17(2): 1071, doi:10.1029/2002GB002023.
- Gotoh, T. and Watanabe, T., 2005. Statistics of transfer fluxes of the kinetic energy and scalar variance. *J. Turbul.*, 6(33): doi 10.1080/14685240500317354.
- Graf, A., Schuttemeyer, D., Geiss, H., Knaps, A., Mollmann-Coers, M., Schween, J.H., Kollet, S., Neininger, B., Herbst, M. and Vereecken, H., 2010. Boundedness of Turbulent Temperature Probability Distributions, and their Relation to the Vertical Profile in the Convective Boundary Layer. *Boundary-Layer Meteorol.*, 134(3): 459-486.
- Grayshan, K.J., Vetelino, F.S. and Young, C.Y., 2008. A marine atmospheric spectrum for laser propagation. *Waves Random Complex*, 18(1): 173-184.
- Green, A.E., 2001. The practical application of scintillometers in determining the surface fluxes of heat, moisture and momentum., Wageningen University, Wageningen, the Netherlands, 177 pp.
- Green, A.E., Astill, M.S., McAneney, K.J. and Nieveen, J.P., 2001. Path-averaged surface fluxes determined from infrared and microwave scintillometers. *Agric. Forest Meteorol.*, 109(3): 233-247.
- Green, A.E., Green, S.R., Astill, M.S. and Caspari, H.W., 2000. Estimating latent heat flux from a vineyard using scintillometry. *Terrestrial Atmos. Oceanic Sci.*, 11(2): 525-542.
- Green, A.E., McAneney, K.J. and Astill, M.S., 1994. Surface-layer scintillation measurements of daytime sensible heat and momentum fluxes. *Boundary-Layer Meteorol.*, 68(4): 357-373.
- Green, A.E., McAneney, K.J. and Lagouarde, J.P., 1997. Sensible heat and momentum flux measurement with an optical inner scale meter. *Agric. Forest Meteorol.*, 85(3-4): 259-267.
- Gu, L.H., Baldocchi, D., Verma, S.B., Black, T.A., Vesala, T., Falge, E.M. and Dowty, P.R., 2002. Advantages of diffuse radiation for terrestrial ecosystem productivity. *J. Geophys. Res.*, 107(D5-6): 4050, doi 10.1029/2001jd001242.

- Guo, X., Zhang, H., Cai, X., Kang, L., Zhu, T. and Leclerc, M.Y., 2009. Flux-variance method for latent heat and carbon dioxide fluxes in unstable conditions. *Boundary-Layer Meteorol.*, 131(3): 363-384.
- Hartogensis, O.K., 2006. Exploring Scintillometry in the Stable Atmospheric Surface Layer, Wageningen University, Wageningen, the Netherlands, 227 pp.
- Hartogensis, O.K., 2007. BSIK-ME2 Scintillometer Network. Meteorology and Air Quality Group (MAQ) of Wageningen University & Research Centre (WUR), Wageningen, the Netherlands.
- Hartogensis, O.K. and De Bruin, H.A.R., 2005. Monin-Obukhov similarity functions of the structure parameter of temperature and turbulent kinetic energy dissipation rate in the stable boundary layer. *Boundary-Layer Meteorol.*, 116(2): 253-276.
- Hartogensis, O.K., De Bruin, H.A.R. and Van de Wiel, B.J.H., 2002. Displaced-beam small aperture scintillometer test. Part II: CASES-99 stable boundary-layer experiment. *Boundary-Layer Meteorol.*, 105(1): 149-176.
- Hartogensis, O.K., Watts, C.J., Rodriguez, J.C. and De Bruin, H.A.R., 2003. Derivation of an effective height for scintillometers: La Poza experiment in Northwest Mexico. *J. Hydrometeorol.*, 4(5): 915-928.
- Hatfield, J.L., 1985. Wheat Canopy Resistance Determined by Energy-Balance Techniques. *Agron. J.*, 77(2): 279-283.
- Hecht, E., 1998. Optics. Addison-Wesley, United States, 694 pp.
- Hetherington, A.M. and Woodward, F.I., 2003. The role of stomata in sensing and driving environmental change. *Nature*, 424(6951): 901-908.
- Heusinkveld, B.G., Jacobs, A.F.G., Holtslag, A.A.M. and Berkowicz, S.M., 2004. Surface energy balance closure in an arid region: role of soil heat flux. *Agric. Forest Meteorol.*, 122(1-2): 21-37.
- Hill, R.J., 1978a. Models of scalar spectrum for turbulent advection. *J. Fluid Mech.*, 88: 541-562.
- Hill, R.J., 1978b. Spectra of fluctuations in refractivity, temperature, humidity, and the temperature-humidity cospectrum in the inertial and dissipation ranges. *Radio Sci.*, 13: 953-961.
- Hill, R.J., 1981. Saturation Resistance and Inner-Scale Resistance of a Large-Aperture Scintillometer - a Case-Study. *Appl. Opt.*, 20(22): 3822-3824.
- Hill, R.J., 1982. Theory of Measuring the Path-Averaged Inner Scale of Turbulence by Spatial-Filtering of Optical Scintillation. *Appl. Opt.*, 21(7): 1201-1211.
- Hill, R.J., 1989. Implications of Monin-Obukhov similarity theory for scalar quantities. *J. Atmos. Sci.*, 46(14): 2236-2244.
- Hill, R.J., 1992. Review of Optical Scintillation Methods of Measuring the Refractive-Index Spectrum, Inner Scale and Surface Fluxes. *Wave Random Media*, 2(3): 179-201.
- Hill, R.J., 1997. Algorithms for obtaining atmospheric surface-layer fluxes from scintillation measurements. *J. Atmos. Ocean. Tech.*, 14(3): 456-467.
- Hill, R.J. and Clifford, S.F., 1978. Modified Spectrum of Atmospheric-Temperature Fluctuations and Its Application to Optical Propagation. *J. Opt. Soc. Am.*, 68(7): 892-899.
- Hill, R.J., Clifford, S.F. and Lawrence, R.S., 1980. Refractive-index and absorption fluctuations in the infrared caused by temperature, humidity, and pressure-fluctuations. *J. Opt. Soc. Am.*, 70(10): 1192-1205.
- Hill, R.J. and Lataitis, R.J., 1989. Effect of Refractive Dispersion on the Bichromatic Correlation of Irradiances for Atmospheric Scintillation. *Appl. Opt.*, 28(19): 4121-4130.
- Hill, R.J. and Ochs, G.R., 1978. Fine Calibration of Large-Aperture Optical Scintillometers and an Optical Estimate of Inner Scale of Turbulence. *Appl. Opt.*, 17(22): 3608-3612.
- Hill, R.J., Ochs, G.R. and Wilson, J.J., 1992. Measuring surface-layer fluxes of heat and momentum using optical scintillation. *Boundary-Layer Meteorol.*, 58(4): 391-408.
- Hoedjes, J.C.B., Zurbier, R.M. and Watts, C.J., 2002. Large aperture scintillometer used over a homogeneous irrigated area, partly affected by regional advection. *Boundary-Layer Meteorol.*, 105(1): 99-117.
- Högström, U., 1996. Review of some basic characteristics of the atmospheric surface layer. *Boundary-Layer Meteorol.*, 78(3-4): 215-246.
- Holtslag, A.A.M. and Van Ulden, A.P., 1983. A Simple Scheme for Daytime Estimates of the Surface Fluxes from Routine Weather Data. *J. Clim. Appl. Meteorol.*, 22(4): 517-529.

- Huband, N.D.S. and Monteith, J.L., 1986. Radiative Surface-Temperature and Energy-Balance of a Wheat Canopy .1. Comparison of Radiative and Aerodynamic Canopy Temperature. *Boundary-Layer Meteorol.*, 36(1-2): 1-17.
- Jacobs, A.F.G., Heusinkveld, B.G. and Holtslag, A.A.M., 2008. Towards closing the surface energy budget of a mid-latitude grassland. *Boundary-Layer Meteorol.*, 126(1): 125-136.
- Kaimal, J.C. and Finnigan, J.J., 1994. *Atmospheric Boundary Layer Flows - Their Structure and Measurement*. Oxford University Press, New York, United States, 289 pp.
- Kaimal, J.C., Izumi, Y., Wyngaard, J.C. and Cote, R., 1972. Spectral Characteristics of Surface-Layer Turbulence. *Quart. J. Roy. Meteorol. Soc.*, 98(417): 563-589.
- Kanda, M., Inagaki, A., Letzel, M.O., Raasch, S. and Watanabe, T., 2004. LES study of the energy imbalance problem with Eddy covariance fluxes. *Boundary-Layer Meteorol.*, 110(3): 381-404.
- Kapralos, B., Jenkin, M. and Milios, E., 2005. Acoustical diffraction modeling utilizing the Huygens-Fresnel Principle. 2005 IEEE International Workshop on Haptic Audio Visual Environments and their Applications: 39-44.
- Katul, G.G., Sempreviva, A.M. and Cava, D., 2008. The temperature-humidity covariance in the marine surface layer: A one-dimensional analytical model. *Boundary-Layer Meteorol.*, 126(2): 263-278.
- Kelliher, F.M., Leuning, R., Raupach, M.R. and Schulze, E.D., 1995. Maximum Conductances for Evaporation from Global Vegetation Types. *Agric. Forest Meteorol.*, 73(1-2): 1-16.
- Kim, J. and Verma, S.B., 1990. Carbon-Dioxide Exchange in a Temperate Grassland Ecosystem. *Boundary-Layer Meteorol.*, 52(1-2): 135-149.
- Kipp&Zonen, 2007. Instruction manual large aperture scintillometer, version 0307, Kipp & Zonen B.V., Delft, the Netherlands, 73 pp.
- Kleissl, J., Gomez, J., Hong, S.H., Hendrickx, J.M.H., Rahn, T. and Defoor, W.L., 2008. Large aperture scintillometer intercomparison study. *Boundary-Layer Meteorol.*, 128(1): 133-150.
- Kleissl, J., Watts, C.J., Rodriguez, J.C., Naif, S. and Vivoni, E.R., 2009. Scintillometer Intercomparison Study-Continued. *Boundary-Layer Meteorol.*, 130: 437-443.
- Kohsiek, W., 1982. Measuring C_T^2 , C_q^2 , and C_{Tq} in the unstable surface-layer, and relations to the vertical fluxes of heat and moisture. *Boundary-Layer Meteorol.*, 24(1): 89-107.
- Kohsiek, W. and Herben, M., 1983. Evaporation derived from optical and radiowave scintillation. *Appl. Opt.*, 22(17): 2566-2570.
- Kolmogorov, A.N., 1941. Local Structure of Turbulence in an Incompressible Viscous Fluid at Very High Reynolds Numbers. *Dokl. Akad. Nauk. SSSR*, 30(4): 299-303.
- Lamaud, E. and Irvine, M., 2006. Temperature-humidity dissimilarity and heat-to-water-vapour transport efficiency above and within a pine forest canopy: The role of the Bowen ratio. *Boundary-Layer Meteorol.*, 120(1): 87-109.
- Lawrence, R.S. and Strohbehn, J.W., 1970. A Survey of Clear-Air Propagation Effects Relevant to Optical Communications. *Proceedings of the IEEE*, 58(10): 1523-1545.
- Lee, R.W. and Harp, J.C., 1969. Weak Scattering in Random Media with Applications to Remote Probing. *Proceedings of the IEEE*, 57(4): 375-406.
- Lenschow, D.H., Mann, J. and Kristensen, L., 1994. How Long Is Long Enough When Measuring Fluxes and Other Turbulence Statistics. *J. Atmos. Ocean. Tech.*, 11(3): 661-673.
- Li, D., Bou-Zeid, E. and De Bruin, H.A.R., 2012. Monin-Obukhov Similarity Functions for the Structure Parameters of Temperature and Humidity. *Boundary-Layer Meteorol.*, 145(1): 45-67.
- Liebenthal, C., Huwe, B. and Foken, T., 2005. Sensitivity analysis for two ground heat flux calculation approaches. *Agric. Forest Meteorol.*, 132(3-4): 253-262.
- Loescher, H.W., Ocheltree, T., Tanner, B., Swiatek, E., Dano, B., Wong, J., Zimmerman, G., Campbell, J., Stock, C., Jacobsen, L., Shiga, Y., Kollas, J., Liburdy, J. and Law, B.E., 2005. Comparison of temperature and wind statistics in contrasting environments among different sonic anemometer-thermometers. *Agric. Forest Meteorol.*, 133(1-4): 119-139.
- Lohse, D. and Mullergroeling, A., 1995. Bottleneck Effects in Turbulence - Scaling Phenomena in R-Space Versus P-Space. *Phys. Rev. Lett.*, 74(10): 1747-1750.
- Lüdi, A., Beyrich, F. and Mätzler, C., 2005. Determination of the turbulent temperature-humidity correlation from scintillometric measurements. *Boundary-Layer Meteorol.*, 117(3): 525-550.

- Lüers, J. and Bareiss, J., 2011. Direct near-surface measurements of sensible heat fluxes in the Arctic tundra applying eddy covariance and laser scintillometry-the Arctic Turbulence Experiment 2006 on Svalbard (ARCTEX-2006). *Theor. Appl. Climatol.*, 105(3-4): 387-402.
- Mahrt, L., 2010. Computing turbulent fluxes near the surface: Needed improvements. *Agric. Forest Meteorol.*, 150(4): 501-509.
- Mauder, M., Desjardins, R.L., Oncley, S.P. and MacPherson, I., 2007. Atmospheric response to a partial solar eclipse over a cotton field in central California. *J. Appl. Meteorol. Clim.*, 46(11): 1792-1803.
- Mauder, M., Liebethal, C., Göckede, M., Leps, J.P., Beyrich, F. and Foken, T., 2006. Processing and quality control of flux data during LITFASS-2003. *Boundary-Layer Meteorol.*, 121(1): 67-88.
- McBean, G.A., 1982. Microscale Temperature-Fluctuations in the Atmospheric Surface-Layer. *Boundary-Layer Meteorol.*, 23(2): 185-196.
- Meijninger, W.M.L., 2003. Surface Fluxes over natural landscapes using scintillometry, Wageningen University, Wageningen, the Netherlands, 164 pp.
- Meijninger, W.M.L., Beyrich, F., Lüdi, A., Kohsiek, W. and De Bruin, H.A.R., 2006. Scintillometer-based turbulent fluxes of sensible and latent heat over a heterogeneous land surface - A contribution to LITFASS-2003. *Boundary-Layer Meteorol.*, 121(1): 89-110.
- Meijninger, W.M.L. and De Bruin, H.A.R., 2000. The sensible heat fluxes over irrigated areas in western Turkey determined with a large aperture scintillometer. *J. Hydrol.*, 229(1-2): 42-49.
- Meijninger, W.M.L., Green, A.E., Hartogensis, O.K., Kohsiek, W., Hoedjes, J.C.B., Zuurbier, R.M. and De Bruin, H.A.R., 2002a. Determination of area-averaged water vapour fluxes with large aperture and radio wave scintillometers over a heterogeneous surface - Flevoland field experiment. *Boundary-Layer Meteorol.*, 105(1): 63-83.
- Meijninger, W.M.L., Hartogensis, O.K., Kohsiek, W., Hoedjes, J.C.B., Zuurbier, R.M. and De Bruin, H.A.R., 2002b. Determination of area-averaged sensible heat fluxes with a large aperture scintillometer over a heterogeneous surface - Flevoland field experiment. *Boundary-Layer Meteorol.*, 105(1): 37-62.
- Mestayer, P., 1982. Local Isotropy and Anisotropy in a High-Reynolds-Number Turbulent Boundary-Layer. *J. Fluid Mech.*, 125: 475-503.
- Moene, A.F., 2003. Effects of water vapour on the structure parameter of the refractive index for near-infrared radiation. *Boundary-Layer Meteorol.*, 107(3): 635-653.
- Moene, A.F., Meijninger, W.M.L., Hartogensis, O.K., Kohsiek, W. and De Bruin, H.A.R., 2004. A review of the relationships describing the signal of a Large Aperture Scintillometer, Lsg Meteorologie en luchtkwaliteit, Wageningen, the Netherlands.
- Moene, A.F. and Schüttemeyer, D., 2008. The effect of surface heterogeneity on the temperature-humidity correlation and the relative transport efficiency. *Boundary-Layer Meteorol.*, 129(1): 99-113.
- Moene, A.F. and Van Dam, J.C., 2012. Transport processes in the atmosphere-vegetation-soil continuum. Cambridge University Press, Cambridge, United Kingdom, in preparation.
- Monin, A.S. and Obukhov, A.M., 1954. Basic laws of turbulent mixing in the layer of the atmosphere near the earth. *Trudy Geofiz. Inst. Akad. Nauk SSSR*, 24.
- Monin, A.S. and Yaglom, A.M., 1971. *Statistical Fluid Mechanics: Mechanics of Turbulence*, 1. The MIT Press Cambridge, United Kingdom, 769 pp.
- Monin, A.S. and Yaglom, A.M., 1975. *Statistical Fluid Mechanics: Mechanics of Turbulence* 2. The MIT Press Cambridge, United Kingdom, 874 pp.
- Monteith, J.L., 1965. Evaporation and environment. *Symp. Soc. Exp. Biol.*, 19: 205-34.
- Monteith, J.L., 1995. A Reinterpretation of Stomatal Responses to Humidity. *Plant Cell Environ.*, 18(4): 357-364.
- Moore, C.J., 1986. Frequency response corrections for eddy correlation systems. *Boundary-Layer Meteorol.*, 37(1-2): 17-35.
- Mott, K.A. and Parkhurst, D.F., 1991. Stomatal Responses to Humidity in Air and Helox. *Plant Cell Environ.*, 14(5): 509-515.
- Nakaya, K., Suzuki, C., Kobayashi, T., Ikeda, H. and Yasuike, S., 2006. Application of a displaced-beam small aperture scintillometer to a deciduous forest under unstable atmospheric conditions. *Agric. Forest Meteorol.*, 136(1-2): 45-55.

- Nieveen, J.P., 1999. Eddy covariance and scintillation measurements of atmospheric exchange processes over different types of vegetation., Wageningen University, Wageningen, The Netherlands 121 pp.
- Nieveen, J.P., Green, A.E. and Kohsiek, W., 1998a. Using a large-aperture scintillometer to measure absorption and refractive index fluctuations. *Boundary-Layer Meteorol.*, 87(1): 101-116.
- Nieveen, J.P., Jacobs, C.M.J. and Jacobs, A.F.G., 1998b. Diurnal and seasonal variation of carbon dioxide exchange from a former true raised bog. *Global Change Biol.*, 4(8): 823-833.
- Obukhov, A.M., 1949. Structure of the temperature field in turbulent flow. *Izv. Akad. Nauk SSSR, Ser. Geograf. Geofiz.*, 13: 58-69.
- Obukhov, A.M., 1953. On the influence of weak atmospheric inhomogeneities on the propagation of sound and light. *Izv. Akad. Nauk SSSR, Ser. Geofiz.*, 2: 155.
- Obukhov, A.M. and Yaglom, A.M., 1951. The microstructure of turbulent flow. *Prikl. Mat. Mekh.*, 15: 3.
- Ochs, G.R. and Wang, T., 1978. Finite Aperture Optical Scintillometer for Profiling Wind and C_n^2 . *Appl. Opt.*, 17(23): 3774-3778.
- Oncley, S.P., 2007. Combining short-term moments for longer time periods. NCAR, Atmosphere Technology Division (ATD), Integrated Surface Flux Facility. <http://www.eol.ucar.edu/instrumentation/sounding/isfs/isff-support-center/how-tos/combining-short-term-moments-for-longer-time-periods>, Accessed 28 September 2010.
- Oncley, S.P., Friehe, C.A., Larue, J.C., Businger, J.A., Itsweire, E.C. and Chang, S.S., 1996. Surface-layer fluxes, profiles, and turbulence measurements over uniform terrain under near-neutral conditions. *J. Atmos. Sci.*, 53(7): 1029-1044.
- Pahlow, M., Parlange, M.B. and Porté-Agel, F., 2001. On Monin-Obukhov similarity in the stable atmospheric boundary layer. *Boundary-Layer Meteorol.*, 99(2): 225-248.
- Papaiouannou, G., Papanikolaou, N. and Retalis, D., 1993. Relationships of Photosynthetically Active Radiation and Shortwave Irradiance. *Theor. Appl. Climatol.*, 48(1): 23-27.
- Paulson, C.A., 1970. The mathematical representation of wind speed and temperature profiles in the unstable atmospheric surface layer. *J. Appl. Meteorol.*, 9(6): 857-861.
- Priestley, C.H.B. and Taylor, R.J., 1972. On the Assessment of Surface Heat Flux and Evaporation Using Large-Scale parameters. *Monthly Weather Review*, 100: 81-92.
- Qian, J., 1984. Universal Equilibrium Range of Turbulence. *Phys. Fluid.*, 27(9): 2229-2233.
- Rotach, M.W., Calanca, P., Graziani, G., Gurtz, J., Steyn, D.G., Vogt, R., Andretta, M., Christen, A., Cieslik, S., Connolly, R., De Wekker, S.F.J., Galmarini, S., Kadyrov, E.N., Kadyrov, V., Miller, E., Neininger, B., Rucker, M., Van Gorsel, E., Weber, H., Weiss, A. and Zappa, M., 2004. Turbulence structure and exchange processes in an Alpine Valley - The Riviera project. *Bull. Amer. Meteorol. Soc.*, 85(9): 1367- 1385.
- Savage, M.J., 2009. Estimation of evaporation using a dual-beam surface layer scintillometer and component energy balance measurements. *Agric. Forest Meteorol.*, 149(3-4): 501-517.
- Scanlon, T.M. and Kustas, W.P., 2010. Partitioning carbon dioxide and water vapor fluxes using correlation analysis. *Agric. Forest Meteorol.*, 150(1): 89-99.
- Schotanus, P., Nieuwstadt, F.T.M. and De Bruin, H.A.R., 1983. Temperature measurement with a sonic anemometer and its application to heat and moisture fluxes. *Boundary-Layer Meteorol.*, 26(1): 81-93.
- Scintec, 2006. Scintec Surface Layer Scintillometer SLS20/SLS40 SLS20-A/SLS40-A User Manual (including OEBMS1)., Scintec Atmosphärenmesstechnik AG, Tübingen, Germany, 105 pp.
- Shuttleworth, W.J., 2007. Putting the 'vap' into evaporation. *Hydrol. Earth Syst. Sci.*, 11(1): 210-244.
- Sreenivasan, K.R., 1996. The passive scalar spectrum and the Obukhov-Corrsin constant. *Phys. Fluid*, 8(1): 189-196.
- Strohbehm, J.W., 1968. Line-of-Sight Wave Propagation through Turbulent Atmosphere. *Proceedings of the IEEE*, 56(8): 1301-1318.
- Stull, R.B., 1988. An introduction to boundary layer meteorology. Kluwer Academic Publishers Dordrecht, The Netherlands, 666 pp.
- Stull, R.B., 2000. *Meteorology for Scientists and Engineers* Brooks/Cole, Pacific Grove, United States, 502 pp.

- Sun, X., Zhu, Z., Xu, J., Yuan, G., Zhou, Y. and Zhang, R., 2005. Determination of averaging period parameter and its effects analysis for eddy covariance measurements. *Science in China, Series D: Earth Sciences*, 48(SUPPL.1): 33-41.
- Tatarskii, V.I., 1961. *Wave propagation in a turbulent medium*. McGraw-Hill Book Company Inc., New York, United States, 285 pp.
- Tatarskii, V.I., Dubovikov, M.M., Praskovsky, A.A. and Karyakin, M.Y., 1992. Temperature-Fluctuation Spectrum in the Dissipation Range for Statistically Isotropic Turbulent-Flow. *J. Fluid Mech.*, 238: 683-698.
- Thiermann, V., 1992. A displaced-beam scintillometer for line-averaged measurements of surface layer turbulence, 10th symposium on turbulence and diffusion, Portland, OR, United States.
- Thiermann, V. and Grassl, H., 1992. The measurement of turbulent surface-layer fluxes by use of bichromatic scintillation. *Boundary-Layer Meteorol.*, 58(4): 367-389.
- Van de Wiel, B.J.H., Moene, A.F., Hartogensis, O.K., De Bruin, H.A.R. and Holtslag, A.A.M., 2003. Intermittent turbulence in the stable boundary layer over land. Part III: A classification for observations during CASES-99. *J. Atmos. Sci.*, 60(20): 2509-2522.
- Van Dijk, A., Moene, A.F. and De Bruin, H.A.R., 2004. *The principles of surface flux physics: theory, practice and description of the ECPACK library*, Meteorology and Air Quality Group, Wageningen University, Wageningen, the Netherlands.
- van Dinter, D., 2009. *Obtaining reliable H₂O and CO₂ fluxes using scintillometry combined with scalar turbulence measurements*, Wageningen University, Wageningen, the Netherlands, 86 pp.
- Van Kesteren, B., 2008. *Sensible and Latent Heat Fluxes with Optical and Millimetre Wave Scintillometers*, Wageningen University, Wageningen, the Netherlands, 99 pp.
- Van Kesteren, B. and Hartogensis, O.K., 2011. Analysis of the Systematic Errors Found in the Kipp & Zonen Large-Aperture Scintillometer. *Boundary-Layer Meteorol.*, 138(3): 493-509.
- Van Kesteren, B., Hartogensis, O.K., van Dinter, D., Moene, A.F. and De Bruin, H.A.R., 2012a. Measuring H₂O and CO₂ Fluxes at Field scales with Scintillometry: Part I – Introduction and Validation of four methods *Agric. Forest Meteorol.*, doi 10.1016/j.agrformet.2012.09.013.
- Van Kesteren, B., Hartogensis, O.K., van Dinter, D., Moene, A.F., De Bruin, H.A.R. and Holtslag, A.A.M., 2012b. Measuring H₂O and CO₂ Fluxes at Field scales with Scintillometry: Part II – Validation and Application of 1-minute Flux estimates. *Agric. Forest Meteorol.*, accepted with major revisions.
- Verhoef, A., Mcnaughton, K.G. and Jacobs, A., 1997. A parameterization of momentum roughness length and displacement height for a wide range of canopy densities. *Hydrol. Earth Sys. Sci.*, 1(1): 81-91.
- Verma, M.K. and Donzis, D., 2007. Energy transfer and bottleneck effect in turbulence. *J. Phys. Math. Theor.*, 40(16): 4401-4412.
- Vickers, D., Thomas, C. and Law, B.E., 2009. Random and systematic CO₂ flux sampling errors for tower measurements over forests in the convective boundary layer. *Agric. Forest Meteorol.*, 149(1): 73-83.
- Vilà-Guerau de Arellano, J., Duynkerke, P.G. and Zeller, K.F., 1995. Atmospheric Surface-Layer Similarity Theory Applied to Chemically Reactive Species. *J. Geophys. Res.*, 100(D1): 1397-1408.
- Wang, T.I., Ochs, G.R. and Clifford, S.F., 1978. Saturation-Resistant Optical Scintillometer to Measure C_n^2 . *J. Opt. Soc. Am.*, 68(3): 334-338.
- Ward, H.C., Evans, J.G. and Grimmond, C.S.B., 2011. Effects of Non-Uniform Crosswind Fields on Scintillometry Measurements. *Boundary-Layer Meteorol.*, 141(1): 143-163.
- Ward, H.C., Evans, J.G., Hartogensis, O.K., Moene, A.F., De Bruin, H.A.R. and Grimmond, C.S.B., 2012. A critical revision of the estimation of the latent heat flux from two-wavelength scintillometry. *Quart. J. Roy. Meteorol. Soc.*, accepted.
- Webb, E.K., Pearman, G.I. and Leuning, R., 1980. Correction of Flux Measurements for Density Effects Due to Heat and Water-Vapor Transfer. *Quart. J. Roy. Meteorol. Soc.*, 106(447): 85-100.

- Weiss, A., 2002. Determination of thermal stratification and turbulence of the atmospheric surface layer over various types of terrain by optical scintillometry. PhD Thesis, ETH Zürich, Zürich, Switzerland, 152 pp.
- Wesely, M.L., 1976. Combined effect of temperature and humidity fluctuations on refractive-index. *J. Appl. Meteorol.*, 15(1): 43-49.
- Williams, R.M. and Paulson, C.A., 1977. Microscale temperature and velocity spectra in the atmospheric boundary layer. *J. Fluid Mech.*, 83(3): 547-567.
- Wilson, K., Goldstein, A., Falge, E., Aubinet, M., Baldocchi, D., Berbigier, P., Bernhofer, C., Ceulemans, R., Dolman, H., Field, C., Grelle, A., Ibrom, A., Law, B.E., Kowalski, A., Meyers, T., Moncrieff, J., Monson, R., Oechel, W., Tenhunen, J., Valentini, R. and Verma, S., 2002. Energy balance closure at FLUXNET sites. *Agric. Forest Meteorol.*, 113(1-4): 223-243.
- Wittich, K.P., 1997. Some simple relationships between land-surface emissivity, greenness and the plant cover fraction for use in satellite remote sensing. *Int. J. Biometeorol.*, 41(2): 58-64.
- Wolf, A., Saliendra, N., Akshalov, K., Johnson, D.A. and Laca, E., 2008. Effects of different eddy covariance correction schemes on a energy balance closure and comparisons with the modified Bowen ratio system. *Agric. Forest Meteorol.*, 148(6-7): 942-952.
- Wrench, C.L., 2003-2010. Chilbolton Facility for Atmospheric and Radio Research (CFARR) data. Science and Technology Facilities Council (STFC), Chilbolton Facility for Atmospheric and Radio Research, <http://badc.nerc.ac.uk/data/chilbolton/>, Accessed March 2009.
- Wyngaard, J. and Kosovic, B., 1994. Similarity of structure-function parameters in the stably stratified boundary-layer. *Boundary-Layer Meteorol.*, 71(3): 277-296.
- Wyngaard, J.C. and Clifford, S.F., 1978. Estimating Momentum, Heat and Moisture Fluxes from Structure Parameters. *J. Atmos. Sci.*, 35(7): 1204-1211.
- Zeiger, E., Farquhar, G.D. and Cowan, I.R., 1987. Stomatal function. Stanford University Press, Stanford, Calif., United States, xiv, 503 pp.

10. Summary

Measurements of atmospheric surface fluxes of momentum, heat, water vapour, carbon dioxide (CO₂) and other atmospheric quantities are of great importance to society, because these measurements are applied in applications that greatly benefit human and environmental wellbeing.

At present, eddy covariance is extensively used to do these flux measurements (Baldocchi, 2003; Shuttleworth, 2007). Eddy covariance, ideally, measures these fluxes in a straight forward manner and its set-up is relatively easy in maintenance. However, the use of the eddy-covariance method has four limitations. Firstly, flow distortion (by the mast or instrument itself) is not negligible for unfavourable wind directions. Secondly, point-sampling measurements only represent a limited area. Thirdly, the eddy-covariance method needs to sample all eddy scales relevant to the turbulent flux (Finnigan et al., 2003). Fourthly, as a point-sampling measurement technique it requires time to adequately sample the largest eddy scales and during the whole flux-averaging interval (10-30 minutes) the turbulence needs to be stationary. However, there are many situations during which the turbulence is not stationary for such prolonged periods, e.g. during periods of rapidly changing cloud cover or during the night when bursts of increased turbulence occur (intermittency). During these situations the eddy-covariance method cannot accurately determine the surface fluxes.

Scintillometry is an indirect flux estimation method that overcomes the above-described limitations of the eddy-covariance method, and thus is useful for measuring fluxes during situations of non-stationary turbulence. A field-scale scintillometer consists of a transmitter and a receiver, which are typically 100 m – 300 m apart. The transmitter emits a beam of electromagnetic radiation with a constant intensity. On its way through the atmosphere the beam gets disturbed, because turbulent whirls called eddies act as lenses and scatter the beam a little. Therefore, the beam irradiance as measured by the receiver is not constant anymore. For that it holds that the stronger the turbulence, the larger the variance of the measured signal. Essential for the scintillometer method is that the atmospheric turbulence is mainly determined by the strength of the wind friction with the earth's surface and by heat that rises from the surface (daytime) or by cooling of the air by the earth's surface (nighttime). By processing the raw scintillometer measurements, the strength of the wind shear (derived from the inner scale, l_0 , and expressed as the momentum flux or friction velocity, u_*) and the strength of the heat flux (derived from the structure parameter of the refractive index, C_n^2 , and expressed as the sensible-heat flux, H) can be determined.

The advantage of scintillometry is that not all eddies that contribute to the flux have to be sampled, but only the eddies of one specific size. As this sampling takes place along the whole scintillometer path, a scintillometer can accurately estimate the flux within one minute, whereby the flux estimate represents the averaged flux over the whole path.

The ideal method one could say. However, there remained several issues that limited the success of the method and that initiated the project “Innovations in Scintillometry - Measuring surface fluxes of water vapour, sensible heat and momentum on field to kilometre scale” from the Dutch Technology Foundation (STW). The first issue is that measurement errors were observed in two commercially available scintillometers, i.e. the large-aperture scintillometer from Kipp&Zonen and the displaced-beam laser scintillometer from Scintec. In the first part of this thesis (chapter 3-4) these measurement errors are dealt with. The innovation of this part of the project lies therein that we want to understand why these systematic errors occur. Furthermore, we developed a prototype scintillometer that should overcome the measurement errors of the Scintec scintillometer and that can be used for scintillometer paths of 200 m or longer.

Second, and this is the main focus of the thesis (chapter 5-7), there is the need for measuring passive-scalar fluxes on field scales (<500 m). Until now, none of the commercially available scintillometers can measure mass fluxes of passive scalar quantities. Prototype scintillometer systems that measure evapotranspiration on large scales (> 1 km) are available (Evans, 2009; Green et al., 2001; Green et al., 2000; Meijninger et al., 2006; Meijninger et al., 2002a) and a commercial system is in preparation, but unfortunately these systems cannot be operated on field scales (< 500m) and cannot measure mass fluxes of CO₂, CH₄, or other passive scalar quantities. Thus, we introduce and validate four methods that combine field-scale scintillometer measurements of stability and friction velocity with additional turbulence measurements of humidity and CO₂. With these methods, the spatial-averaging advantages of scintillometry can be used to accurately evaluate evapotranspiration, CO₂ flux and other mass fluxes of passive scalars over averaging intervals as short as 1 minute.

Chapter 3: Analysis of the systematic errors found in the Kipp & Zonen large-aperture scintillometer

Studies have shown a systematic error in the Kipp & Zonen large-aperture scintillometer (K&ZLAS) measurements of the sensible heat flux, H . We improved on these studies by doing an own study in which we compared four K&ZLASs with a Wageningen large-aperture

scintillometer at the Chilbolton Observatory. The scintillometers were installed such that their footprints were the same and independent flux measurements were made along the measurement path. This allowed us not only to compare scintillometer measurements of H with independent methods (eddy-covariance), but also the direct scintillometer output, the refractive index structure parameter, C_n^2 . Furthermore, spectral analysis was performed on the raw scintillometer signal to investigate the characteristics of the error. In this chapter the results of this study were presented. Firstly, correlation coefficients ≥ 0.99 confirm the robustness of the scintillometer method. Secondly, we discovered two systematic errors: the low- C_n^2 error and the high- C_n^2 error. The low- C_n^2 error is a non-linear error that is caused by high-frequency noise, and we suspect the error to be caused by the calibration circuit in the receiver. It varies between each K&ZLAS, is significant for $H \leq 50 \text{ W m}^{-2}$, and we propose a solution to remove this error using the demodulated signal. The high- C_n^2 error identified by us is the systematic error found in previous studies. We suspect this error to be caused by poor focal alignment of the receiver detector and the transmitter light-emitting diode that causes ineffective use of the Fresnel lens in the current Kipp & Zonen design. It varies between each K&ZLAS (35% up to 240%) and can only be removed by comparing with a reference scintillometer in the field. These results were communicated with Kipp & Zonen, who based on these results and some other issues, completely redesigned their large-aperture scintillometer, which recently (2011) became available.

Chapter 4: Instrument development: Revisiting a scintillometer design

The SLS20/SLS40 displaced-beam laser scintillometer, DBLS, is a small-aperture scintillometer that provides measurements of the inner scale of turbulence, l_0 , and the structure-parameter of the refractive index, C_n^2 . The DBLS typically provides fluxes at field scales. Heat fluxes derived from the DBLS have been shown to compare well with local eddy-covariance measurements, whereas measurements of C_n^2 and l_0 systematically seem to differ from these eddy-covariance measurements. The first part of this chapter focuses on the intercomparison of five DBLSs, to compare the variability of the l_0 and C_n^2 measurements. It was shown that the measurements can differ as much as 42%, both for l_0 and C_n^2 . This suggests that for each DBLS specific instrument calibration is required, a solution which by now (2012) is implemented by Scintec in their production process. The second part of this chapter focuses on the development of a prototype scintillometer. Besides the systematic errors, the DBLS of Scintec is susceptible to saturation for path lengths that are longer than 200 - 300 m. Therefore, we investigated the possibility of measuring l_0 and C_n^2 based on a

method that uses a scintillometer with two beams that have different aperture sizes. One aperture should be small and thus sensitive to l_0 , whereas the other aperture should be large and thus sensitive to C_n^2 . Based on theoretical considerations, we concluded that the combination of a 1-cm aperture and a 10-cm aperture yields the best sensitivity to l_0 and prevents saturation over paths longer than 200 m. In the framework of the LITFASS-2012 experiment, we conducted a field experiment during which we operated the prototype scintillometer with apertures of 1.75 cm and 10 cm. Unfortunately, we could not operate the scintillometer with a 1-cm aperture, because the emissivity of the light-emitting diode was not strong enough (or the sensitivity of the detector). Independent eddy-covariance measurements showed that the scintillometer was not able to reproduce u^* and H , because the combination of a 1.75-cm aperture and a 10-cm aperture is insensitive to l_0 for l_0 in the range from 2 mm – 6 mm (a big part of the natural range during daytime). However, the method in itself works well. Using a combination of a laser and a 1.75-cm aperture or a 10-cm aperture, resulted in accurate estimates of l_0 and C_n^2 .

Chapter 5: Measuring H₂O and CO₂ fluxes at field scales with scintillometry: Part I – introduction and validation of four methods

This study introduces four methods for determining turbulent water vapour and carbon dioxide flux densities, the evapotranspiration and CO₂ flux respectively. These methods combine scintillometer measurements with point-sampling measurements of scalar quantities and consequently have a faster statistical convergence than the eddy-covariance method. The scintillometer measures the friction velocity and sensible-heat flux averaged over space, allowing the time averaging to be a minute or less in homogenous conditions. This chapter aims to thoroughly test the methods by validating the methods with 30-minute eddy-covariance data and analysing their sensitivity to the variables that go into the method. Introduced are: the Bowen-variance method, the flux-variance method, the structure-parameter method, and the energy-balance method. Sensitivity analysis shows that each method is sensitive to the turbulence measurements of the scalar quantities that are specific to the method, as well as to the friction velocity. This demonstrates that the accuracy of the flux results from a correct representation of the turbulence variables used by the methods. Furthermore, a 30-min flux validation shows that the methods compare well to the independent eddy-covariance fluxes. We find that the structure-parameter method performs best – a low scatter (the correlation coefficient, $r = 0.99$) and a 5% underestimation were observed. Also the other methods perform well, although the energy-balance did not close,

and during the night the variance methods were negatively influenced by non-stationarity in the measurement signal. Finally, we suggest using the correlation coefficients between temperature and scalar quantities to acquire the sign of the fluxes (neither scintillometers nor the combined methods give the flux sign). Data for this study were gathered in May - June 2009 over a wheat field near Merken, Germany, in the framework of the TransRegio32 program.

Chapter 6: Measuring H_2O and CO_2 fluxes at field scales with scintillometry: Part II – evapotranspiration for 1-30 minute averaging intervals

In this chapter we continue the evaluation of four methods to obtain 1-minute averaged estimates of evapotranspiration, L_vE . The focus is on the accuracy of 1-minute estimates of L_vE . To validate the combined methods for these short averaging intervals, two methods were applied. Firstly, we determine the averaging-time-dependent systematic and random error in L_vE measurements. Secondly, we validate the combined methods with a set-up of the Penman-Monteith model that neglects storage changes and assumes a constant canopy resistance. Using these validation methods, we show that both the eddy-covariance method and the energy-balance method are unsuitable for estimating 1-min L_vE . The eddy-covariance method suffers from large systematic and random errors and the energy-balance method suffers from neglecting storage changes in the energy balance. The other three combined methods are found to be more successful in determining 1-min L_vE . The random error is approximately half that of the eddy-covariance method, but still some issues limit the success. The Bowen-variance method has a 0.05 systematic error and moreover, 30% of the data had to be omitted, because the method requires more stringent conditions. Furthermore, the flux-variance method has a -0.15 systematic error. The structure-parameter method performs best of all methods and accurately resolves 1-min L_vE . With this method, we confirm that for a homogeneous area over which the ensemble average can be estimated by spatial averaging, Monin-Obukhov similarity theory is valid for 1-minute averaging intervals. Furthermore, we showed that wheat plants affect L_vE within two minutes upon changes in solar radiation.

Chapter 7: Measuring H_2O and CO_2 fluxes at field scales with scintillometry: Part III – carbon-dioxide fluxes and vegetation processes for 1-30 minute averaging intervals

In this chapter we finished the evaluation of four methods to obtain 1-minute averaged estimates of evapotranspiration and the CO_2 flux. The aim is to evaluate the accuracy of the CO_2 flux, FCO_2 , and to use the 1-min fluxes to investigate flux and plant responses under

conditions of non-stationary turbulence. The validation of FCO_2 is in agreement with that of L_vE , from which we concluded that these results are valid for the flux of any passive scalar. The validation showed that the eddy-covariance method is unsuitable for measuring 1-min averaged fluxes. The three combined methods are more successful in determining 1-min FCO_2 . The averaging-time-dependent random error is approximately half that of eddy covariance, but still some issues limit the success. The Bowen-variance method has a +0.09 systematic error and moreover, 30% of the data had to be omitted, because the method requires more stringent conditions. Furthermore, the flux-variance method has a -0.16 systematic error. The structure-parameter method performs best of all methods and accurately resolves 1-min FCO_2 . With this method, we did a final validation by using the LITFASS-2009 data (measured in Lindenberg, Germany). Thus we showed that also under drier conditions (Bowen ratio ~ 2.5) the method accurately resolves FCO_2 , although L_vE was more difficult to resolve. In the last part, the structure-parameter method is successfully applied under conditions of non-stationary turbulence. We show that L_vE and FCO_2 have a different step response upon abrupt changes in solar radiation, because different processes drive these fluxes. Also, we observe a 2-min time lag between solar radiation and 1-min fluxes and show the relevance of taking this into account for determining light-response curves of the plants for both 1-min and 30-min averaging intervals. Furthermore, we show the relevance of 1-min fluxes for studying the light-response curves of plants for conditions with different temperature and humidity. Hereby it is clearly shown that plants deal more efficiently with light when the water-vapour deficit in the atmosphere is small. Finally, we show that accurate estimates of 1-min averaged canopy resistances can be determined via the resistance expressions for sensible heat and L_vE . As such, we show that a wheat vegetation can indeed modify its canopy resistance significantly within several minutes (because the plants close their stomata) and so alter the surface fluxes. However, whether they do so or not depends on the local circumstances.

11. Samenvatting

Metingen van de nabij het aardoppervlak voorkomende atmosferische stroomdichtheid (flux) van impuls, warmte, waterdamp, koolstofdioxide (CO₂) en andere atmosferische grootheden zijn van groot belang voor de samenleving omdat deze metingen gebruikt worden in vele toepassingen die het menselijke welzijn ten goede komen.

In principe is er een goede meettechniek beschikbaar voor het meten van oppervlakte fluxen, de eddy-covariantietechniek. Deze techniek wordt op zeer grote schaal toegepast omdat de fluxen er tamelijk rechttoe rechtaan mee gemeten kunnen worden en onderhoud in het veld relatief eenvoudig is (Balocchi, 2003; Shuttleworth, 2007). Echter, de methode heeft vier beperkingen. Hierbij gaat het om het verstoren van de metingen door het instrument zelf, de ruimtelijke representativiteit van de metingen, en vooral het feit dat alle wervels die bijdragen aan de flux voldoende bemonsterd moeten worden. Daarnaast moet ook gedurende die bemonsteringsperiode (10-30 minuten) de turbulentie stationair zijn. Er zijn echter veel situaties waarbij de turbulentie niet stationair is over dergelijke lange periodes, denk daarbij aan wisselende bewolking of nachtelijke turbulentie die soms met tussenpozen ineens op kan komen. Gedurende dit soort situaties kan de eddy-covariantietechniek de fluxen niet nauwkeurig bepalen.

Scintillometrie is een indirecte fluxbepalingstechniek, die vrijwel niet gehinderd wordt door de hierboven beschreven beperkingen van de eddy-covariantietechniek en daardoor geschikt is om fluxen te meten tijdens niet stationaire omstandigheden. Een veldschaalscintillometer bestaat uit een zender en een ontvanger, die ongeveer 100 m tot 400 m uit elkaar moeten staan. De zender zendt een laserstraal uit met een constante lichtintensiteit. Op zijn weg door de atmosfeer wordt deze straal verstoord doordat turbulente wervelingen, eddies genaamd, net zoals lenzen de straal een beetje verstrooien, zodat de intensiteit van de straal zoals die gemeten wordt door de ontvanger niet constant is. Daarbij geldt, hoe sterker de turbulentie, hoe groter de gemeten variantie van het signaal. Essentieel voor de scintillometertechniek is dat de atmosferische turbulentie vooral wordt bepaald door de sterkte van de windwrijving met het aardoppervlak en door de warmte die vanaf het aardoppervlak opstijgt (overdag) of door de afkoeling die door het koude aardoppervlak plaatsvindt ('s nachts). Door de scintillometermetingen uit te werken kunnen de windwrijving (afgeleid van de binnenschaal van turbulentie, l_0 , en uitgedrukt in de impulsflux of wrijvingssnelheid, u^*) en de warmteflux (afgeleid van de structuurparameter van de brekingsindex, C_n^2 , en uitgedrukt als de voelbare warmtestroom, H) bepaald worden.

Het voordeel van de scintillometer zit hem daarin dat niet alle eddies bemonsterd worden, maar alleen eddies van een bepaalde grootte. Deze bemonstering vindt plaats over het hele scintillometerpad, waardoor de scintillometer binnen 1 minuut de waarde van de flux nauwkeurig kan bepalen die representatief is voor het hele pad. Kortom, de ideale techniek om fluxen te bepalen zou je zeggen. Toch zijn er nog enige kwesties die het onderzoek initieerde dat werd uitgevoerd binnen het project “Innovaties in de scintillometrie – het meten van oppervlakte fluxen van waterdamp, voelbare warmte en impuls over veld- tot kilometerschalen” van de Nederlandse stichting voor technologie en wetenschap (STW). De eerste kwestie is dat er systematische meetfouten waargenomen zijn in twee commercieel beschikbare scintillometers, namelijk in de “large-aperture” scintillometer van Kipp & Zonen en in de “displaced-beam” laserscintillometer van Scintec. In het eerste gedeelte (hoofdstuk 3-4) van dit proefschrift worden deze meetfouten behandeld. Het innovatieve in dit deel van het proefschrift zit hem daarin dat we wilden begrijpen waarom de meetfouten optreden. Daarnaast hebben we een prototype veldschaalscintillometer ontwikkeld, die geen last zou moeten hebben van de meetfouten die in de laserscintillometer zijn waargenomen en die bovendien gebruikt kan worden voor scintillometerpaden die langer zijn dan 200 m.

Ten tweede, en dit is het voornaamste deel van het proefschrift (hoofdstuk 5-7), is er de noodzaak om op veldschaal de massafluxen van grootheden te kunnen bepalen die passief door de turbulentie getransporteerd worden zoals waterdamp, CO₂ enz. Tot nu toe is er nog geen scintillometer commercieel beschikbaar die de massafluxen van deze passieve grootheden kan meten. Prototypes die verdamping over grote gebieden (> 1 km) kunnen bepalen zijn beschikbaar (Evans, 2009; Green et al., 2001; Meijninger et al., 2006; Meijninger et al., 2002a) en een commercieel systeem is in ontwikkeling. Deze scintillometers kunnen echter niet gebruikt worden voor veldschalen (< 500 m) en ze kunnen ook geen massafluxen van CO₂, CH₄, of fluxen van andere passieve grootheden bepalen. Daarom introduceren we in dit proefschrift vier methodes die de scintillometermetingen van de voelbare warmtestroom en de wrijvingssnelheid combineren met extra turbulentiemetingen van bijvoorbeeld waterdamp of CO₂. Dankzij deze methodes kunnen de voordelen van scintillometers gebruikt worden om de fluxen van passieve grootheden nauwkeurig te bepalen met een tijdsresolutie van 1 minuut.

Hoofdstuk 3: Analyse van de systematische fouten, gevonden in de Kipp & Zonen scintillometers met grote openingen (large-aperture scintillometers)

Studies hebben aangetoond dat de Kipp & Zonen scintillometers met grote openingen (K&ZLAS) systematische meetfouten vertonen bij het bepalen van de voelbare

warmtestroom, H . Op het observatorium van Chilbolton (Groot-Brittannië), hebben we een eigen studie gedaan waarin we vier K&ZLASsen hebben vergeleken met een scintillometer met grote opening van Wageningen universiteit. Daarbij hebben we de meetopstelling van de vorige studies verbeterd. De scintillometers waren zo opgesteld dat ze exact hetzelfde gebied bemonsterden en verder werden er langs het scintillometerpad onafhankelijke fluxmetingen gedaan. Dit stelde ons in staat om niet alleen H te vergelijken met onafhankelijke technieken (eddy-covariantie), maar ook de directe scintillometermetingen, de structuurparameter van de brekingsindex, C_n^2 . Verder hebben we een spectrale analyse toegepast om de onbewerkte metingen van de scintillometer te kunnen analyseren en zo de meetfouten te kunnen karakteriseren. In dit hoofdstuk zijn de resultaten van deze studie gepresenteerd waarbij twee belangrijke aspecten naar voren kwamen. Ten eerste bevestigt het onderzoek de robuustheid van de scintillometertechniek doordat de correlatiecoëfficiënten van de onderlinge vergelijkingen tussen de scintillometers altijd hoger waren dan 0.99. Ten tweede toont het onderzoek aan dat er twee soorten systematische meetfouten zitten in de K&ZLAS: een hoge- C_n^2 fout en een lage- C_n^2 fout. De lage- C_n^2 fout is een niet lineaire fout die veroorzaakt wordt door hoogfrequente ruis, die waarschijnlijk afkomstig is van het kalibratiecircuit dat in de ontvanger ingebouwd is. Deze fout is voor elke K&ZLAS verschillend, hij is significant voor $H \leq 50 \text{ W m}^{-2}$ en we stellen een oplossing voor om deze fout te elimineren met behulp van het gedemoduleerde signaal van de scintillometer. De meetfout die wij hebben gedefinieerd als de hoge- C_n^2 fout is dezelfde fout als die die is waargenomen in eerdere studies. Waarschijnlijk wordt deze meetfout veroorzaakt door een slechte plaatsing in het focale punt van de lens van zowel de lichtbron in de zender als de detector in de ontvanger. Hierdoor wordt in het huidige ontwerp van Kipp & Zonen niet de gehele lens effectief gebruikt. Deze fout is voor elke K&ZLAS verschillend (35% tot 240%) en hij kan alleen geelimineerd worden door een kalibratie te doen met een referentiescintillometer. Deze resultaten zijn met Kipp & Zonen gecommuniceerd, die aan de hand daarvan en nog een paar andere kwesties hun scintillometer helemaal opnieuw ontworpen hebben. Deze nieuwe scintillometer is onlangs (2011) op de markt gekomen.

Hoofdstuk 4: Instrumentele ontwikkeling: De terugkeer naar een scintillometerontwerp

De SLS20/SLS40 laserscintillometer met verschoven bundels (DBLS) is een scintillometer met een kleine opening, die metingen levert van de binnenschaal van turbulentie, l_0 , en de structuurparameter van de brekingsindex, C_n^2 . Kenmerkend voor de DBLS is dat hij fluxen bepaalt op veldschalen. Het is aangetoond dat warmtefluxen die bepaald zijn met de DBLS in

goede overeenstemming zijn met lokale eddy-covariantiemetingen, terwijl de specifieke metingen van l_0 en C_n^2 systematisch lijken te verschillen van de eddy-covariantiemetingen. Het eerste deel van dit hoofdstuk richt zich op de onderlinge vergelijking van vijf DBLSen, waarbij de variabiliteit van de l_0 - en C_n^2 -metingen is vergeleken. Het vergelijkingsexperiment is uitgevoerd in het kader van het LITFASS-2009 experiment. We hebben laten zien dat de metingen 42% van elkaar kunnen afwijken, zowel voor l_0 als voor C_n^2 . Dit suggereert dat voor elke DBLS een specifieke instrumentkalibratie noodzakelijk is, een oplossing die Scintec inmiddels (2012) in haar productieproces heeft geïmplementeerd. Het tweede deel van dit hoofdstuk richt zich op de ontwikkeling van een nieuwe veldschaalscintillometer. Naast het probleem van de systematische meetfouten is de DBLS van Scintec namelijk ook gevoelig voor verzadiging als het pad van de scintillometer langer wordt dan 200 – 300 m. Dit heeft er toe geleid een methode te onderzoeken die l_0 en C_n^2 meet door gebruik te maken van twee bundels met verschillende openingsgroottes. Eén opening moet klein zijn en daarmee gevoelig voor l_0 en de andere opening moet groot zijn en daarmee gevoelig voor C_n^2 . Theoretische overwegingen leidden tot de conclusie dat de combinatie van een 1-cm opening en een 10-cm opening de beste gevoeligheid geeft voor l_0 en tegelijkertijd ook voldoende de verzadiging tegen gaat voor paden langer dan 200 m. Deze scintillometer hebben we getest in het kader van het LITFASS-2012 experiment. De openingen van de scintillometer waren gedurende het experiment ingesteld op 1.75 cm en 10 cm, maar helaas lukte het niet met een openingsgrootte van 1 cm te werken omdat de signaalsterkte van de lichtbron niet sterk genoeg was (of de gevoeligheid van de ontvanger). Onafhankelijke eddy-covariantiemetingen lieten zien dat de scintillometer de fluxen niet goed kon reproduceren. De combinatie van een 1.75-cm opening en een 10-cm opening is namelijk vrijwel ongevoelig voor l_0 , als l_0 zich in de range van 2 mm – 6 mm bevindt (een groot deel van de natuurlijke range overdag). De methode an sich functioneert echter goed, want met een combinatie van een laser en een 1.75-cm opening of een 10-cm opening konden zowel l_0 als C_n^2 nauwkeurig bepaald worden.

Hoofdstuk 5: Het meten van H₂O en CO₂ fluxen over veldschalen met scintillometers: Deel I - introductie en validatie van vier methodes

In dit hoofdstuk introduceren we vier methodes voor het bepalen van turbulente stroomdichtheden van waterdamp en de koolstofdioxide, oftewel de verdamping en CO₂ flux. Deze methodes combineren scintillometermetingen met puntmetingen van de atmosferische grootheden (waterdamp, CO₂, etc.). Het voordeel hiervan is dat de flux sneller nauwkeurig bepaald kan worden dan door alleen gebruik te maken van de eddy-covariantietechniek. De

scintillometer bepaalt namelijk de gemiddelde waarden van de wrijvingsnelheid en voelbare warmtestroom voor het hele scintillometerpad (ruimtelijke middeling). Hierdoor hoeft de tijdsmiddeling maar 1 minuut te zijn als er gemeten wordt in gebieden met homogene turbulentie, zoals bijvoorbeeld een tarweveld. Het doel van dit hoofdstuk is om deze methodes uitvoerig te testen. Dit wordt gedaan door hun gevoeligheid te analyseren voor de grootheden die in de methodes gaan en door de methodes te valideren met eddy-covariantie data voor tijdsmiddelingintervallen van 30 minuten. De methodes waarom het gaat zijn: de Bowen-variantiemethode, de flux-variantiemethode, de structuurparametermethode en de energiebalansmethode. De gevoeligheidsanalyse laat zien dat elke methode gevoelig is voor zowel de wrijvingsnelheid als voor de turbulentiemetingen van de atmosferische grootheden die specifiek zijn voor die methode. Daaruit volgt dat de nauwkeurigheid van de fluxbepaling het resultaat is van een juiste weergave van de turbulentiegrootheden die door de methodes worden gebruikt. Daarnaast, toont de vergelijking van de 30-minuten fluxen aan dat de fluxschattingen van de methodes goed overeenstemmen met die van onafhankelijke fluxschattingen (de eddy-covariantietechniek). De structuurparametermethode komt het best overeen – de spreiding was laag (de correlatiecoëfficiënt, $r = 0.99$), terwijl de methode de verdamping met maar 5% onderschatte. Ook de andere methodes doen het goed ondanks het feit dat de energiebalans niet sloot en de variantiemethodes 's nachts negatief beïnvloed werden door het niet stationair zijn van het meetsignaal. Tot slot presenteren we nog een methode om de richting van de flux te bepalen (noch scintillometermetingen noch deze vier methodes geven namelijk een fluxrichting). Deze methode maakt gebruik van de correlatiecoëfficiënten tussen temperatuur en geeft in 95% dezelfde resultaten als eddy covariantie. De data die voor deze studie gebruikt zijn, werden verzameld in mei en juni 2009 over een tarweveld bij Merken, in Duitsland, in het kader van het Transregio32 programma.

Hoofdstuk 6: Het meten van H₂O en CO₂ fluxen over veldschalen met scintillometers: Deel II – verdamping voor 1-30 minuten tijdsmiddelingintervallen.

In dit hoofdstuk zetten we de evaluatie voort van vier methodes die de verdamping, L_vE , en CO₂ flux kunnen bepalen over 1 minuut. De focus ligt hierbij op de nauwkeurigheid van de 1-minuut gemiddelden van L_vE . Om de methodes te valideren voor deze korte middelingintervallen hebben we twee technieken toegepast. Ten eerste hebben we de systematische en willekeurige fout in L_vE bepaald die afhankelijk zijn van de middelingstijd. Ten tweede hebben we de methodes gevalideerd met een opzet van het Penman-Monteithmodel dat de warmte- en vochttopslagtermen negeert en er vanuit gaat dat de

gewasweerstand van het gewas constant is. Door gebruik te maken van deze twee validatietechnieken kunnen we aantonen dat de eddy-covariantietechniek en de energiebalansmethode ongeschikt zijn voor het bepalen van 1-min L_vE . Bij de eddy-covariantietechniek wordt dit veroorzaakt door de grote systematische en willekeurige meetfouten die de techniek heeft bij toepassing over 1-min middelingsintervallen en bij de energiebalansmethode wordt dit veroorzaakt door het negeren van de opslagstermen in de energiebalans. De drie andere methodes waren succesvoller in het bepalen van 1-min L_vE . De middelingstijd-afhankelijke fout was nog maar de helft van die van de eddy-covariantietechniek. Toch zijn er nog een paar dingen die het succes beperken. De Bowen-variantiemethode heeft een systematische meetfout van 0.05 en daarnaast kon 30% van de data niet gebruikt worden omdat de methode alleen werkt onder strengere voorwaarden en verder heeft de flux-variantiemethode een systematische fout van -0.15. De structuurparametermethode doet het het best van allemaal en bepaalt de 1-min L_vE nauwkeurig. Met deze methode hebben we kunnen bevestigen dat voor een homogeen gebied waarover het ensemblegemiddelde bepaald kan worden door middel van ruimtelijke middeling, Monin-Obukhov gelijkheidstheorie ook geldig is voor 1-min tijdmiddelingsintervallen. Daarnaast hebben we met deze methode kunnen aantonen dat de tarweplanten L_vE beïnvloeden, terwijl de turbulentie, het transport mechanisme, constant blijft.

Hoofdstuk 7: Het meten van H_2O en CO_2 fluxen over veldschalen met scintillometers: deel III – koolstofdioxidefluxen en vegetatieprocessen voor 1-30 minuten tijdmiddelingsintervallen

Dit is het laatste hoofdstuk dat de evaluatie behandelt van vier methodes die de verdamping, L_vE , en CO_2 flux, FCO_2 , kunnen bepalen over een tijdmiddelingsinterval van 1 minuut. Het doel is de nauwkeurigheid van de FCO_2 schatting te bepalen en de 1-min fluxen te gebruiken om flux- en vegetatiereactie die volgt op veranderende zonnestraling te bestuderen. De validatie van FCO_2 komt overeen met die van L_vE , waaruit we concluderen dat deze resultaten geldig zijn voor de flux van elke willekeurige passieve grootheid in de atmosfeer. De validatie toont aan dat de eddy-covariantietechniek ongeschikt is voor het bepalen van 1-min fluxen, terwijl de drie andere methodes duidelijk succesvoller zijn. De middelingstijd-afhankelijke meetfout van de drie methodes is maar de helft van die van de eddy-covariantietechniek. Toch zijn er ook hier nog wat kwesties die het succes beperken. Weer heeft de Bowen-variantiemethode een middelingstijd-afhankelijke systematische meetfout van +0.09 en ook hier kan 30% van de data niet gebruikt worden omdat de methode alleen werkt

onder strengere voorwaarden. Daarnaast heb ik ook de flux-variantiemethode weer een -0.16 systematische meetfout. De structuurparameter methode doet het het best en bepaalt FCO_2 nauwkeurig. Met deze methode hebben we nog een laatste validatie gedaan met behulp van LITFASS-2009data (gemeten in Lindenberg, Duitsland). Hiermee hebben we kunnen aantonen dat ook onder drogere omstandigheden (Bowen ratio ~ 2.5) de methode nauwkeurig FCO_2 kan bepalen, hoewel L_vE lastiger was te bepalen. Tot slot hebben we de structuurparameter methode succesvol toegepast op omstandigheden met niet-stationaire turbulentie. Ten eerste, konden we zo aantonen dat FCO_2 en L_vE een verschillende staprespons hebben als gevolg van abrupte veranderingen in de zonnestraling. Dit komt doordat verschillende processen deze fluxen aansturen. Ten tweede, hebben we aangetoond dat er een tijdsverschuiving van 2 minuten zit tussen de fluxen en de straling. Het in acht nemen van deze tijdsverschuiving is essentieel voor het bepalen van lichtverzadigingskrommen, zowel wanneer deze gebaseerd zijn op 1 als op 30 minuutgemiddelden. Hierbij hebben we meteen ook de relevantie laten zien van de 1-minuut fluxen voor het bepalen van lichtverzadigingskrommen voor omstandigheden met verschillende temperatuur en luchtvochtigheid. Daarbij lieten we zien dat de tarweplanten efficiënter met licht omgaan als het vochttekort in de atmosfeer klein is. Ten derde, laten we zien dat de 1-min gewasweerstand nauwkeurig kan worden bepaald via de weerstandsuitdrukkingen voor H en L_vE . Daarmee konden we bevestigen dat de tarwe zijn gewasweerstand binnen enkele minuten significant kan veranderen (doordat de planten hun huidmondjes sluiten) en zo de turbulente fluxen binnen een paar minuten kan beïnvloeden. Of ze dat ook daadwerkelijk doen is afhankelijk van de lokale omstandigheden.

Dankwoord/Acknowledgements/Danksagung

Na vier jaar is het dan zo ver, het proefschrift is af. De negen jaar die ik in Wageningen heb doorgebracht zijn voorbij gevlogen, wat uiteindelijk geresulteerd heeft in dit proefschrift. Natuurlijk is het niet alleen mijn eigen werk en had ik het nooit kunnen volbrengen zonder de ondersteuning, hulp en vriendschap van velen.

Als eerste wil ik hier natuurlijk Oscar bedanken. Jij zag het al zitten dat ik een promotietraject ging doen een jaar voordat ik klaar was met mijn studie. Wat mij betreft was het een groot succes en ik wil je in ieder geval enorm bedanken voor alle dingen die je me bijgebracht hebt. Al het experimentele werk, het geduld met mijn schrijfvaardigheid, onze discussies, de artikelen, alles komt hier samen in het proefschrift dat het resultaat is van een samenwerking die uiteindelijk bijna 6 jaar heeft geduurd, eerst als student en later als promovendus. Dank je wel daarvoor! Ook Arnold wil ik bedanken voor alle discussies die we gehad hebben. Het heeft me goed gedaan om ook bij jou binnen te kunnen vallen om dingen door te spreken en van gedachten te wisselen over gewassen, fotosynthese, structuurparameters en al wat er nog niet meer voorbij kwam. Daniëlle, Miranda, Anneke en ook Linda, ik wil jullie bij deze graag bedanken voor al jullie hulp bij de experimenten en jullie inzet daarbij. Jullie weten als geen ander dat je experimenteel werk niet alleen kan doen. Ook het ondersteunende werk van Frits, Willie en Kees kan ik niet vergeten, want zonder hen zou ons experimentele werk heel wat lastiger zijn. Verder wil ik ook alle andere mensen van de vakgroep bedanken die eerst in een klein aantal, maar later in steeds grotere getale, elke dag op de vakgroep te vinden waren. Mensen, dank jullie wel voor alle collegialiteit, lunchpauzes, etentjes, (rare) discussies en ondersteuning in alle aspecten.

Then, I would also like to thank our British colleagues, who during the Chilbolton experiment greatly supported us. First of all I thank Charles Wrench and Darcy Ladd from the Chilbolton Observatory for making their wonderful facilities available to us. Also, I thank Sue Grimmond and Mariana Gouvea from King's College London for their help and making available to us two large-aperture scintillometers. Furthermore, I thank Jan, Mal, Judy, Joe, Owain, Dave, and Lorna for their assistance, kindness and hospitality during all parts of the Chilbolton experiment. Without you guys it would have been impossible. Finally, I thank Helen Ward and Jonathan Evans from the Centre for Ecology and Hydrology (CEH), Wallingford for his great help during the Chilbolton experiment and the LITFASS-2009 campaign. Jon, thank you for providing both your large-aperture scintillometer and your

microwave scintillometer to us, the wonderful cooperation with you and giving me the possibility to visit the CEH and the beautiful city of Oxford.

Auch meinen Deutschen Kollegen will ich gern danken. Die Zusammenarbeit fing schon während meiner Praktikumszeit in Lindenberg an. Es hat mir sehr gut gefallen mit euch zu arbeiten und es war mir in den letzten Jahren immer wieder eine Freude zurück zu kommen. Besonders will ich hier Frank Beyrich danken. Frank, danke für dein Engagement in der Scintillometerarbeit bzw. meiner Scintillometerarbeit, sowie deine effiziente und gute Leitung während der LITFASS-Experimenten und anverwandter Experimenten/Treffen. Das alles wäre allerdings unmöglich gewesen ohne die Hilfe und das Wohlwollen der MOL2-Mitarbeiter. Ullrich, Petra, Claudia, Georg, Peter, Udo, Jens, Sieghard, Doreen, Gerd und alle anderen, danke für eure Hilfe und euren Einsatz, die es uns immer wieder ermöglichten, die Experimente erfolgreich durch zu führen. Weiterhin möchte ich noch meinem Kollege Alexander Graf des Forschungszentrums Jülich für seine Hilfe bei den beiden Transregio-Experimenten und bei der Auswertung der Daten ganz herzlich danken.

Ook op het persoonlijke vlak zijn er nog velen die een rol van betekenis hebben gespeeld. Natuurlijk zijn er de Ichthianen uit Wageningen met wie ik vele middagen en avonden door heb gebracht op kringavonden, maaltijden en vele andere activiteiten die een vereniging als Ichthus rijk is. Mensen ook jullie allemaal hartelijk bedankt voor jullie tijd, het met elkaar plezier hebben, nadenken over God, gezamenlijke weekenden, en nog zoveel meer mooie dingen. Ik heb ervan genoten. Loek ook jou wil ik hier graag bedanken, simpelweg voor het feit dat je altijd een luisterend oor hebt en me zo vaak in Megen hebt willen ontvangen. Dankjewel daarvoor!

Gerd, Anne, Lena, Karl und Georg, ohne euch hätte die Welt ganz anders ausgesehen. Danke für eure Gastfreiheit und Freundschaft, ihr alle habt mir bei euch ein Heim geschaffen, wo ich mich recht wohl fühle. Danke für alle Schachspiele, Gespräche, Kuchen, das Draußensein, und den Fakt, dass ich die Glienicker Räuber und ihre Burgen mit Graben und ihre Ruinen kennen lernen konnte. Karl, Gerd, ich kann euch sagen, von mir aus können die Saurier gegrillt werden, ich bin fertig :-).

Natuurlijk wil ik ook mijn ouders en broer en zus nog bedanken. Paps, mamschen, Joost en Inge dank jullie voor jullie support en ondersteuning in al die jaren. Ik hoop dat ik er een beetje in geslaagd ben duidelijk te maken waar het nou allemaal om ging bij mijn werk. Hoe het ook zij, ik denk dat we in ieder geval kunnen stellen dat het allemaal is goed gekomen!

And last but not least, my dear friend Annemarie. The time of writing my thesis and emails to you finally seems to end. Really, what would this thesis be without you? I simply want to thank you here. Thank you for listening to me when I was excited about the research as well as when I was fed up with it. Furthermore, I want to thank you for the wonderful design of this thesis cover. However, above all thank you that you kept waiting for me to be finished, that you always could laugh about things, that you showed me that there are more things important than work. Thank you for being my friend.

Mijn dankwoord wil ik eindigen met een tekst die me over de afgelopen jaren steeds weer heeft geïnspireerd. Het gaat over Job, een man die worstelde met God. Een man, die zich realiseert hoe geweldig de mens is. Toch vraagt ook hij zich af waar de wijsheid (het vermogen om verstandig te handelen) gevonden wordt: Job 28:20-28:

De wijsheid dus, waar komt zij vandaan,

en waar is de plaats van het inzicht?

Zij is bedekt voor de ogen van alle levenden,

en voor de vogels in de lucht is zij verborgen.

Het verderf en de dood zeggen:

Met onze oren hebben wij slechts een gerucht over haar gehoord.

God begrijpt haar weg,

en Hij kent haar plaats.

Want Hij ziet tot aan de einden der aarde,

Hij ziet onder heel de hemel,

terwijl Hij de kracht van de wind bepaalt,

en de wateren meet met een maat.

Toen Hij een verordening maakte voor de regen,

en een weg voor het weerlicht van de donder –

toen zag Hij haar, en peilde haar.

Hij stelde haar vast en ook onderzocht Hij haar.

Maar tegen de mens heeft Hij gezegd:

Zie, ontzag voor de Heer, dat is wijsheid,

en zich afkeren van het kwade, dat is inzicht.

Sense certificate



Netherlands Research School for the
Socio-Economic and Natural Sciences of the Environment

C E R T I F I C A T E

The Netherlands Research School for the
Socio-Economic and Natural Sciences of the Environment
(SENSE), declares that

A.J.H. van Kesteren

born on 26 November 1984 in Tilburg, the Netherlands

has successfully fulfilled all requirements of the
Educational Programme of SENSE.

Wageningen, 17 December 2012

the Chairman of the SENSE board

Prof. dr. Rik Leemans

the SENSE Director of Education

Dr. Ad van Dommelen

The SENSE Research School has been accredited by the Royal Netherlands Academy of Arts and Sciences (KNAW)



K O N I N K L I J K E N E D E R L A N D S E
A K A D E M I E V A N W E T E N S C H A P P E N



The SENSE Research School declares that **Mr. A.J.H. van Kesteren** has successfully fulfilled all requirements of the Educational PhD Programme of SENSE with a work load of 40 ECTS, including the following activities:

SENSE PhD Courses

- o Environmental Research in Context
- o Research Context Activity: Co-organizing SENSE Symposium on Land-Water-Atmosphere Interactions, Wageningen, 9 March 2010
- o The art of modelling
- o Biogeochemistry and physics of the lower atmosphere

Other PhD Courses

- o Scientific Publishing
- o PhD competence assessment
- o The art of writing
- o Techniques for Writing and Presenting Scientific Papers
- o Scientific Writing

Didactic Skills Training

- o Supervision of one MSc thesis
- o Lecturer for the course *Inleiding Atmosfeer*
- o Lecturer for the Meteorology and Air Quality Group orientation day

External training at a foreign research institute

- o Scintillometer intercomparison- experiment, Meteorological observatory Lindenberg, Germany

Oral Presentations

- o *A new method to obtain minute interval mass fluxes of H₂O and CO₂ using scintillometry and scalar turbulence measurements.* Awarded as Commendable Presentation at the 30th AMS Conference on Agricultural and Forest Meteorology, 29 May – 1 June, 2012, Boston, USA.
- o *Measuring turbulent fluxes of heat, momentum and water vapour with optical field scale scintillometers.* Optical Propagation through the Turbulent Atmosphere (OPTA), 20-21 October 2009, St. Louis, France, and Buys-ballot research school (BBOS) meeting, 28-30 October 2009, Oisterwijk, the Netherlands
- o *Combining scintillometry and scalar turbulence measurements to obtain minute interval mass fluxes of H₂O and CO₂.* SENSE Symposium 'Land Water Atmosphere Interactions', 9 March 2009, Wageningen, the Netherlands

SENSE Coordinator PhD Education and Research

Mr. Johan Feenstra

Professional CV



Personal information

Name: A.J.H. (Bram) van Kesteren, MSc

Date of birth, place: 26 November 1984, Tilburg (NL)

Nationality: Dutch

Education

Since 09/2008
Defence (17 December 2012) PhD on the project “Innovations in Scintillometry: Measuring surface fluxes of water vapour, sensible heat and momentum on field to kilometre scale”, Meteorology and Air Quality group, Wageningen University

09/2006 – 09/2008 Master Meteorology and Air Quality, Wageningen University

09/2003 – 08/2006 Bachelor Soil, Water and Atmosphere, Wageningen University

08/1997 – 06/2003 VWO (pre-university education), Dr. Mollercollege, - Kaatsheuvel/Waalwijk

Award

Commendable presentation award for the presentation: “A new method to obtain minute interval mass fluxes of H₂O and CO₂ using scintillometry and scalar turbulence measurements”, Presented at the Agricultural and Forest meteorology conference in Boston, 1 June 2012.

Scientific publications

- Van Kesteren, B.**, Hartogensis, O.K., van Dinther, D., Moene, A.F., De Bruin, H.A.R., Holtslag, A.A.M., 2012, *Measuring H₂O and CO₂ fluxes at field scales with scintillometry: Part II – validation and application of 1-minute flux estimates*. Agric. Forest. Meteorol., accepted with major revisions
- Van Kesteren, B.**, Hartogensis, O.K., van Dinther, D., Moene, A.F., De Bruin, H.A.R., 2012, *Measuring H₂O and CO₂ fluxes at field scales with scintillometry: Part I – introduction and validation of four methods*. Agric. Forest. Meteorol., doi 10.1016/j.agrformet.2012.09.013
- Beyrich, F., Bange, J., Hartogensis, O.K., Raasch, S., Braam, M., van Dinther, D., Gräf, D., **Van Kesteren, B.**, Van den Kroonenberg, A.C., Maronga, B., Martin, S., Moene, A.F., 2012, *Towards a validation of scintillometer measurements: The LITFASS-2009 experiment*, Boundary-Layer Meteorol., 144:83-112
- Van Kesteren, B.** and Hartogensis, O.K., 2011, *Analysis of the systematic errors found in the Kipp & Zonen large-aperture scintillometer*, Boundary-Layer Meteorol., 138: 493-509
- Van Kesteren B.**, 2008, Sensible and latent heat fluxes with optical and millimetre wave scintillometers. Master Thesis, Wageningen University, Wageningen, the Netherlands, 99pp (Master thesis, not published)

Participated in the field experiments

2012	LITFASS 2012
2011	BLLAST 2011 http://bllast.sedoo.fr/campaigns/2011/
2009, 2010	LITFASS 2009 http://meetingorganizer.copernicus.org/EMS2011/EMS2011-806.pdf
2008, 2009	Transregio32/FLUXPAT http://tr32.uni-koeln.de/index.php
2008 – 2012	Educational energy-/water-balance experiments in the Hupsel catchment.
2007	Chilbolton 2007 http://nora.nerc.ac.uk/3016/

Personal interests

Cycling, hiking in the mountains, being in nature, reading, meeting friends, listening music, have a fascination for people with faith.

Index

amplitude fluctuations	45
aperture size	50, 60, 75, 83
atmospheric resistance	154
averaging	15, 123, 132, 136, 137
Born approximation	43
bottleneck phenomenon	28, 177
boundary layer	3, 11
Bowen ratio	56, 98
Bowen-variance method	98, 107, 113, 134, 139, 143, 159, 161, 163
Buckingham-Pi theory	14
budget equations	11, 31
canopy resistance	154, 170
chemical quantities	175, 176
Chilbolton experiment	60
CO ₂ flux	5, 110, 116, 149, 166
combined methods	98
convection	3
covariance	15
diffraction	39
dispersion	39
dissimilarity	36, 99, 113, 175
dissipation range	23, 28
eddies	21, 39, 47, 53
eddy covariance	5, 95, 101, 132, 136, 139, 158, 161, 163
energy cascade	21, 23
energy-balance closure	101, 115, 140, 154, 171, 178
energy-balance method	101, 108, 115, 134, 140
ensemble averaging	<i>See</i> averaging
entrainment	3, 175
error	
averaging-time-dependent	124, 132, 136, 158, 161
high- C_n^2	69, 74
LAS	59
low- C_n^2	69, 71, 89
measurement	59, 81, 88, 89, 103
SLS	81, 103
evapotranspiration	5, 6, 13, 34, 36, 110, 121, 166
fast-response hygrometer	<i>See</i> eddy covariance
flux direction estimation	118
flux divergence	32
flux-variance method	98, 107, 112, 134, 139, 143, 159, 161, 163
footprint	49, 116
free convection	36
Fresnel zone	40, 84
friction velocity	33, 36, 87, 109
geometrical optics	42
heterogeneous	<i>See</i> turbulence
Hill bump	28, 177

homogeneous	<i>See</i> turbulence
inertial sub-range	22, 27
inner scale	23, 24, 26, 57, 79, 90, 106, 176
intensity fluctuations	46
irradiance	46
Kolmogorov micro scale	21
latent-heat flux	<i>See</i> evapotranspiration
light-response curve	168
LITFASS-2009	79, 156
LITFASS-2012	85
logarithmic amplitude fluctuations	45
logarithmic intensity fluctuations	46
Maxwell equations	41
momentum flux	<i>See</i> friction velocity
Monin-Obukhov similarity theory	33, 106, 136, 175
Navier-Stokes equations	12, 31
Obukhov length	33, 36
Ogive	126, 159
passive scalar	31, 94, 163, 175
path averaging	<i>See</i> averaging
path weighting	<i>See</i> scintillometer
Penman-Monteith	129, 140, 154, 171
photosynthesis	5, 153
plant physiology	145, 171
polarization	42
production range	22
radiation-response curve	168
refraction	39
refractive index	38
relative transport efficiency	99, 114
resistance expressions	154, 170
respiration	153
Reynolds decomposition	15
Reynolds number	21
Rytov method	43
saturation	51, 83
scalars	13
scattering	39, 53
scintillometer	6, 123, 137
development	79, 176
displaced-beam	6, 52, 79
eddy weighting	48
equation	45
flux direction estimation	118
large-aperture	6, 51, 59
path weighting	47, 48, 49, 84
point-source	45
sensible-heat flux	5, 6, 34, 36, 87, 109
sensitivity analysis	105
similarity theory	<i>See</i> Monin-Obukhov similarity theory

SLS	<i>See</i> scintillometer
sonic anemometer	<i>See</i> eddy covariance
spectral bump	28
spectrum	19
atmospheric	22
dissipation range	28
inertial sub-range	27
measured	69, 88
temperature	27
stomata	145, 171
stomatal resistance	<i>See</i> canopy resistance
storage changes	<i>See</i> energy-balance closure
structure function	16
structure parameter	35, 54, 115, 126, 135
measuring	28, 100
refractive index	54
temperature	26, 55
velocity	25
structure-parameter method	100, 108, 115, 134, 139, 143, 159, 161, 163, 164
surface layer	5, 33
time lag	139
Transregio-2008	156
Transregio-2009	101, 130, 155
turbulence	143
atmospheric	21
heterogeneous	176
homogeneous	16, 20, 32, 136, 175
isotropic	16, 20
locally homogeneous	17, 20
locally isotropic	18, 20
stationary	16, 17, 19
turbulent eddies	21
turbulent flux	4, 5, 33, 34
variance	15, 19
water-use efficiency	145, 169
water-vapour deficit	168, 171
wave equation	41
wave propagation	38

The research described in this thesis was financially supported by the Dutch Technology Foundation (STW) under project number WTC7478.

Financial support from Wageningen University for printing this thesis is gratefully acknowledged.